NASA SP-286

SIGNIFICANT ACCOMPLISHMENTS IN SCIENCES

Goddard Space Flight Center, 1970

A symposium held at

GODDARD SPACE FLIGHT CENTER

January 14, 1971

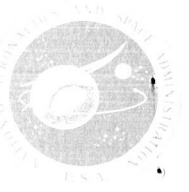

NATIONAL AERONAUTICS AND SPACE ADMINISTRATION

NASA SP-286

SIGNIFICANT ACCOMPLISHMENTS IN SCIENCES

GODDARD SPACE FLIGHT CENTER, 1970

The proceedings of a symposium held at the NASA Goddard Space Flight Center, January 14, 1971

Prepared by Goddard Space Flight Center

Scientific and Technical Information Office 1972
NATIONAL AERONAUTICS AND SPACE ADMINISTRATION
Washington, D.C.

FOREWORD

This is an almost-verbatim transcript of a symposium held at Goddard Space Flight Center, Greenbelt, Maryland, on January 14, 1971. No attempt has been made to introduce editorial or stylistic uniformity in the talks; on the contrary, an effort has been made to retain the informality of the proceedings.

The sole major change results from NASA policy, which now requires in all formal publications the use of international metric units according to the Systeme International d'Unites (SI). However, in certain cases, utility requires the retention of other systems of units in addition to the SI units. The conventional units stated in parenthesis following the computed SI equivalents are the basis of the measurements and calculations reported here.

NATIONAL AERONAUTICS AND SPACE ADMINISTRATION

For sale by the Clearinghouse for Federal Scientific and Technical Information
Springfield, Virginia 22151 – Price $3.00

CONTENTS

*National Academy of Sciences resident research associate

*National Academy of Sciences resident research associate

*National Academy of Sciences resident research associate

INTRODUCTION

Dr. Leslie H. Meredith
Deputy Director of Space and Earth Sciences

I think most of the people who are going to make it through the storm in the reasonably near future are here now, so we will start the meeting. You will note that the first change in the program is that Dr. Pieper, who is the session chairman, is not here. My name is Les Meredith.

I would like, of course, to thank everybody who did make the effort to come. There are certain advantages to having a small audience. I think that it will make it possible to have questions after the individual talks. If we get very far behind in the schedule, I will have to restrict things, but until then feel free to ask questions.

So without postponing things further, I will call on the first speaker, Dr. Short, who will be talking on the geological features in Wyoming as seen from Nimbus 1.

GEOLOGICAL FEATURES IN WYOMING FROM NIMBUS 1

Dr. Nicholas Short

The main product of the earth resources technology satellites will be multispectral photographs in which ground scenes are displayed as patterns described by variations in gray level. Until more sophisticated techniques evolve, early interpretations will depend heavily on correlation of the patterns with existing ground truth information, and particularly with maps of different kinds.

Just how effective will these correlations be, and what limitations do we face? To see this, I have examined one of the best TV images yet obtained from Nimbus satellites to compare its information content with data acquired for this region by specialists in several disciplines.

Two words of caution: First, Nimbus TV imagery tells us little that is new about the permanent ground scene, owing to its limited resolution, at best about a kilometer. In adequately studied areas, surface mapping provides much more detail and at higher accuracy than is possible for many Nimbus images.

Second, for most regions there is a glaring scarcity of maps at Nimbus scales which define, locate, and depict specific categories of objects responsible for variations in and reflectivity of albedo. Most such maps show the distribution of features, some of which are nonsurficial or three-dimensional, that have little relation to the spectral characteristics of groups of different objects at the surface.

So, restating the basic question, to what extent can we identify and analyze the ground features displayed in Nimbus photos and, by inference, ERTS photos, by direct comparisons with topography, geology, soils, and vegetation maps?

Figure 1 is a Nimbus 1 photo, covering about 500 kilometers on a side, that shows the southwestern third of Wyoming, the northwestern part of Colorado, the northeastern part of Utah, and a small part of Idaho. We can readily see such major features as the Wind River, the Uinta and the Wasatch Mountains, the Green River, Wind River, and Uinta basins, and the headwaters of the Wind River and the Green River.

A glance at a topographic map of the same area clearly shows a relation between topographic highs, or uplands, and darker areas on the photos. Why? Largely

because of the association of Douglas fir and spruce with the higher elevations. Grasslands, appearing as intermediate gray tones, occur in the higher parts of the basins. Within the lower basins, the prevailing vegetation is sage, saltbrush, and greasewood, spatially distributed in densities too low to be a major influence on the more highly reflective soils, alluvium, and sedimentary rocks responsible for the lighter gray tones.

The correspondence between geology, topography, and vegetation is again evident when we compare the Nimbus photo with a geological map of the region (Figure 2). For this area, the variations in altitude that give rise to striking differences in tonal patterns are caused mainly by structural uplifts and deformations. We can readily recognize the folded Wyoming, Hoback, and northern Wasatch ranges because of their forest cover. The string of small dark patches extending south of the Sweetwater arch are block-faulted and folded mountains rising high enough above the basins to develop thick stands of deciduous and coniferous trees.

Generally, very different rock types, such as the granites of the Wind River and the Uinta mountains as compared with the sediments of the basin, have similar albedos, so that they cannot be differentiated by tone alone. Note, however, that bands of intermediate gray correspond broadly to upper Cretaceous rocks. These units are generally sandy and foster the growth of grass, sage, and small cedars in denser clusters. It is this effect that allows the Rock Springs uplift to be seen.

Why do we see tonal variations in basins? Comparison of the gray-scale patterns with a soils map for the Green River (Figure 3) indicates that here and there we get crude matches between soils types and distinct tonal patterns. But the correlation is broad and poor at most. Thus, this northeast band fails to associate with any soils distribution at all. I suspect that the distribution of the generally sparse vegetation within these semidesert basins is rather insensitive to variations in soils types. However, the previous criteria by which pedologists have been categorizing different soils may bear little direct connection with their spectral properties at the surface, so that our maps are valid only when the subsurface soil profile is included in the definition.

The main conclusions from this study are these: In a semiarid region, high topographic relief shows good coassociation with exposed geology and with vegetation and, to a lesser degree, with soils types, leading to strong correlations between scene patterns and ground truth. In the lower, flatter basins, most tonal patterns are related to subtle variations in soil color and percentage of vegetation cover, with the latter changing seasonally.

A detailed field program involving reflectance measurements of individual and mixed objects is clearly required to establish the controlling factors. Even then, we will probably need to generate new kinds of maps based mainly on spectral parameters as the proper descriptors of surface features.

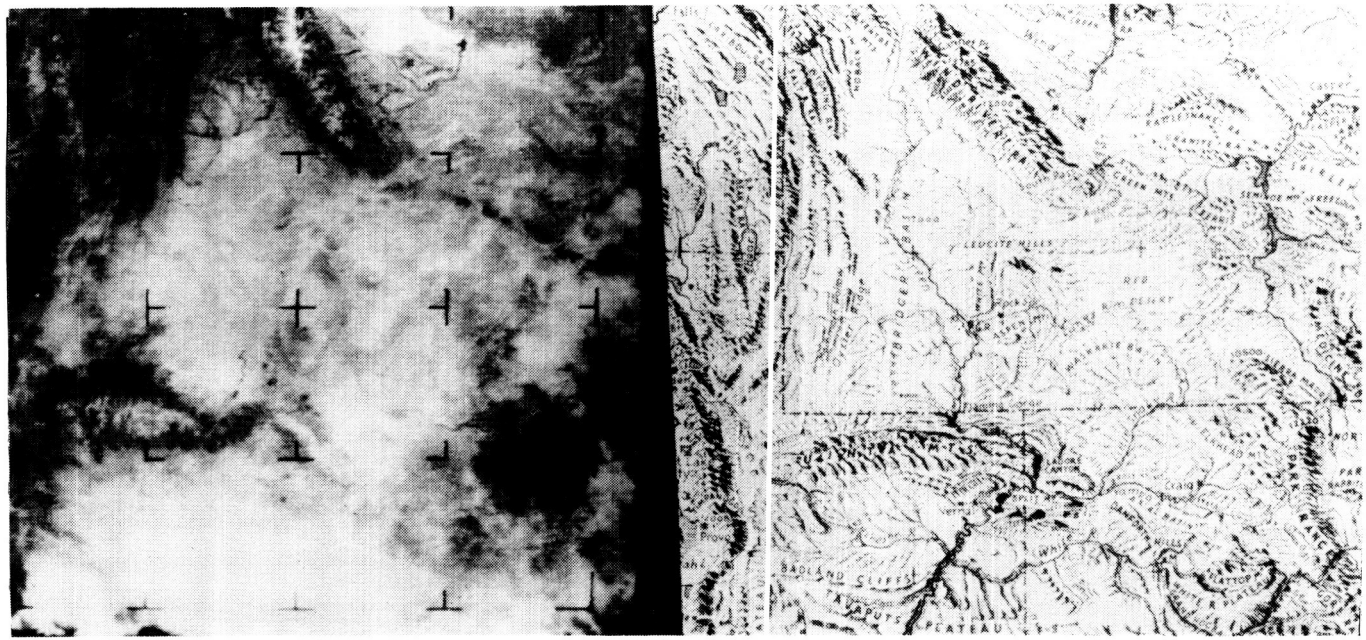

Figure 1: Left: A photographic image taken by the Advanced Vidicon Camera System (AVCS) on Nimbus I during Orbit 109 (Sept. 4, 1964) from an altitude of 725 km showing parts of Wyoming, Colorado, Utah and Idaho; Right – A portion of the Physiographic Map of the United States (E. Raisz) in which the main topographic features on the Nimbus image have been identified (Note: image is unrectified).

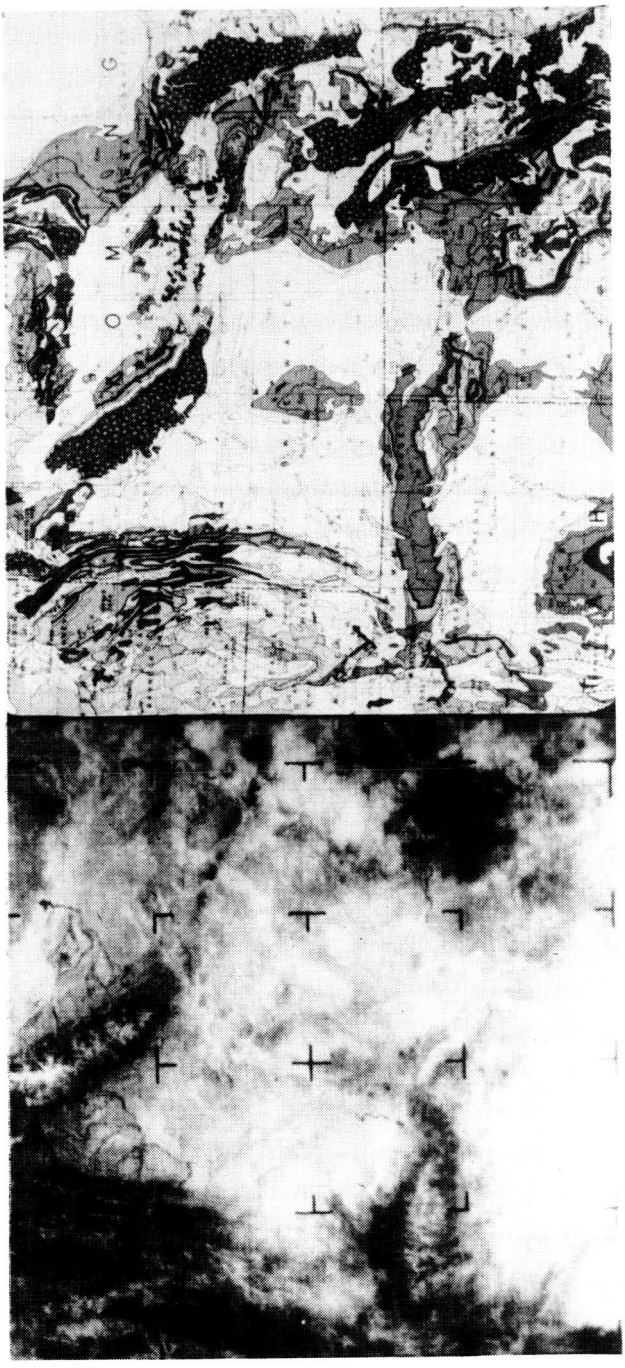

Figure 2. Left: Same as Figure 1 left. Right: A portion of the Geologic Map of the United States in which the area corresponds with that in Figure 1, right and left.

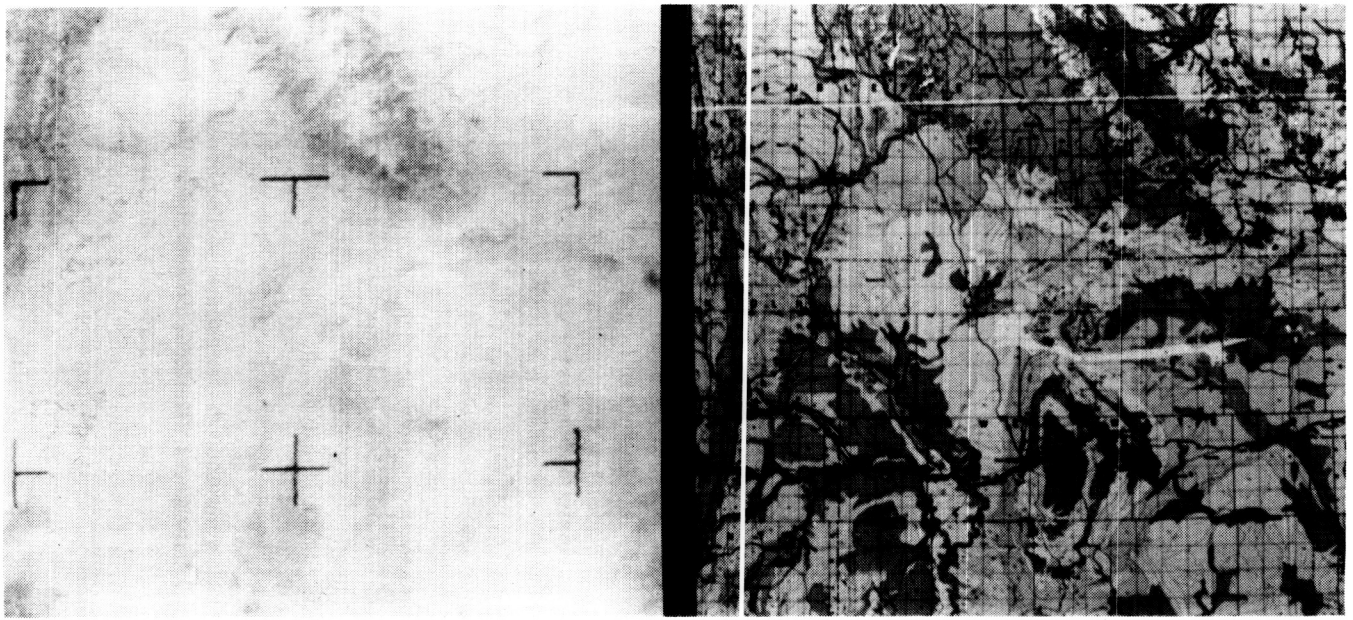

Figure 3. Left: A part of the Nimbus I image enlarged to show only the area within the Green River basin; Right – The same area, displayed in the Soils Map of Wyoming.

HYDROLOGY OF THE NIGER RIVER FROM NIMBUS HRIR

Dr. Norman MacLeod

This paper describes the seasonal changes in aspect of the Niger River in the Republic of Mali, West Africa, as seen in daytime imagery obtained by the high-resolution infrared radiometer on Nimbus 3. This imagery is produced by reflection of solar radiation in the spectral region from 0.7 to 1.3 micrometers, principally at 1 micrometer. As water absorbs most of the radiation at 1 micrometer, the oceans, lakes, and rivers appear dark. Clouds reflect most of the radiation and are bright; quartz sands, such as those in the Sahara Desert, are almost as bright as clouds.

Plant communities vary systematically in reflectance; for example, Figure 1 shows a tropical rain forest on the south coast of West Africa that is brighter than the broad band of savannah to the north. The desert steppe north of the savannah is brighter than the savannah, but not as bright as the sands of the Sahara. The imagery thus forms an ecological map of the region, one that changes with time.

Figure 1 shows the aspect of the area in May 1969: the course of the Niger River is visible, rising in the highlands of Guinea, the Ivory Coast, and Upper Volta, and flowing east-northeast through Bamako to Segou, as shown on the map of Figure 2. At Mopti, the Niger is joined by the Bani, which flows due north to this junction. The combined river flows northward almost as far as Tombouctou, just east of the dark arrowhead (Lac Fagubine), and eastward from Tombouctou to Gao.

The Niger then turns south and flows through Niger and Nigeria to its delta at the Atlantic Ocean. The difference in elevation between Segou and Goa is about 40 meters, though the linear distance is some hundreds of kilometers; the country is thus very flat, and the hydraulic gradient between Segou and Mopti is very small.

In this region, a summer monsoon that penetrates to Tombouctou by late June continues until early August; Tombouctou gets about 254 millimeters (10 inches) of rainfall each summer, and is very dry and dusty the rest of the year. Further south, in Bamako and Mopti, the monsoon starts in May and lasts through October. The southern coast of West Africa has rain 12 months of the year. The change in the aspect of the Niger basin from May (Figure 1) to July (Figure 3) is due to the accumulation of runoff in a huge area of Mali

known as the Inland Delta. The open-water surface of this region is approximately 41,440 kilometers^2 (16,000 square miles) at maximum flood stage. The water of the Inland Delta is nonsaline, even though the Sahara Desert is directly to the north; indeed, the northern sector of the Inland Delta is filled with sand dunes. In Figure 3, there seems to be at Segou an older channel of the Niger that runs to the northwest. It is possible that the channel appears darker here than in Figure 1 because of the subsurface flow of water; this information is not visible in the IDCS (visible-region) data. This channel may prove useful for irrigation purposes in the future.

By November (Figure 4), the Inland Delta is full of water and appears very dark in the image. The precipitation from the monsoon ceased a month earlier, and only a third of the water passing Segou and Mopti passes Gao; the remainder is lost through seepage, infiltration, and evaporation. Little is used for irrigation, because the region is used for grazing and shifting cultivation. The amount of water lost is equal to about two-thirds the volume of Lake Erie.

What can we learn from this imagery? It is apparent that an enormous supply of fresh water – far larger than that subsurface water recently discovered in Libya – has been found flowing through an arid region and is renewed yearly during the summer monsoon. The Inland Delta is a natural irrigation structure located in the middle of the desert. Nimbus imagery makes obvious that which was known earlier by some specialists, by providing an integrated view of the entire watershed on a daily basis. The imagery may also reveal useful routes for irrigation channels, such as that from Segou northwest; the existence of this channel is not obvious. Perhaps Nimbus imagery can point out future roads to a greener desert.

Data from Nimbus can now be handled quantitatively, as well as in the qualitative mode used here; it may thus enable estimations of the location, amount, and seasonal changes in water available, even with the low resolution of the Nimbus sensor. These data can be made available to governments for their use in better management of natural resources, in this case to the Republic of Mali and its part of the Niger River.

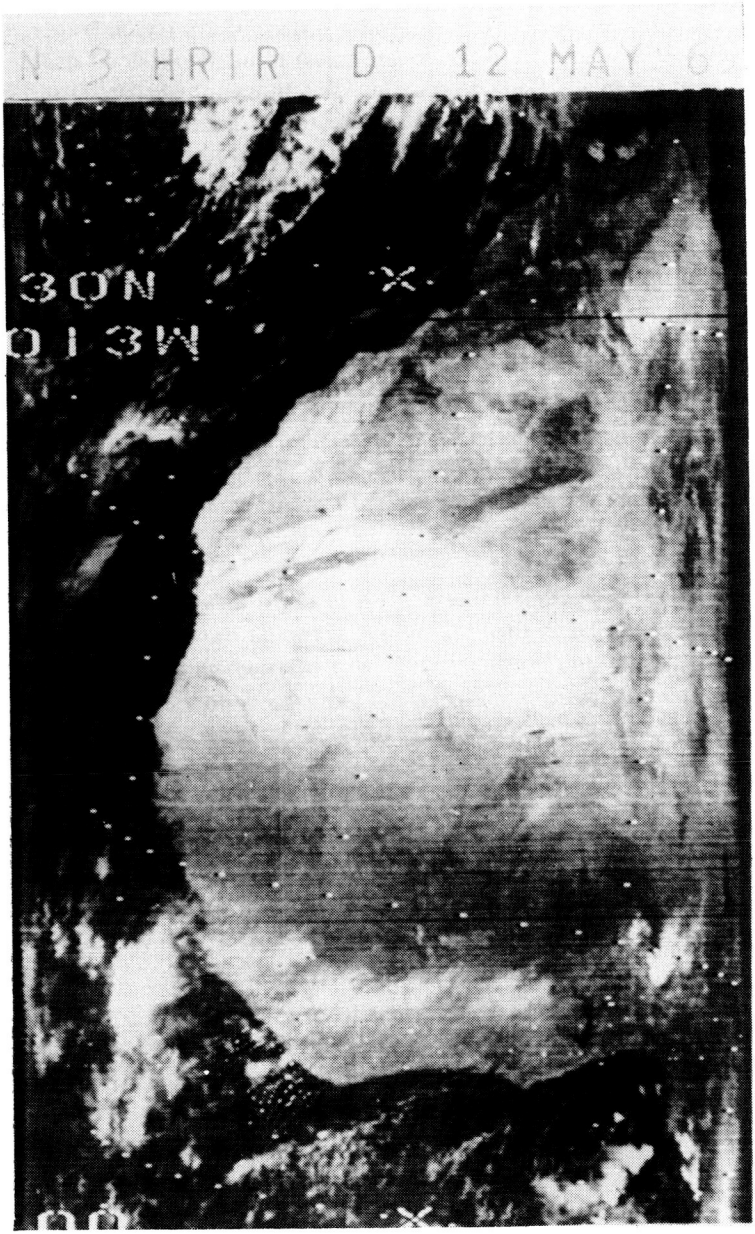

Figure 1

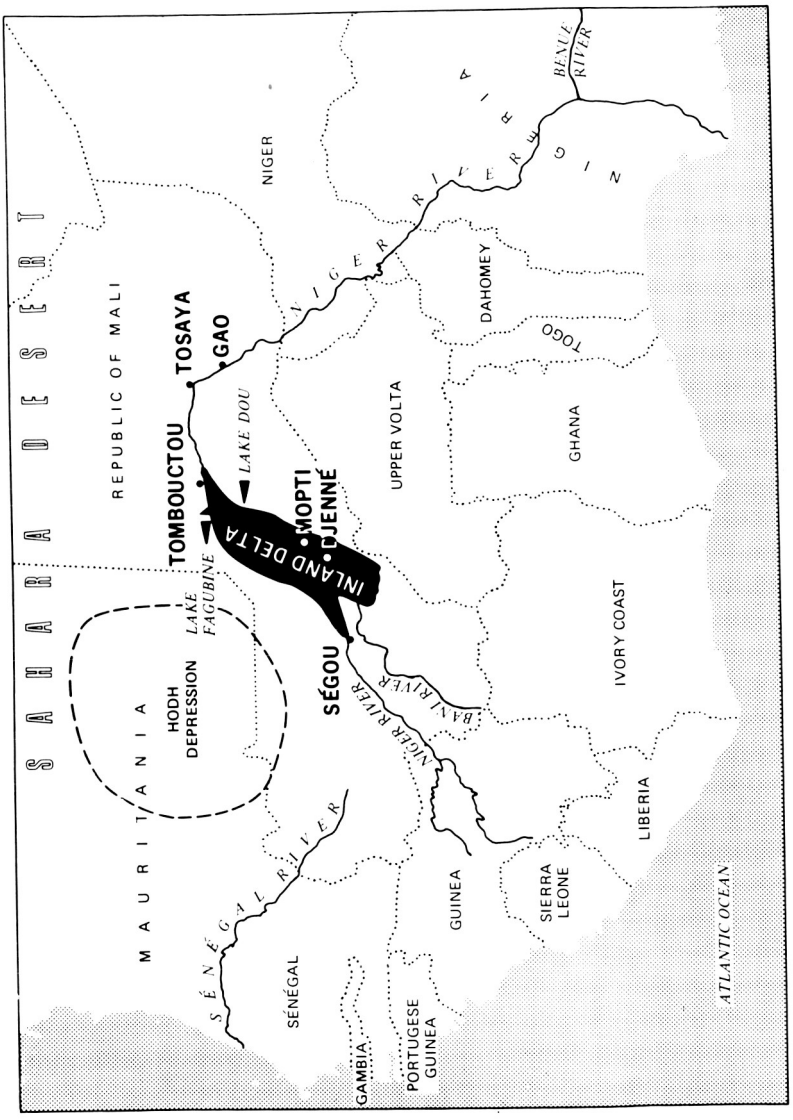
SAHARA DESERT
REPUBLIC OF MALI
NIGER
TOSAYA
GAO
TOMBOUCTOU
LAKE DOU
INLAND DELTA
MOPTI
DJENNÉ
SÉGOU
NIGER RIVER
BENUE RIVER
NIGERIA
DAHOMEY
TOGO
UPPER VOLTA
GHANA
IVORY COAST
LIBERIA
SIERRA LEONE
GUINEA
PORTUGESE GUINEA
GAMBIA
SÉNÉGAL
SÉNÉGAL RIVER
BANI RIVER
MAURITANIA
HODH DEPRESSION
LAKE FAGUBINE
ATLANTIC OCEAN

Figure 2

Figure 3

Figure 4

NIMBUS OBSERVATION OF OCEANIC UPWELLING

Dr. Karl-Heinz Szekielda*

The term upwelling summarizes oceanic processes that transport cold water from deeper regions to the surface. This transport can be induced by winds or by the geostrophic slope of the thermocline in current systems.

One of the largest regions of upwelling appears along the northeast coast of Africa during the southwest monsoon. By measuring the emission of the ocean's surface with infrared radiometers on Nimbus satellites, we have been able to follow the development of cold-water areas as a function of the prevailing winds over relatively long periods.

The upper part of Figure 1 shows the typical temperature distribution as obtained with the high-resolution infrared radiometer aboard the Nimbus 2 satellite during July 1966 along the northeast coast of Africa. Isolines were drawn at temperatures in the water of 273.15K (1° Celsius).

The origin of the upwelling water is near the coast, but the satellite measurements indicated that the cold water is transported clockwise away from the coast. This is manifested by temperatures below 296.15K (23 degrees) which appear gray in Figure 1.

Warm water with temperatures higher than 297.15K (24 degrees) was found in the inner part of the gyre.

The transfer of cold water from the deeper layers of the oceans brings nutrients to the surface water. A high production of organic matter by microorganisms results; because plankton and also fishes graze on the stock of organic matter, the areas of upwelling have a very high potential for the fishing industry.

Measurements of the dissolved phosphate in the surface water along the Somali coast show that the phosphate concentration in the core of upwelling was about ten times that of the open ocean.

Because of its origin, this nutrient-rich water is characterized by its low temperatures. Thus we can rapidly estimate the biological potential of an area from temperatures telemetered by satellites.

---

*National Academy of Sciences resident research associate

A conventional parameter used to measure the standing stock of organic matter in the oceans is the chlorophyll concentration. Beneath the temperature chart on Figure 1, the chlorophyll distribution from the northeast coast of Africa to 60 degrees East along 10 degrees North is given for the surface, to show the effect of upwelling on the biomass. These data were obtained by research vessels in a different year, but in the monsoon season as before.

The data have to be interpreted in the following way: Near the coast, chlorophyll concentrations are low because the plankton needs time to grow. During the transport of the cold-water masses away from the coast, the growth of plankton organisms starts and the chlorophyll concentration increases. Passing the inner part of the gyre, still along 10 degrees North, only small concentrations of chlorophyll are detected. The cold water that was transported around the warmer pattern again shows high concentrations of chlorophyll.

For our expeditions with ships into regions with upwelling, we need real-time processing of remotely sensed temperature data in order to adapt the sampling program aboard the ship to the hydrography. We included in our program the use of a direct real-time readout with an APT station, and an immediate color display aboard the research vessels of the information obtained.

Figure 2, an example from recent studies with the Nimbus 4 data along the Somali coast, shows an analysis of infrared recordings in the 11.5-micrometer window.

The original infrared black-and-white imagery from one cloudfree daytime pass was color-displayed. The land mass of Africa and Arabia appears black because it has a very high radiation during daytime, while the upwelled cold water along the coast was enhanced to be a light green. With this analysis, the cold water was detected to be at about 9 degrees North.

This information can be obtained within a few minutes. Modeling the biological cycle within the upwelling, we are able to predict the locations of the highest concentrations of organic compounds, and consequently the highest potential for fisheries.

MEMBER OF AUDIENCE:

Was there any knowledge – were these potentials for fishery known before that?

DR. SZEKIELDA:

There are some indications of higher fishery potential.

MEMBER OF AUDIENCE:

Like for instance the Grand Banks of Newfoundland?

DR. SZEKIELDA:

Yes, but no one is fishing in this area. Are there any other questions?

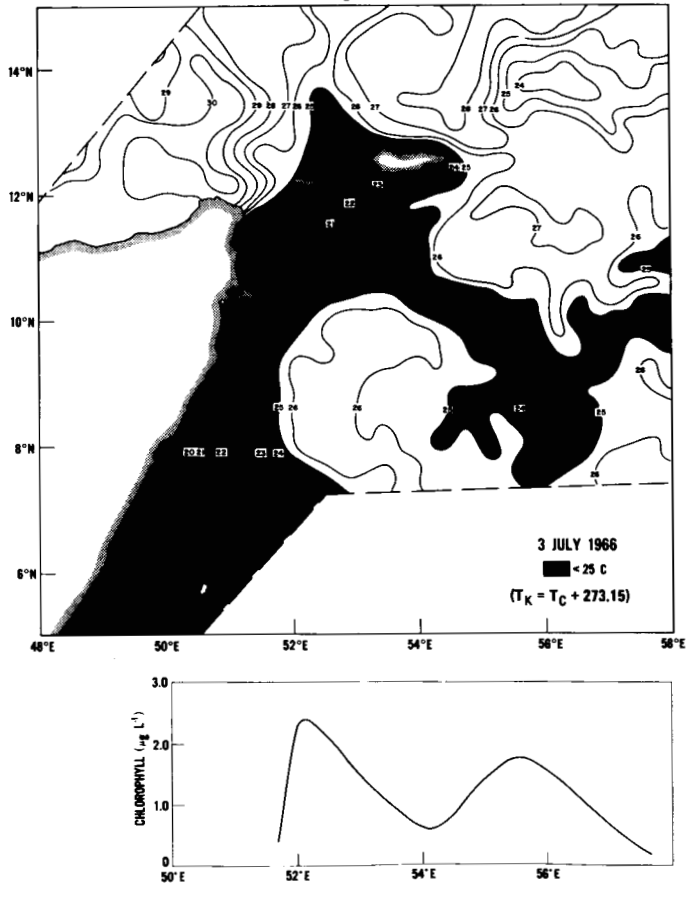

Figure 1. Typical temperature distribution along northeast coast of Africa, July 1966, from Nimbus 2 HRIR

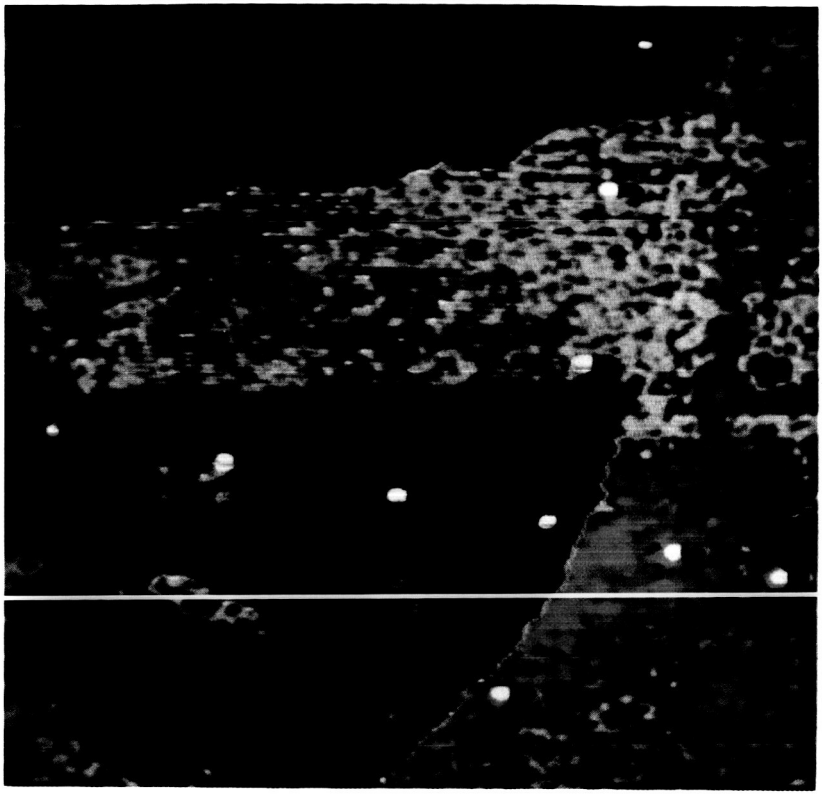

Figure 2. Infrared temperature recordings along Somali coast, from Nimbus 4 data

MICROWAVE EMISSION OF ARCTIC SEA ICE

Dr. Per Gloersen

Aircraft flights were conducted to demonstrate the feasibility of microwave radiometers to be carried on the Nimbus E and F missions. As a result of one of these flights, it was discovered that the passive microwave signatures of Arctic Sea ice relate very specifically to the structure and type of ice.

Two main categories of ice could be distinguished: that is, radiometrically hot and cold, corresponding to gray and white ice respectively as observed visually and photographically.

Glacialists have determined that the cold or white ice is relatively undisturbed Arctic Sea ice, while the warm or gray ice is heavily hummocked, having undergone considerable dynamic activity.

Figure 1 shows some examples of the radiometric signatures of the two kinds of ice. This is an image of the signals received from a 1.5-centimeter wavelength mapping radiometer of the type to be flown on Nimbus E. With the usual cloudcover over the Arctic, it would not be possible to obtain views such as this, either visually or photographically, at altitudes over 304.8 meters (1000 feet).

The aircraft was flying directly over the center of the views shown to the left and right. Hot on the color scale is strictly a relative term; red corresponds to about 270 kelvins. The aircraft altitude was 150 meters over the Arctic Sea ice at a location north of Point Barrow, Alaska, where these measurements were taken last June.

The prominent dark streaks in the picture result from the polynas, or open water in the cracks of the sea ice. The polynas are considered to be of major importance in the energy balance in the polar regions, since their total contribution to the energy balance with the atmosphere is an order of magnitude higher than that of the ice, even though the polynas are estimated to constitute only 10 percent of the area involved.

The observed microwave brightness temperature difference between open water and ice ranges from 100 to 105K.

The varying colors on these images correspond to ice with varying microwave brightness temperatures. The maximum temperature differences shown on the ice range from 30 to 40K. In this particular image, such temperature differences between the gray and white ice show up as streaks, revealing the interlacing of dynamically active and relatively quiescent ice zones.

It was also determined from the aircraft observations that the ability to distinguish between the two types of ice is strongly wavelength-dependent, while the brightness temperature difference between the polynas and the ice remains nearly the same at all wavelengths.

Figure 2 summarizes the gray ice-white ice contrast observed at several different microwave wavelengths. Here, the abscissa is the radiometer frequency and the ordinate is the emissivity difference between the gray ice and the white ice. The images shown on the previous figure were taken at this point, about 20 GHz. The plot shows that the contrast increases with decreasing wavelength, at least down to 0.8 of a centimeter, which appears at 37 GHz on the abscissa.

It is not practical to consider shorter wavelengths for ice surveys with satellites or aircraft, since atmospheric absorption and reemission obscures the emission from the surface.

All measurements shown here were made in the presence of a solid overcast of stratus clouds extending over the entire region north of Alaska, which is the normal weather condition for that part of the globe.

We believe that we have discovered a powerful new tool for conducting ice surveys from both aircraft and spacecraft with remote sensors, and that we have clearly demonstrated the feasibility not only of measuring the distribution of open water and ice in the polar regions, but also of distinguishing between two significant types of ice with the 0.8-centimeter microwave radiometer to be flown on Nimbus F.

We expect that a complete assessment of energy storage in the polar icecaps will result from mapping the ice-and-water contrasts, and that a better understanding of ice dynamics and sheer zones will be obtained from mapping the two ice types.

Thank you.

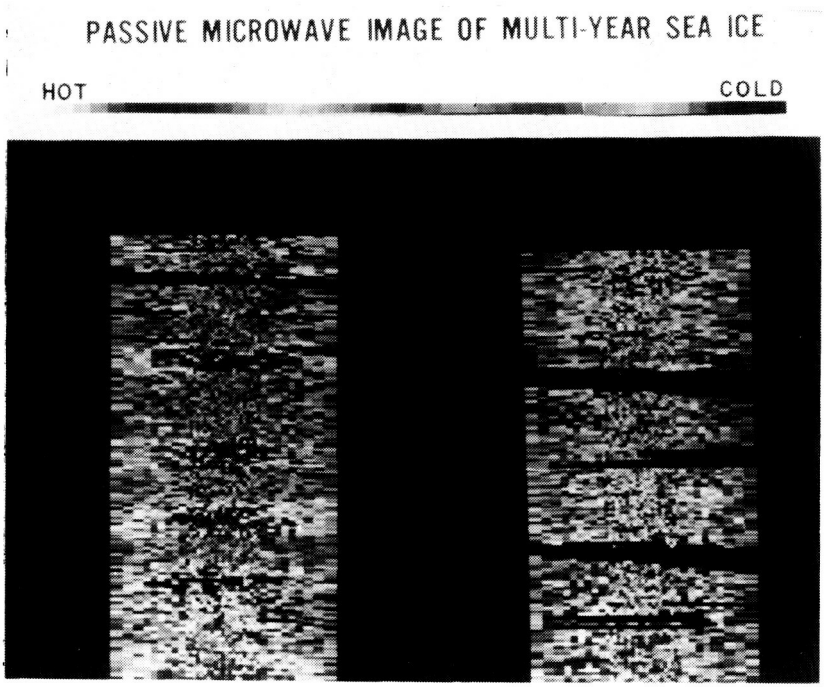

Figure 1

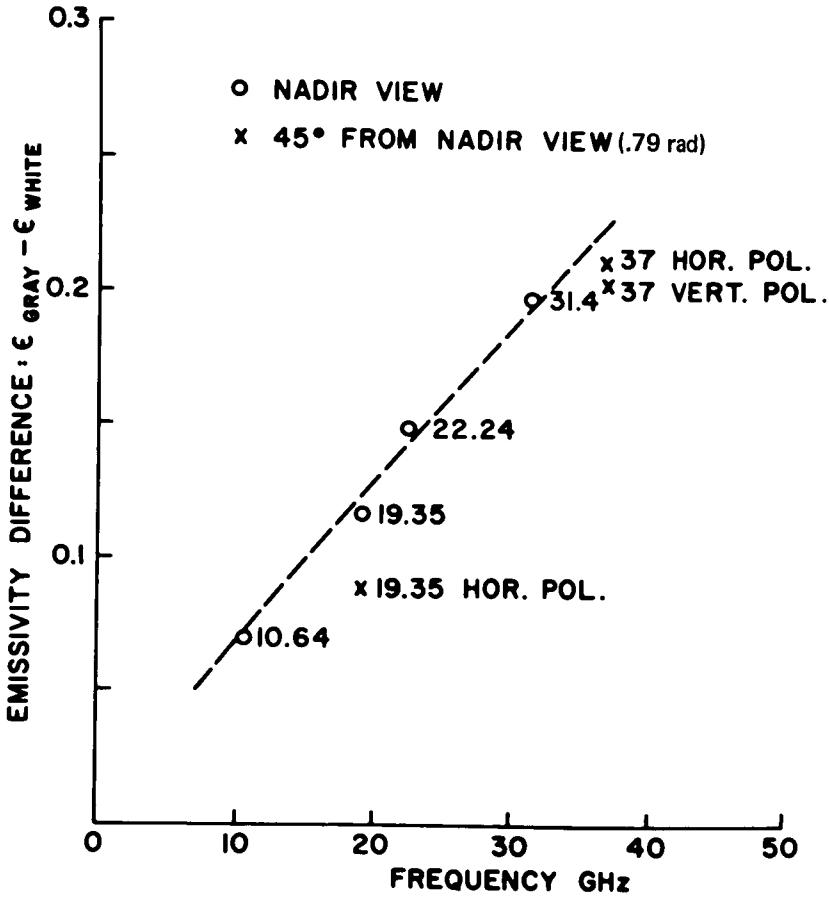
0.3
0.2
0.1
0
10
20
30
40
50
EMISSIVITY DIFFERENCE: $\epsilon_{GRAY} - \epsilon_{WHITE}$
FREQUENCY GHz
o NADIR VIEW
x 45° FROM NADIR VIEW (.79 rad)
x 37 HOR. POL.
x 37 VERT. POL.
31.4
22.24
19.35
x 19.35 HOR. POL.
10.64

Figure 2

MICROWAVE MEASUREMENTS OF SEA STATE

Dr. Thomas Wilheit

Outside of its obvious interest to those who operate ships on the oceans, the determination of sea roughness is also of interest to meteorologists because of its relationship to surface winds and the flux of energy and momentum at the ocean-atmosphere interface. We have made some passive microwave measurements that offer great promise toward making such determinations remotely.

At microwave frequencies, the magnitude of the complex index of refraction of sea water is large, as much as 10. This causes the ocean surface to be quite reflective. Thus, when we view the thermal microwave emission of the ocean surface, we see to a large extent the reflection of cold space. The resultant brightness temperature of the ocean is on the order of 100 to 150 kelvins, certainly much colder than its physical temperature. However, if the surface is roughened by wind, the reflectivity is reduced and the surface appears warmer. The generally cited and widely accepted theory for this fact – that held by Stogren – treats only the large-scale irregularities through geometric optics. It predicts little increase in brightness unless we view the surface at inconveniently oblique angles.

We have some data (Figure 1) that contradict this theory. These data are from the 1.55-centimeter radiometer on board the NASA Convair 990 airborne observatory, and were taken over the Salton Sea, the North Atlantic, and the North Sea. They express brightness temperature increase due to the wind for viewing normal to the sea surface. Note that, for winds greater than about 10 meters per second, there is a significant increase in brightness temperature; it appears that this is due to a phenomenon ignored by Stogren, foam coverage.

One would expect foam to be a lossy, but only weakly refractive, medium for microwaves, so that a thick layer of foam completely filling the radiometer field-of-view should have a brightness temperature much closer to its physical temperature. The data shown in Figure 2 support this contention.

What we have here is radiometer output as a function of time. The cases are lettered in order of increasing wind speed, and correspond to five of the data points in the previous illustration. They were taken from an

altitude of about 120 meters, so the field-of-view is about 7 meters in diameter. The spikes at the higher wind speeds appear to be the effect of foam areas.

The sea surface was photographed at 1-second intervals in support of the microwave measurements, and some of the larger spikes have been correlated with specific foam areas on these photographs. The spikes are as much as 100K above background, presumably corresponding to large thick foam areas completely filling the 7-meter field-of-view of the radiometer. When seas similar to those in case c were viewed from 5500 meters, such spikes were absent; from this altitude, the field-of-view has a diameter of 275 meters, so that we are unable to resolve individual foam patches and must resort to measuring an average foam cover.

A densitometric technique was applied to the photographs of the sea surface to determine the degree of foam coverage corresponding to each of these data points; the results of this appear as X's and the dot on the third illustration.

The upper righthand square is the point corresponding to 100-percent foam coverage as deduced from the maximum spike amplitude. The dashed line is the relationship we would expect if the microwave brightness were independent of foam thickness. We would expect the optical measurements to be sensitive to thinner foam than the microwave measurement, which would cause the data points to lie somewhat below this line. As you can see, they do.

Thus it appears that we can measure surface winds greater than about 10 meters per second, or 20 knots, with much greater sensitivity than predicted by the Stogren theory. The presumption that this increased sensitivity is due to foam coverage is consistent with both the detailed microwave signature of the sea surface, and the foam coverage as deduced from the supporting photographs.

DR. NORDBERG:

I would like to just make a comment, so that no one will be misled here. The physics still holds from satellite altitude, but practically it would be very difficult to conceive of a satellite distance that would observe foam coverage in this fashion, because clouds would also cause an effect similar

to the foam, and in these particular measurements the clouds were accounted for because the aircraft was flying below the clouds. So we will have to account for cloud coverage when making this kind of an observation from a satellite, and that we don't yet know how to do. So, this is an excellent method for measuring air-sea interaction from aircraft, but it is not yet conceivable from a satellite.

MEMBER OF THE AUDIENCE:

Does an oil slick produce a similar image?

DR. WILHEIT:

Oil slicks do have their own microwave signature, which is different from this. Where it is thin, of course, they reduce the roughness in the foam coverage so that they make the sea appear colder; and then, where it is thick, it improves your matching, so it would make it appear hotter. But that is certainly a different effect, that in principle can be sorted out but would be difficult in practice.

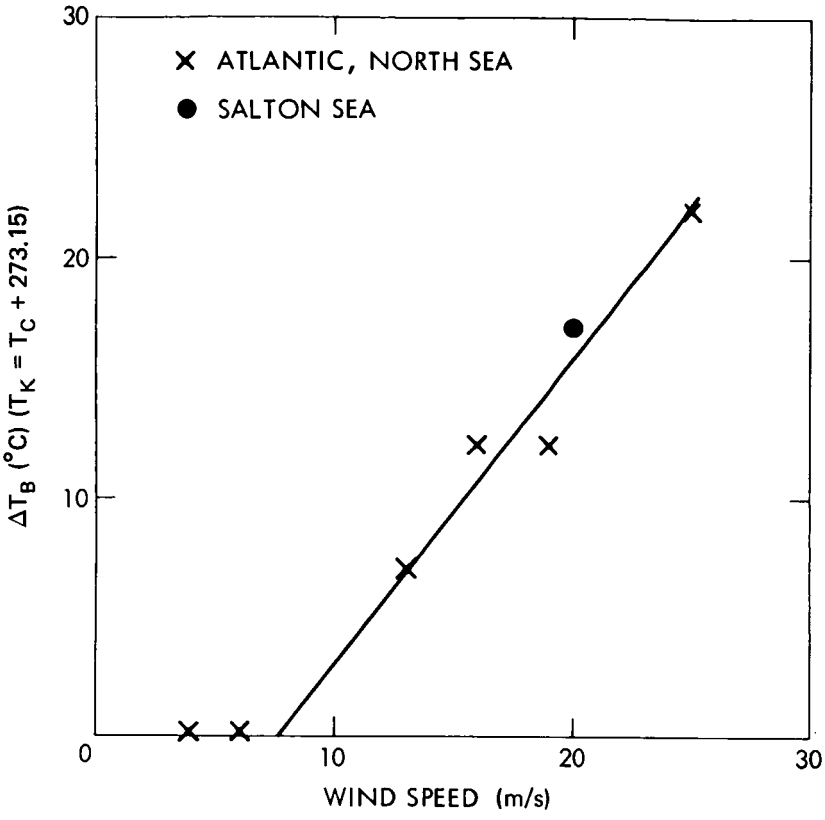
30
20
10
0
10
20
30
ATLANTIC, NORTH SEA
SALTON SEA
ΔT_B (°C) ($T_K = T_C + 273.15$)
WIND SPEED (m/s)

Figure 1

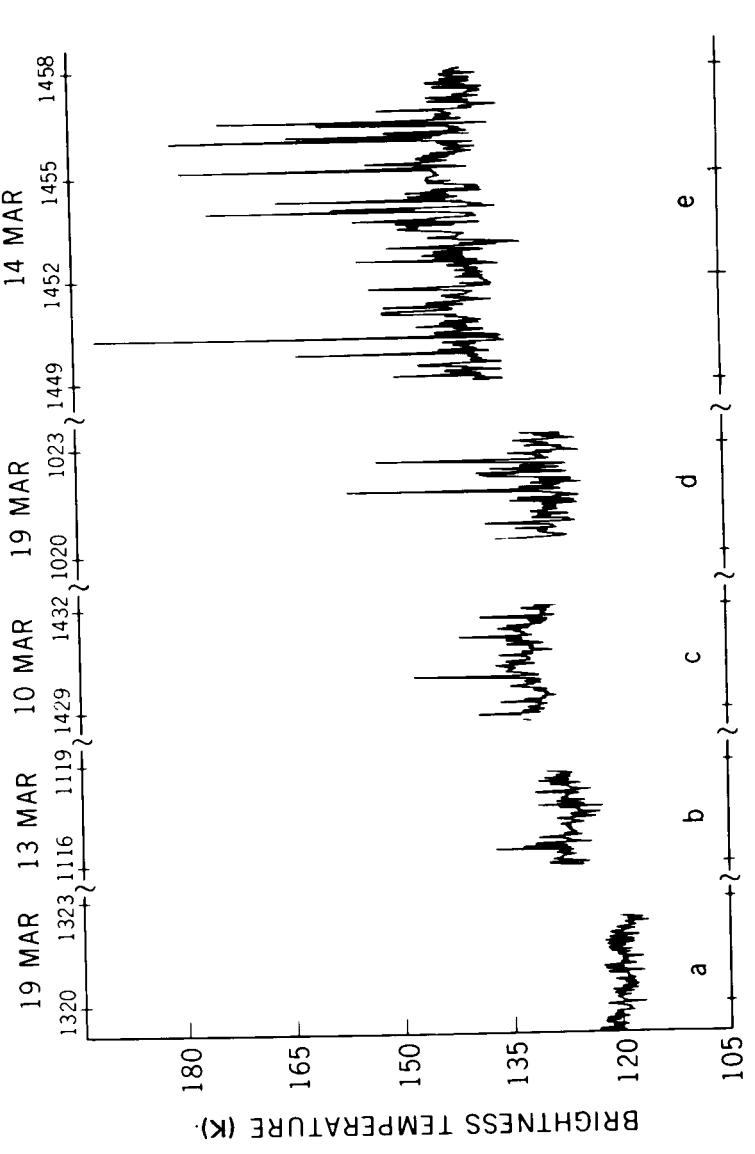
BRIGHTNESS TEMPERATURE (K)
180
165
150
135
120
105
19 MAR
1320
1323
13 MAR
1116
1119
10 MAR
1429
1432
19 MAR
1020
1023
14 MAR
1449
1452
1455
1458
a
b
c
d
e
TIME (GMT)

Figure 2

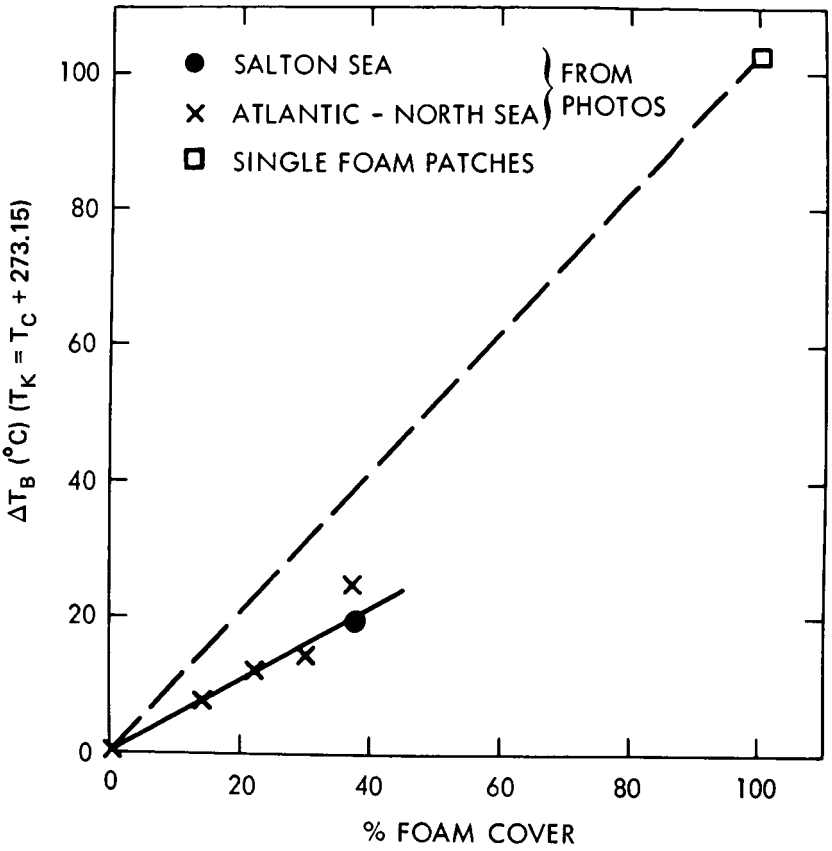
SALTON SEA
ATLANTIC - NORTH SEA
FROM PHOTOS
SINGLE FOAM PATCHES
100
80
60
40
20
0
0
20
40
60
80
100
ΔT_B (°C) ($T_K = T_C + 273.15$)
% FOAM COVER

Figure 3

AIR-SEA INTERACTION IN THE PACIFIC OCEAN

Lewis Allison

The understanding of the interaction of the tropical oceans with the atmosphere is one of the most important long-range problems to resolve in meteorology and oceanography today.

As an initial step in a research study on this subject, daily TIROS and ESSA satellite television nephanalyses over the Pacific Ocean were collected and monthly cloud charts produced.

Figure 1a shows the variation of the monthly cloudiness over the Intertropical Zone of Convergence (IZC) in the eastern tropical Pacific from August 1962 to October 1970. Note the 30- to 36-month cycle of maximum cloud, 1963, 1966, and 1969.

In order to try to explain this cloudiness cycle, monthly sea-surface temperatures in the same region were converted to three-monthly sea-surface temperature-anomaly summaries, using published U. S. Navy long-term means as a reference base.

The histogram, Figure 1b, shows the seasonal variation in this same region of the area covered by a positive sea-surface temperature anomaly. A -0.70 correlation coefficient and a +9-month lag were determined by comparing these data, using statistical computer techniques. In other words, cold water entered this latitude band after 9 months following the advent of heavy tropical cloudiness. This relationship indicates the feedback loop from a localized "Hadley circulation" in the eastern tropical Pacific Ocean.

Monthly rainfall was next chosen as a substitute for satellite-detected cloudiness, in order to extend the study back to 1949. Data from eleven tropical islands in the central Pacific were selected because their common location in the south equatorial current resulted in a coherent rainfall periodicity.

Twenty years of these data on rainfall tabulated in 12-month running means were compared with eastern tropical Pacific sea-surface temperature anomalies, and a 0.90 to 0.94 correlation coefficient was determined.

With this surprisingly good statistical relationship as a base, tropical sea-surface temperatures were derived by linear regression techniques from prior rainfall data for the years 1905 to 1949, a period of sparse oceanographic coverage.

Thirteen other parameters have since been correlated during this initial study. One of these – the variations of the 70-kilonewton/meter^2 (700-millibar) height field – was found to lead the onset of tropical sea-surface temperature anomalies by a 5- to 9-month period.

Figure 2a shows the changes of the (70-kN/m^2) (700-millibar) level in the northeast Pacific, and the occurrence of sea-surface temperature anomalies 5 months later at 0° to 10° South. Note that generally warm water occurs in the 70-kN/m^2 (700-millibar) troughs, and cool water under the ridges.

Figure 2b is a graph of the correlation coefficients and timelag between these two parameters. Note the peak (0.70 correlation coefficient) and the 5-month lag in the occurrence of the tropical sea-surface temperature anomaly after the 70-kN/m^2 (700-millibar) height changes.

Since sea-surface temperatures are a basic concern of the U. S. Navy and our commercial fishery industry, these preliminary air-sea relationships with further refinement may become useful for operations in the tropical Pacific Ocean.

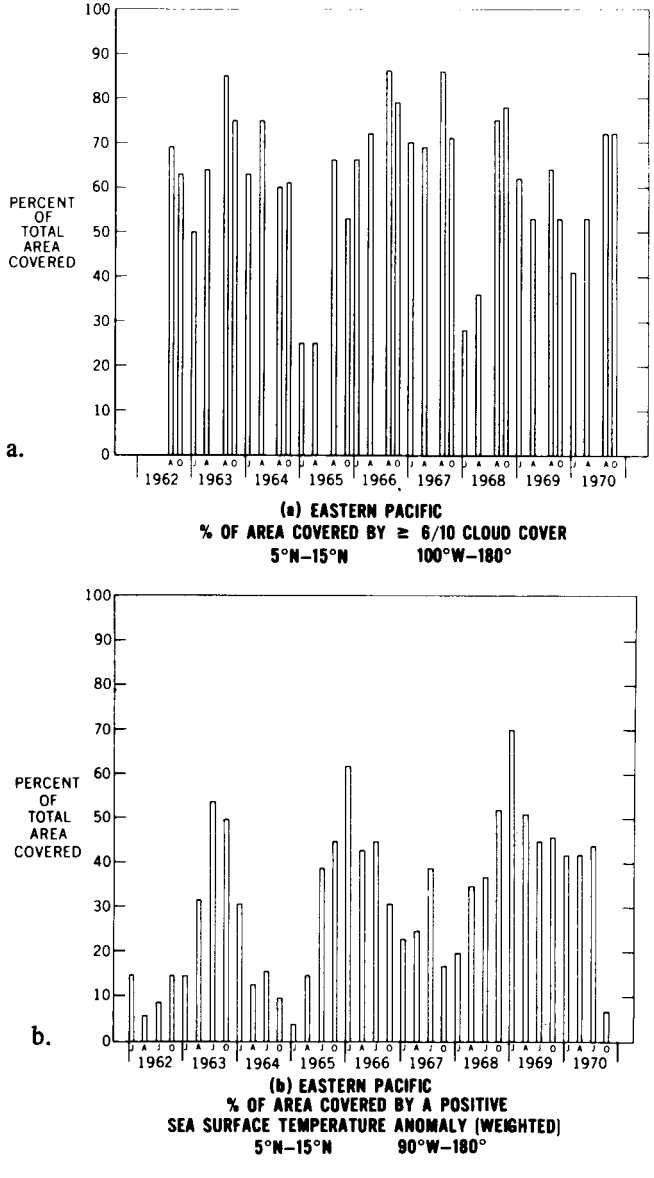
a.
PERCENT OF TOTAL AREA COVERED
100
90
80
70
60
50
40
30
20
10
0
1962
1963
1964
1965
1966
1967
1968
1969
1970
(a) EASTERN PACIFIC
% OF AREA COVERED BY ≥ 6/10 CLOUD COVER
5°N–15°N 100°W–180°
b.
PERCENT OF TOTAL AREA COVERED
(b) EASTERN PACIFIC
% OF AREA COVERED BY A POSITIVE
SEA SURFACE TEMPERATURE ANOMALY (WEIGHTED)
5°N–15°N 90°W–180°

Figure 1

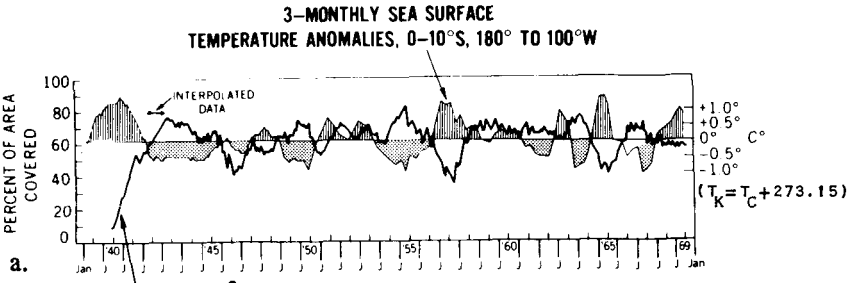

a.

(a) 70 kN/m^2 (700MB) POSITIVE HEIGHT ANOMALIES
(12 Month Running Mean)

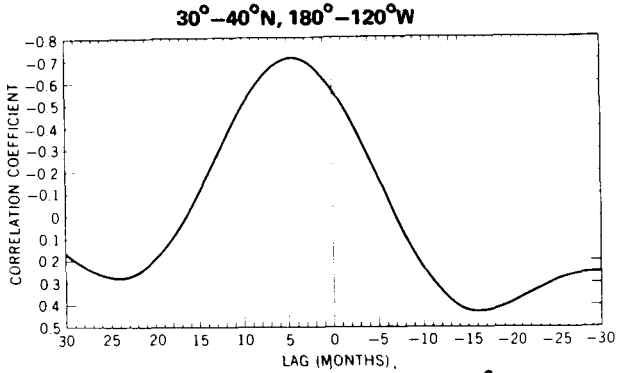

b.

(b) CORRELATION BETWEEN 70 kN/m^2 (700MB) HEIGHT VARIATION AND (0-10°S) SEA SURFACE TEMPERATURE ANOMALIES

Figure 2

GLOBAL WINDS FROM NIMBUS TEMPERATURE DATA FOR JULY 1970

Dr. Joseph S. Hogan*

For the past year, Jastrow and Halem at the Institute for Space Studies have been doing simulation studies to determine the best techniques for making use of infrared vertical sounding data on atmospheric temperatures. Their simulation studies indicate that satellite temperature data alone, if inserted into an atmospheric model continuously, day after day for a period of several weeks or more, will control global winds and pressures without any other input. In particular, no direct measurements of wind or pressure need be made.

The results of these simulation studies were limited in three ways: first, by the deficiencies of the model; second, by the fact that simulated data were used, since adequate amounts of real data were not available at the time; and third, by the fact that test of the accuracy of the wind determinations was not a comparison with measured winds but, rather, with winds computed from the model. In other words, there was no connection with the real world.

They have now taken an important step beyond the simulation studies by using real SIRS radiance data from Nimbus 4 for June and July 1970, and inserting these data into the model and comparing the results with real observations. Thus, although deficiencies in the models still remain, the second and third limitations present in the original simulation studies have been removed.

This work was done in collaboration with Drs. Smith, Hayden, and Wolff of the National Environmental Satellite Service. These men combined their temperature-retrieval programs with the Institute version of the Mintz-Arakawa two-level general circulation model.

There are two main results from this work. First, the model accepts real radiance or temperature data on a continuing four-dimensional asynoptic basis without any indigestion.

---

*National Academy of Sciences resident research associate

Theoretical meteorologists had expected that real data introduced asynoptically into the model without smoothing or balancing would destroy the numerical integration. The simulation studies indicated that no difficulty would be encountered, but proof has only now been obtained through these latest experiments that there really is no problem with this technique of data utilization in meteorology.

The second result is that the real temperature data do in fact determine the winds to a useful degree of accuracy.

In the most important experiment that Jastrow and Halem carried out, SIRS radiance data and temperature data from the National Meteorological Center were inserted into the Mintz-Arakawa model on a continuing basis, starting on June 18, 1970.

It was found that the SIRS data can supply temperature at the lower level of the model (80-kN/m^2) (the 800-millibar level) only about 20 percent of the time, because of the presence of clouds. Therefore, the SIRS data at the upper (40-kN/m^2) (400-millibar) level in the model were combined with NMC data at the 80-kN/m^2 (800-millibar) level. The SIRS data were used asynoptically, while the NMC data were used synoptically at 12-hour intervals.

Initial values in this experiment for winds and pressures on June 18, 1970, were chosen at random and had no correlation whatsoever with the observed state of the atmosphere on that day.

Temperature insertion was continued for 30 days after June 18, 1970.

By July 15, 1970, the circulation generated by the model was in good general agreement with the major features of the observed northern-hemisphere circulation (Figure 1). In fact, very good agreement was obtained over the continental United States and western Europe. At the top of Figure 1 are the NMC observations for July 15, 1970, 1200Z. At the bottom of the figure are the pressures of the geopotential surfaces generated by the Mintz-Arakawa model on the same day with SIRS-NMC temperature insertions. It is possible to distinguish approximately seven major points of agreement between observed and predicted geopotential patterns in this figure. No major points of disagreement are visible in these patterns.

As a control, the experiment was repeated by running the model forward for 30 days from the same initial conditions (the randomly chosen initial conditions on June 18, 1970) but this time without data insertion.

In the top and bottom maps of Figure 2, the observations are compared with the control case. Approximately three points of agreement can be found between the control and the observations, and approximately seven points of major disagreement. Presumably, the three points of agreement represent the degree of accidental correspondence to be anticipated in experiments of this kind.

To my knowledge, this is the first time that real satellite data have been used directly to drive an atmospheric circulation model. Work is now in progress with Smith, Hayden, and Wolff of NESS to develop a new technique to partially eliminate the cloud effects and to increase the amount of coverage.

Jastrow and Halem hope that the increased frequency of insertion of SIRS data which this new technique will make possible will further improve the agreement with the observations.

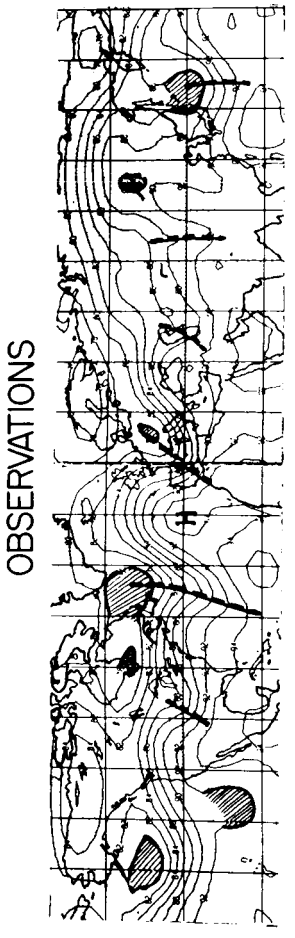

Figure 1

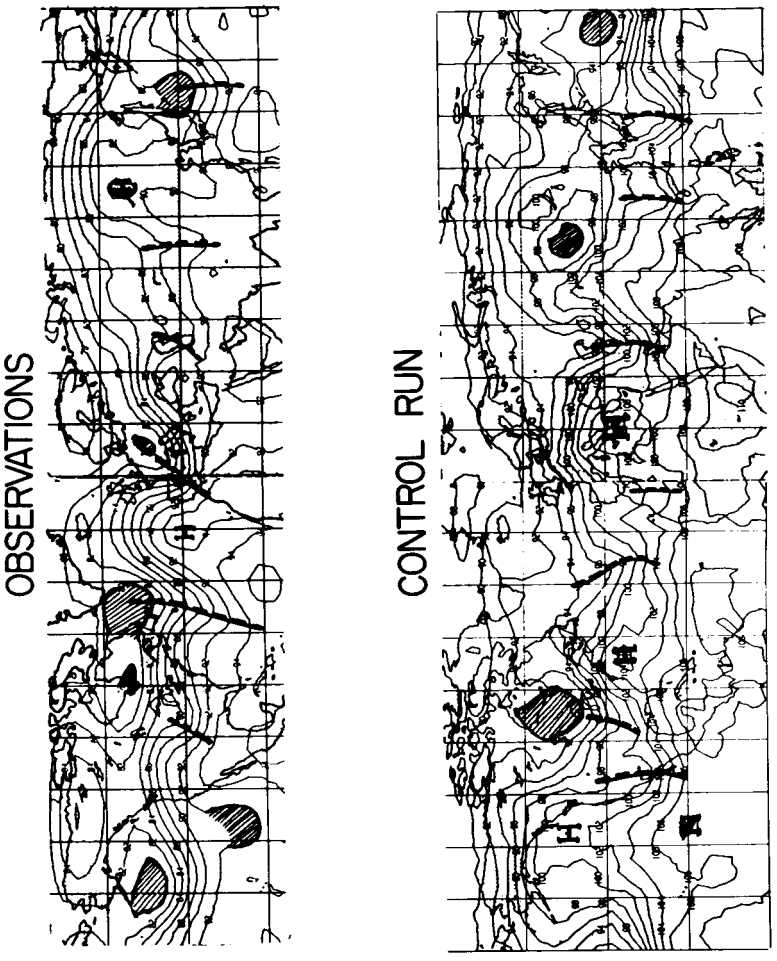

Figure 2

CLIMATIC MODIFICATION BY CO_2, H_2O, AND AEROSOL

Dr. Ichtiaque Rasool

The rate at which human activities are modifying the atmosphere of the earth has suddenly become a problem of great climatological concern. In the last few years, the amount of CO_2 in the atmosphere of the earth has been increasing at a rate of 0.2 percent per year, corresponding to an accumulation-doubling time of 23 years.

At the same time, the amount of dust and smoke in the atmosphere has increased about 30 percent in the last 20 years, and the estimated accumulation-doubling time is about 10 years.

The important question one would like to ask is what effect these changes have had on the surface temperature and the climatology of the earth, and, if the rate of increase continues for the next 100 to 200 years, what climatic changes can be expected.

Will the temperature of the earth increase so much that a runaway greenhouse effect may take place on the earth, like that on Venus? That is one question we would like to ask.

We have started a program of research in this direction in collaboration with Dr. Steve Schneider, NRC-NAS resident research associate, and I would like to report on the first results of the study which are just coming out.

We start by describing a model of the atmosphere of the earth.

Table 1 shows the parameters we used. The temperature of the ground is 288 kelvins. Lapse rate is 11.34 centirad (6.5 degrees) per kilometer. The relative humidity is 75 percent. Cloudcover is 48 percent. Effective cloud height is about 7 kilometers. Carbon dioxide is 0.3 of a part per thousand, which is the present value. Aerosol density is 2 times 10^6 per square centimeter, and the size of these particles is about 0.2 micrometer (0.2 μ).

Now we compute by numerical integration the total flux going out from such an atmosphere into space. This flux is in balance with the incoming solar radiation for a planetary albedo of 33 percent, which is close to the observed value. This is our model.

In the model, we now increase the amount of CO_2 by a factor of 2, 4, 6, 8, 10. Because of the increase of CO_2 in the atmospheric model, the radiation going out to space decreases because of the increased capacity of the atmosphere in the infrared. But the solar radiation has not changed, because the albedo has not changed. Therefore, in our model, we must increase the temperature of the atmosphere and of the earth's surface, in order to balance the two radiations again.

Figure 1 shows the increase of temperature in the whole troposphere that is required to offset the increased opacity of CO_2, and to put the radiation from earth and from space in equilibrium.

In this illustration, the lower curve shows temperature increase because of the addition of CO_2 alone. However, when the CO_2 increases and the relative humidity remains constant, then the total amount of water vapor in the atmosphere will increase, and this plus the increase in temperature will produce an added greenhouse effect. So the top curve is for CO_2 with water, and here the increase in temperature is a little more than for CO_2 alone.

This figure shows two main results: first, if the CO_2 in the atmosphere is doubled, we expect an increase of about 0.6 kelvin in the surface temperature. Similar estimates have been made by Menabe and many other people, who all agree that the increase is about 1 K. This result is therefore consistent with earlier studies.

The second point is that, if the increase in CO_2 continues to a factor of 10 or 20 or 100, the curve flattens out and the increase levels off. The reason for this is that the CO_2 absorption takes place in the 15-micrometer (15-micron) band, and this band becomes saturated. And there is no more extra attenuation of the radiation going out.

However, if the CO_2 increases by a factor of 1000 or 2000 or 10,000, and the total pressure of the atmosphere starts changing, then the curve will run away and earth may become as hot as Venus. But this timescale is in millions of years. On the other hand, we do have oceans that absorb the CO_2, and the atmospheric CO_2 may never increase so much. The conclusion to be drawn from this calculation is that the runaway greenhouse effect from the accumulation of manmade CO_2 alone is probably not possible.

The next question is, what does the aerosol do to the temperature of the earth? Here the problem is a little more complicated, because, when you put dust and smoke into the atmosphere, they change both the albedo of the planet and the outgoing infrared radiation from the earth. If both of these change by the same amount, there will be no change in surface temperature.

Now, there are no qualitative estimates available in the literature on this subject, and my colleague and I therefore embarked on determining the scattering properties of aerosols – fine particles – in the visible and in the infrared.

A careful study by Jim Hansen, my colleague at the Institute, has indicated that, for aerosols of a size about 0.2 micrometer (0.2 μ), the scattering cross section in the visible is about ten or fifteen times greater than in the infrared. This is the important result shown in Figure 2.

As the amount of dust particles in the atmosphere increases, the first thing that changes is the visible backscattering in the albedo. The albedo increases very fast, compared to the opacity in the infrared; as the albedo increases, the solar radiation decreases, and the surface temperature goes down. And, if you accept that there is a factor-of-10 increase in the next thirty years, then the temperature could go down as much as about 3K.

At this point, the dust is so much that the infrared opacity starts increasing, and the albedo does not change much because the dust has already covered the earth and the backscattering is finite (for a case of single scattering). So then the temperature starts to increase again, after the dust amount has increased by a factor of 100 or so.

The important thing here is that the 3K temperature decrease is a very critical value. Several climatologists have suggested that a 3K decrease in global temperature is sufficient to trigger an Ice Age!

$T_s = 288\ K$

$\frac{dT}{dz} = -6.5°/km$ (11.34 centirad)

R.H. = 75%

Cloud Cover = 48%

Cloud Height = 7.2 km

CO_2 = 0.3 (parts per thousand)

Aerosol Density = $2 \times 10^6\ /cm^2$

Aerosol Size = 0.2 μ (0.2 micrometer)

Planetary Albedo = 33%

Table 1

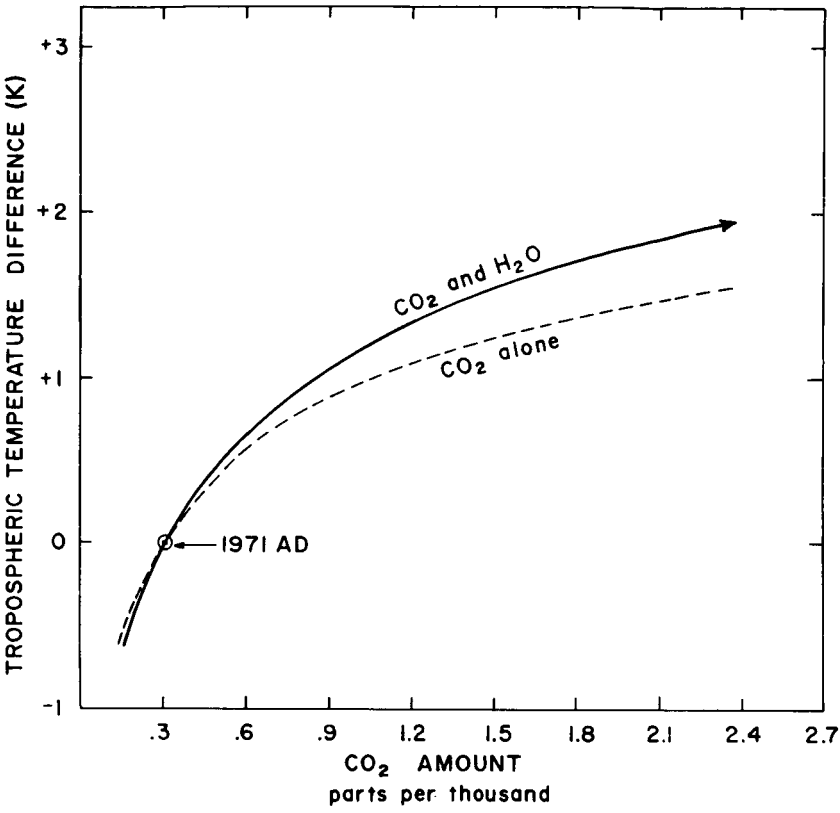
TROPOSPHERIC TEMPERATURE DIFFERENCE (K)
+3
+2
+1
0
-1
CO_2 and H_2O
CO_2 alone
1971 AD
.3
.6
.9
1.2
1.5
1.8
2.1
2.4
2.7
CO_2 AMOUNT
parts per thousand

Figure 1

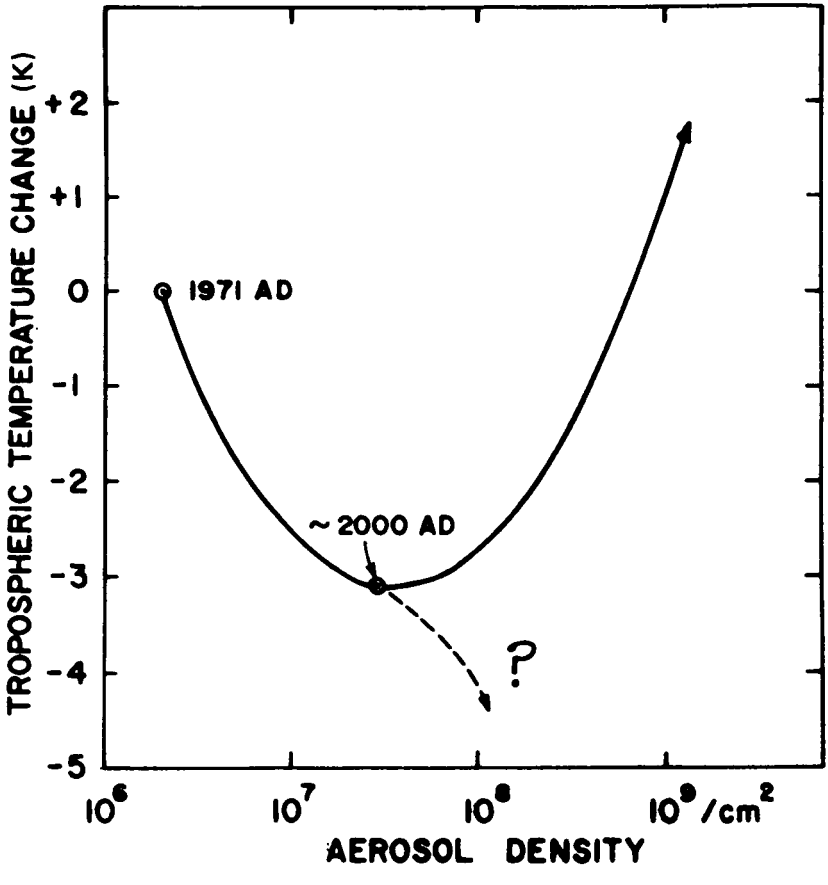
TROPOSPHERIC TEMPERATURE CHANGE (K)
+2
+1
0
-1
-2
-3
-4
-5
1971 AD
~2000 AD
?
10^6
10^7
10^8
10^9/cm^2
AEROSOL DENSITY

Figure 2

COMPARISON OF PROBE AND RADAR IONOSPHERE TEMPERATURES

Dr. Walter Hoegy

The temperature of ionosphere electrons is measured by two quite different techniques: Langmuir electrostatic probes, and radar backscatter. The probe technique determines the temperature from the current-collection characteristic, and the backscatter technique determines it from the density fluctuations of the plasma. Comparison of electron temperatures determined by the probe and backscatter techniques has revealed a discrepancy that lies outside the error limits of the two techniques (Figure 1).

This comparison reveals two important points about the discrepancy: first, it occurs in a certain altitude range, from about 350 km to about 800 km; second, the probe temperatures are consistently higher than the radar temperatures.

The evidence indicates that the temperature discrepancy results from the fact that the ionosphere is not in equilibrium. This state of nonequilibrium causes a distortion of the energy distribution from a Maxwell distribution. In general, the probe and radar temperature parameters are distinct physical quantities; also, the probe and radar temperatures are numerically equal only in the case of a Maxwell energy distribution. Therefore, in the altitude region where the electron-energy distribution is significantly non-Maxwellian, one would expect the probe and radar temperatures to be different.

Figure 2 illustrates the difference in the definitions of the probe and radar temperatures. The radar and the probe measure temperature in different energy ranges of the electron-energy distribution. The equations demonstrate the basic difference in the formulas defining the temperatures.

A model calculation of the electron-energy distribution carried out by Dr. Hans Mayr shows that the degree to which the energy distribution is distorted increases as the magnitude of the electron mean free path relative to the density scale height. Figure 3 illustrates the altitude dependence of the mean free path and the density scale height. It shows that the mean free path is greatest relative to the density scale height in the shaded portion above about 350 km, which corresponds to the region of the temperature discrepancy. Qualitatively, the model non-Maxwellian distribution is found

to result in a radar temperature lower than the probe temperature. Thus it appears that the non-Maxwellian energy distribution provides an explanation for both the direction of the temperature discrepancy (lower radar temperatures) and the altitude region in which the discrepancy occurs.

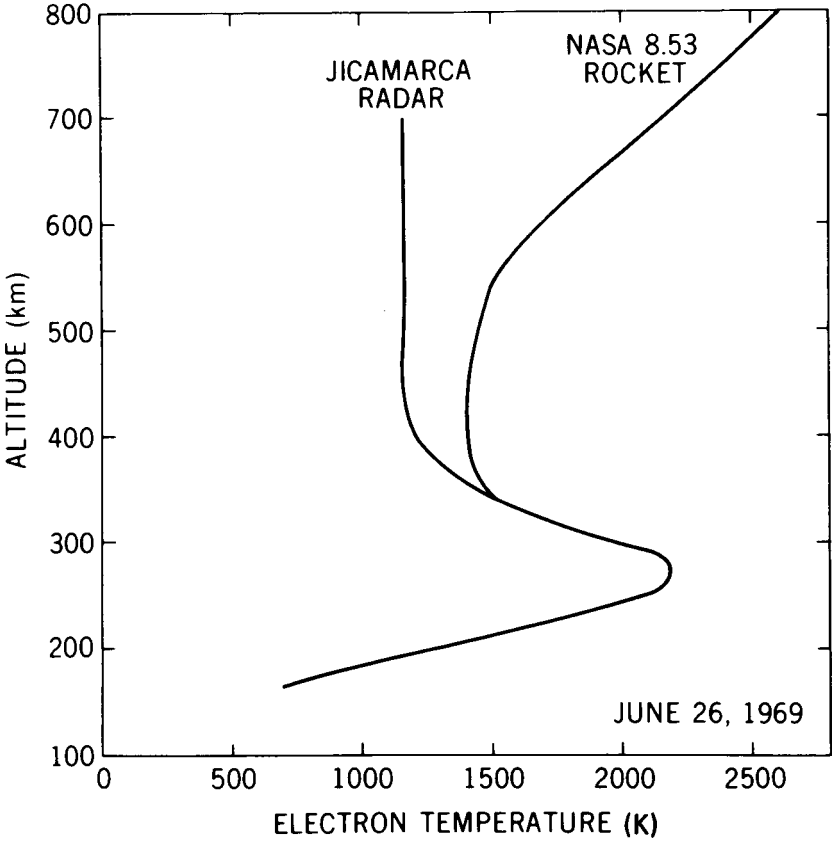

Figure 1

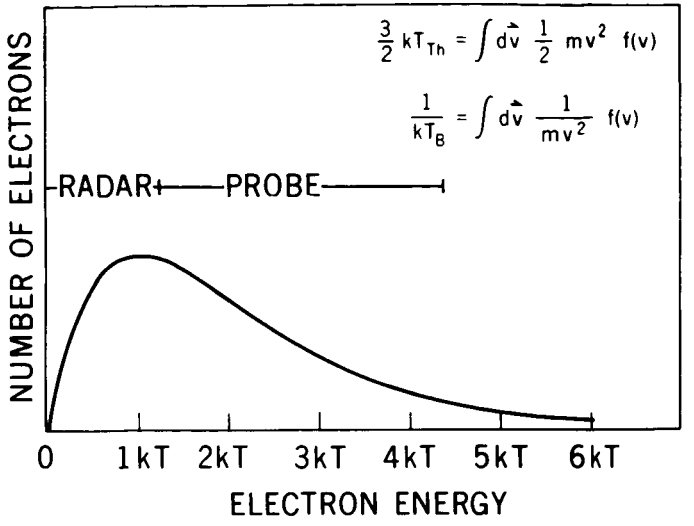

Figure 2

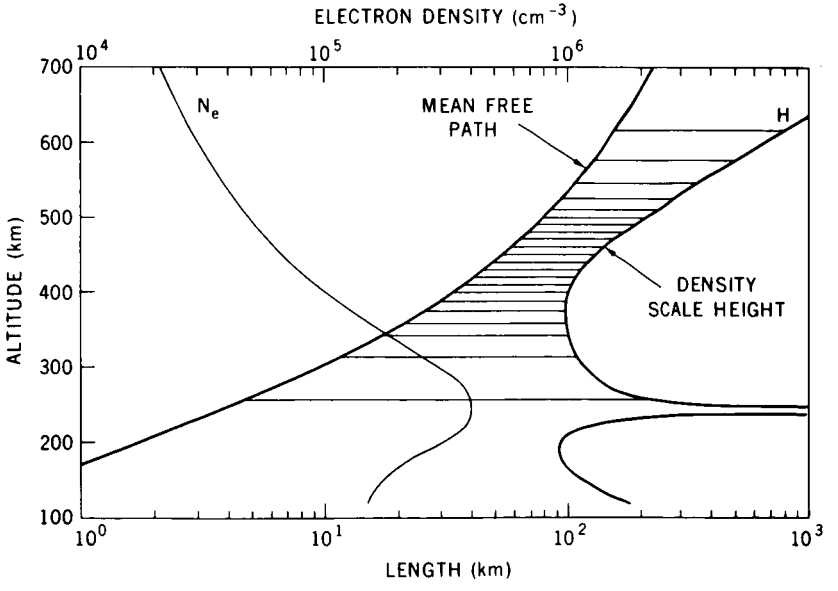

Figure 3

THE IONOSPHERE DURING A SUBAURORAL RED ARC

Dr. Eugene Maier

Two of the optical emissions from the atmosphere that have been studied both from the ground and from spacecraft are the red and green lines of atomic oxygen. Occasional significant enhancements of the red 630-nanometer (6300-angstrom) line occurred during the last two times of maximum solar activity. These brightenings were characterized by their location in the midlatitude region. For example, the green line of the same species is not enhanced.

In addition, the emissions seem to be stable over a period of the order of a day, and they extend over a wide range of latitudes covering at least the night side of the earth. So the question arises: what is the nature of this phenomenon? Is it evidence of a major new effect in the ionosphere?

Figure 1 is a pictorial representation of the circumstances under which we obtained definitive data describing the ionosphere during the red arc observed on the 29th of September, 1967. The telescope generally in the center represents the Fritz Peak photometry station which observed the emission – shown as the red band – to extend over the entire midwestern United States. The yellow band depicts the generally vertical (L = 2.5) magnetic-field surface extending upward from the ground, through the emission region, to the orbital altitudes of two spacecraft. Both Explorer 31 (DMEA) and OGO-4 were obtaining data, under a program of general geophysical studies.

Well after the arc event was identified, we looked and were fortunate in finding data from several passes through the region of interest. The critical factor here was that values of the various ionospheric parameters were obtained at several altitudes: 880 kilometers for OGO-4, and 2500 kilometers for Explorer 31.

Figure 2 is a plot of the observed electron and ion temperatures on the vertical scale versus the McIlwain L parameter on the horizontal axis. Data recorded during the night of the arc, as well as about one week earlier, are shown. The readings on the left were obtained from OGO-4 at about 880 kilometers; those on the right from Explorer 31 at 2100 and 3000 kilometers.

Several points are clear from the figures: First, there is an enhanced plasma temperature in the region near L = 2.5, which corresponded to the region of the optical emissions. Note the increase in the arc region, whereas in the non-arc day there was no substantial increase in that region. Second, there is a difference of about 1000K between the plasma temperature at 880 kilometers and that at 2100, the first several curves on the right. Also, there is an increase of about 1000K between the temperatures at 2100 and 3000. Both these sets of observations yielded a temperature gradient of about 1K per kilometer extending over a very wide altitude range.

The third point is that the ion temperatures, the dashed curves, are comparable to but less than the electron temperatures.

From these observations we conclude that there was an energy flow from the magnetosphere, downward through the highly conductive plasma into the lower ionosphere.

Figure 3 shows what happened to the ion composition during the arc event. The top two graphs compare the three major species of concentrations at 880 kilometers for arc and non-arc conditions. Note that, at this altitude, there is no significant change in total density – perhaps a slight decrease. There is, however, a complete inversion from a situation where the light and heavy ions are present in approximately equal numbers, to a situation where oxygen is the predominant ion in the arc region. Finally, at the bottom of the figure, there are shown the observed fluxes of 1.6-3.2 attojoule (10- to 20-electron-volt) electrons measured during the same spacecraft transits through the region of interest. Note that there is no significant difference between the levels of low-energy electrons present. Thus we infer that the energy is being conducted by the thermal plasma rather than by a flow of precipitating particles.

These observations of all the critical parameters lead directly to a conclusion regarding the source of the red arc: Thermal conduction of energy from the magnetosphere, which is consistent with the observed temperature gradient, could result in an enhancement of the 630-nanometer (6300-angstrom) line without causing excitation of the higher state.

Unfortunately, the entry of energy at the top of the ionosphere – in the form of hot electron plasma conducting heat downward – would not

serve to decrease the electron density and produce the ion-composition changes that are observed. Something more is required. That additional factor is a simultaneous change in neutral composition at the lower boundary of the ionosphere.

Theoretical work has shown that ion-composition changes of the type observed here occur during magnetic storms, and are associated with neutral changes at the lower boundary of the ionosphere.

Magnetic storms, however, are relatively common, and are not normally accompanied by red arcs. Thus, we believe that red arcs are observed only when there is heat flow from above, combined with the higher temperatures and decreased electron density caused by composition changes at the lower boundary.

MEMBER OF THE AUDIENCE:

Would you elaborate a little on what is happening in the ionosphere during the time of this arc?

DR. MAIER:

We believe there is nothing particularly unusual happening; it is just that, during magnetic storms, changes normally occur – changes in the ratio of neutrals – oxygen and nitrogen, for example. One only sees the arc when there are particular circumstances involving both a critical flux of energy, which causes the emission intensity to go above what you get from recombination radiation, and recombination reactions down below, where the critical threshold is caused by particular values – of oxygen density for example. In other words, neither effect by itself is dominant.

Figure 1

ELECTRON AND ION TEMPERATURES AT DIFFERENT ALTITUDES IN THE RED ARC REGION

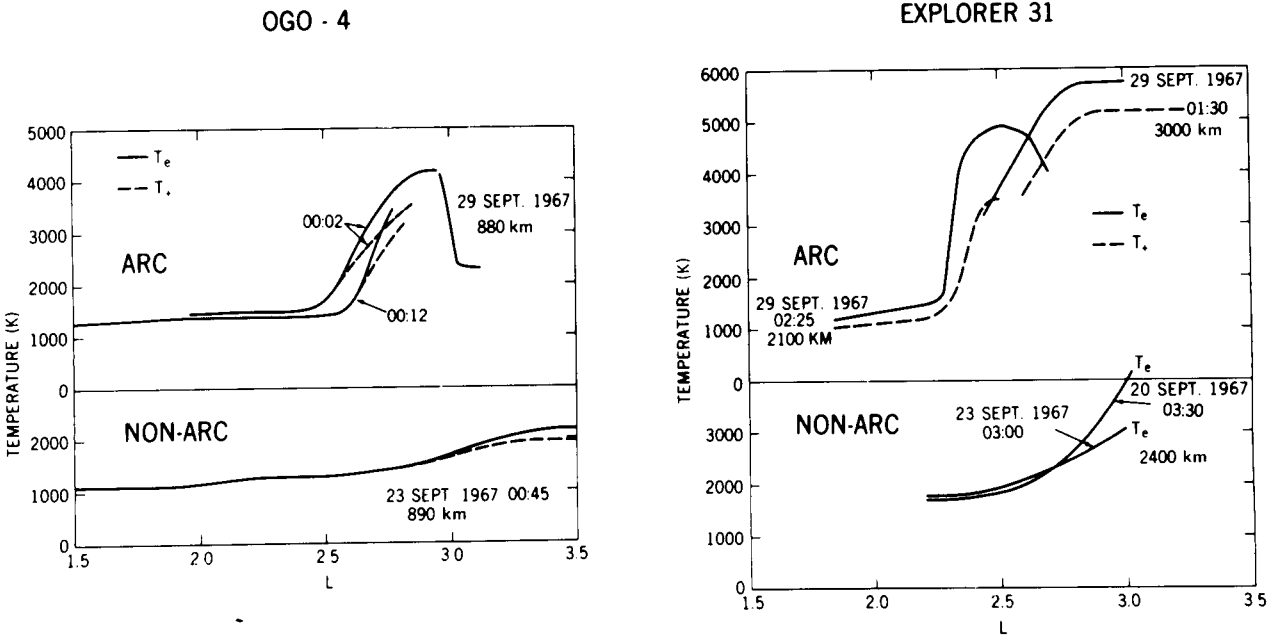

Figure 2

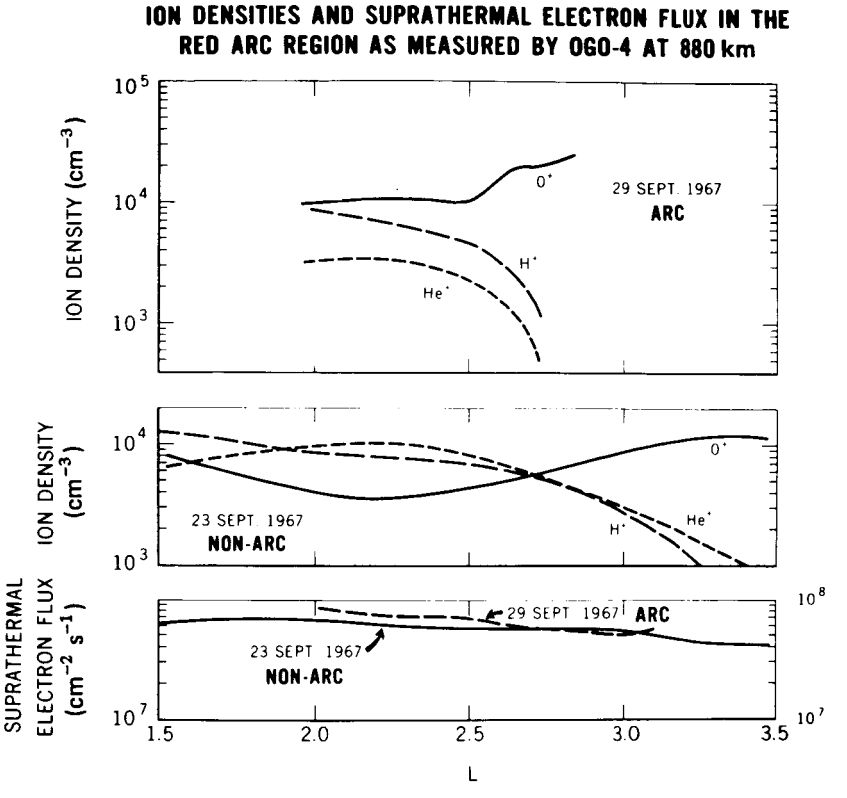
ION DENSITIES AND SUPRATHERMAL ELECTRON FLUX IN THE RED ARC REGION AS MEASURED BY OGO-4 AT 880 km
ION DENSITY (cm⁻³)
10⁵
10⁴
10³
O⁺
H⁺
He⁺
29 SEPT. 1967
ARC
ION DENSITY (cm⁻³)
10⁴
10³
23 SEPT. 1967
NON-ARC
O⁺
H⁺
He⁺
SUPRATHERMAL ELECTRON FLUX (cm⁻² s⁻¹)
10⁸
10⁷
29 SEPT. 1967 ARC
23 SEPT. 1967
NON-ARC
1.5
2.0
2.5
3.0
3.5
L

Figure 3

EVIDENCE FOR THE TROUGH WIND

Henry Brinton

Altitude profiles of thermal-ion concentration derived from Explorer 32 ion-mass spectrometer data indicate the existence of an upward flow of ionization along trough-field lines. The trough is that region located at approximately 65 degrees magnetic latitude wherethe concentrations of electrons and light ions are sharply reduced.

Figure 1 shows the region of the trough wind; we call it so because of the similarity of this upward flow of ionization to the polar wind that is operable at higher latitudes. This drawing illustrates schematically the earth and the near-earth magnetosphere, and indicates in black the location of our thermal-ion measurements.

The near-earth field may be considered in three regions. First, within the plasmasphere bounded approximately by the L = 4 shell, the thermal-ion density is high. Our ion-composition measurements inside the plasmasphere indicate that this region is controlled by diffusive equilibrium.

The second region, called the trough, is located immediately outside the plasmasphere. This is a closed-field line region, and here the concentrations of electrons and thermal ions are sharply reduced. Our measurements in the trough indicate that diffusive equilibrium does not hold here, and we interpret this finding as evidence for an upward flow of ionization along trough-field lines, which we call the trough wind. The trough-field lines are closed out to an L of approximately 10, and the arrows shown on the lines indicate the upward flow of ionization.

The third region of the near-earth field corresponds to the high-latitude areas characterized by open-field lines. On these lines there exists a supersonic upward flow of ionization, which has been called the polar wind because of the high latitude of its origin. The Explorer 32 orbit didn't cover polar latitudes, so we don't have measurements of the polar wind.

Figure 2 shows measurements made within the plasmasphere within 3 hours of local noon, between L = 1.8 and 2.2. This is a plot of ion concentration versus altitude for the primary ions observed, O^+ and H^+. The

important thing here is that, where H^+ is the minor ion, its concentration is increasing with increasing altitude, in agreement with the diffusive-equilibrium model shown.

Figure 3 displays the ion-concentration profiles for oxygen and hydrogen measured in the trough between L = 5 and 10.5 at the same local time as the plasmasphere data. Here we observe a strong decrease in H^+ concentration with increasing altitude when it is the minor ion, in disagreement with diffusive equilibrium. To show the degree to which H^+ departs from the diffusive-equilibrium model, we have plotted that model in dashed lines for H^+ and O^+; although the O^+ measurements are appropriate to diffusive equilibrium, the H^+ measurements depart radically from it. In fact, at an altitude of 2500 kilometers, the difference observed is approximately a factor of 50.

If, however, we now invoke the existence of a trough wind (that is, an upward flow of protons along trough-field lines), we can construct a model to fit the observed behavior of H^+. The solid-line profiles in this figure were computed using a flux model developed by Hans Mayr and Joseph Grebowsky of our laboratory. The lines clearly show that, for both O^+ and H^+, the flux model (or trough-wind model) fits the observations. At an altitude of 2500 kilometers, a relatively high proton velocity – corresponding to a Mach number of 0.85 – is required to produce the observed behavior of H^+. This result suggests that the trough wind may be closely related to the supersonic polar wind, with trough particles escaping by flowing across the field to open-field lines where the polar wind carries them to the magnetic tail.

In summary, our measurements have indicated a very different behavior in the altitude distribution of ionized hydrogen inside the plasmasphere, as compared with that in the trough region. This difference may be explained by invoking the existence of a trough wind, an upward flow of protons at near-sonic speed along closed trough-field lines, analogous and closely related to the polar wind that exists at higher latitudes.

MEMBER OF THE AUDIENCE:

Did you observe this at nighttime too?

BRINTON:

For various reasons, the nighttime data aren't as easy to interpret as the daytime; in fact, it has proved to be quite difficult, and we are not certain at this point as to the reason. For instance, the nighttime concentrations exhibit considerably more scatter, and it is difficult to determine exactly what the altitude profile is doing. So I can't really say what is happening at night – we are working on it.

MEMBER OF THE AUDIENCE:

Is the latitudinal intercept of the northern boundary of the trough wind around 78 degrees north latitude, and how wide is the latitudinal width at the earth's surface for these two regions?

BRINTON:

Those latitude intervals were adopted in the reduction of the data, based on the way the data appeared. I don't believe that the upper latitude boundary of the trough is known; it certainly varies with magnetic activity, and perhaps with time of day.

MEMBER OF THE AUDIENCE:

Is it around 75 to 80 degrees?

BRINTON:

I guess you might say that the upper boundary of the trough corresponds to the upper latitude boundary of closed-field lines that go up to at least L = 10; this would be, I suppose, on the order of 75 to 80 degrees latitude. I don't recall the correspondence exactly.

MEMBER OF THE AUDIENCE:

I have another question: If that is the case, then we would say that there are field-aligned currents flowing along that field line.

BRINTON:

That's correct.

MEMBER OF THE AUDIENCE:

So can you translate the upward flux of your H^+ into particles per cm^2 per second? We need something near 10^8 to 10^{10}.

BRINTON:

The magnitude of the flux is of the order 7×10^7 particles per cm^2 per second.

MEMBER OF THE AUDIENCE:

What is the origin of these protons? Are electrons also flowing, to keep the plasma neutral?

BRINTON:

I am not sure whether the electrons are flowing up in equal numbers, but they may be.

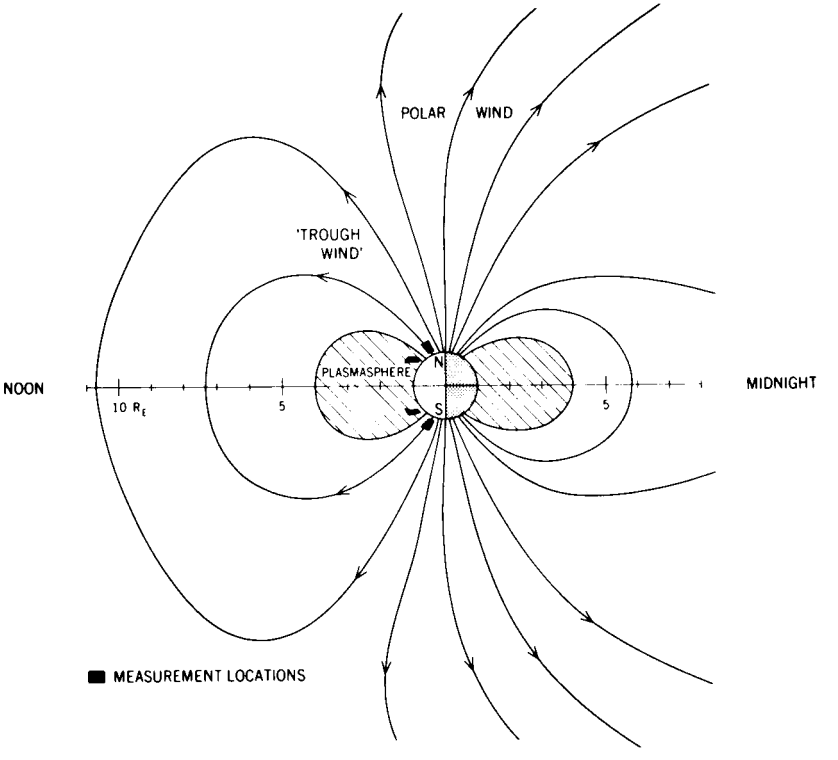
POLAR WIND
'TROUGH WIND'
PLASMASPHERE
N
S
NOON
MIDNIGHT
10 R_E
5
5
MEASUREMENT LOCATIONS

Figure 1

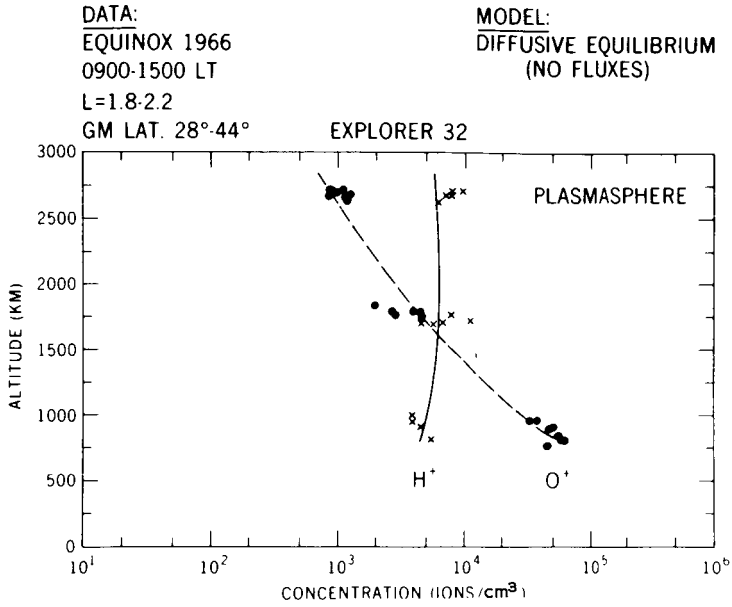

Figure 2

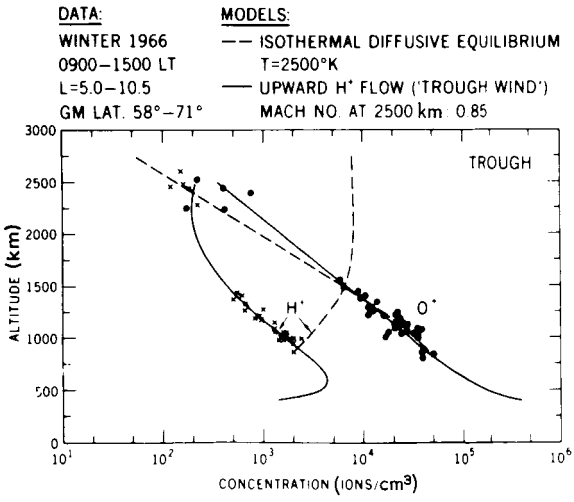

Figure 3

ELECTRON IMPACT IONIZATION OF H

Dr. F. H. M. Faisal*

DR. MEREDITH:

We have one more paper before the coffee break, and it will be from Dr. Faisal, who will be talking about electron impact ionization.

DR. FAISAL:

I shall be reporting here a theoretical work on an important reaction between electrons and negative hydrogen atoms which has been of astrophysical interest for quite a long time – about three decades. For the past ten years, people have been attempting to solve this problem theoretically, and the results they have come out with are widely divergent among each other.

Only very recently, there have been several experimental observations. Here I shall report some results of our theoretical calculations for this process.

The process I have in mind is an electron colliding with a negative hydrogen ion and neutralizing the hydrogen ion by stripping the loosely bound electron from it, and the two free electrons moving away.

In any atomic process, we ought to take account of the phenomenon of collision in a quantum mechanical manner: in other words, we should describe the electrons and the target particles as probability waves in phase space. But, as this is usually extremely complicated to handle, we present here a semi-quantum description of the process which is quite tractable: we describe the target in terms of quantum mechanics, whereas we describe the projectile electron in a classical fashion.

Figure 1, a picture of the collision system, shows the electron coming from the left and colliding with the target with an impact parameter b, and going away in a hyperbolic repulsive trajectory; the angle theta is the scattering angle.

---

*National Academy of Sciences resident research associate

Now, if we look at the situation closely, we see that the electron is interacting with the target, with an interaction potential of this kind which I have presented, in a multipole expansion fashion. We can use what is perhaps the simplest possible theory to describe the cross section calculation (a time-dependent perturbation theory), and come out eventually with an expression for the cross section like the one shown here. The quantities of interest here are the B_λ and the f_λ; the B_λ's describe all the properties involved in the target system (in a quantum mechanical manner), and the f_λ's describe the property of the electron moving away, calculated semiclassically. The complete expression for f_λ looks something like this, (expression 3), where the required I_λ integrals could be worked out analytically (or, if one wants, numerically too). The various quantities are defined below the equation.

Figure 2 shows some of the results of the calculation: the circles with bars are the experimental observations, and the dashed line represents a previous calculation before the experiment – a planewave calculation that assumed the electron to be traveling planewaves. But that is not proper, because the electron is traveling against a charged system, so that it really should be a Coulomb wave. The result of our calculations, the solid curve, is almost embarrassingly good considering the simplicity of the approximations, when compared with the results of the experimental observations. Finally, the dotted curve shown represents a calculation by two authors (Belly and Schwartz) who attempted to solve the problem in an entirely quantum-mechanical manner. They could attempt this only by analyzing the problem in partial waves, and this introduces the problem of tackling many partial waves, so that they had to cut off their sum over partial waves after a certain point. They don't describe how many partial waves they took, however. And this dotted line is their quantum mechanical result, up to this highest energy.

Now, before I finish, I would like to explain why we should expect an agreement of the kind we obtained, even from a semi-quantum calculation. First of all, we could be sure that, at high energies, the quantum particles would behave more like a classical particle because of the shortening of the wavelength as they speed up. So, at high energies, we could already expect the agreement to be fairly good. In fact, all the calculations – whether planewave or Coulomb-trajectory calculations – seem to agree with the experiments at high energies.

But the reason why it should also be reasonably good at lower energies lies in the peculiar property of the Coulomb potential itself. Recall the very well known case of the Rutherford-scattering cross section: whether you calculate it classically or quantum-mechanically, the results agree completely with each other! There is a certain parameter – called the Sommerfeld parameter – that equals the product of the charges of the two colliding particles, divided by the velocity of collision. Now, if this parameter is very much higher than 1, then the behavior of quantum phenomena in the Coulomb field tends to be well described by its classical picture. In the present problem, we find that, as the velocity goes down, the Sommerfeld parameter exceeds unity, and we therefore expect that our classical description will be good.

A second condition must also be satisfied if the classical description is to be valid, and that is this: the trajectory shown in the first figure should not change much from the initial to the final condition. In other words, the energy transfer should not be very large. And, in fact, in a collision system like this, where hydrogen minus has a very small binding energy, the change of energy is indeed small.

So, for these two reasons, we expect that our semiclassical calculation will be reliable for almost all energies. This work was done in collaboration with Dr. A. K. Bhatia.

Thank you.

DR. MEREDITH:

Are there any questions?

MEMBER OF THE AUDIENCE:

Are the curves you presented naturally cross sectioned, or are they normalized to get a best shape?

DR. FAISAL:

All the curves presented here are absolute, except the one referred to as "present": that calculation contains one unspecified parameter that arises

because of the multipole expansion of the potential. To handle this, we do an independent calculation at a very high energy, using the Born approximation, and fit the calculation to this curve at one point to obtain results for the entire range.

DR. MEREDITH:

Fine. Thank you very much. Let's take a 10-minute coffee break and then get back for the rest of the morning program.

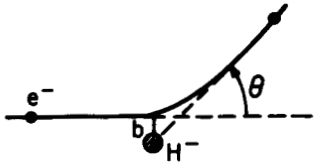

$$V_{\text{interaction}}(t) = \sum_{\lambda=1}^{\infty} \left\{ \frac{r_1^{\lambda} P_{\lambda}(\hat{r}_1 \cdot \hat{r}(t))}{r(t)^{\lambda+1}} + \frac{r_2^{\lambda} P_{\lambda}(\hat{r}_2 \cdot \hat{r}(t))}{r(t)^{\lambda+1}} \right\} \quad (1)$$

$$\sigma(E_1) = \sum_{\lambda=1}^{\infty} (2\lambda+1) |B_{\lambda}(K)|^2 \alpha^{-2\lambda+2} \frac{m_0}{2E_i} f_{\lambda}(\xi), \quad (2)$$

$$f_{\lambda}(\xi) = \frac{16\pi^3}{(2\lambda+1)^3} \sum_{\mu} |Y_{\lambda}^{\mu}(\tfrac{\pi}{2},0)|^2 \int_0^{\pi} |I_{\lambda\mu}(\theta,\xi)|^2 \frac{\cos\theta/2}{\sin^3\theta/2} d\theta \quad (3)$$

E = INCIDENT ENERGY

K^2 = EJECTION ENERGY

m_0 = REDUCED MASS

α = HALF THE DISTANCE OF CLOSEST APPROACH

θ = SCATTERING ANGLE

$\xi = \frac{1}{v_f} - \frac{1}{v_i}$

Figure 1

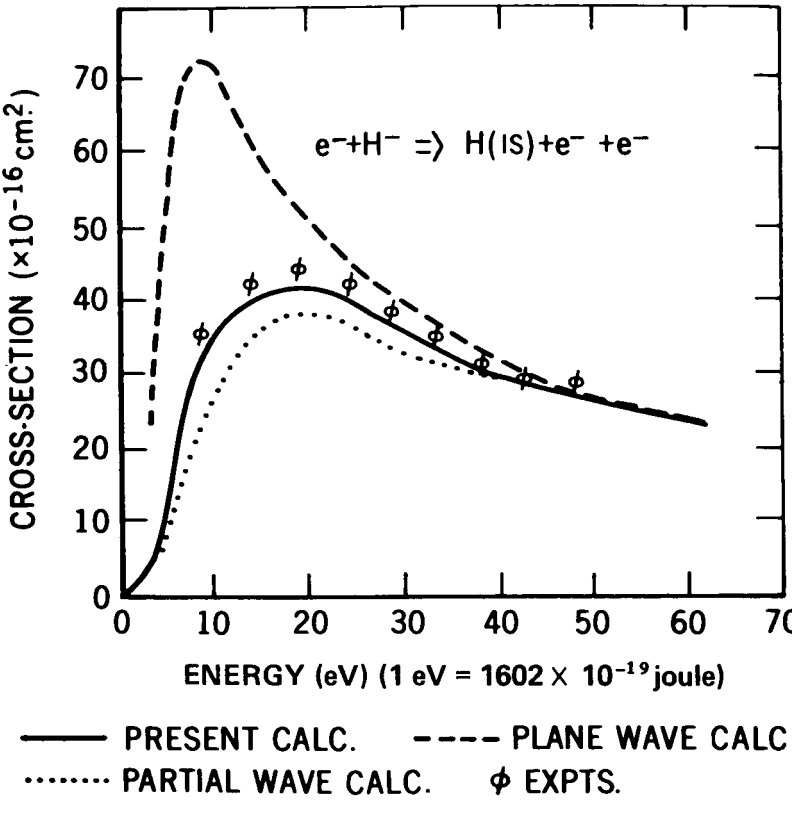
CROSS-SECTION (×10⁻¹⁶cm²)
70
60
50
40
30
20
10
0
e⁻+H⁻ ⇒ H(1S)+e⁻ +e⁻
0
10
20
30
40
50
60
ENERGY (eV) (1 eV = 1602 × 10⁻¹⁹joule)
PRESENT CALC.
PLANE WAVE CALC
PARTIAL WAVE CALC.
ϕ EXPTS.

Eigure 2

STABILITY OF THE VENUS IONOPAUSE

Dr. Jay Herman

DR. PIEPER:

Ladies and gentlemen, if you will take your seats we will proceed with the program.

To proceed with the program, we have moved from the area of earth resources and meteorology into the region of the ionosphere, and we will continue with the ionosphere, the magnetosphere, and the moon and interplanetary physics during this section. The first paper, which will be given by Dr. Jay Herman, is concerned with the stability of the Venus ionopause.

DR. HERMAN:

The Venus electron-density data obtained by Mariner 5 clearly showed a sharp cutoff at an altitude of about 500 kilometers on the day side, and 2500 kilometers on the night side, of the planet. The sharp cutoff arises as a direct consequence of the solar-wind interaction with the highly conducting topside Venus ionosphere, which is able to deflect the incoming solar wind around the planet into the far side.

Figure 1 shows this interaction schematically. Here we see the solar wind impinging on the planet from the left, with a velocity of 590 km per second. The first line is the bow shock, which was about 50,000 km from the surface of the planet at the Mariner 5 orbit, as shown in the lower righthand corner. The observed data pertinent to the solar wind was a density of 3 per cubic centimeter, with a temperature of 3×10^5 kelvins and pressure as indicated.

The inner black region represents the ionosphere and atmosphere. The boundary between the light and the dark regions represents the ionopause surface, which is essentially an interface between the solar wind and the ionosphere. The dashed line schematically represents the night-side tail as the solar wind is deflected around the planet and into the region behind the planet. The position of the ionopause is largely governed by the requirements of a balance in pressure between the solar-windstream pressure and the internal ionospheric kinetic-plus-magnetic field pressure.

As a consequence of the pressure balance, it is the purpose of this talk to show that the ionopause may not be a stable feature of the Venus ionosphere.

When the equations for temperature and density of each of the constituents of the Venus ionosphere are solved for conditions appropriate to the Mariner 5 flyby, it is possible to obtain a good fit to the observed data that includes the electron-density cutoff at 500 km altitude. In a similar manner, a series of solutions for temperature and density can be given for any angular position as measured from the subsolar-wind point. The result is that the lines of constant pressure for charged particles vary only slightly in altitude with angular position. However, the incoming solar-wind pressure varies in proportion to $\cos^2 \psi$, where ψ is the solar-wind aspect angle.

Thus, from the Mariner 5 occultation point, the effective solar-wind presure approximately doubles at the subsolar-wind point, and falls to a small value near the terminator. Under these conditions, an approximate shape can be given for the ionopause boundary, as shown schematically in Figure 2. Here again we see the solar wind impinging from the left; the ionopause boundary is indicated by the blunt-nosed shape. The altitude at the Mariner 5 occultation point was about 500 km, and the density was 1.2×10^4 per cubic centimeter (these are the observed values). When we take into account the solar-aspect angle, the calculated theoretical value for the ionopause position is at about 250 km – i.e., pushed in sharply. And, once again, the observed value on the night side is about 3500 km, where the density was observed to be about 300 per cubic centimeter.

The ionopause altitudes in this figure were calculated for a solar-wind speed of 590 km per second. At times when the solar-wind speed is reduced (to 400 km per second, for example), the ionopause level must move out to greater distances from the planet, about 500 km near the subsolar-wind point, and move about 2000 km down near the Mariner 5 occultation point.

The solar-wind speed is known to change significantly over time periods on the order of hours. Since the pressure balance is proportional to the value of the speed, the adjustments in ionopause altitudes would be very rapid. This would mean that the data from Mariner 5 (Figure 3) constitute merely a snapshot of a highly dynamic system, and therefore represent ionospheric conditions only at the time of occultation. In the sense of our experience with the earth's ionosphere, such a Venus ionosphere can be classified as unstable.

Not enough is known at present to make us certain of these conclusions: for example, the instability is avoidable if about half the heating of the topside of the Venus ionosphere comes from the solar-wind energy.

A possible mechanism is the deposition of energy by collisionless damping of fast-mode hydromagnetic waves originating in the ionopause region; such waves are likely to propagate inwards at approximately the acoustic speed, and dissipate over distances on the order of 100 km (Figure 4). If from 1 to 5 percent of the available solar-windstream energy is thus dissipated in the topside ionosphere as heat in the electron and ion gases, a feedback mechanism will exist to stabilize the ionopause.

However, in order for this or any other source of stabilization by heating to be effective, it is necessary that a small nearly horizontal magnetic field be present in the topside ionosphere to reduce the downward heat conduction of the charged particle. We have been able to show that just such a magnetic field, of strength about 10 nanotesla (10 gamma) and dip angle about 5 degrees, must be present for the Mariner 5 electron-density data to be consistent with the solar-wind data.

With this magnetic field, approximately 1 to 5 percent solar-wind heating will serve to maintain a pressure balance between internal charged particles and the solar-windstream pressure over the expected range of solar-wind speeds. Although solar-wind heating will tend to produce the required stabilization, the degree of this tendency depends on the efficiency with which streaming energy is converted into thermal energy. We hope that the proposed Venus orbiter will be able to pass through the interaction region and thus help resolve a major problem of planetary ionospherists.

DR. PIEPER:

Any question on the stability of Venus's ionopause?

MEMBER OF THE AUDIENCE:

Where will the Venus orbiter be?

DR. HERMAN:

If I remember, the last time I discussed this with Dr. Bauer I think the orbiter was planned to be a variable-altitude satellite, and at various times it will be at about 1000 km, or even further out. Also, I believe the lowest altitude it was planned to go was about 300 km, which would mean that it definitely would pass through the interaction region, which is at about 500 km.

MEMBER OF THE AUDIENCE:

Have you calculated the atmospheric temperatures?

DR. HERMAN:

I have not done so, but in a sense the interaction between the solar wind and the ionosphere gives you a parameter that enables you to calibrate your neutral-temperature calculations in the ionosphere. These temperatures, in turn, can be used to calculate downward into the atmosphere.

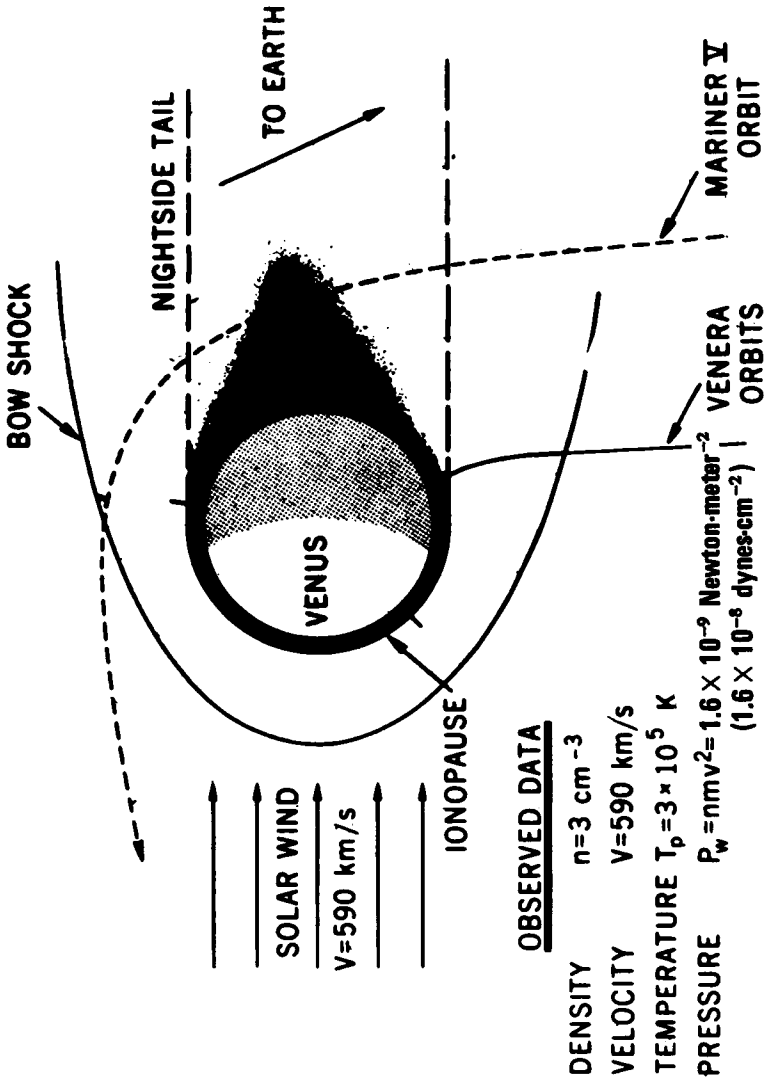
BOW SHOCK
NIGHTSIDE TAIL
TO EARTH
MARINER V ORBIT
VENUS
VENERA ORBITS
IONOPAUSE
SOLAR WIND
V=590 km/s
OBSERVED DATA
DENSITY n=3 cm⁻³
VELOCITY V=590 km/s
TEMPERATURE $T_p = 3 \times 10^5$ K
PRESSURE $P_w = nmv^2 = 1.6 \times 10^{-9}$ Newton-meter^{-2} (1.6×10^{-8} dynes-cm^{-2})

Figure 1

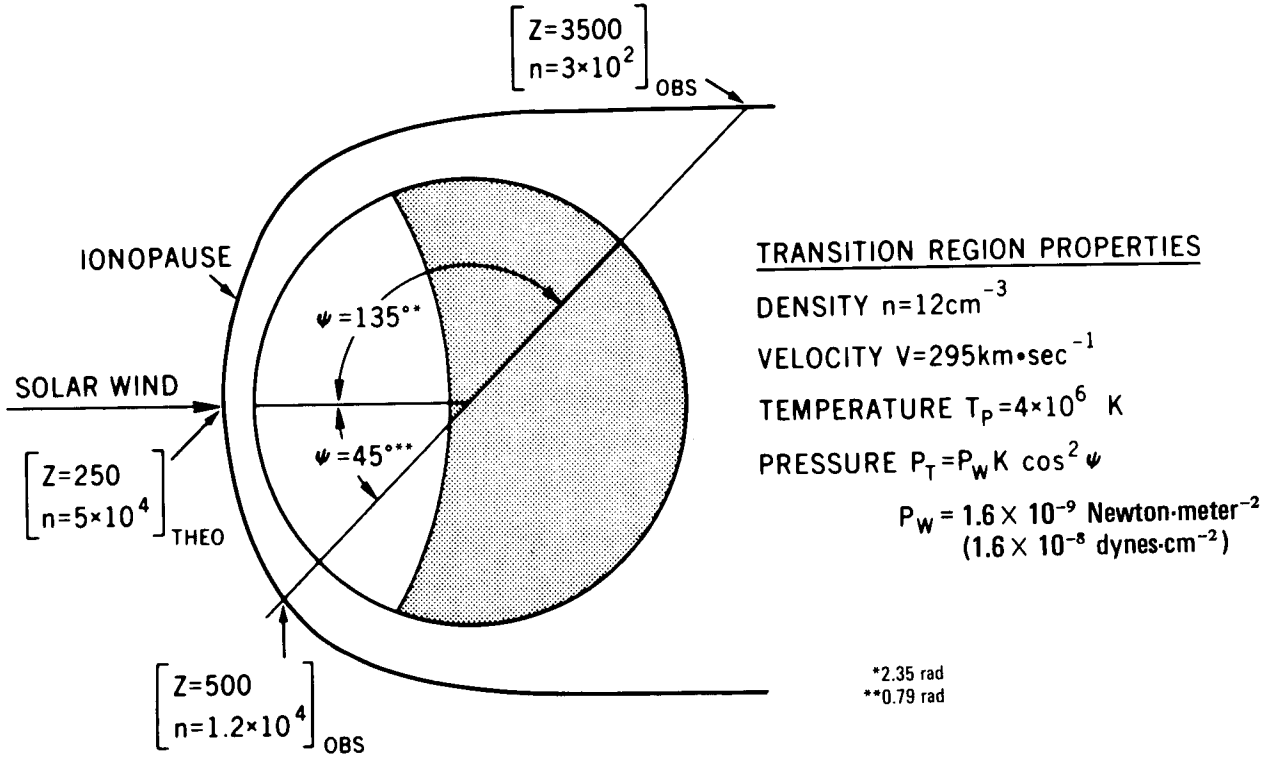
Z=3500
n=3×10^2
OBS
IONOPAUSE
ψ=135°*
SOLAR WIND
ψ=45°**
Z=250
n=5×10^4
THEO
Z=500
n=1.2×10^4
OBS
TRANSITION REGION PROPERTIES
DENSITY n=12cm^-3
VELOCITY V=295km•sec^-1
TEMPERATURE T_p=4×10^6 K
PRESSURE P_T=P_W K cos^2 ψ
P_W = 1.6 × 10^-9 Newton·meter^-2
(1.6 × 10^-8 dynes·cm^-2)
*2.35 rad
**0.79 rad

Figure 2

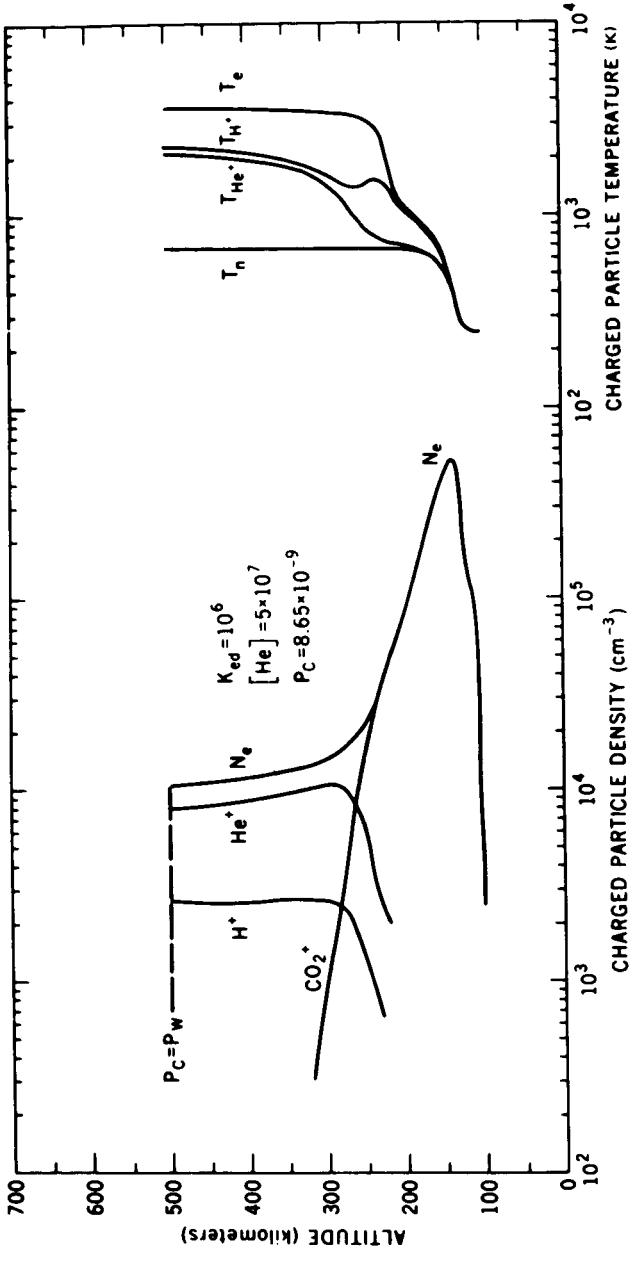
ALTITUDE (kilometers)
700
600
500
400
300
200
100
0
$P_C=P_w$
H^+
He^+
N_e
CO_2^+
$K_{ed}=10^6$
$[He]=5\times10^7$
$P_C=8.65\times10^{-9}$
N_e
10^2
10^3
10^4
10^5
CHARGED PARTICLE DENSITY (cm^{-3})
T_n
T_{He^+}
T_{H^+}
T_e
10^2
10^3
10^4
CHARGED PARTICLE TEMPERATURE (K)

Figure 3

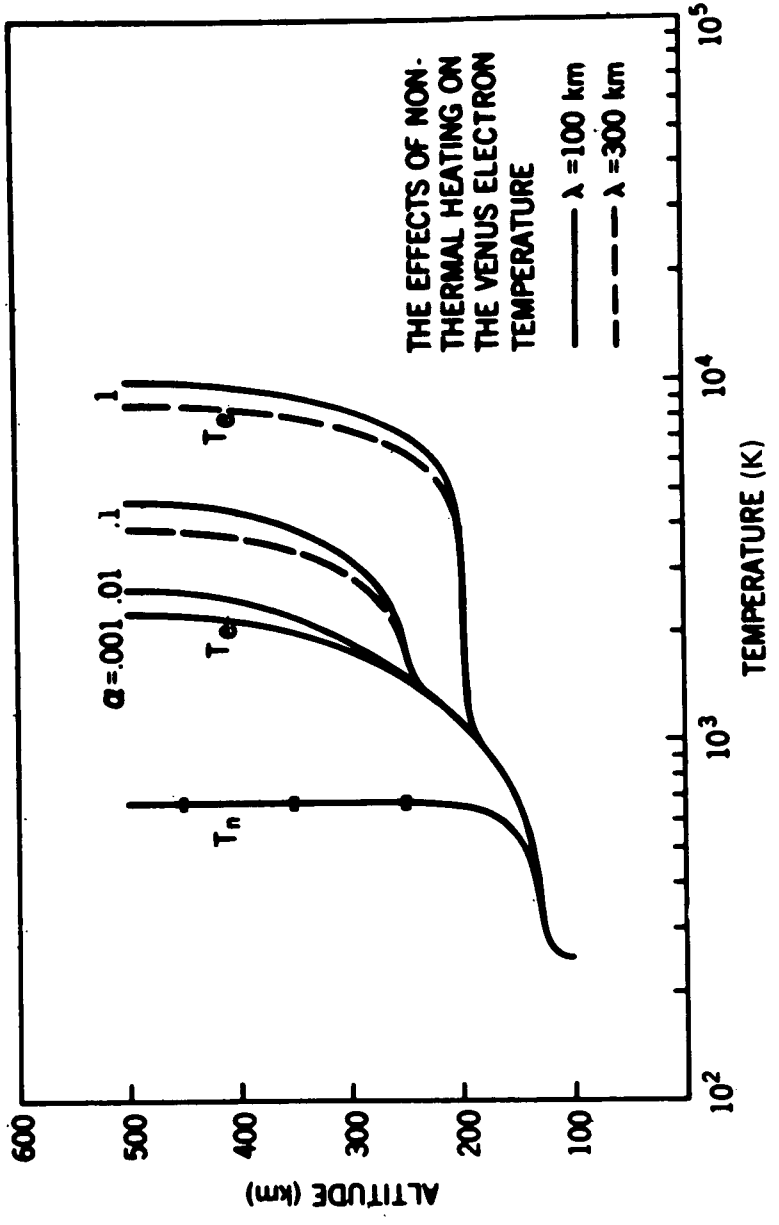
THE EFFECTS OF NON-THERMAL HEATING ON THE VENUS ELECTRON TEMPERATURE
λ =100 km
λ =300 km
α=.001 .01 .1 1
T_e
T_n
ALTITUDE (km)
600
500
400
300
200
100
10^2
10^3
10^4
10^5
TEMPERATURE (K)

Figure 4

ADIABATIC INVARIANCE

Dr. David Stern

I would like to describe here some theoretical work bridging the gap between celestial mechanics and the motion of charged particles in magnetic fields.

Celestial mechanics, as you know, is the study of the orbital motion of celestial bodies. Such motion may usually be described as a perturbed periodic motion – that is, to the lowest order of approximation, a planet or satellite moves in an ellipse around the center of attraction according to Kepler's laws – and then, superimposed on this, come what we call "small perturbations" due to the attraction of other bodies, due to the bulge of the earth, and so forth.

The fact that, in the lowest approximation, the motion is periodic is of great help here (since periodic quantities are bounded and average up to zero); in fact, Poincare and others have developed rather powerful methods of using this property to predict the motion for relatively long times in advance.

In recent years, another example of perturbed periodic motion has attracted interest, and that is the motion of low-energy charged particles in a magnetic field. If such a field is constant in direction and magnitude, the particle simply spirals around field lines (as shown in Figure 1), and this is a periodic motion of sorts.

In a more general magnetic field, the spiral is slowly perturbed because of the curvature and convergence of field lines, and because of time dependence and associated electric fields. Nevertheless, under suitable conditions, it may still be viewed as a perturbed version of the motion in a constant field.

This sort of motion – the so-called guiding-center motion – has been analyzed successfully, more or less from first principles, and this has led to a set of approximate constants of the motion known as adiabatic invariants. Higher-order results and invariants have been derived by an approach worked out by Kruskal from the Krylov-Bogliubov method; this, however, tends to be lengthy and complicated, so we may well ask whether the usual methods of celestial mechanics might be adapted for this problem.

I have carried out such an adaptation, obtaining forms of both the method of Poincare and that of Krylov and Bogliubov, which is usable with either method; and – what may be just as interesting – it reveals the full relationship between the two methods as well as their relationship to other approaches. This, by the way, works in both directions: it has also given us, as a byproduct, a simplification and generalization of methods used in celestial mechanics. The substance of this work appears in a series of rather theoretical papers which are clearly outside the scope of this presentation. Let me point out just one of several differences between the two cases which constitute the reason why the methods of celestial mechanics must be modified before they can be used in the new context.

In celestial mechanics, the perturbation is always considered small: for instance, the attraction of Jupiter that perturbs the earth's orbit is always smaller by a factor of several thousand than the attraction of the sun. By contrast, for a radiation-belt particle sliding along its guiding field lines, the perturbation is not small; it may sense changes in field intensity amounting to a factor of 100. What is true, however, is that – between any two consecutive gyrations of this particle – the change in the field is small. Such perturbations are called slow, or adiabatic, perturbations, and they require somewhat different handling.

As a test of the method, the motion of a slowly perturbed harmonic oscillator was solved as shown in Figure 2 by a rather straightforward calculation. This is a relatively simple problem that can be physically represented by a pendulum which is slowly being drawn up, or by a particle in a magnetic field which is constant in space but varies slowly in time. As you can see, the lowest order invariant equals the energy divided by the frequency; this is a well-known result, equivalent to the zero-order magnetic moment of the charged particle. Added to this are three orders of correction terms, all but one of them varying periodically at twice the frequency of the oscillation.

I am in the process of adapting the equation of motion of charged particles to Hamiltonian form, the one best suited for such methods. When this is complete, we will I hope, gain a better understanding of adiabatic invariants and better methods for cranking them out to any desired order, in addition to the satisfaction of bringing together two quite distinct subjects into a single theoretical framework.

PERTURBED PERIODIC MOTION

PLANETARY MOTION

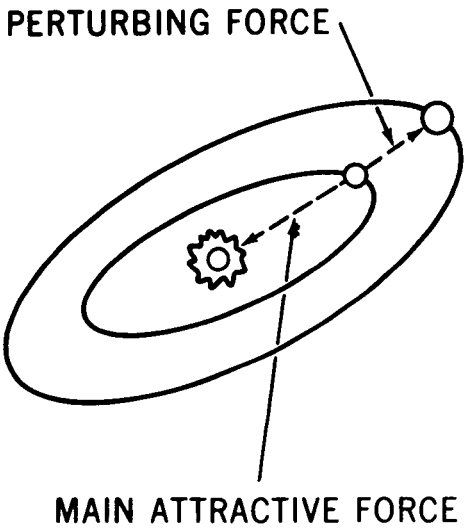

CHARGED PARTICLE

IN HOMOGENEOUS MAGNETIC FIELD:

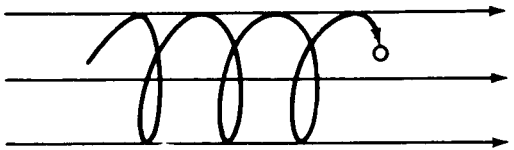

IN SLIGHTLY INHOMOGENEOUS FIELD:

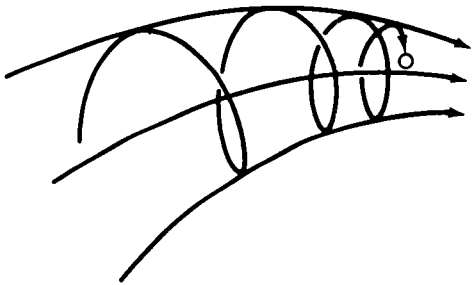

Figure 1

SLOWLY PERTURBED HARMONIC OSCILLATOR

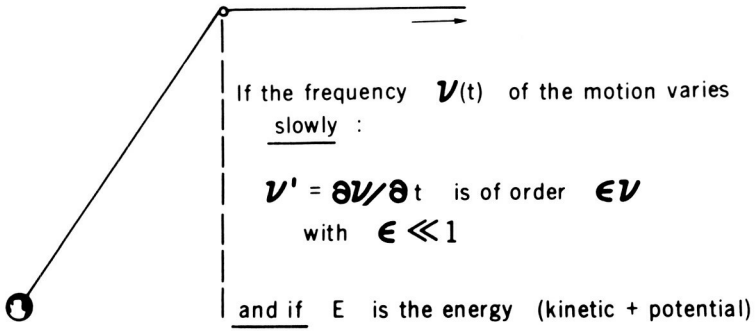

THEN AN ADIABATIC INVARIANT OF THE MOTION IS

$$J = \frac{E}{\nu}\left\{1 + \frac{1}{2}\left(\frac{\nu'}{4\pi\nu^2}\right)^2 + \frac{1}{4\pi\nu}\left(\frac{\nu'}{4\pi\nu}\right)' \cos(4\pi\Omega)\right.$$

$$\left. + \sin(4\pi\Omega)\left[\left(\frac{\nu'}{4\pi\nu^2}\right) + \frac{1}{2}\left(\frac{\nu'}{4\pi\nu^2}\right)^3 - \frac{1}{4\pi\nu}\left\langle\frac{1}{4\pi\nu}\left(\frac{\nu'}{4\pi\nu^2}\right)'\right\rangle'\right]\right\} + O(\epsilon^4)$$

Figure 2

MAGNETOSPHERIC RADIO NOISE

Michael Kaiser

The first Radio Astronomy Explorer, which we call RAE, was primarily intended to observe the galactic background and fast-drift solar bursts at frequencies below those in use at the surface of the earth. Thus far, about a dozen papers have been published or presented discussing these observations. In fact, the results of some of this work will be reported here later this afternoon.

However, with all due respect to the astronomical objects, there is another source of radio noise which is observed a high percentage of the time on each and every orbit. Now, this source is – not too surprisingly – the earth, or at least the earth's magnetosphere. Observations made by the illfated ATS-2 spacecraft showed the existence of radio-noise bands at 700 kilohertz and below; these bands were diagnosed at the time as the well-known noise enhancement that occurs near the local plasma frequency. This same type of noise has been seen by RAE, and is a nearly continuous feature on some of the receiver records. However, the high sampling rate of RAE permits us to see a surprising amount of fine detail.

Figure 1 shows data from two adjacent observing frequencies versus relative intensity and time. These anticorrelations in the data appear quite frequently within 611 to 698 millirad (35 to 40 degrees) of the equator, and we see individual events as short as 5 seconds superimposed on events such as this, which are 25 to 30 minutes long. The larger scale events have a plausible, but by no means final explanation: We think that, at the beginning of one of these events, the lower frequency is observing the plasma noise while the higher frequency is seeing in the galactic background; then the satellite crosses into a region of enhanced electron density that has the effect of raising the plasma noise, so that the upper observing frequency sees the noiseband instead of the lower frequency.

This explanation calls for density changes on the order of, say 50 percent. This is not an unreasonable number for a large area, but – for the 5-second events I mentioned – we're still working toward an explanation.

Also, before launch, we expected that RAE would observe a certain amount of ground-based emission leaking through the ionosphere. High-intensity noise coming from the general direction of the earth is seen, but its origin is not as obvious as we expected. Figure 2 shows two orbits of data collected simultaneously from the upward-pointed and the downward-pointed antennas, displayed as intensity versus time. The noise I am talking about is the events between 17 and 18 hours, and 21 and 22 hours, and possibly the small event at 19 hours. Comparing the upper and lower data, you can see that this noise is a factor of 10 or 15 times more intense in the downward direction. The noise appears to some extent on practically every orbit, and is always characterized this way, by a very sharp onset followed some time later by an abrupt drop. This noise is seen primarily above 3 MHz. Until a few months ago, we assumed without too much question that it was simply manmade noise breaking through the ionosphere at places where the critical frequency was below 3 MHz.

However, with the addition of recent data, this explanation is a little less certain. Figure 3 is a short segment of data from the fast-sampling radiometer attached to the nondirectional dipole antenna; this again shows relative intensity versus time for all six observing frequencies. These near-sinusoidal oscillations have been observed at these frequencies on practically every orbit of RAE since launch, and for some time they were catalogued and classified according to the period of the oscillations, their temporal development, their special arrangement, and so on.

The possible explanations that were offered ranged from multipath interference to synchrotron emission from modulated precipitating electrons.

However, a recent comparison of data from two different types of receivers showed – surprisingly – that the oscillations at these low frequencies and the intense noise at the higher frequencies occurred at precisely the same time. If ground breakthrough is to be considered as the possible cause of this phenomenon, a fairly sophisticated theory is needed to explain this low-frequency part of the spectrum; direct breakthrough cannot happen here, because of the ionospheric reflection. To further complicate the

picture, it now appears that the noise may be connected in some way to the angle between the sun and the earth, with this angle controlling the latitude and extent of the observed noise. However, considerably more data must be analyzed before this connection can be firmly stated.

Needless to say, with these tantalizing and frankly puzzling observations we have added a new object of study for radio astronomers. We are starting to spend a little more time thinking about what is below RAE.

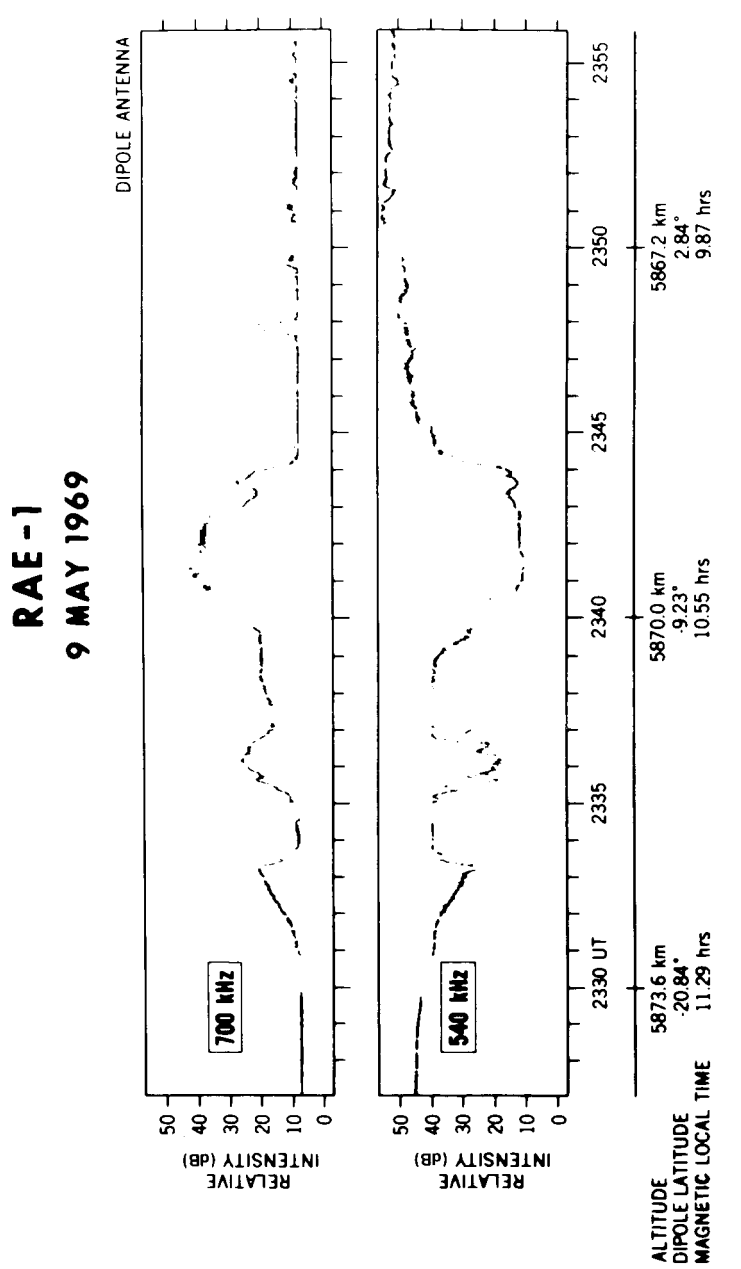
RAE-1
9 MAY 1969
DIPOLE ANTENNA
700 kHz
540 kHz
RELATIVE INTENSITY (dB)
50
40
30
20
10
0
2330 UT
2335
2340
2345
2350
2355
ALTITUDE
DIPOLE LATITUDE
MAGNETIC LOCAL TIME
5873.6 km
-20.84°
11.29 hrs
5870.0 km
-9.23°
10.55 hrs
5867.2 km
2.84°
9.87 hrs

Figure 1

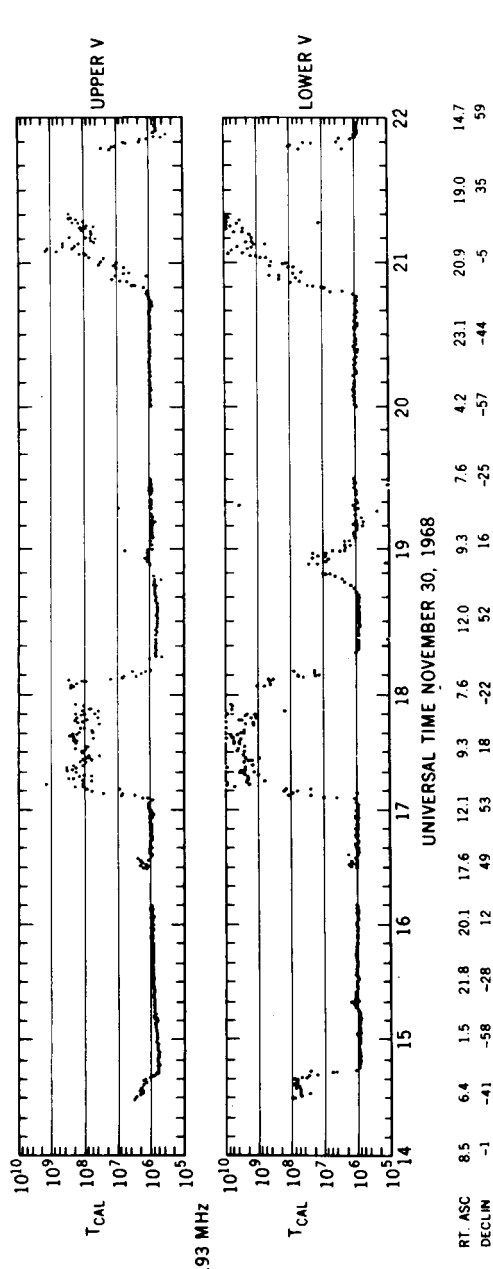
UPPER V
LOWER V
T_{CAL}
3.93 MHz
UNIVERSAL TIME NOVEMBER 30, 1968
RT. ASC 8.5 6.4 1.5 21.8 20.1 17.6 12.1 9.3 7.6 12.0 9.3 7.6 4.2 23.1 20.9 19.0 14.7
DECLIN -1 -41 -58 -28 12 49 53 18 -22 52 16 -25 -57 -44 -5 35 59

Figure 2

OSCILLATIONS OBSERVED BY RAE-1 NOVEMBER 4, 1969

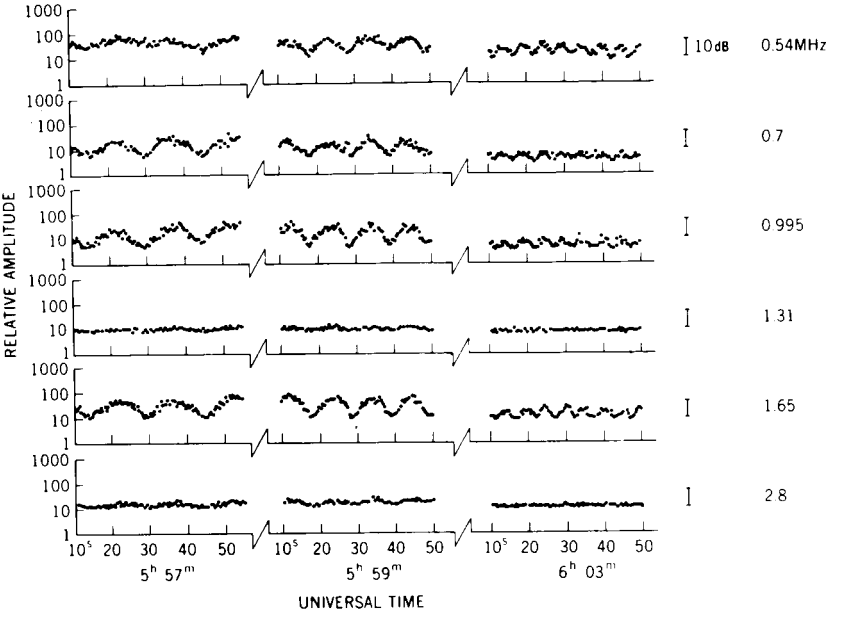

Figure 3

MAGNETOSPHERIC BOUNDARIES

Dr. Donald Fairfield

The location of the outer boundary of the geomagnetic field, or magnetopause, and the location of the earth's bow shock have been known approximately since the flights of Explorer 12 and IMP-1. Recently, I have compiled data from the first six IMP spacecraft in an effort to further redefine the information on the location of these boundaries, and to study their variation from the average.

Figure 1 shows data points that represent the average location of the magnetopause in the ecliptic plane, as defined by Dr. Ness's magnetometer on about 250 spacecraft passes through the region of the magnetopause. Data points have been rotated into the ecliptic plane, assuming axial symmetry, and only data within 7 earth radii of the ecliptic plane have been included. All points have been rotated by 70 millirad (4 degrees), to eliminate the expected effects of aberration due to the earth's motion about the sun.

We have written a computer program to obtain the best-fit ellipse to this data, and this curve is represented by the solid curve in the figure. The fit was made by eliminating data at the lunar orbit; a straight line has simply been drawn to the ellipse at a point 15 earth radii behind the earth. We then compared these data with the theory of Olson, represented by the dashed line: this is the conventional theory, which equates the solar-wind pressure with the vacuum geomagnetic field pressure of the magnetosphere. When the theoretical curve is normalized to the data near the subsolar point, we find that the theoretical curve lies inside the experimental curve in the dawn and dusk meridian planes; this is probably due to a deficiency of the theory, which neglects the effects of the upstream bow shock and also the effects of plasma pressure within the magnetosphere.

Figure 2 shows comparable data for the earth's bow shock; again, each point represents an average position of the bow shock, and again we have obtained the best-fit curve to the data, which in this case is a hyperbola. We compare these data to the gas-dynamics theory of Spreiter and Jones, represented by the dashed curve, and the agreement is quite good.

In performing these gas-dynamics calculations, one uncertainty is that the ratio of specific heats γ for the solar wind is not precisely known. Now it turns out that the standoff distance of the bow shock from the magnetopause depends on γ in a rather sensitive fashion. As we have a good experimental number here for the standoff distance of the bow shock, we can use this as an indication of the appropriate gamma: this number turns out to be between 5/3 and 2. Each of these average bow-shock positions is located within about 2 earth radii of the average curve; as a matter of fact, the most distant bow-shock crossing previously reported in the literature is represented by a point only about 4 earth radii upstream from the average position. In the process of searching through several years of satellite data, I found several instances where the bow shock was located very much further upstream; these cases are indicated by the line segments in the upstream region. Each of these line segments represents the spacecraft's trajectory during an interval when multiple bow-shock crossings were observed. The number associated with each point is the number of crossings observed during the interval. The most distant of these is a series of eight IMP-3 crossings located about 22 earth radii upstream from the average position. During most of these intervals, there is evidence that the solar-wind velocity and density are quite low, and the field is often unusually high. But these distant positions cannot be explained by the location of the magnetopause at a comparably distant position: they must rather be associated with an increased standoff distance for the bow shock. This is consistent with the theoretical prediction of what should happen under the conditions of unusually low Alfvén Mach number observed at these times. During one of these instances, the solar-wind plasma sampled by the Explorer 35 spacecraft was of such low intensity that the instrument could not measure the plasma. It is possible that, at this time, the solar wind may even have been sun-Alfvénic. But, since we can't measure the plasma, we can't say for certain.

I have also studied these orbit variations in the average position of the magnetopause, and I find that they can be explained fairly well on the basis of the changing flux of the solar wind, which compresses the magnetosphere to a greater or lesser extent. The magnetopause also appears to lie somewhat closer to the earth when the interplanetary field is southward.

DR. PIEPER:

Is there any question or comment with respect to Dr. Fairfield's analysis of magnetospheric boundary position as a function of time?

MEMBER OF THE AUDIENCE:

Did you say these were points of all crossings you had? Did you make some selection according to K_p?

DR. FAIRFIELD:

Not according to K_p; the only restriction was to measurements made within 7 earth radii of the ecliptic plane. This eliminates roughly half the points.

MEMBER OF THE AUDIENCE:

Have you studied the variation of boundary positions with K_p?

DR. FAIRFIELD:

No, not with K_p, but I did confirm the result of Meng, who shows that abnormally earthward magnetopause positions may correspond to either quiet or disturbed geomagnetic conditions, whereas distant magnetopause conditions invariably correspond to a quiet geomagnetic AE index. I feel that comparing boundary positions with actual solar-wind parameters, as I have done, answers more fundamental questions than comparison with K_p.

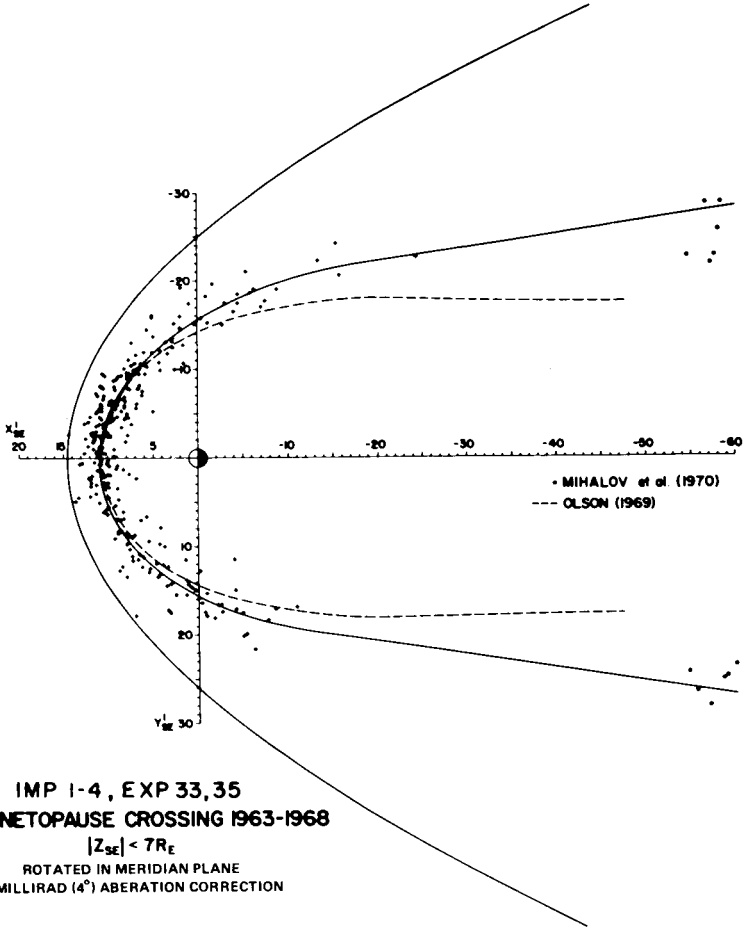
-30
-20
-10
X_{SE}^{I}
20
15
5
-10
-20
-30
-40
-50
-60
• MIHALOV et al. (1970)
--- OLSON (1969)
10
20
Y_{SE}^{I} 30
IMP I-4, EXP 33,35
MAGNETOPAUSE CROSSING 1963-1968
$|Z_{SE}| < 7R_E$
ROTATED IN MERIDIAN PLANE
70 MILLIRAD (4°) ABERATION CORRECTION

Figure 1

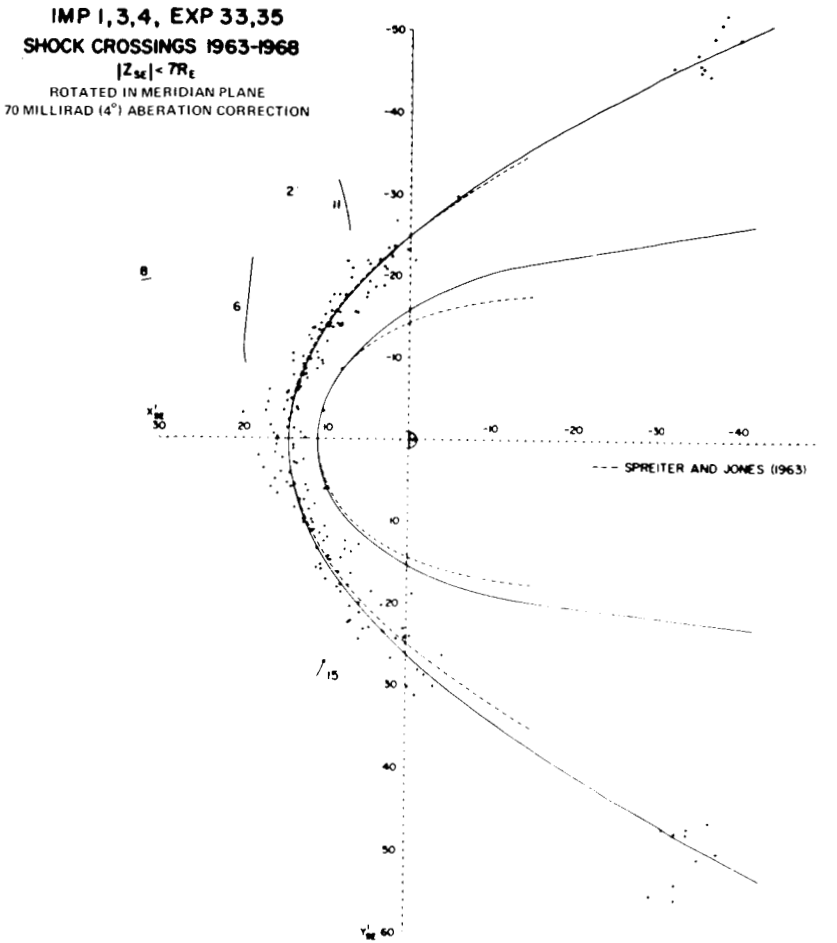
IMP 1,3,4, EXP 33,35
SHOCK CROSSINGS 1963-1968
$|Z_{SE}| < 7R_E$
ROTATED IN MERIDIAN PLANE
70 MILLIRAD (4°) ABERATION CORRECTION
2
11
8
6
15
X'_{SE}
Y'_{SE}
--- SPREITER AND JONES (1963)

Figure 2

CRUSTAL ANOMALIES

Dr. Joseph Cain

The ambient geomagnetic field as measured a short distance above the earth's surface consists primarily of the 30-to 60-microtesla (0.3- to 0.6-Gauss) component generated by the fluid motions in the earth's core. In addition, there are small (<0.1 microtesla (<100γ) (100γ = 0.1 microtesla = 0.001 Gauss) and variable external components from ionospheric currents and plasma interactions on the magnetosphere. The only other known source is from magnetization of materials in the earth's crust to a depth of the order of 20 km, where the temperature rises above the Curie point for all known materials. The mantle, which lies between the crust and the core 2900 km below, is not thought to generate any magnetic field.

The crustal or magnetic anomaly component is extremely variable in intensity at the earth's surface, as reflected in the varying composition of materials, but weakens rapidly with altitude. A famous case is that of the Kursk magnetic deposit in Russia, which creates a 20-microtesla (0.2 Gauss) anomaly at the surface but is not seen at 6100m (20,000-foot) altitude. At satellite altitudes of 250 to 500 km, it has been assumed that any effect from crustal anomalies would be undetectable. Recently Zietz, Andreasen, and Cain made a statistical analysis* of the Cosmos-49 data, performing heat-flow and tectonic correlations with detailed features on a residual-anomaly map of North America, reproduced in color here as Figure 1. Shown are the residuals from a fitting surface having a wavelength greater than 4400 km. As this surface fits the data to a standard error of 21 nanotesla (21γ) (1γ = 1 nanotesla (10^{-5} Gauss), and some of the feasures are defined by a spread of only a few standard errors, it us useful to look for independent means to corroborate these results.

The advantage of the Cosmos-49 data is that the spacecraft flew lower than any other magnetic experiment (250 to 490 km) and would be expected to detect more detail than measurements made at a higher altitude. Thus, the

*Zietz, I., G. E. Andreasen, and Joseph C. Cain. Magnetic anomalies from satellite magnetometer. J. Geophys. Res. 75, 4007-4015. 1970.

magnetic data from the POGO spacecraft (OGO-2, -4, and -6), whose altitudes ranged from 400 to about 1000 km, would not be expected to show as much detail, but should show the features whose wavelengths are commensurate with the altitude.

Note the dotted line on Figure 1: it shows an area across the United States where the field is noticeably weaker than to the north or south. There are of course several cells of lows and highs, one of which appears to parallel the Appalachian mountains. Figure 2 shows a typical POGO pass across mid-United States, plotted together with the Cosmos-49 averages and their standard errors. Although the correlation appears good here, the variance of the Cosmos averages is so large that we should not rely on many of the detailed features shown in Figure 1. In attempting to similarly average the POGO data over the same area, we found the variations large and highly variable south of 30 degrees, because of external sources. However, even though the individual profiles varied in character below 30°N, and in level everywhere, it is possible to pick out one consistent feature over the United States which correlates well with Cosmos-49.

Figure 3 shows a set of six POGO profiles from 25 to 45°N at various longitudes over the United States. The persistent feature of these curves is the minima in the range between 40 and 43°N, and maxima about 33 to 35°N. Although the level of each curve differs and the behavior south of 30°N varies, this signature is generally present on these examples and on every other profile over these longitudes. The feature appears a little to the north near 95°W and cannot be followed east of the Appalachians or west of the Rockies. Although the Cosmos-49 averages illustrated in Figure 1 do show the characteristic mid-United States low, bounded by highs to the north and south, the agreement is obscured by the low cells running northwest from Louisiana and the lows continuing in the far west. Neither of these details shows up consistently on the POGO data, and it is difficult to see how such large discrepancies could appear at only about 200-km lower altitude; it seems more likely that some of the detailed cells below 40° latitude shown on Figure 1 must represent noise resulting from data errors or uncorrected time variations.

The wavelength of the feature shown in Figure 3 is only about 20 degrees, too small to be a product of the fitting technique, which can produce waves in the ΔF curves as large as 36 degrees or longer. Its amplitude is

consistent to within 25 percent, and decreases somewhat with altitude. It thus appears that there is a broak weak negative magnetic anomaly running through the central United States, bounded approximately by the two major mountain chains. This feature has not been noted in surface magnetic surveys, because it is too broad and weak to be detectable in the surface-anomaly noise.

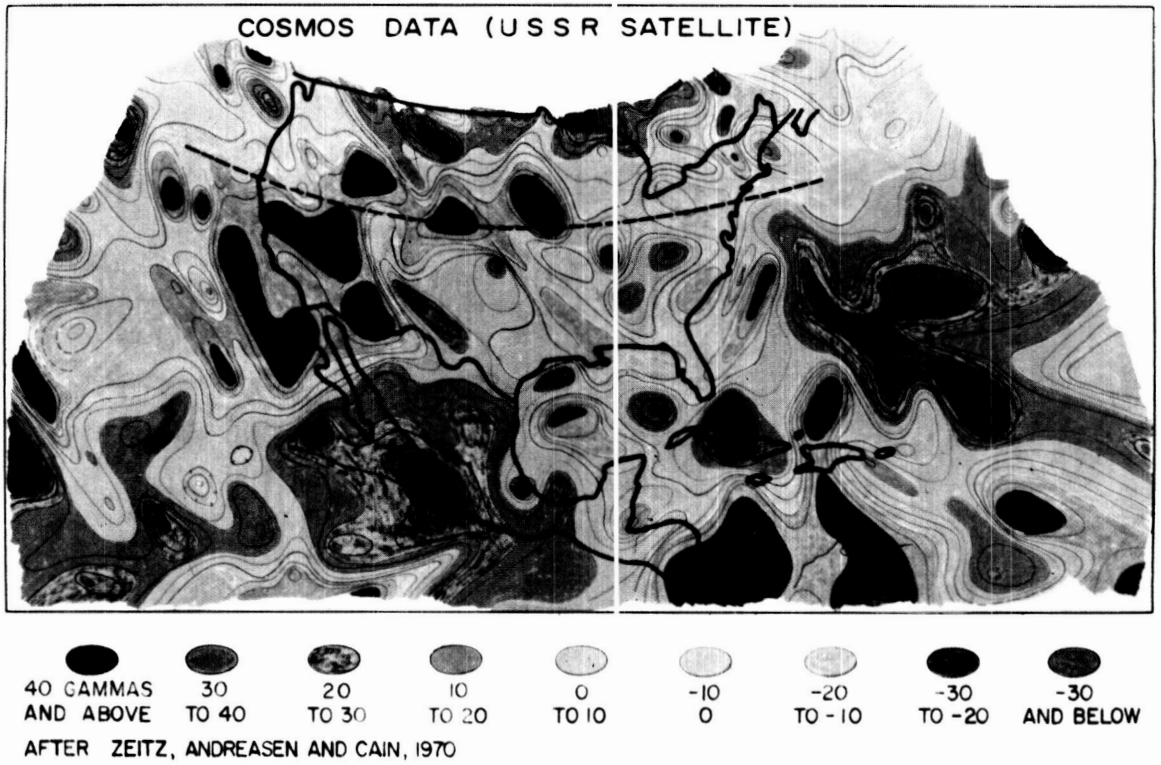
COSMOS DATA (USSR SATELLITE)
40 GAMMAS AND ABOVE
30 TO 40
20 TO 30
10 TO 20
0 TO 10
-10 0
-20 TO -10
-30 TO -20
-30 AND BELOW
AFTER ZEITZ, ANDREASEN AND CAIN, 1970

Figure 1

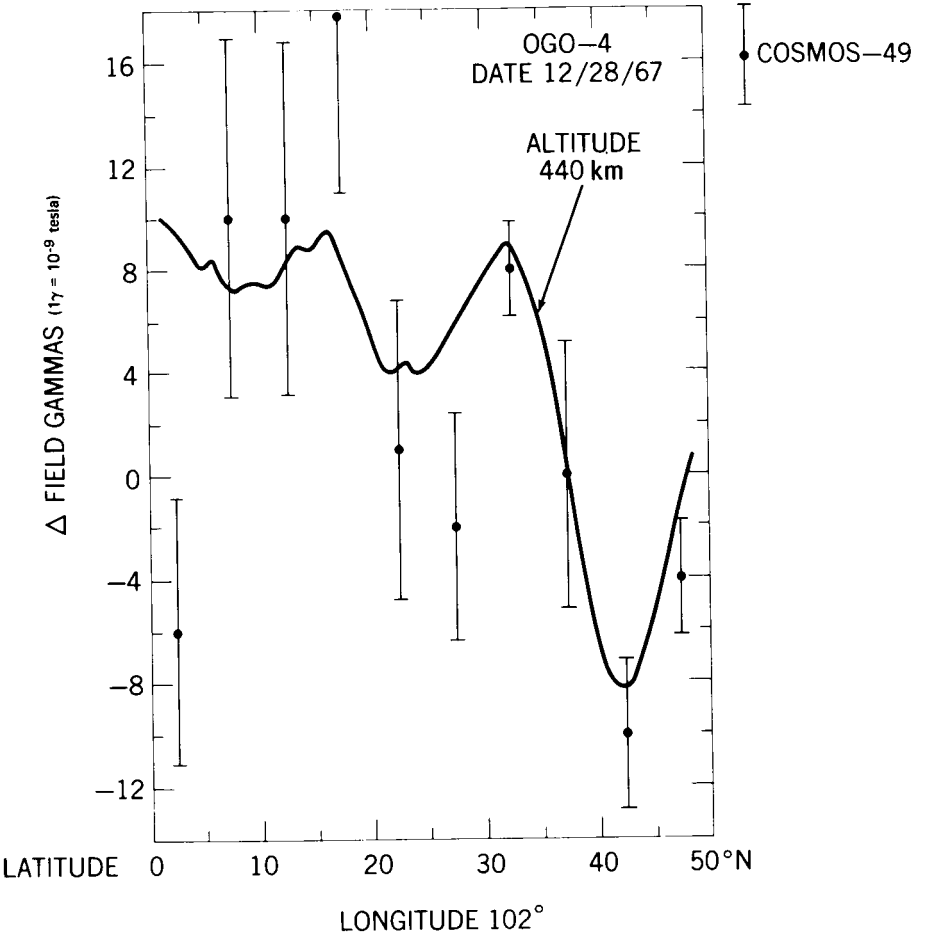
OGO–4
DATE 12/28/67
ALTITUDE
440 km
COSMOS–49
Δ FIELD GAMMAS (1γ = 10⁻⁹ tesla)
16
12
8
4
0
–4
–8
–12
LATITUDE
0
10
20
30
40
50°N
LONGITUDE 102°

Figure 2

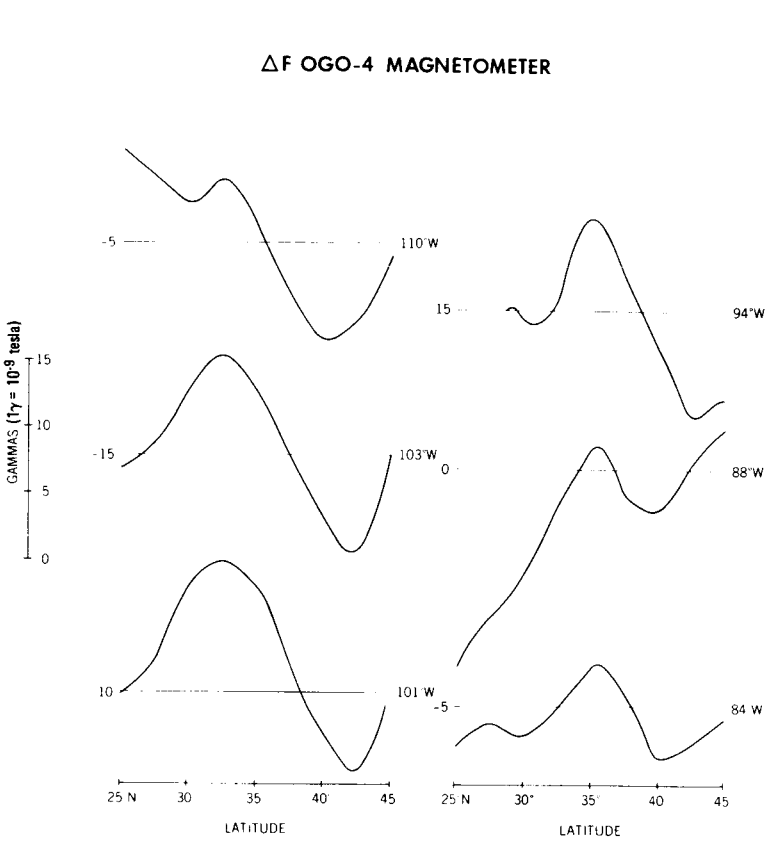
ΔF OGO-4 MAGNETOMETER
GAMMAS (1γ = 10⁻⁹ tesla)
15
10
5
0
-5
110°W
-15
103°W
10
101°W
25°N
30°
35°
40°
45
LATITUDE
15
94°W
0
88°W
-5
84°W
25°N
30°
35°
40°
45
LATITUDE

Figure 3

MASCON DISTRIBUTION ON THE MOON

James Murphy

New results concerning the distribution of mascons on the moon have been obtained from an analysis of all four Apollo lunar-orbit missions (i.e., Apollos 8, 10, 11, and 12). The orbital characteristics for Apollo orbits were such that the spacecraft were all close to the lunar surface, orbiting approximately 110 km above it. The orbits were nearly circular, and two of them were inclined to the equator by only a degree or so; two others, Apollo 8 and 10, were inclined between 12 and 15 degrees. The perturbations of the orbit plane, reflected in the perturbations and the inclination of the inertial node, were fairly severe for all these missions.

The current operational Apollo lunar-gravity mode, the L-1 model, failed to predict almost all of this perturbation. It turns out that the coefficients of degree 4 and order 1 in the spherical harmonic expansion of the gravity field could explain most of this perturbation; this coefficient was sensitive to the motion of the plane. And so we used the actual orbital elements, the inclination and the node, to deduce values for these coefficients by a weighted least-squares technique. The values we obtained compared favorably with others obtained from an analysis of lunar-orbiter tracking data and lunar-orbiter Kepler-element histories.

At this point I would like to mention that there are two conflicting theories of mascon distribution: The first of these was obtained by people at the Jet Propulsion Laboratory from an analysis of lunar-orbiter tracking data. The other result was obtained by a group at Cornell, using contour maps obtained from the derivation of gravity fields and lunar-orbiter photographic data.

The value of the 4-1 coefficients that we obtained can be interpreted in terms of areas of positive and negative anomaly on the moon.

Figure 1 shows areas of positive anomaly, obtained from an interpretation of the 4-1 coefficient; we find that the major mascons under the ringed mare and some other small ones obtained by the JPL group generally fall into the areas of positive anomaly.

As Figure 2 shows, the group at Cornell found mascons not only on the front side, but even larger ones at the limb, and they found the largest one on the far side. On their map, the three largest mascons appear in areas of negative anomaly as far as the 4-1 coefficient is concerned. Now, we have here a qualitative result from an independent source – in this case, Apollo orbit-plane evolutions – that verify one mascon-distribution result and argue against another one.

Figure 3 represents a verification of this result from a trajectory-computation point of view. We find that, when we add the 4-1 coefficient to the current model – the L-1 model – to form a modified L-1 model called ML-1, we are able to better predict the evolution of the inclination not only of Apollo orbits, whose data we used in deriving it, but also in this case of an arc of Lunar Orbiter 3. This Lunar Orbiter 3 orbit was at twice the mean height that Apollo spacecraft flew, and it was in a prograde orbit instead of a retrograde orbit: it was a fairly different orbit. If we had agreed with the Cornell result, we would have had our inclination evolutions going in an opposite direction; we would also have had different signs on our gravity coefficient.

So, our conclusion is that the tugging and pulling by the moon on the Apollo orbit plane yields qualitative information concerning the distribution of mascons on the moon.

DR. PIEPER:

Any comment or question about the distribution of mascons, or discussion about other people's ideas?

MEMBER OF THE AUDIENCE:

At the science review here last year, one speaker thought that the residuals attributed to mascons could be alternatively ascribed to artifacts in the orbital computational procedures.

DR. PIEPER:

Perhaps we have someone from that group who could speak to that in detail; as far as I know, the work has progressed somewhat, but there

hasn't been anything definitive that shows it is really a satisfactory solution to the problem, and that mascons are required apparently to explain the gravity field of the moon. The strongest evidence for the mascons is the fact that they exist where physical features are actually observable, in the lunar surface. This would be fun to pursue, but we had probably better go on.

THE (4,1) COEFFICIENTS AND THE FRONTSIDE MASCON RESULTS

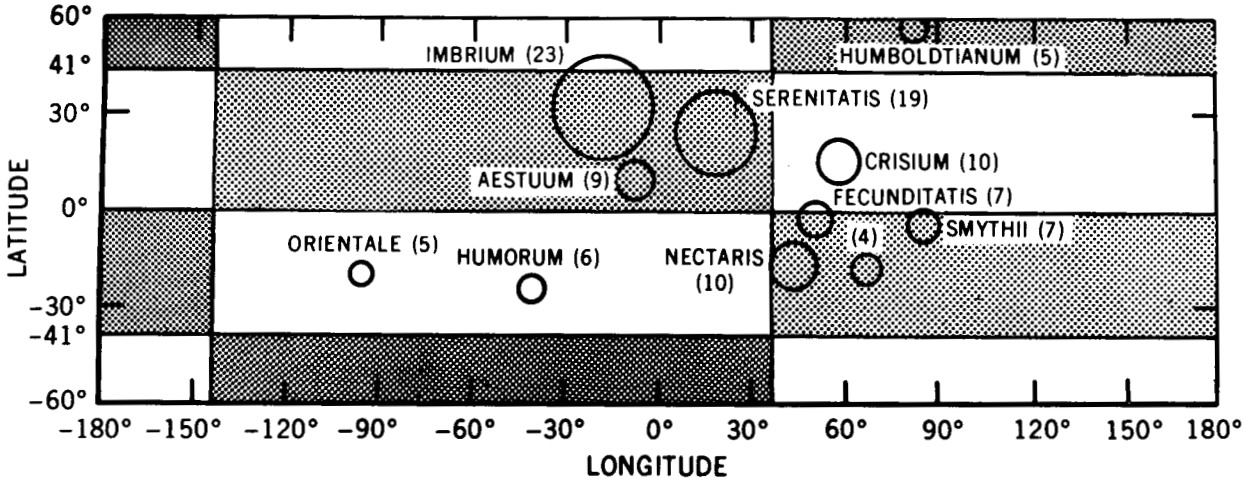

NOTE: SHADED AREA IMPLIES A POSITIVE ANOMALY. MASSES ARE GIVEN IN PARENTHESES IN UNITS OF MILLIONTHS OF LUNAR MASS

NASA-GSFC-T&DS
MISSION & TRAJECTORY ANALYSIS DIVISION
BRANCH 552 DATE November 1970
BY J. P. Murphy PLOT NO. 2172

Figure 1

THE (4,1) COEFFICIENTS AND THE FARSIDE MASCON RESULTS

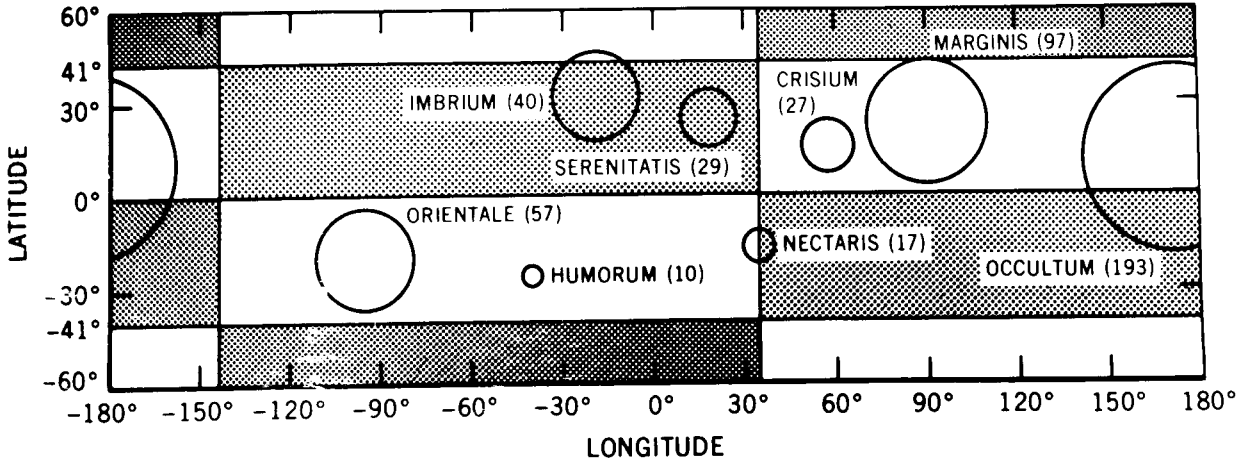

NOTE: SHADED AREA IMPLIES A POSITIVE ANOMALY. MASSES ARE GIVEN IN PARENTHESES IN UNITS OF MILLIONTHS OF LUNAR MASS

NASA-GSFC-T&DS
MISSION & TRAJECTORY ANALYSIS DIVISION
BRANCH 552 DATE November 1970
BY J. P. Murphy PLOT NO. 2174

Figure 2

INCLINATION OF LUNAR SATELLITES

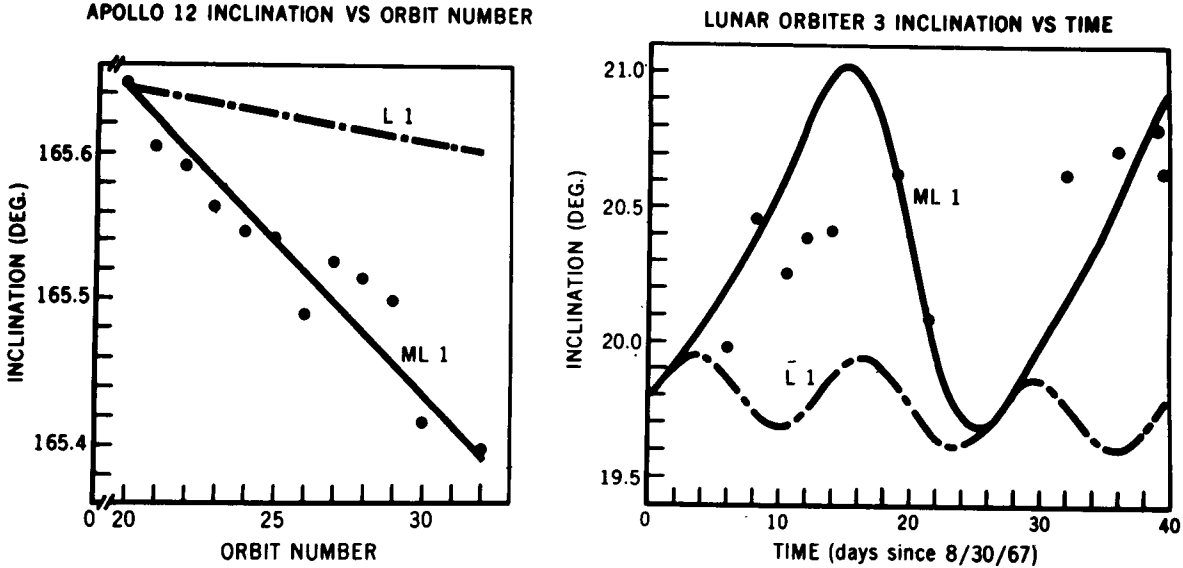

DOTS ARE ACTUAL INCLINATION VALUES OBTAINED FROM TRACKING DATA

NASA-GSFC-T&DS
MISSION & TRAJECTORY ANALYSIS DIVISION
BRANCH 552 DATE November 1970
BY J. P. Murphy PLOT NO. 2173

Figure 3

SEARCH FOR MAGNETIC MONOPOLES IN THE MOON

Dr. Kenneth Schatten

The possible existence of a magnetic monopole in the moon was first proposed by Dirac. The Dirac monopole was permitted by quantum theory, and also provided a basic symmetry if incorporated into Maxwell's equations. The monopole is a subatomic particle like an electron or a proton; however, it possesses an inherent magnetic charge, rather than an electric charge. Many experimentalists have unsuccessfully searched for these particles in a wide variety of natural locations, in ocean slurry, in magnetic outcrops on the earth's surface, and in fragments of stony iron meteorites. They have also attempted to create them by manmade means in our largest particle accelerators, and have searched for them in cosmic radiation.

The undetected monopole flux in cosmic rays allows the possibility that heavenly bodies still possess a net magnetic charge, possibly arising during the formation of these bodies. Our portion of the universe is asymmetrical with respect to matter and antimatter; it is therefore not unreasonable to suggest an asymmetry with respect to magnetic charge. The earth is not a very suitable body to use in observing any net charge, because it possesses a strong inherent magnetic field with a complicated structure; the moon appears to be a more suitable object to investigate, as it possesses no observed large-scale magnetic field.

In order to search for these particles within the moon, we used the magnetic observations from Dr. Norman Ness's magnetometer experiments on Explorer 33 and 35.

The structure of a magnetic field near a monopole-rich moon would appear as a radially diverging field if the moon were embedded in a vacuum. However, when it is not passing through the extension of the earth's magnetic field, the moon is embedded within the solar wind. This hot tenuous plasma flows approximately radially away from the sun at the orbit of the earth, and carries with it the extended solar magnetic field. This interplanetary magnetic field is frozen into the highly conducting plasma and is swept past the moon at super-Alfvénic velocities. For this research investigation, the interplanetary field represents a noise signal that must be removed. The observations of Explorer 33 located within the ambient interplanetary field were used to provide a monitor of the background magnetic field for comparing calculations of the field observed in the lunar vicinity.

Figure 1 shows the theoretical influence of a magnetic-monopole source within the moon upon the field geometry in the lunar vicinity. The dashed line shows the undistorted field; the dashed and dotted line shows the influence of the plasma umbra and penumbral regions on the magnetic field. The distortions of the magnetic field due to the presence of a monopole source within the moon is shown by the solid line. These distortions are confined to the region of the lunar wake, and are such that the magnetic field suffers a net displacement toward the sun as the lunar wake is traversed. It is this displacement that will be investigated, and will provide evidence as to any net magnetic-monopole charge within the moon.

Figure 2 shows a sample plot of the field line across the lunar wake on April 29, 1968. The curved line represents the orbit of Explorer 35 about the moon on that day; the line AB shows the average magnetic field, half an hour before and after the lunar-wake traversal. Line AD shows the field-line trace behind the moon as measured by Explorer 35 while it was in the lunar-wake region, and line AC shows the field-line trace using interplanetary observations from Explorer 33.

If there were a net magnetic-monopole source within the moon line, AC and AB would be consistently close together, and line AD would be continually displaced up or downstream from the other two. As can be seen, there is very little difference between lines AC and AD, suggesting that no magnetic-monopole charge exists within the moon.

A series of 37 orbital plots was analyzed in this way to obtain better statistical evidence. This analysis shows that the net number of magnetic monopoles is less than 1 per 10^7 cm^3, which is equivalent to the difference in the number of northern and southern magnetic monopoles within the moon being less than 1 per 10^{31} nucleons.

The analysis provides a smaller upper limit for the net magnetic charge of matter than that previously known; previous estimates of the number of magnetic monopoles are located near 1 per 10^{26} nucleons. Thus we can further add that, if there are as many as 1 monopole per 10^{26} nucleons, then there are an equal number of positive and negative monopoles to within 1 part in 10^5. I would like to add further that the Alvarez group at Berkeley has more recently searched for monopoles from lunar samples, and also have no evidence for them.

DR. PIEPER:

Thank you. The monopole remains as elusive as ever. Any questions or comments of Dr. Schatten? It is very nice to get a result like that out of a magnetometer going around the moon. It seems to me that that is just delightful.

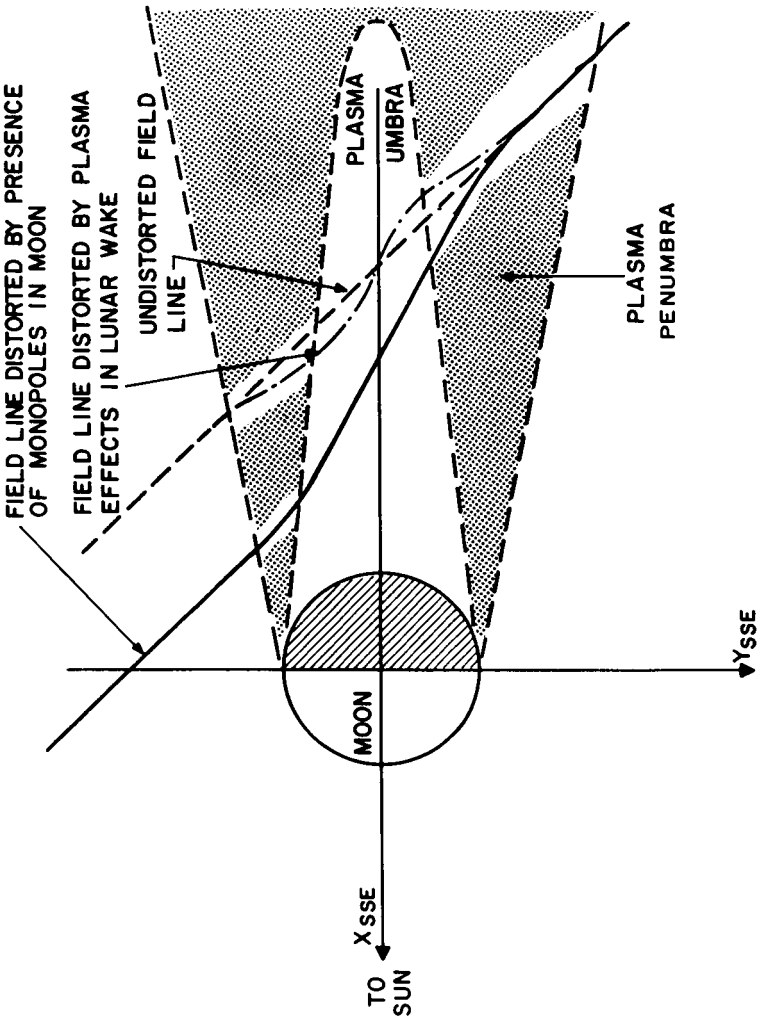
FIELD LINE DISTORTED BY PRESENCE OF MONOPOLES IN MOON
FIELD LINE DISTORTED BY PLASMA EFFECTS IN LUNAR WAKE
UNDISTORTED FIELD LINE
PLASMA
UMBRA
PLASMA PENUMBRA
MOON
YSSE
XSSE
TO SUN

Figure 1

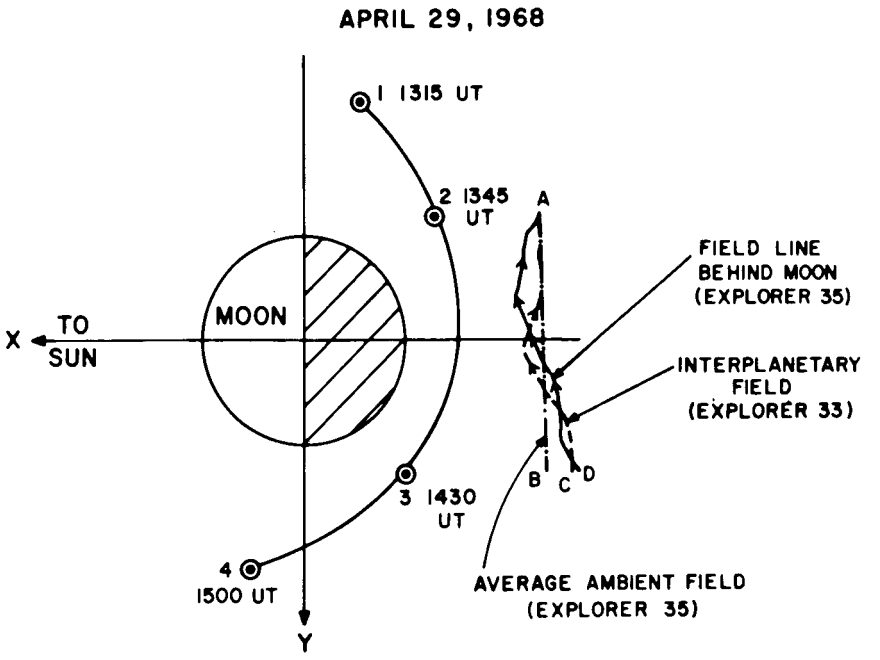

FIELD LINE TRACE IN LUNAR WAKE

Figure 2

AUGER ELECTRONS

Dr. Lo I. Yin

In the past few years, Auger and photoelectron spectroscopy has been established as a powerful technique in the areas of surface studies, chemical analysis, valence states, and chemical bonding.

The extraordinary sensitivity of this procedure to surface contamination, down to a fraction of a monolayer, led to our interest in this technique as an effective means of monitoring the surfaces of vessels to be used for returning lunar samples, and examining the effect of surface contaminants on the coatings of mirrors for flight. Among other things, we are also interested in using this technique to study the valence states in lunar samples.

An important aspect of such investigations is the identification of characteristic lines in the electron spectra. This presentation will briefly describe our efforts in assigning proper electron transitions to the Auger lines of copper.

Whenever a vacancy is created in one of the inner electronic shells of an atom, a transition may occur in which the vacancy is filled by an electron from an outer shell. The excess energy can be expended either in the emission of an X-ray, the fluorescence X-ray, or in the ejection of another outer-shell electron, the Auger electron. Today we will be mostly concerned with Auger electrons.

Figure 1 shows schematically the designation of Auger transitions. For example, if a vacancy in the K shell is filled by an electron from L_1 shell and an L_2 electron is ejected, this is labeled as a KL_1L_2 Auger transition. Similarly, if the initial vacancy is in the L_3 shell and the final vacancies are in the M shell, this transition is labeled as L_3MM.

In practice, the initial vacancy in the atom is usually created by either electron bombardment or X-ray bombardment. With the electron bombardment, only Auger electrons are characteristic of the sample, whereas, with X-ray excitation for a given X-ray energy, both photoelectrons and Auger electrons are characteristic of the sample. The kinetic energy of the photoelectrons is simply the difference between the X-ray energy and the binding energy of the shell from which the photoelectron is ejected.

So far, information concerning the outer-shell Auger transitions such as the LMM type is rather scarce. Recently, because of the enormous potential usefulness of Auger spectroscopy, there is a renewed interest in and demand for the systematic study of these outer-shell Auger spectra.

In the February 1970 issue of Physical Review, Haas and his colleagues catalogued the outer-shell Auger spectra of the transition metals, using electron excitation. They found similar features among elements of the same period, and from their energies specific Auger transitions were assigned to these features.

The top of Figure 2 shows the electron-excited Auger spectrum of copper as obtained by Palmberg, whose energy values were quoted by Haas. The kinetic energy of the electron is plotted on the X-axis. All three peaks in the spectra were assigned to be of L_2MM type, for all elements in the period from scandium to copper. The bottom of the figure shows the copper spectrum as obtained with X-ray excitation, using aluminum K α X-ray. We see the same Auger group, much better resolved, but in addition we also see the photoelectrons ejected from various shells: L_1 shell, L_2, L_3, M_1, M_2 and M_3, and the conduction band of copper.

As we know the precise energies of photoelectrons, we can use them as internal-energy calibrations for the Auger lines. In this way, we have determined the position of these lines to within $\pm$ 0.32 attojoule (2 electron volts), and our values are about 4.8 attojoule (30 electron volts) lower than those quoted by Haas from the top spectrum.

From the energies determined by us, the first and third Auger lines can be unambiguously assigned to be L_3MM type rather than L_2MM as determined by Haas.

Energetically, the second peak (A_2) fits either an L_3MM or L_1MM; therefore, additional information is needed to make a unique assignment. This information, fortunately, is readily available to us in the photoelectron part of the spectrum. The relative intensities of the photoelectron peaks give an indication of the relative photoelectric cross sections of the various shells. It is obvious, then, that L_3 shell is more highly ionized than L_2 shell, and both are about a factor of 5 higher than L_1. This would therefore favor the assignment of L_3MM to the second Auger peak as well. Thus, using X-ray excitation and higher resolution, all three prominent Auger peaks of copper are determined to be L_3MM type rather than L_2MM type.

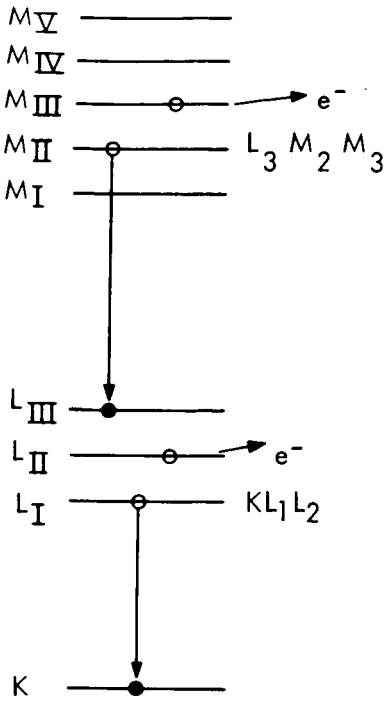

DESIGNATION OF AUGER ELECTRONS

Figure 1

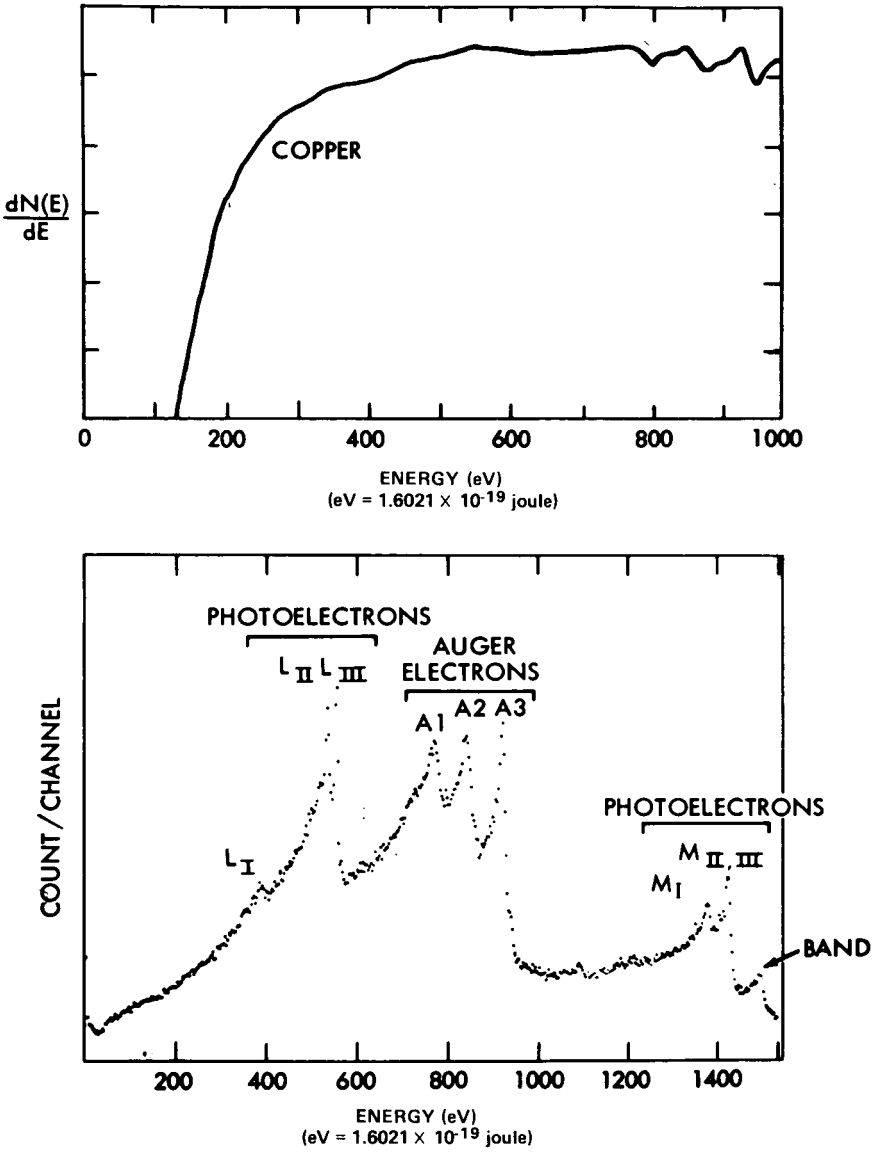
COPPER
dN(E)/dE
0
200
400
600
800
1000
ENERGY (eV)
(eV = 1.6021 × 10-19 joule)
PHOTOELECTRONS
LII LIII
AUGER ELECTRONS
A1 A2 A3
LI
PHOTOELECTRONS
MII, III
MI
BAND
COUNT/CHANNEL
200
400
600
800
1000
1200
1400
ENERGY (eV)
(eV = 1.6021 × 10-19 joule)

Figure 2

PERIODIC MOTIONS IN THE PROBLEMS OF THREE BODIES

Lloyd Carpenter

One of the difficult and interesting problems in celestial mechanics is that of capture. For example, you might consider the case of the periodic comets in the solar system, for which there is evidence that they have been captured at some time in the past. This is a difficult problem to solve, either analytically or numerically; but today I would like to give you an example of such a capture orbit for a simple problem, and indicate how it may be related to some practical problems in the solar system.

If you consider the general problem of three bodies, you have three massive bodies: we don't assume any of the masses to be zero. I will take the special case where two of the masses are equal. Start initially with the equal masses on the horizontal axis, and the third body at the origin midway between the two, then impart a vertical velocity to the two equal masses so that they go up, come together, and collide. Adjust the initial velocity so that they will return again to the initial position, and the motion will be periodic.

Figure 1 is a depiction of this type of motion, which is symmetric about the vertical axis, so that only the right half is shown here. We see the motion of one of the two equal masses with respect to the third body, which is at the origin; this is the periodic orbit, starting on the horizontal axis at $X = 1$. The particle moves upward and to the left until the collision on the vertical axis, then returns to the initial position, followed by another collision below the origin, and then by continuous oscillation.

The system is conservative: energy is conserved so that it is possible to compute what we call a zero-velocity curve. At some points in space, the kinetic energy will be zero, depending on the particular energy of the orbit; for this particular energy, there are points in space where the velocity is zero, and these points form the zero-velocity curve. The significance of this is that any orbit with this energy must stay within this region – it cannot cross this curve. In this case, the curve is open, so that it is possible to have an orbit with this energy which escapes to infinity, either above or below.

So, let's consider another orbit with the same energy, but starting at X = 0.9 rather than at X = 1. Impart an initial vertical velocity again, such that the energy of the system is the same as before. Figure 2 shows what happens: a lot of the oscillations around the origin have been omitted, because this region is filled in with curves that you can't separate with your eye. There are many oscillations, after which the particles escape to infinity. Going backward in time, it came in from infinity from the other direction. So we have what we call a temporary capture orbit, the two particles coming in from infinity, then many oscillations, and then finally escape again.

Let's see what this suggests as a possible application in the solar system. The form of the zero-velocity curve is really the feature that makes capture-type motion possible, and this depends on the energy of the orbit that we are studying.

Figure 3 shows schematically some zero-velocity curves in the restricted problem of three bodies: the four separate diagrams correspond to four different values of the energy. You can consider the central body in each case to be the sun, the body to the left to be Jupiter, and the curves to correspond to zero velocity for different energies. The third body can move only in the open area – not in the shaded area. Starting with the upper left figure, the third body may move in the region around the sun or around Jupiter, or outside the system. In the upper righthand situation, these two curves have come together to form a cusp, so that – increasing the energy slightly, as in the lower left figure – you would have communication between Jupiter and the sun as a possibility. Finally, in the figure on the lower right, you could have particles starting from outside the system, passing through near Jupiter, and being temporarily captured in the region around the sun.

As a possible practical application, if you wanted an orbit to stay in the neighborhood of Jupiter for some period of time, you could find a stable periodic orbit around Jupiter with an energy corresponding to that used in the lower lefthand figure, so that – by changing initial conditions slightly – it may be possible to find an orbit that is captured by Jupiter and then, after a period of time, escapes back to the sun.

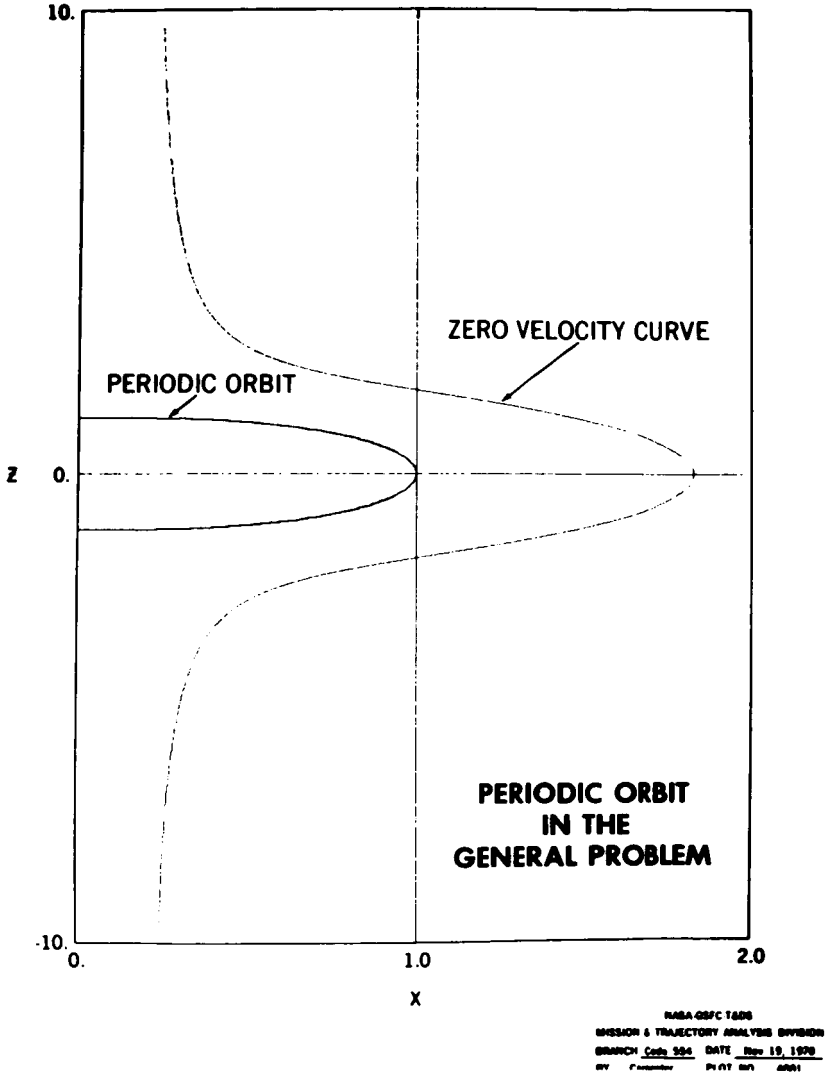
10.
ZERO VELOCITY CURVE
PERIODIC ORBIT
Z
0.
PERIODIC ORBIT
IN THE
GENERAL PROBLEM
-10.
0.
1.0
2.0
X

Figure 1

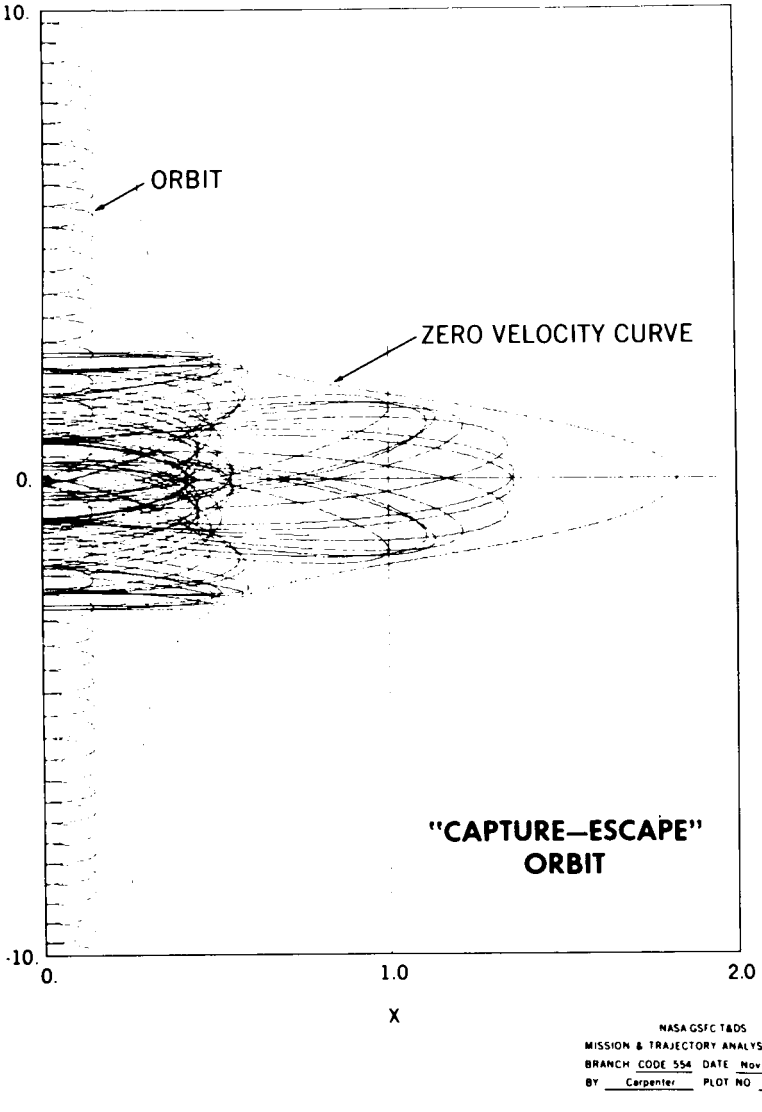
10.
ORBIT
ZERO VELOCITY CURVE
0.
"CAPTURE—ESCAPE"
ORBIT
-10.
0.
1.0
2.0
X
NASA GSFC T&DS
MISSION & TRAJECTORY ANALYSIS DIVISION
BRANCH CODE 554 DATE Nov 19 1970
BY Carpenter PLOT NO 4002

Figure 2

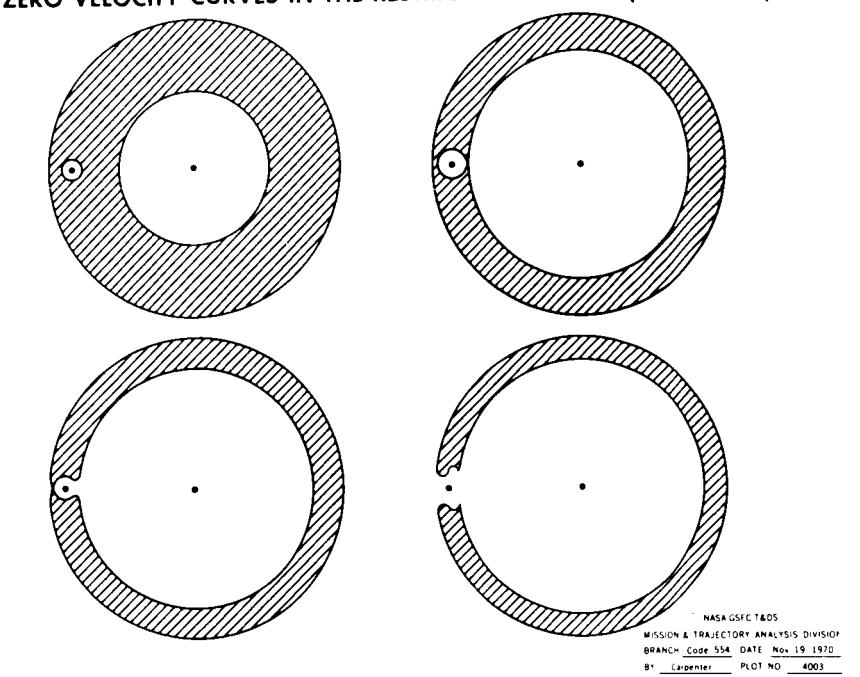
ZERO VELOCITY CURVES IN THE RESTRICTED PROBLEM (SCHEMATIC)
NASA GSFC T&DS
MISSION & TRAJECTORY ANALYSIS DIVISION
BRANCH Code 554 DATE Nov 19 1970
BY Carpenter PLOT NO 4003

Figure 3

INTERPLANETARY COSMIC DUST FLUX

Otto Berg

Figure 1 shows the basic sensor system of the Pioneer cosmic-dust experiments that have gathered data for a combined period of more than 5 years. These experiments were designed to respond to two physical phenomena that occur when a hypervelocity microparticle impacts upon a surface: the production of an ionized plasma, and the transfer of momentum.

A cosmic-dust particle entering the experiment passes through the very thin front film, producing a plasma that is separated into ions and electrons and collected on the film and grid respectively, producing a positive and a negative pulse in coincidence. As the particle proceeds, it impacts on the rear plate, again producing a plasma and resulting in a positive and a negative pulse in coincidence.

The speed of the particle is derived from the time of flight between the front sensor array and the rear sensor array. If the particle has enough momentum, it registers on the microphone plate as a damped sinusoidal wave. As the illustration shows, as many as five coincident data pulses from a single event are used to positively identify the true impact events from noise events.

The multiple coincidence sensors, the sensor controls, and the electronic monitors designed into the experiment have yielded data on the meteoroid environment that are consistent and believed to be exceptionally reliable.

Figure 2 shows the relationship between the cosmic-dust flux rates derived from Pioneer data and flux rates derived from other methods of measurement. The log particle mass in grams is shown versus the log cumulative flux rate in particles per square meter per second, per 2π steradian.

Pioneer data are in agreement with astronomy theory, zodiacal-light measurements, and ground-based observations, but differ markedly from the high flux rates deduced from earlier in situ measurements. As many as seven orders-of-magnitude separate the small-particle end of the high and low flux curves, as the figure shows. The high flux curve is based principally on acoustical-sensor data obtained from numerous in situ

measurements preceding Pioneers 8 and 9, gathered over a period of more than 2 decades. The low flux curve shown as a shaded area is based on Dohnanyi's model of a cometary source for micrometeorites, supported by zodiacal-light studies. In consideration of radiation-pressure theory, the model shows an absence of particles having masses of less than 10^{-11} grams. The recent measurements from the Pioneer experiments superimposed on the model verify the particle-size cutoff.

One interesting feature of the Pioneer data is that they provide a plausible explanation for the seven-orders-of-magnitude discrepancy between the high and the low flux curves.

Figure 3 shows time correlation between two major solar-proton events and the output response from the microphone sensors in both Pioneers 8 and 9, separated by millions of kilometers. The upper line is the proton flux; the middle line represents microphone events from Pioneer 8 in events per day, and the lower line events per day for the microphone in Pioneer 9. These peaks, which occurred within a 2-month period, represent a total of sixteen similar peaks that have been recorded and positively identified with high solar-proton activity. The sources of the microphone peaks were immediately suspect, because of the lack of coincident pulses from other sensors; an additional indication of the extraneous nature of the microphone data was revealed by the control microphone, which is identical in sensitivity and exposed to the same spacecraft conditions and space environment as the main microphone, but has only one-fifteenth the impact area. Thus, we would expect a ratio of approximately one to fifteen for the number of micrometeorite impacts on the control microphone, as compared to the main microphone. In both of the satellite experiments, however, the control microphone shows essentially the same impact rate as the main microphone, indicating that the source of the acoustic sensor data was not primarily cosmic dust.

In conclusion, the data from the multicoincidence cosmic-dust sensors on Pioneers 8 and 9 have not only measured a very low flux for micrometeorites, which is in keeping with astronomy theory, but have also shown clearly how a high-flux theory may be based on faulty data.

MEMBER OF THE AUDIENCE:

How do your flux rates compare with the zodiacal-light measurements?

BERG:

Roughly, the Pioneer measurements fall on Dohnanyi's curve; they compare favorably – slightly higher than the zodiacal-light predictions.

MEMBER OF THE AUDIENCE:

Well, you can make the zodiacal-light estimates fall anywhere you want to. The estimates of mass densities observed can vary anywhere from 10^{-18} to 10^{-24} per cubic centimeter.

DR. PIEPER:

Well, it is nice to have a problem cleared up – I think we have finally got this one cleared up; it has been a long, long time.

MEMBER OF THE AUDIENCE:

Silverberg noted interesting effects during comet operations, such as Encke for example. Do you have any correlations with any cometary debris?

BERG:

Yes, in the 5 years of data, we have sixteen time-of-flight events; and one of those time-of-flight events can be tied in with the comet Encke. Other data from front-film events alone (which are from very low-energy impacts) did show response to the orbit of the comet Encke. The second time around the Pioneer orbit, however, we did not see those effects. We are awaiting data from the third time around the orbit to look for Encke particles.

MEMBER OF THE AUDIENCE:

Did you say you did see Encke particles?

BERG:

Well, the first time we did, but the second time we did not. So we are waiting for the third time.

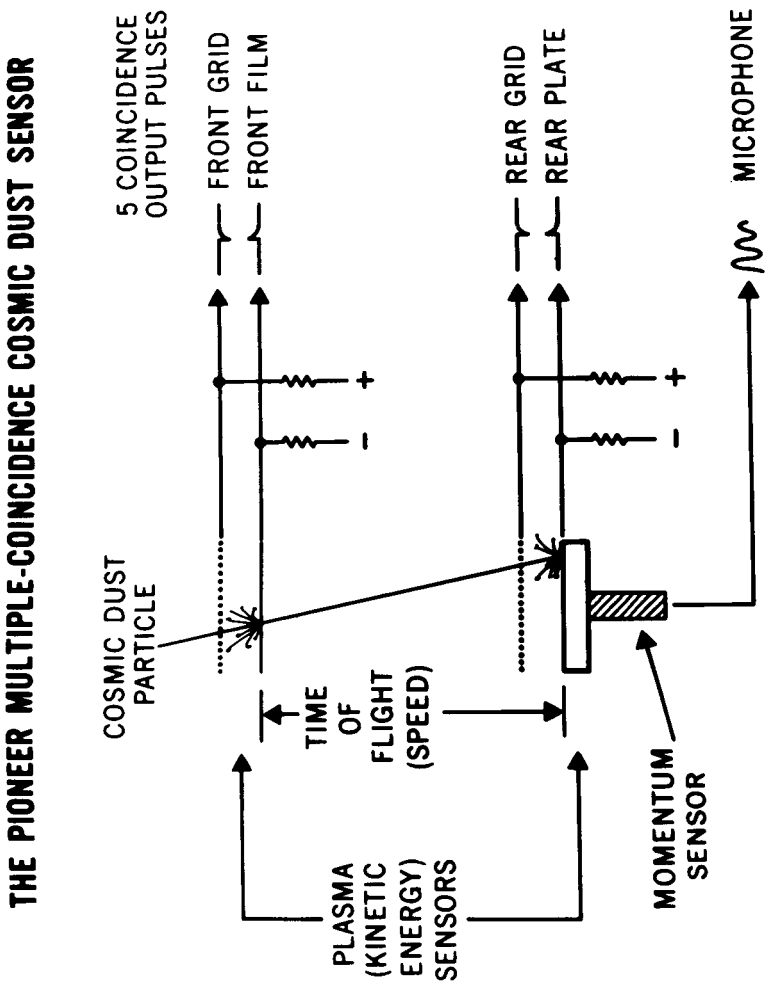
THE PIONEER MULTIPLE-COINCIDENCE COSMIC DUST SENSOR
5 COINCIDENCE OUTPUT PULSES
FRONT GRID
FRONT FILM
REAR GRID
REAR PLATE
MICROPHONE
COSMIC DUST PARTICLE
TIME OF FLIGHT (SPEED)
PLASMA (KINETIC ENERGY) SENSORS
MOMENTUM SENSOR
+
-
+
-

Figure 1

FLUX OF METEOROIDS

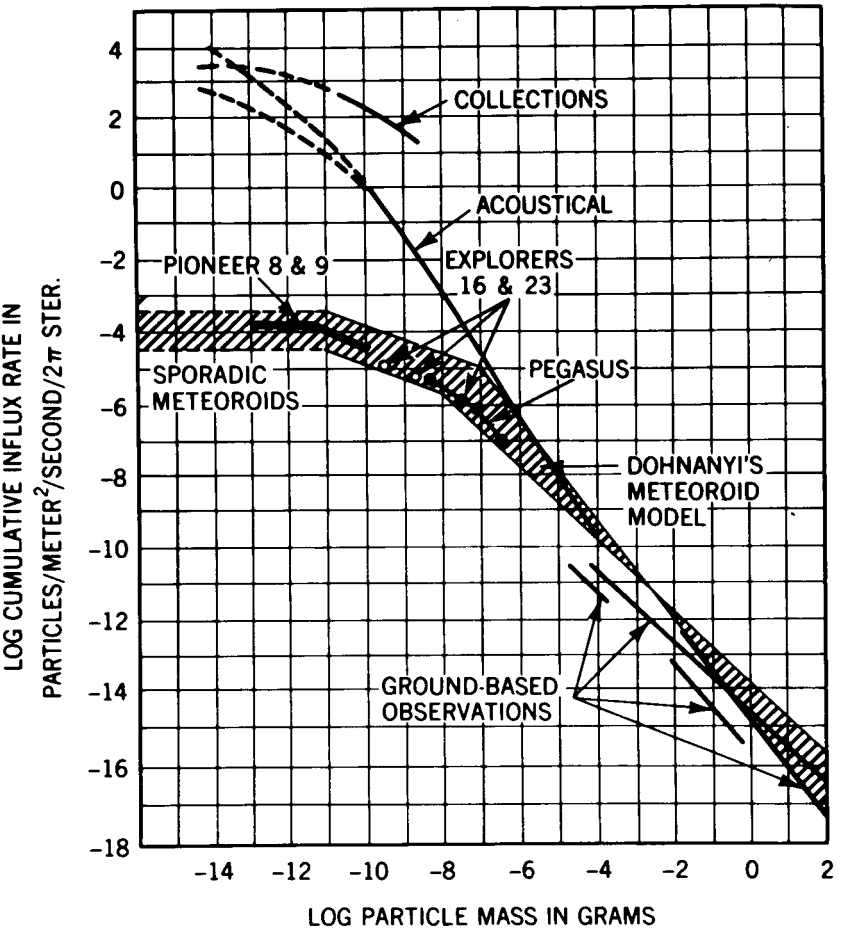

Figure 2

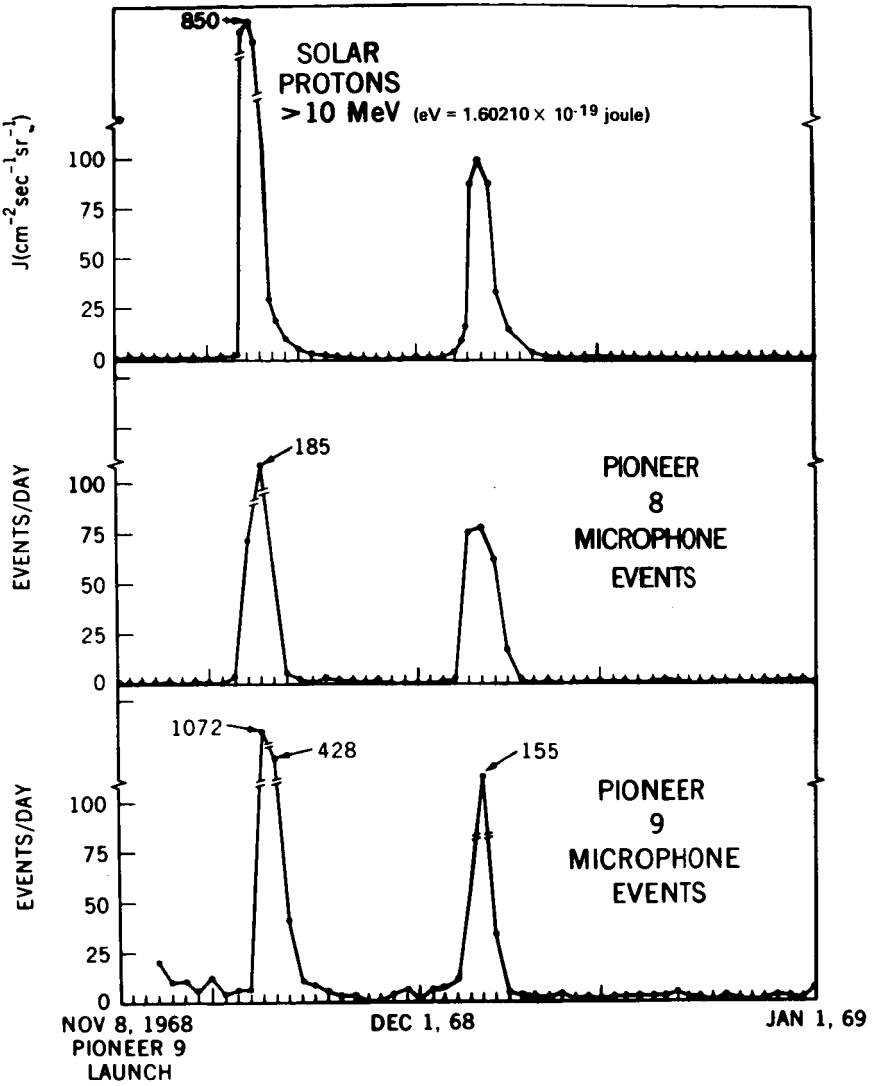
850
SOLAR
PROTONS
>10 MeV (eV = 1.60210 × 10-19 joule)
J(cm-2sec-1sr-1)
100
75
50
25
0
185
EVENTS/DAY
PIONEER
8
MICROPHONE
EVENTS
1072
428
155
EVENTS/DAY
PIONEER
9
MICROPHONE
EVENTS
NOV 8, 1968
PIONEER 9
LAUNCH
DEC 1, 68
JAN 1, 69

Figure 3

THE GEGENSCHEIN AND DISTRIBUTION OF INTERPLANETARY DUST

Dr. Robert Roosen

The Gegenschein is a faint oval patch of light some tens of degrees across, located at a point directly in opposition to the sun, otherwise known as the antisolar point. It is presumably due to sunlight reflected from interplanetary dust. However there has been some question as to the location of this dust: I would like to describe a technique by which it is possible to determine the source of the Gegenschein.

The basic tool used in my investigations is that many of the theories suggested to explain the Gegenschein require such a concentration of material near the earth that the earth's shadow should be visible in the center of the Gegenschein.

First, let me show you some of the observations. Figure 1 shows the sum of nine scans in declination that I made with a pulse-counting photometer attached to the 36-inch reflector at McDonald Observatory. The observed relative brightness is plotted here as a function of angular distance from the antisolar point, from 122 millirad (7 degrees) south of it to 105 millirad (6 degrees) north of it. The points well above the mean curve are due to stars passing through the field-of-view; the solid line is the mean of over 100 scans made in March 1969 and February 1970. The probable error of the mean is indicated by the width of the line.

Now I would like to show you some of the models predicted for various possible distributions of Gegenschein-producing material. In Figure 2, the dashed line indicates what the earth's shadow would look like if the Gegenschein were completely due to material concentrated at the Lagrangian point opposite the sun, 235 earth radii from the earth. If this theory were correct, a very dark shadow would be visible; hence, the Lagrangian-point hypothesis is untenable.

Both the gas and dust-tail theories are based on the incorrect belief that the center of the Gegenschein is displaced 3 degrees westward from the antisolar point. Hence, the base of the tail in either case would be quite

close to the earth, and a shadow should again be visible. Since the earth's umbra extends well beyond the outer limits of the hypothetical earth's dust cloud, the Gegenschein cannot be due to earth-orbiting dust.

There are a number of other quite valid arguments against these theories, but time does not permit listing them. In any case, the only theory that would seem to fit the shadow test is the heliocentric-cloud hypothesis. However, some limits can also be placed on this theory.

Models of the zodiacal cloud generally assume that the amount of reflecting material decreases with distance from the sun, following an inverse power law. Figure 3 shows the shadows that would be associated with the two most commonly suggested radial distributions.

Essentially, all of the comets that have been suggested as sources for the interplanetary material are short-period comets with perihelia less than 1 astronomical unit. In particular, Whipple has stated that, over the past several thousand years, comet Encke has been quite probably the major support for maintaining the quasi-equilibrium of the zodiacal cloud. Both Bandermann and Southworth have shown that the radial distribution of dust from these comets would be proportional to 1 over $R^{2.5}$, where R is heliocentric distance. The lack of an observed earth shadow on the Gegenschein indicates that this radial distribution cannot be correct, and hence comets are not the source of the material producing the Gegenschein – at least, the comets suggested by Whipple are not.

Figure 3 also shows the shadow predicted for a 1 over R distribution; this distribution would result from the Poynting-Robertson effect acting on a cloud of particles with initial perihelia much larger than 148.6 gigameters (1 AU). Again, the absence of a shadow rules out this simple explanation.

Even if the density of reflecting material did not decrease, but remained constant, a shadow would have been observed; therefore, the density of reflecting material must increase outside the earth's orbit. The source for this material that immediately springs to mind is the asteroid belt. It is, in fact, a simple job to reproduce the Gegenschein brightness with a model based on collisionally produced asteroidal debris.

There is an additional simple test to distinguish between the cometary and asteroidal hypotheses: it requires that a photometer on a space probe traveling toward the outer solar system observe the Gegenschein brightness. If the Gegenschein is due to asteroidal debris, its brightness will remain almost constant until the probe goes further than 299.2 gigameters (two astronomical units) from the sun; if, on the other hand, cometary material produces the Gegenschein, the observed brightness will steadily decrease, and the Gegenschein will appear only a tenth as bright as 299.2 gigameters (2 AU) as when seen from the earth's distance.

Let me briefly summarize my conclusions:

First, the Gegenschein is an effect, not a thing. By that, I mean it is due to an increase in the reflectivity, near opposition, of dust particles in heliocentric orbits, and is not due to an accumulation of material near the earth.

Second, the density of reflecting particles increases outside the earth's orbit. Therefore, the Gegenschein can be explained quite well by appealing to dust produced by collisions between asteroids. A cometary origin for the material is unlikely.

DR. PIEPER:

Discussion or comment?

MEMBER OF THE AUDIENCE:

How do you know that the true phase function of the particles producing the Gegenschein doesn't have a peak at opposition that fills in the predicted shadow?

DR. ROOSEN:

When the observer is not situated on the earth-sun line, he is looking through the umbra at an angle, and hence the earth's shadow is symmetrical. Since any phase function you might use to fill in the shadow must be symmetrical about the antisolar point, an asymmetrical Gegenschein brightness would be observed.

MEMBER OF THE AUDIENCE:

The $1/R^{2.5}$ radial distribution is subject to selection effects, and if you try to correct for them you end up with a different distribution.

DR. ROOSEN:

No, the $1/R^{2.5}$ radial distribution comes from dynamical arguments, not from observations.

MEMBER OF THE AUDIENCE:

Have you ever seen the Gegenschein with your naked eye?

DR. ROOSEN:

Oh, yes. In fact, I should have brought along a photograph and shown it. I will be happy to send you one.

MEMBER OF THE AUDIENCE:

What was the field-of-view for the observations shown?

DR. ROOSEN:

A 96-arc-second-diameter circle.

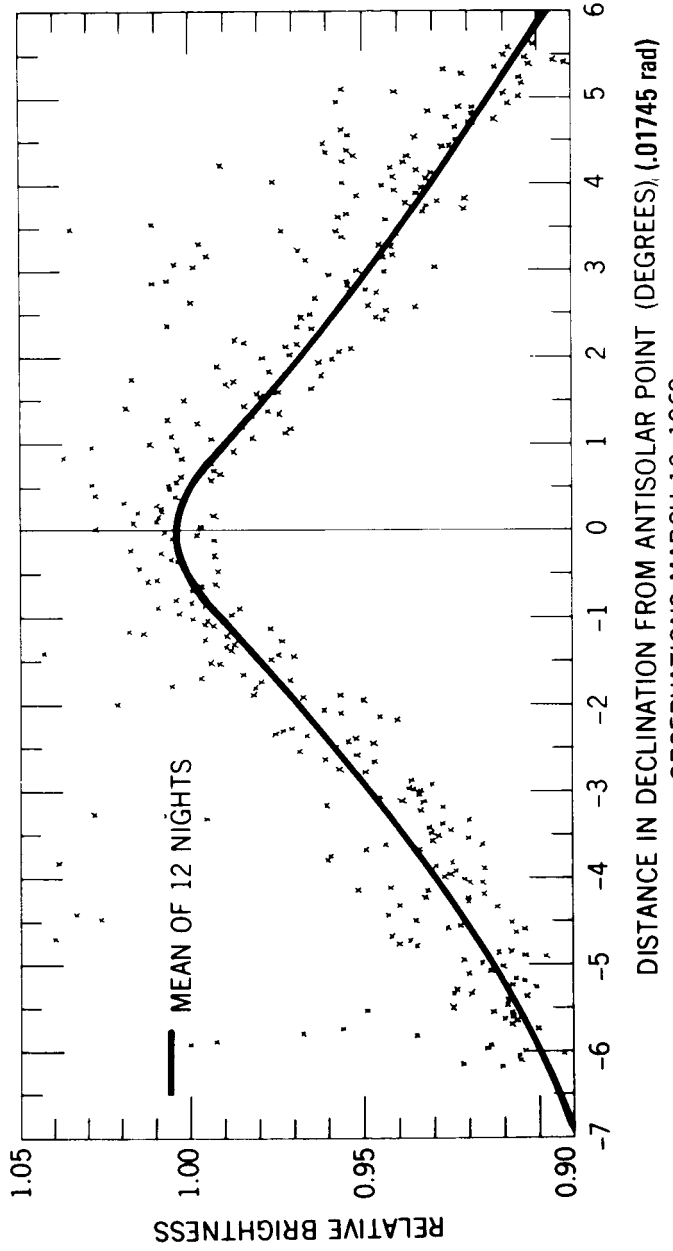
RELATIVE BRIGHTNESS
1.05
1.00
0.95
0.90
MEAN OF 12 NIGHTS
-7
-6
-5
-4
-3
-2
-1
0
1
2
3
4
5
6
DISTANCE IN DECLINATION FROM ANTISOLAR POINT (DEGREES), (.01745 rad)
OBSERVATIONS MARCH 12, 1969

Figure 1

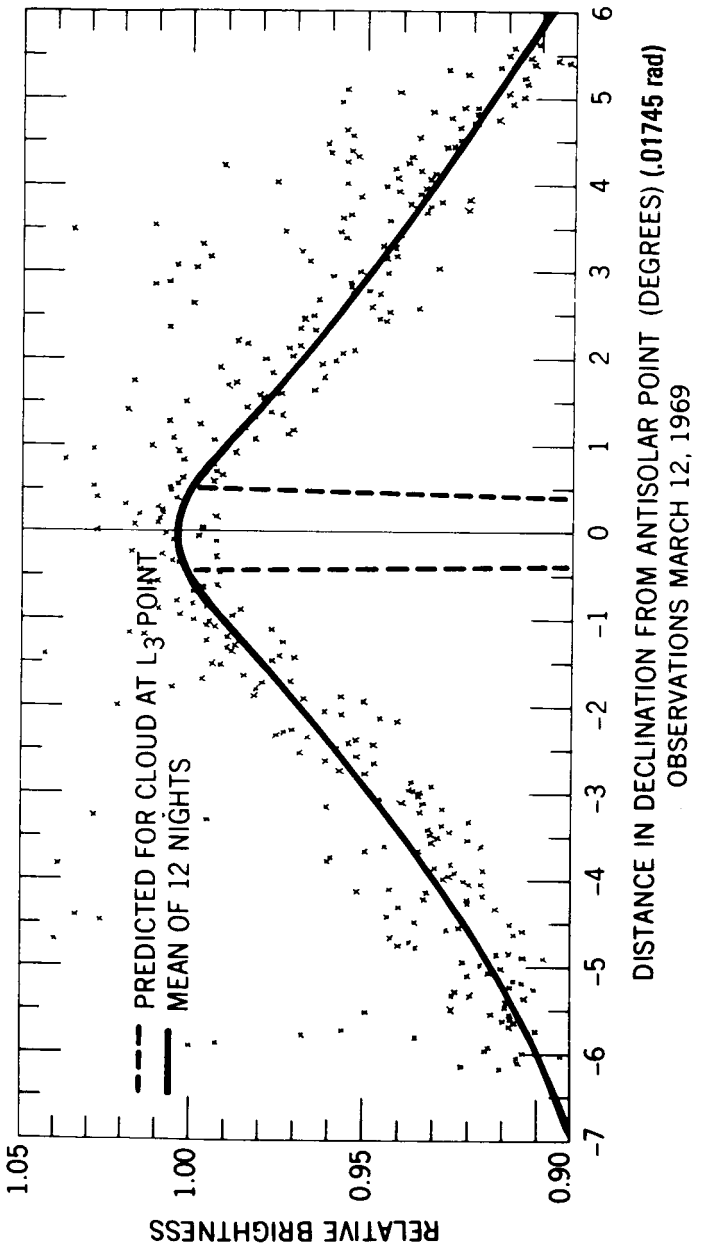
PREDICTED FOR CLOUD AT L_3 POINT
MEAN OF 12 NIGHTS
RELATIVE BRIGHTNESS
1.05
1.00
0.95
0.90
-7
-6
-5
-4
-3
-2
-1
0
1
2
3
4
5
6
DISTANCE IN DECLINATION FROM ANTISOLAR POINT (DEGREES) (.01745 rad)
OBSERVATIONS MARCH 12, 1969

Figure 2

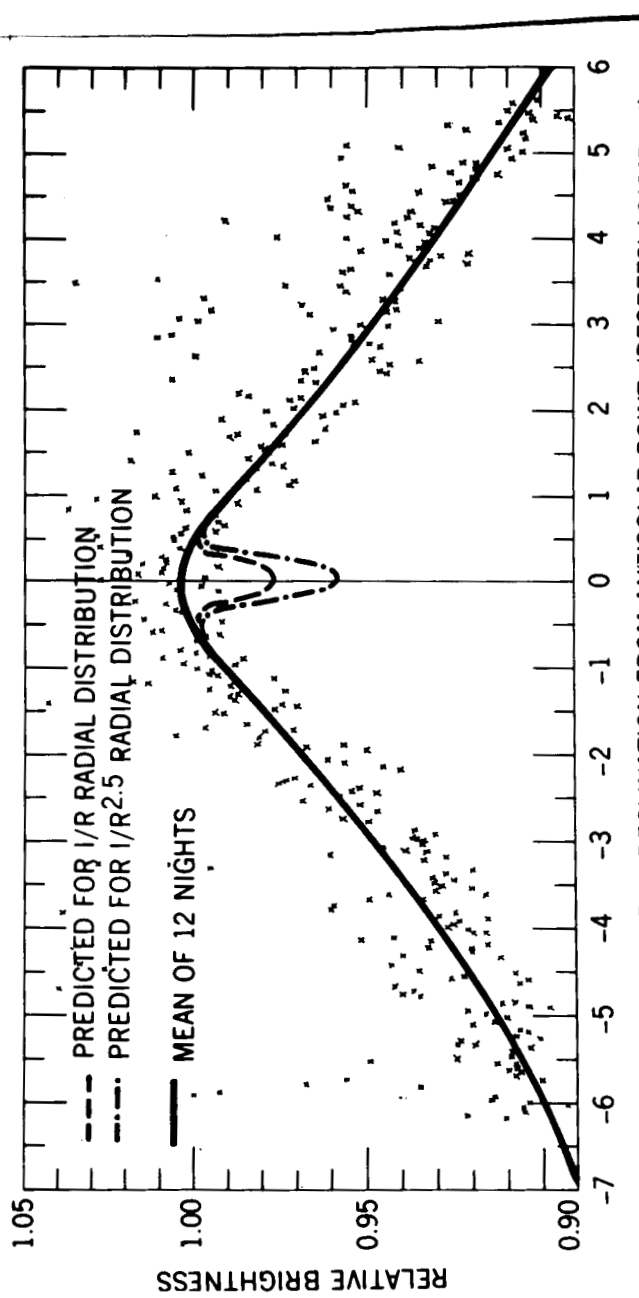
PREDICTED FOR I/R RADIAL DISTRIBUTION
PREDICTED FOR I/R^2.5 RADIAL DISTRIBUTION
MEAN OF 12 NIGHTS
RELATIVE BRIGHTNESS
1.05
1.00
0.95
0.90
-7
-6
-5
-4
-3
-2
-1
0
1
2
3
4
5
6
DISTANCE IN DECLINATION FROM ANTISOLAR POINT (DEGREES) (.01745 rad)
OBSERVATIONS MARCH 12, 1969

Figure 3

PHOTOCHEMISTRY AND LIFETIMES OF INTERSTELLAR MODULES

Dr. Louis Stief

The interstellar medium, which was once thought to be rather primitive and simple, has been shown just within the last few years to be a complex chemical system. Efforts from the beginning of the century until 2 years ago have come up with evidence for about ten atomic or diatomic species. Within the last 2 years, there have been discovered an equal number of polyatomic molecules, half of them having from four to six atoms. Most of these observations have been by radioastronomy.

We are thus presented with an unexpected and a very rapid increase in both the number and the complexity of interstellar molecules, and this raises a number of questions: it raises questions concerning the means of their production, and it raises questions concerning their fate in the interstellar radiation field.

Although the first question remains obscure, there seems to be little doubt concerning the second; these molecules will be decomposed by interstellar photons. And it is this question which I would like to address myself to this morning – a quantitative discussion of the lifetime against photodecomposition, or the probability of photodecomposition, of interstellar molecules. Now, it is really proper to discuss this first, because – if you have a steady state (a balance between the rate at which molecules are being formed and the rate at which they are being decomposed) – in order to say something about the mechanisms of formation, you have to know something about the decomposition rates, and the lifetimes of the molecules will give this to you.

There seems to be an association of observed interstellar molecules with dust clouds, and this indicates that these molecules require protection. These dust clouds attenuate the ultraviolet light. So, we need to look at the photochemistry and the lifetimes not just in the regions free of any protection, but within these clouds which provide protection from ultraviolet light. And, of course, this means that we have to make some assumptions about the way these clouds attenuate ultraviolet light.

Luckily, we have observations to go on: Figure 1 illustrates the observations of the so-called continuous interstellar extinction. By combining data such as Johnson's in the visible and Ted Stecher's rocket observations in the ultraviolet, we get a total curve from which transmissivities have been calculated as a function of wavelength. We have done this in Figure 1 for four values of opacity of the cloud, or for four zones of increasing opacity within a single cloud where the extinction in the visual (A_V) goes from one to four magnitudes.

Now we have to combine these data with absorption cross sections for the molecules as a function of wavelength, and with decomposition probabilities, or what photochemists would call the quantum yields. And we have done this for five interstellar molecules: methane, ammonia, water, formaldehyde, and carbon monoxide. These are the only molecules for which there are sufficient quantitative data; in fact, the formaldehyde data were obtained within the last year in our own laboratory. The spectroscopy (absorption cross section) was examined by Dr. Mentall and Mr. Gentieu, and the photochemistry (quantum yield) was studied by Dr. Glicker and myself.

Figure 2 shows the final results of the calculation as a plot of lifetime τ versus extinction in the visual A_V. The results show that, except for CO, all the molecules considered here have comparable lifetimes of less than 100 years in unobscured regions. Thus, these molecules can exist only in dense clouds, and can never have been exposed to unobscured radiation. This implies that polyatomic molecules were formed, or released, in the gas phase in the clouds where they now occur. The calculations further show that the lifetimes in clouds of moderate opacity (a few magnitudes' extinction in the visual) are of the order of 10^6 years. The lifetime for CO in unobscured regions will be between 100 and 1000 years if the dissociation probability is between unity and one tenth. The smaller dissociation probability leads to a lifetime comparable to that of other diatomics, such as H_2, OH, and CH. This means that CO molecules require considerably less protection than formaldehyde and the other polyatomics, and readily explains the observation that the size of a CO cloud is at least an order-of-magnitude larger than that of a typical formaldehyde cloud.

In addition to photodissociation, molecules can also be destroyed by interaction with high-energy radiation (X- and gamma rays) and energetic

particles. These processes are much less effective than destruction by ultraviolet radiation. However, when the ultraviolet is highly attenuated in clouds, the energetic radiation and particles will persist and will become relatively more important. The ultimate lifetimes in clouds may depend upon these processes, and may be shorter than those shown in Figure 2; these processes require further study.

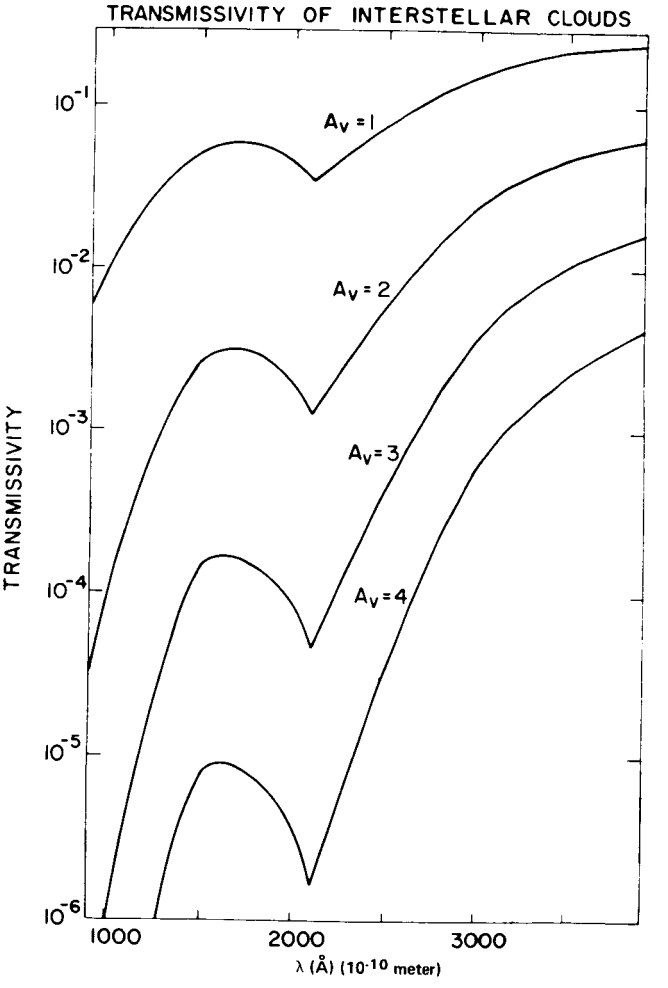

Figure 1

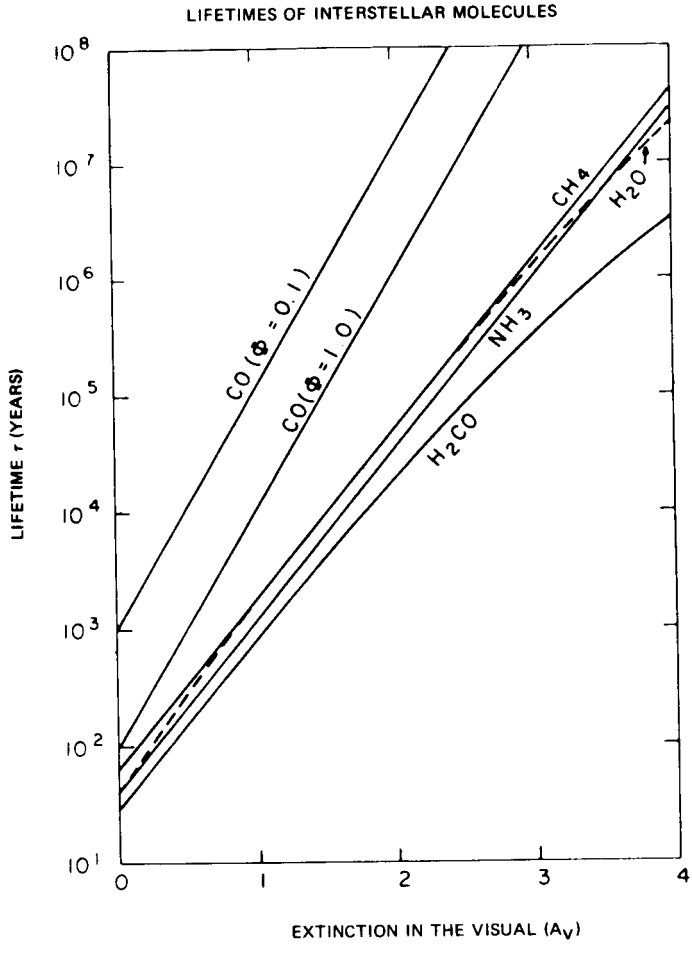
LIFETIMES OF INTERSTELLAR MOLECULES
LIFETIME τ (YEARS)
10^8
10^7
10^6
10^5
10^4
10^3
10^2
10^1
0
1
2
3
4
EXTINCTION IN THE VISUAL (A_V)
CO(Φ = 0.1)
CO(Φ = 1.0)
CH4
H2O
NH3
H2CO

Figure 2

INTERPLANETARY SHOCK NORMALS

Dr. Ronald Lepping

Peter Argentiero of GSFC and I have developed a scheme to improve the estimate of an interplanetary shock normal by using both magnetic-field and plasma data from a single spacecraft. Previously, only magnetic-field data were used for single spacecraft estimates. Figure 1 shows an example of the type of study for which greater certainty in estimating shock normals is necessary: the study concerns the shape of an interplanetary shock surface. Figure 1 shows a portion of such a surface as observed by two spacecraft, located approximately in the ecliptic plane and separated widely enough in solar-longitude difference θ to resolve the shape. The R-T-N system is righthanded such that $\vec{R}$ and $\vec{T}$ lie in the ecliptic plane. The figure also shows the shock normals $\vec{n}_p$ and $\vec{n}_e$ and their associated error-cone angles, which must be small enough to make the shape resolution possible. Other studies that require accurately estimated shock normals are those concerning the interaction of the interplanetary shock and the bow shock, and those that attempt to separate the bulk flapping motion of the bow-shock surface from possible surface undulatory structure.

Figure 2 is a schematic drawing of the basic shock model used in the scheme. For the magnitudes of the relevant shock parameters shown, the model consists of an abrupt ($\lesssim$ few seconds) step function with superimposed stationary uncorrelated noise. $\vec{B}$ refers to the magnetic field, $\vec{V}$ to the plasma velocity, and N to the plasma number density; the subscripts 1 and 2 refer to before and after the shock passage, respectively. In practice, the velocity difference $\vec{W}$ is used rather than $\vec{V}_1$ and $\vec{V}_2$ separately. The time intervals shown are approximately representative of the date intervals actually considered.

This calculation employs a subset of the eight magnetohydrodynamic conservation relations (the Rankine-Hugoniot relations) for a shock in an isotropic medium; this subset consists of those six equations that are devoid of pressure and temperature terms. These equations are represented in a shock-stationary frame of reference; when transposed to an arbitrary frame of reference, they yield three equations which we call the overdetermination equations. The remaining equations can be used to give an expression for the shock normal itself, which is given in terms of the magnetic field, in this fashion:

$$n = \frac{(\vec{B}_2 - \vec{B}_1) \times (\vec{B}_1 \times \vec{B}_2)}{|(\vec{B}_2 - \vec{B}_1) \times (\vec{B}_1 \times \vec{B}_2)|} \qquad (1)$$

Previously, when a normal was calculated from single-spacecraft data, average values for the magnetic fields were used in expression (1). When the error-cone angles associated with the magnetic fields $\vec{B}_1$ and $\vec{B}_2$ were comparable to the angle between the fields themselves, the cross product factor must have a large error associated with its direction. Also, a comparable directional error is sometimes associated with $(\vec{B}_2 - \vec{B}_1)$, although it is usually smaller than the error associated with the cross product factor. When these two factors are multiplied through the final cross product operation, the directional error is propagated through calculation (1), giving an error that is even increased, or amplified, for the normal's estimate.

What we do, however, is use a sigma-weighted least-squares loss-function technique to best fit the overdetermination equations with respect to the entire eleven parameters of our system: the five plasma parameters, as well as the six magnetic-field parameters. In doing so, we obtain best-fit shock parameters for the entire set, of which the six magnetic-field parameters can then be used in expression (1). This procedure usually yields a normal much more accurate than the one obtained using magnetic-field values alone.

While simultaneously obtaining best-fit parameters, the scheme yields an associated covariance matrix and uses it (along with a Monte Carlo method) to rigorously estimate the error cone for the least-squares best-fit normal.

Figure 3 gives an example of the use of the technique on the data for the shock of August 29, 1966. Here we were able to perform the estimate at Pioneer 7 only, and not at Explorer 33 where the shock was also seen; even though the onset time was obtained accurately at Explorer 33, there was a plasma-data gap behind the shock. By making the assumption that the shock surface was locally plane and propagated from Explorer 33 to Pioneer 7 with some constant speed associated with the region between the two spacecraft, and by also assuming that the shock normal was constant over this region, we were able to calculate what we call an observed shock speed.

As a byproduct of our scheme, we obtain a calculated local shock speed, provided that the preshock plasma velocity is known with sufficient accuracy – as it was, in this case (at Pioneer 7). By comparing these two speeds, we were able to give a quantitative check on the merit of the scheme; it turned out that 471 km/s was the value for the observed shock speed, and 467 km/s for the calculated speed. We feel that this check was a reasonably fair indication of the scheme's expected capability.

I wish to thank Dr. N. F. Ness for the magnetic-field data and Drs. A. J. Lazarus and J. K. Chao of MIT for the plasma data used in this study.

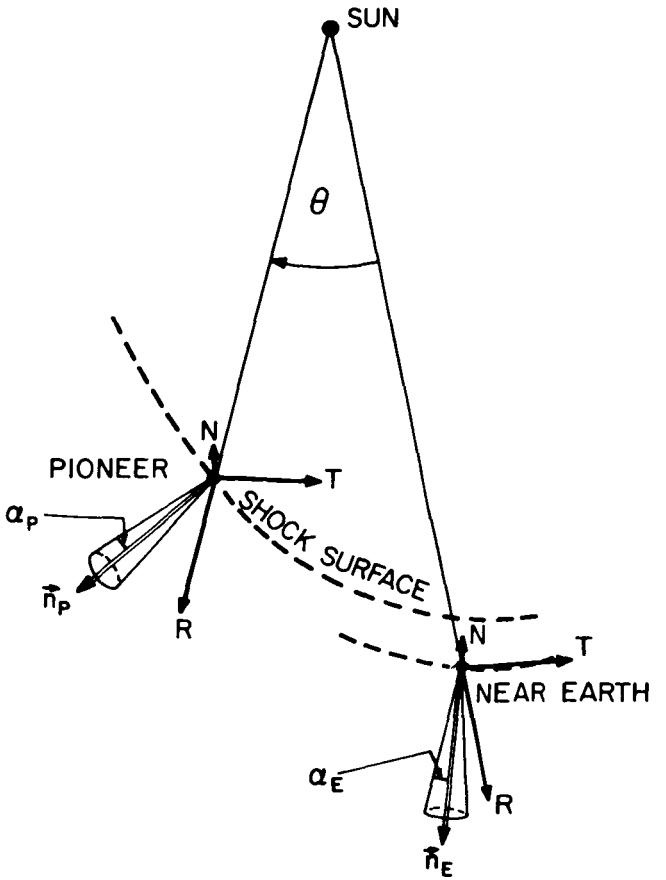

Figure 1

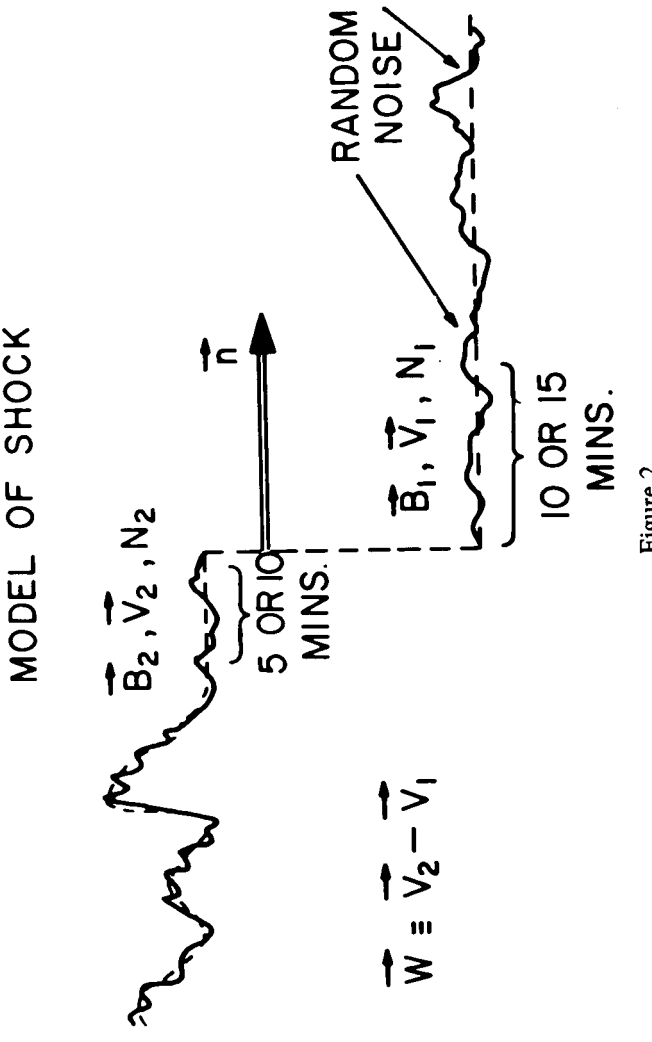
MODEL OF SHOCK
$\vec{B}_2, \vec{V}_2, N_2$
5 OR 10 MINS.
$\vec{n}$
$\vec{B}_1, \vec{V}_1, N_1$
RANDOM NOISE
10 OR 15 MINS.
$\vec{W} \equiv \vec{V}_2 - \vec{V}_1$

Figure 2

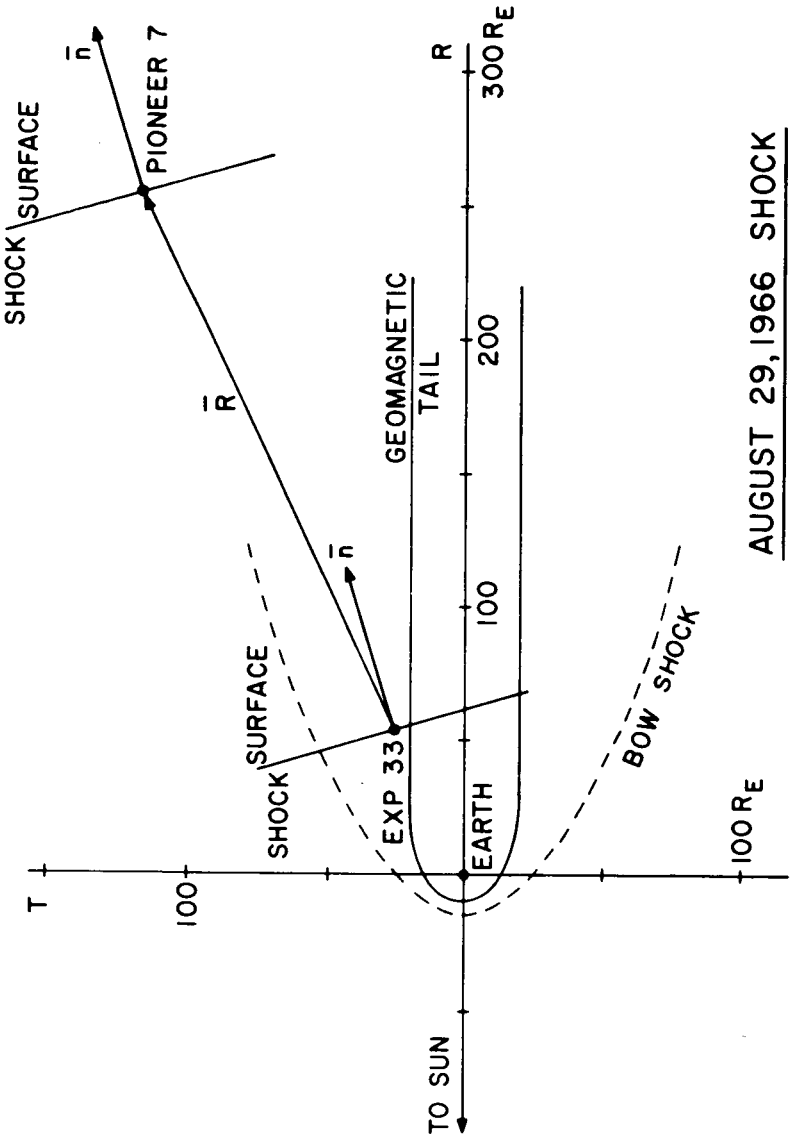
AUGUST 29, 1966 SHOCK
SHOCK SURFACE
PIONEER 7
$\bar{n}$
$\bar{R}$
GEOMAGNETIC TAIL
R
300 R_E
200
100
SHOCK SURFACE
EXP 33
EARTH
BOW SHOCK
100 R_E
T
100
TO SUN

Figure 3

THE STABILITY OF TANGENTIAL DISCONTINUITIES

Dr. Thomas Birmingham

Several features of the solar wind are very well explained by magnetohydrodynamics (MHD, for short). The solar wind is regarded as an ionized fluid whose motion is determined by internal pressure gradients and electric and magnetic fields. Dr. Burlaga here at Goddard has studied the solar-wind observations; he has identified several instances of what he considers to be MHD tangential discontinuities. Figure 1 shows one of Dr. Burlaga's observations.

Tangential discontinuities are sharp spatial variations in the properties of an MHD system: in this case, the solar wind. Depicted here as a function of time are the magnitude and direction of the solar-wind magnetic field, and the number density, thermal speed, and flow speed of solar-wind protons. In this observation, the spacecraft speed is much slower than the solar-wind speed, so that the time variation shown here is interpreted as a pure spatial variation in the solar-wind rest frame. It appears here as a time variation because the solar wind is convecting over the spacecraft. The jumps in these various properties are related to one another by the MHD equations.

I should point out that the jump relations for tangential discontinuities are quite distinct from the jump relations for shocks discussed by the previous speaker. In particular, a tangential discontinuity is always at rest with respect to the MHS fluid – the solar wind, in this case.

Observations frequently resolve internal structure to the tangential discontinuities, and thus "tangential forms" is a more appropriate terminology. I shall use this latter coinage for the rest of my talk.

You may note some indication of structure in these data, although these are not high-resolution data; the high-resolution data indicate that the properties of a tangential form change from their initial state to their final state in a variety of ways. They may do so monotonically; they may do so in a slightly nonuniform manner; or they may do so completely erratically.

The same tangential form is also frequently observed by two or more spacecraft widely separated in the solar wind. The tangential form propagates over distances of tens of earth radii, and perhaps further, without alteration of its basic structure. Such longevity suggested to Ted Northrop and me that tangential forms are stable structures. By stability, I mean that if a tangential form is perturbed – say, by a jet of high-energy plasma thrown out from the sun – this perturbation will die out with time instead of interacting with the tangential form and destroying the tangential form itself.

Our intuition regarding the stability of tangential forms has been borne out by a linear stability analysis of the MHD equations. In performing this calculation, we have used the model (typical of a tangential form) shown in Figure 2. The tangential form is always tangent to an X-Y plane (the X and Y directions shown) and has a finite thickness in the Z direction. The magnetic field is always tangent to an X-Y plane – hence, the name tangential form. However, the magnetic field may otherwise vary arbitrarily in amplitude and in direction as one moves in the dimension Z into the form, so long as it has only X and Y components. The dotted line is a typical locus of the tip of the magnetic-field vector as one moves through the form. There is no plasma flow in this particular model, which thus corresponds to the solar-wind rest frame. The plasma kinetic temperature, or kinetic pressure, also varies with distance through the form, but it varies in just such a manner that the total pressure – plasma plus magnetic – is constant as one moves through the form.

We have used an energy-minimization method for proving the stability of tangential forms: in this method, one takes an equilibrium of the form shown in Figure 2 and makes an arbitrary virtual displacement of each plasma element in the equilibrium. One calculates the change in total energy – plasma plus magnetic – due to the perturbation. In doing so, one uses the formula shown in Figure 3. δW is the total energy change, plasma plus magnetic; ξ is the displacement of the plasma element that was located at an equilibrium position where the equilibrium magnetic field was $\underset{\sim}{B}$, and the equilibrium pressure was P. The integration extends over the entire plasma.

In this particular form, you will note that two of the terms are positive definite. It just so happens that the third term vanishes identically when

the equilibrium is a tangential form. Thus, δW is always greater than or equal to zero. According to MHD theory, this is a necessary and sufficient condition for stability.

This type of stability analysis is analogous to the test of the stability of an equilibrium point in a mechanical potential. In the mechanics problem, one takes an equilibrium configuration and displaces a test particle away from the equilibrium point by an arbitrary amount. If, for an arbitrary virtual displacement of the test particle, the potential energy of the particle always increases, then one concludes that the equilibrium is a stable equilibrium. Regarding the tangential forms, our conclusion is that our intuition happens to be right in this case: they are MHD-stable.

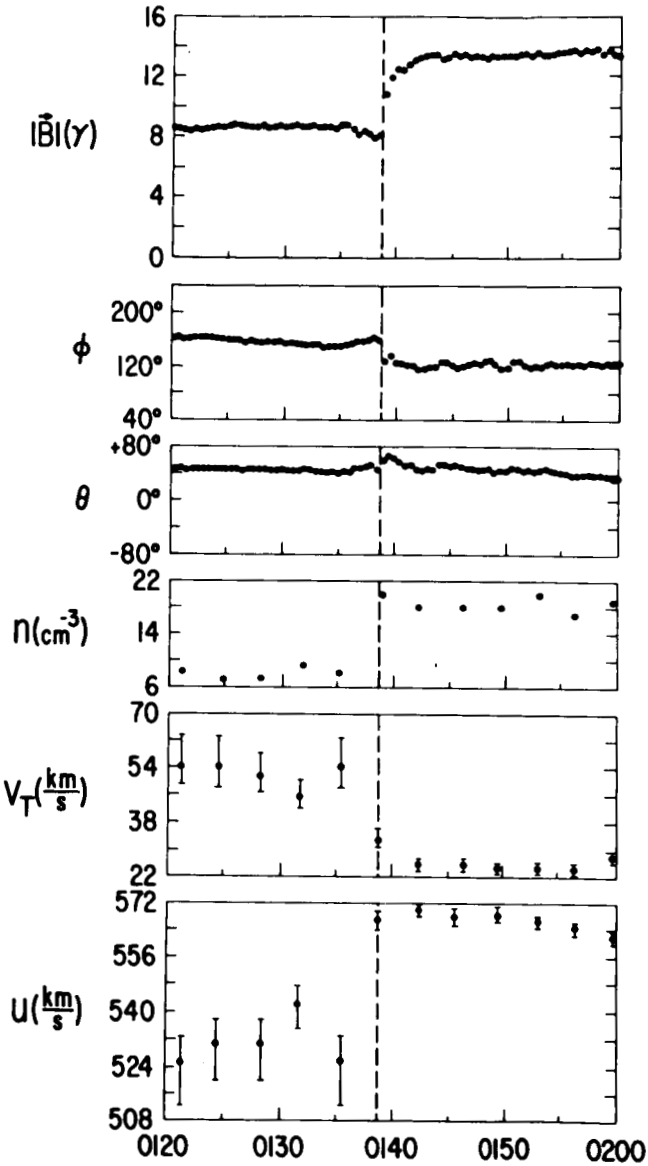
|B|(γ)
16
12
8
4
0
φ
200°
120°
40°
θ
+80°
0°
-80°
n(cm⁻³)
22
14
6
V_T(km/s)
70
54
38
22
U(km/s)
572
556
540
524
508
0120
0130
0140
0150
0200

Figure 1

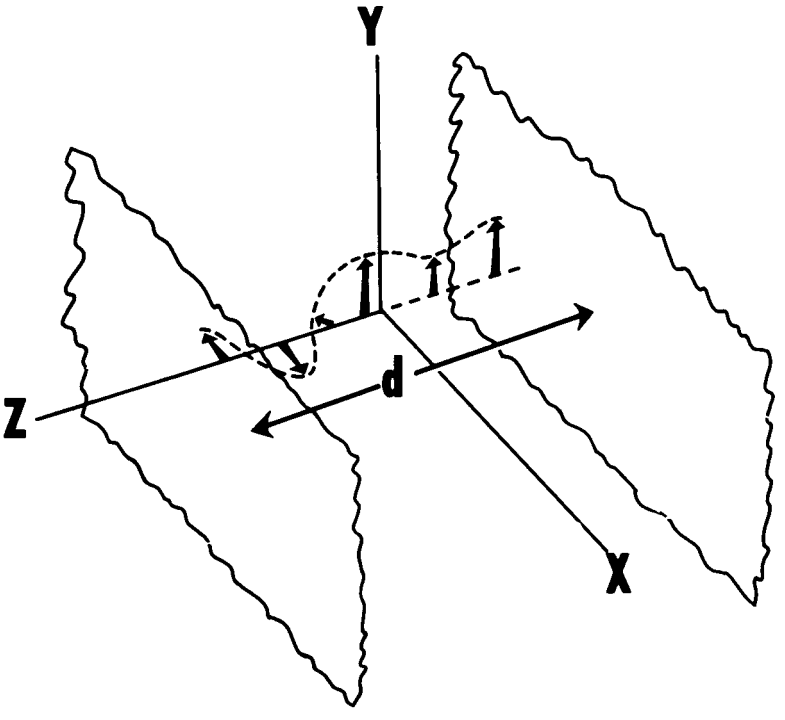

Figure 2

$$\delta W = \frac{1}{2}\int dV \left\{ \left(\underset{\sim}{B}\cdot\underset{\sim}{\nabla}\underset{\sim}{\xi} - \underset{\sim}{B}\underset{\sim}{\nabla}\cdot\underset{\sim}{\xi}\right)^2 + \underset{\sim}{\nabla}\left(P + \frac{B^2}{2}\right)\cdot\left(\underset{\sim}{\xi}\underset{\sim}{\nabla}\cdot\underset{\sim}{\xi} - \underset{\sim}{\xi}\cdot\underset{\sim}{\nabla}\underset{\sim}{\xi}\right) + \frac{5}{3}P\left(\underset{\sim}{\nabla}\cdot\underset{\sim}{\xi}\right)^2 \right\}$$

$$\delta W \geq 0 \text{ FOR ALL } \underset{\sim}{\xi} \Rightarrow \text{STABILITY}$$

Figure 3

HYDROMAGNETIC HEATING IN THE SOLAR WIND

Dr. Richard Hartle

The two-fluid solar-wind model proposed earlier for an ideally quiet sun predicted values of wind speed in proton temperature that were lower than average observed values. However, these predictions are consistent with an empirical relation obtained by Burlaga and Ogilvie of Goddard, in which the square root of the proton temperature varies linearly with the wind speed. If this relation is a fundamental property of the solar-wind flow, then it must be explainable by a model of the wind that predicts a continuous range of wind speeds and proton temperatures. To account for this variability, we conclude that energy must be supplied by dissipation of nonthermal energy from an external source. In a recent paper we have shown that such energy deposition should take place inside about 25 solar radii from the coronal base.

Of all the heating mechanisms proposed, we have concluded that only the qualitative model suggested by Barnes of Ames satisfies these requirements. We have quantitatively investigated with Dr. Barnes this model which I will now discuss.

Figure 1 is a drawing of the heating model, in which fast-mode hydromagnetic waves propagate outward from below the base and deposit energy by collisionless damping. We treated the wave propagation by "geometrical hydromagnetics," since the wavelengths are small relative to macroscopic scale lengths. In this case, the ray paths are found by solving Hamilton's equations. A typical ray path in the solar wind is shown by the dashed lines. Note that a ray trajectory starting from the base of the model at 2 solar radii bends toward the radial direction, usually becoming radial at about 5 or 10 solar radii, and then remains radial. The corresponding wave vectors $\vec{k}$ point approximately in the same direction at all points on the path and, at large distances, point along the ray path or radial direction. As the ray propagates along its path, it will damp, supplying thermal energy to the solar-wind gas.

The heating strength is principally dependent upon the plasma beta, and the angle between the wave vector and the magnetic field. When the beta (the ratio of the kinetic pressure to the magnetic pressure) is greater than

about a tenth, the damping rate is large. This condition obtains beyond the coronal base. In general, when the wave vector is more nearly parallel to the magnetic field, energy is primarily damped into the ions; on the other hand, when the wave vector is more nearly normal, energy is principally deposited in the electron gas, and there is no damping when the wave vector is exactly parallel or perpendicular to the field. However, since the wave periods of interest are 1 to 10 minutes, there is only collisionless damping into the proton gas.

For the particular case shown, with a spiral magnetic field, we note that the angle between the magnetic field and the wave vector continually decreases along the trajectory approaching zero as the ray path becomes radial, then increases again as the spiral angle becomes larger. In this case, energy deposition is strong in the proton gas near the base and out to about four solar radii. Moving out further, where the vectors are almost aligned, there is essentially no damping. Finally, as the spiral angle becomes large, deposition becomes strong again and the ray loses the remaining portion of its energy.

We see that this heating mechanism appears to satisfy the previously mentioned requirement, that of energy deposition over an extended range from the base. To determine the consequence of this mechanism acting on the solar wind, we derived a hydromagnetic heat source with an isotropic distribution of wave vectors at the base, self-consistent with the momentum and heat-transport equations. In Figure 2, the square root of the proton temperature is plotted against the wind speed. The proton temperature is given in kilo-kelvins. The band corresponds to the empirical values of Burlaga and Ogilvie. The solid curve is the analytical result, with corresponding values of density shown at selected points.

When the wave energy flow to the system is increased, the solution points move upward toward higher wind speeds and proton temperatures, while remaining within the range of observation. Electron densities in this model are slightly higher than the reported average observed values of 5 to 8; electron temperatures for these cases were essentially constant at 200,000 K, also within the range of observation.

The strong agreement of these results with observations is a clear indication that the primary nonthermal heat source in the solar wind is the collisionless damping of hydromagnetic waves.

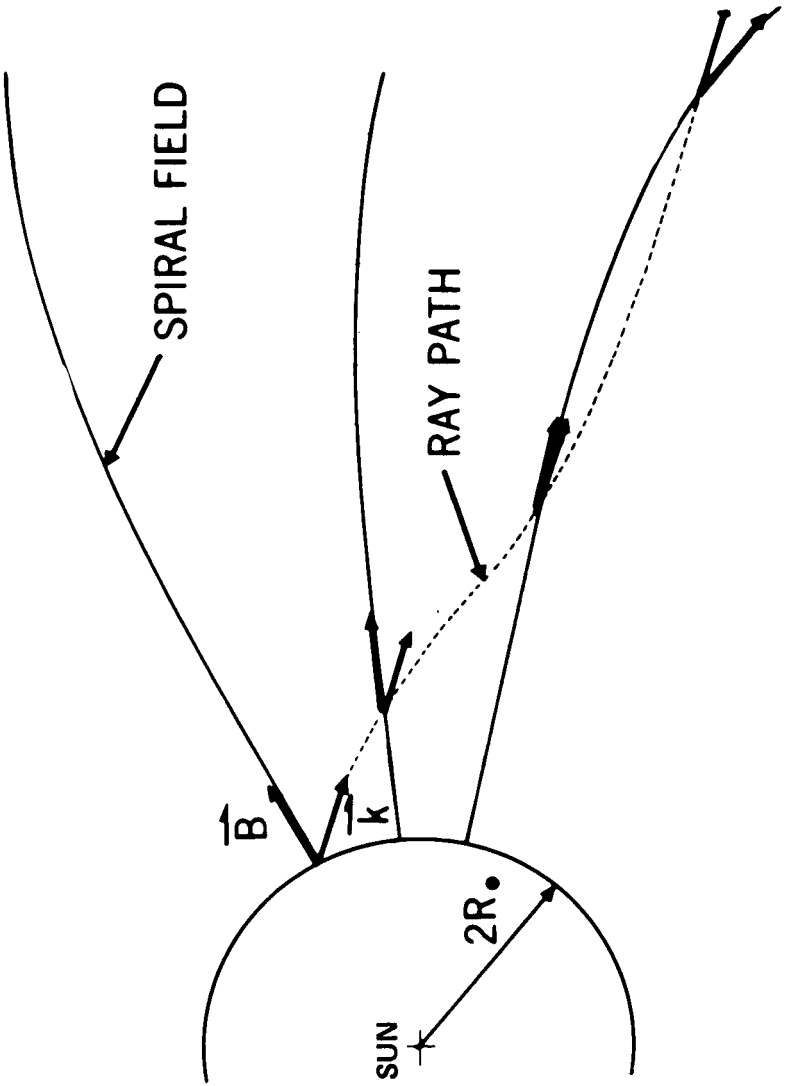

Figure 1

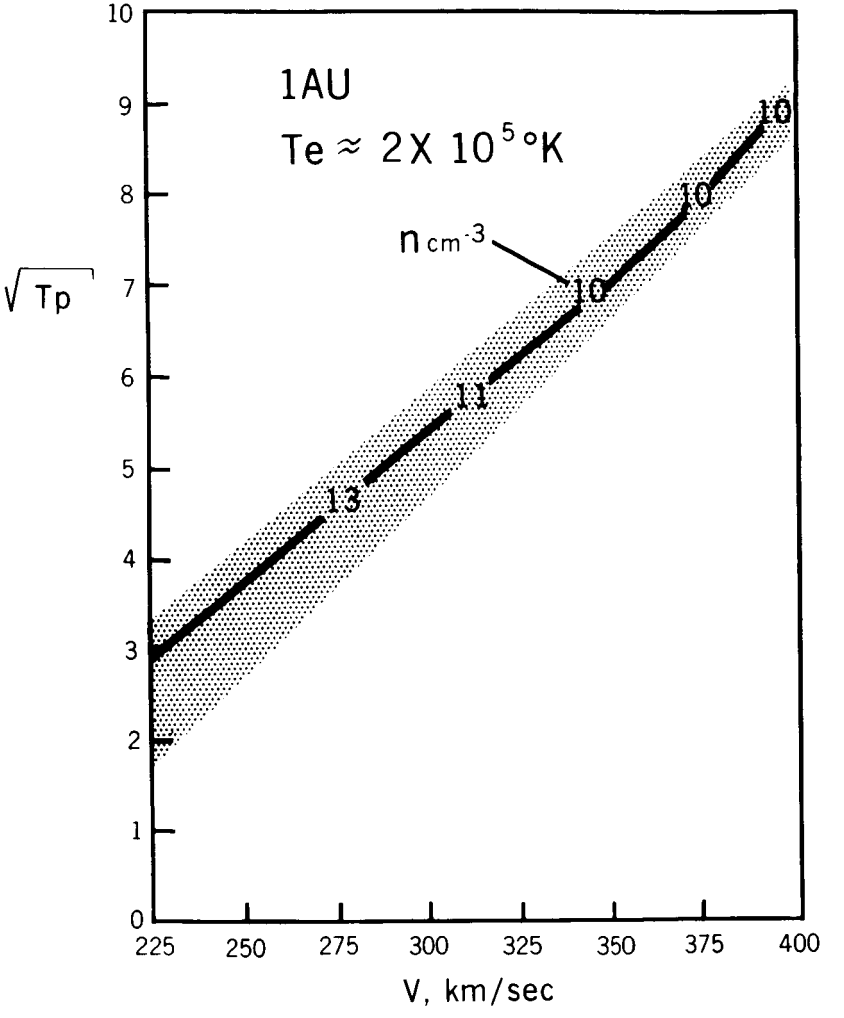
1AU
Te ≈ 2X 10⁵°K
n cm⁻³
10
10
11
13
√Tp
V, km/sec
0
1
2
3
4
5
6
7
8
9
10
225
250
275
300
325
350
375
400

Figure 2

SOLAR-WIND HEAT FLOW

Jack Scudder

When a theoretical solar-wind model emerges that is applicable for bulk speeds seen in nature of approximately 400 km per second, one of its first and crucial tests will be its ability to predict the energy-flux density due to heat conduction. Today I would like to talk about a recent experimental determination of this parameter.

Because of their high thermal conductivity, electrons are the primary agents of heat conduction from the sun. Theoretical estimates indicate that the heat due to electrons carried by electrons is approximately a thousand times that due to protons.

Figure 1 illustrates schematically the approximate average interplanetary magnetic-field configuration and, to facilitate discussion, defines the solar and antisolar cone axes about the field line, and the detector "look" directions with respect to these cone axes.

The interplanetary medium is a collisionless magnetized high-beta plasma in which one would expect the net energy-flux direction to be associated with enhanced energy-flux observations seen in the solar cone of observation. In order to demonstrate this phenomenon qualitatively, and to deduce the heat flux quantitatively, the analysis that follows uses simultaneous data from the electron plasma experiment of Ogilvie and Lind, and the vector magnetic-field data of Heppner and Sugiura on OGO 5.

The electron-spectrometer system had three simultaneously operating mutually perpendicular detectors, inclined at equal angles to the oriented nonspinning spacecraft. In time, the instantaneous interplanetary magnetic field made a variety of angles theta with a given detector. This configuration allowed a variety of look directions with respect to the magnetic field to be sampled.

Previous observations from experiments carried on the Vela satellites have shown that there are different velocity spectra for electrons in the solar and antisolar directions, as is also indicated in the data of Figure 2. The differences between the spectra in the forward cone and in the nonforward

cone primarily evidence themselves above 6000 km; these differences have been attributed by Hundhausen et al. to electrons carrying heat. There generally is a tail for spectra in the solar (or forward) cone directions, and not one in the antisolar cone.

The heat conduction H is a component of the net particle-energy flux along the field line in the stationary frame moving with bulk speed U from the sun.

Plotted in Figure 3 is the integrand of the necessary energy-flux integral versus theta for a 6-hour period on March 13, 1968. The ordinate is the differential energy-flux contribution in ergs per centimeter square, per second, per radian (10 milliwatts/meter^2/radian) and the abscissa θ is in radians and is the angle between the antilook direction of a given detector and the field line. The crosses are average values in 0.087-rad (5-degree) intervals with worst-case error flags indicated.

Two points should be made clear: The positive area indicates energy transport coming down the field lines from the sun, and the negative area is that portion of the energy flux that is observed traveling toward the sun. Also, the positive area is substantially larger than the negative area; when one computes this numerical integral, one gets a value for this example of $3.4 \pm .1 \times 10^{-5}$ watts/meter/s ($3.4 \pm 1 \times 10^{-2}$ ergs/cm^2/sec). In other data samples, E varies from 1.3 to 8.0.

To obtain these results, we have assumed the time-independence of the electron velocity distribution on the timescale of several hours. This hypothesis is supported by the near-constancy in time of the electron temperatures of interplanetary electrons as noted by us and by the Vela experimenters.

The value deduced here is somewhat higher than the Vela result of approximately 0.7×10^{-2}; this discrepancy can be traced to the contamination of the present velocity distribution by electrons associated with solar activity. Thus, the value reported is certainly an upper bound for H. Recent work has found lower values for E when this type of contamination of the velocity distribution was not present. Those data provided a lower bound for H, which was $1.0 \pm .5 \times 10^{-2}$.

On the strength of two independent, different, and consistent experimental determinations of the conduction heat flux by electrons at 149.6 gigameters (1 AU), we can say that the models for the solar wind must be able to predict a value for the heat conduction in the range 0.7 to 0.8 X 10^{-2} in order to be in agreement with the observations.

Further study of this parameter is continuing in the OGO-E data, and will investigate solar-wind heating as a function of radial distance from the sun on the upcoming Mercury-Venus flight opportunity.

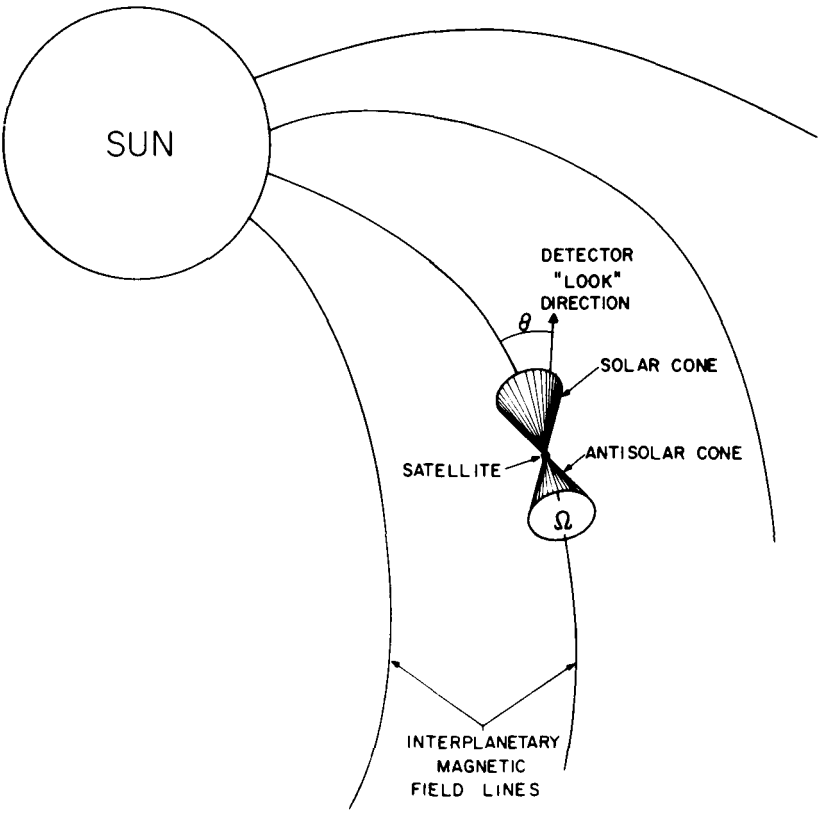

Figure 1

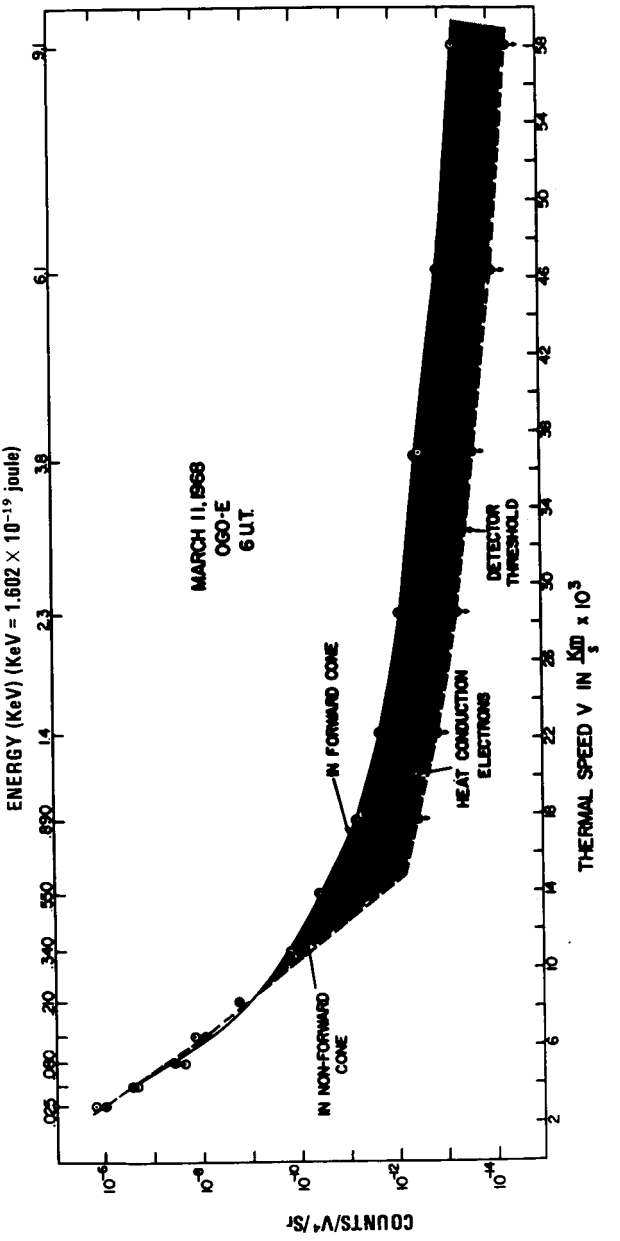
ENERGY (KeV) (KeV = 1.602 × 10⁻¹⁹ joule)
MARCH 11, 1968
OGO-E
6 U.T.
IN FORWARD CONE
IN NON-FORWARD CONE
HEAT CONDUCTION ELECTRONS
DETECTOR THRESHOLD
THERMAL SPEED V IN Km/s x 10³
COUNTS/V⁴/Sr

Figure 2

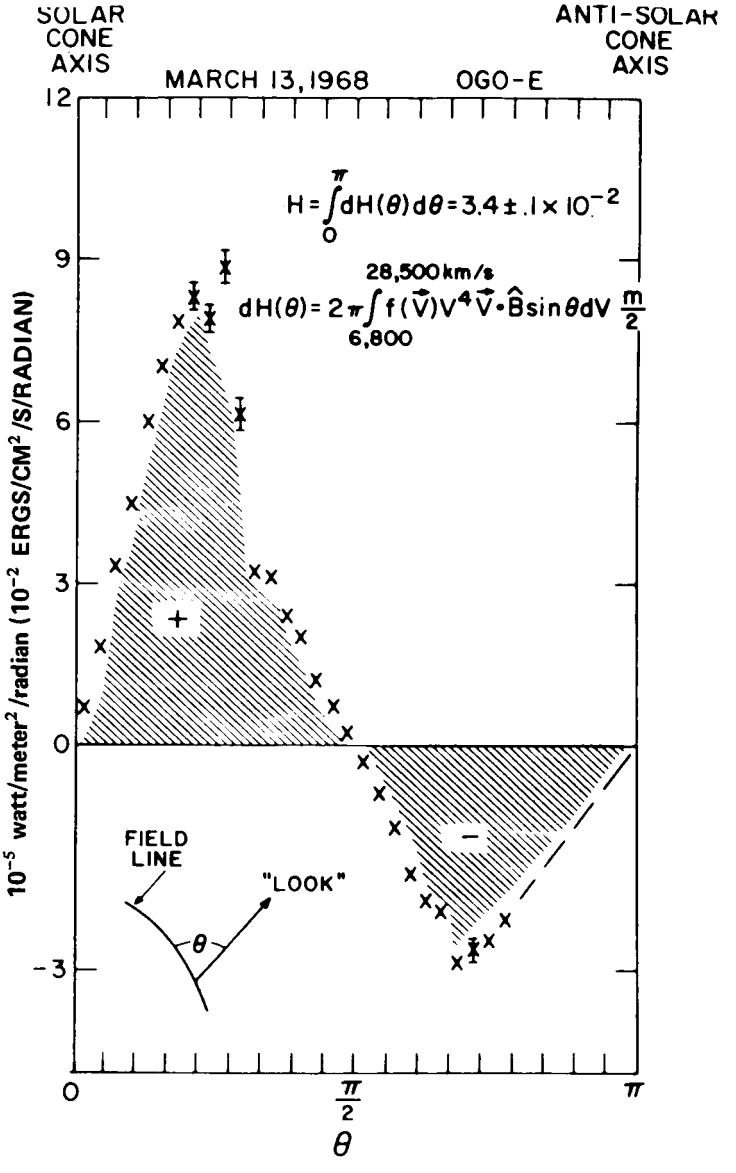
SOLAR CONE AXIS
ANTI-SOLAR CONE AXIS
MARCH 13, 1968
OGO-E
$H = \int_0^{\pi} dH(\theta)d\theta = 3.4 \pm .1 \times 10^{-2}$
28,500 km/s
$dH(\theta) = 2\pi \int_{6,800} f(\vec{V})V^4 \vec{V} \cdot \hat{B} \sin\theta dV$
10^{-5} watt/meter^2/radian (10^{-2} ERGS/CM^2/S/RADIAN)
12
9
6
3
0
-3
+
−
FIELD LINE
"LOOK"
θ
0
$\frac{\pi}{2}$
π
θ

Figure 3

LOCATIONS OF SOLAR RADIO BURSTS

Richard Fitzenreiter

Solar bursts are intense radio emissions associated with active regions on the sun, and measurements of the positions of the sources of these radio bursts at decameter wavelengths – that is, in the 20- to 60-MHz range – provide information about physical conditions in a region of the corona extending from about one-half to several solar radii from the surface of the sun.

For example, type 3 bursts are a class of sporadic radio emission believed to be caused by a stream of electrons moving outward from an active region on the sun and radiating at a frequency equal to the local plasma frequency. The plasma frequency, which is proportional to the square root of electron density, generally decreases along the path of the electron stream as it moves out into the corona, away from the surface of the sun. Therefore, high-frequency radiation is emitted from a point in the corona closer to the sun than the low-frequency radiation.

The significance, then, of position measurements of a type 3 source over a wide frequency range is that they are a means of obtaining a measure of the electron density along the path of the burst exciter.

Another example of the importance of accurate position measurements in this frequency range is the observation of a stable long-lasting wideband type of solar burst, known as decametric continuum. Positive measurements of the continuum source may be definitive in settling the current question as to whether the emission mechanism is gyrosynchrontron radiation or plasma radiation, the process responsible for type 3 bursts. If the continuum is due to plasma radiation, then one would expect the source to be extended like the type 3 source; however, if all frequencies appear to come from the same level in the corona, then the gyrosynchrotron process would be responsible.

Position measurements in the 20- to 60-MHz range are made with the Clark Lake sweep-frequency grating interferometer. Although the resolution of the instrument is sufficient to measure source position accurately, the highly variable effect of refraction in the earth's ionosphere severely

limits the observations nearly all the time, distorting position determinations to such an extent as to make much of the position data useless unless ionospheric refraction can be taken into account.

We have developed a way to remove the refractive effect from the data, and so are able to determine true source position. Figure 1 is an example of the technique; the data points are position measurements made simultaneously over the entire 20- to 60-MHz frequency range of one of several type 3 bursts associated with an active region located near the east limb of the sun. The horizontal scale is the position east and west relative to the center of the disc, in minutes of arc; the vertical scale is 1 over frequency squared. (The data are plotted against 1 over frequency squared because the deviation in observed position due to refraction is proportional to 1 over frequency squared.) If all the data points over the entire frequency range were to lie on a straight line, then the variation of observed position with frequency would be due to ionospheric refraction entirely, and it may be assumed that there is no variation of actual position with frequency; the true source position then would be the intercept of the straight line.

If, on the other hand, the data points are not linear (which is the case here), then there is another component of the frequency dependence of the observed position besides refraction, and the source may be assumed to be extended. Analysis of these data will permit determination of the ionospheric refraction at any frequency, so that the true source position at each frequency is known. The results appear in Figure 2.

The figure shows the disc of the sun, looking down from the north pole; the dashed vertical lines indicate the simultaneously measured positions at 60 and 20 MHz. Measurements at frequencies throughout the 20- to 60-MHz range lie between. The solid vertical lines indicate the 60- and 20-MHz positions after the refraction correction. Note the magnitude of the refractive effect, which is the difference between the observed and the true positions. These corrected source positions are consistent with the model of the type 3 burst exciter, moving away from the active region (as shown in Figure 2), radiating at the local plasma frequency. First the high, then the low frequencies are radiated.

Figure 2 makes clear how radiation affects the determination of the spatial extent of the source; the actual extent of the source is the difference

between the true plasma levels. The difference in observed positions at 20 and 60 MHz would be the apparent extent of the source, if refraction were not taken into account.

This analysis has assumed that the refraction is due entirely to the earth's ionosphere – that refraction in the corona is negligible – because type 3 bursts are believed to originate in regions of local density enhancement.

We are confident that we can account for refraction over a wide range of ionospheric conditions and can determine radio-source positions accurately, and that we are now in a position to measure the spatial extent of radio sources that will provide information about emission processes and physical parameters in the corona.

MEMBER OF THE AUDIENCE:

How do you account for motion of the burst exciter which is not along the line east-west?

FITZENREITER:

If the motion is not in the direction I have indicated here, east-west, but in some other direction, the east-west projection of the source is observed.

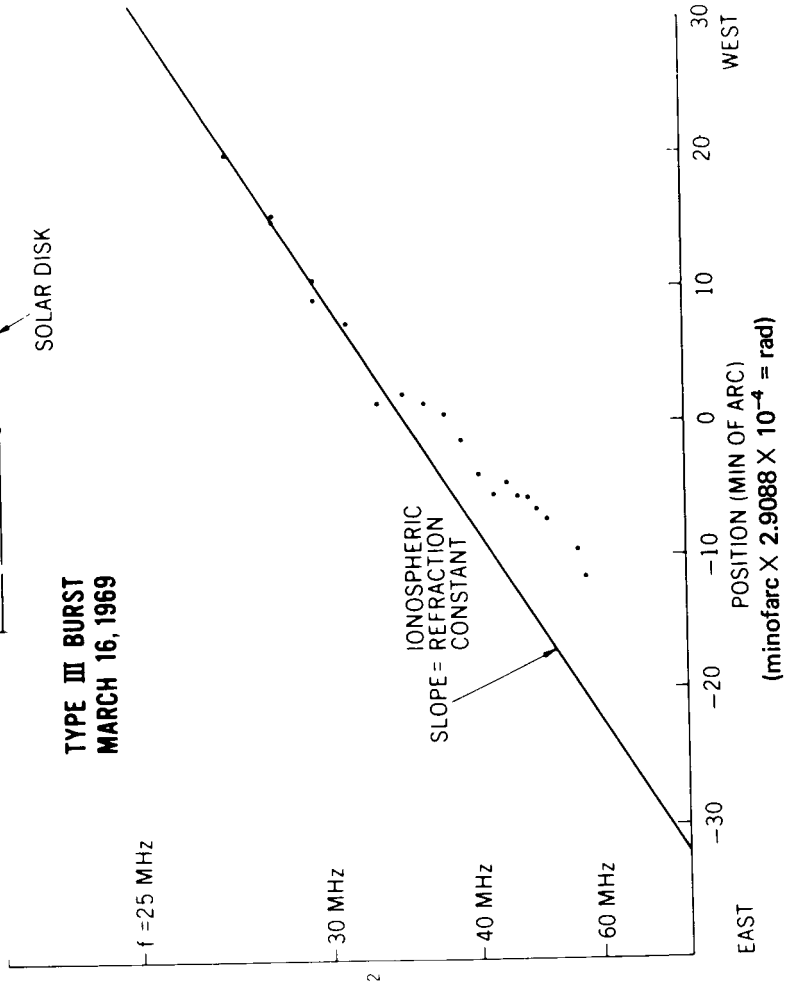
SOLAR DISK
TYPE III BURST
MARCH 16, 1969
f = 25 MHz
30 MHz
40 MHz
60 MHz
1/f²
SLOPE = IONOSPHERIC REFRACTION CONSTANT
EAST
WEST
POSITION (MIN OF ARC)
(minofarc X 2.9088 X 10⁻⁴ = rad)
30
20
10
0
−10
−20
−30

Figure 1

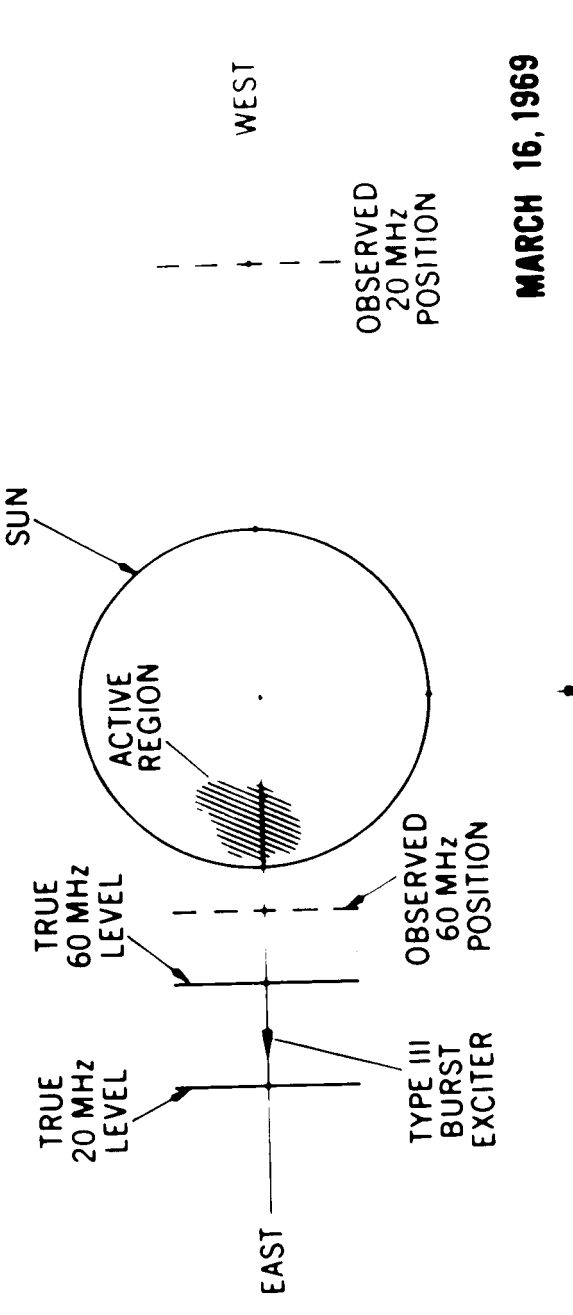
WEST
OBSERVED 20 MHz POSITION
MARCH 16, 1969
SUN
ACTIVE REGION
TRUE 60 MHz LEVEL
OBSERVED 60 MHz POSITION
TRUE 20 MHz LEVEL
TYPE III BURST EXCITER
EAST
TO EARTH

Figure 2

DISCOVERY OF A HECTOMETRIC SOLAR CONTINUUM

Harriet Malitson

The hectometric range of wavelengths centers around 100 meters, or, in terms of frequency, 3 MHz. It is one decade down in frequency from the decametric observations just described. Solar continuum refers to radio emission from the sun that is smooth in structure as opposed to the various kinds of solar bursts.

Figure 1 presents a sample of data from the first radio-astronomy Explorer satellite, RAE-1. We are looking at the sun, and the figure shows samples of data for various discrete frequencies: 1.00 MHz, 1.31 MHz, 1.65 MHz, and 2.80 MHz. A 2-week period in August 1968 is shown on the timescale at the bottom. For each frequency, minimum values of the radio flux for certain 10-minute samples of data are plotted relative to the cosmic background (the cosmic background is the radio emission that comes from our galaxy and is always present).

There are no solar bursts in progress in the illustration, because we have deliberately taken the quietest times – i.e., the minimum fluxes. During a period of about 6 days, with the exception of one where the activity went down, there is a particular active region on the sun, and there is enhanced flux coming from this region. This is the first time that solar-continuum emission has been detected in the hectometric range, and it has started us thinking about continuum emission over the whole range of frequencies emitted by the sun.

The lower part of Figure 2 presents schematically the various types of continuum observed, and the upper part shows the regions of the solar corona where they originate. The cross-hatched area represents the photosphere of the sun; the shading indicates an active center on the sun, starting with a sunspot on the photosphere and extending up through the chromosphere and corona of the sun in the form of an active-region streamer. As we move outward along the streamer, the electron density falls off, but it always remains higher than that of the ambient corona.

An active region such as the one of August 1968 produces a continuum in the metric range called the metric noise storm that can last for several days

(Figure 2). Superimposed on the smooth background are many so-called type 1 bursts having a bandwidth of about 6 MHz and lasting about a half-second each. The amplitude distribution of these bursts is predominantly toward the lower amplitudes, just detectable over the background. Although type 1 storms have been well observed from ground-based facilities for more than 25 years, there is still disagreement about the mechanism that produces them: the leading contenders are probably plasma-wave radiation and gyroradiation.

Decametric continuum, identified in 1965 from ground observations, also can last for several days, and is strongly associated in time with the type 1 storms. However, the overlying burst structure is entirely different, consisting of type 3 or fast-drift bursts. These bursts drift from high to low frequencies in several seconds, lasting up to a minute at the lower frequencies. Type 3 bursts are fairly well understood theoretically as coming from plasma oscillations produced at the appropriate plasma levels in a coronal streamer by the passage of a packet of superthermal electrons moving out with a velocity of approximately a third that of light – i.e., 1.60 to 16.02 femtojoule (10- to 100-keV) electrons.

Hectometric continuum is quite similar to decametric continuum, showing that the phenomenon extends out in the corona to at least 50 solar radii, or 36.4 gigameters (0.25 AU), which would be out to about the edge of Figure 2. An interesting point is that the amplitude distribution and the bandwidth of type 3 bursts associated with hectometric continuum are the same as those of type 1 bursts associated with the metric noise storm. Those for type 3 bursts that are not associated with continuum are different, and include more of the stronger bursts.

After looking at the total picture, we believe that the storm radiation all the way from metric through hectometric can be accounted for by plasma-wave radiation. This means that streams of superthermal electrons are continuously coming out of active regions such as the one of August 1968; these streams must originate in the photosphere, or low chromosphere, of the active region in order to pass through the level where metric storms originate. As they travel outward through the interplanetary medium, they produce plasma waves that result in metric, decametric, hectometric, and probably kilometric storms.

In support of this theory, the measurements of Lin and Anderson, and of Van Allen and Krimigis, show long-period enhanced fluxes of approximately 6.41 femtojoule (40-keV) electrons near the earth during times of high solar activity. We believe that these are the same electrons.

DR. PIEPER:

Thank you very much, Harriet. The paper that has been written on this discovery has just been accepted for publication in Astrophysical Journal letters. If there are no questions, I would like to take about 10 seconds to make a comment of my own: Last year there were at least two papers from RAE that were of considerable significance. This year, two of the last three scientific papers have been from the RAE spacecraft. Yesterday there were four papers about it, which concerned the thermal analysis from RAE, the flexible spacecraft dynamics program, and the orbital eccentricity and perturbations expected for the second RAE from studies of the dynamical in-orbit behavior of RAE-1. I think the RAE program represents the sort of thing that Goddard does well and enjoys doing: it employs the best talents of our scientists and our technologists, and it has in retrospect certainly been one of the prize programs that we have done around here. I think it has been just first-class all around; I am very proud of it.

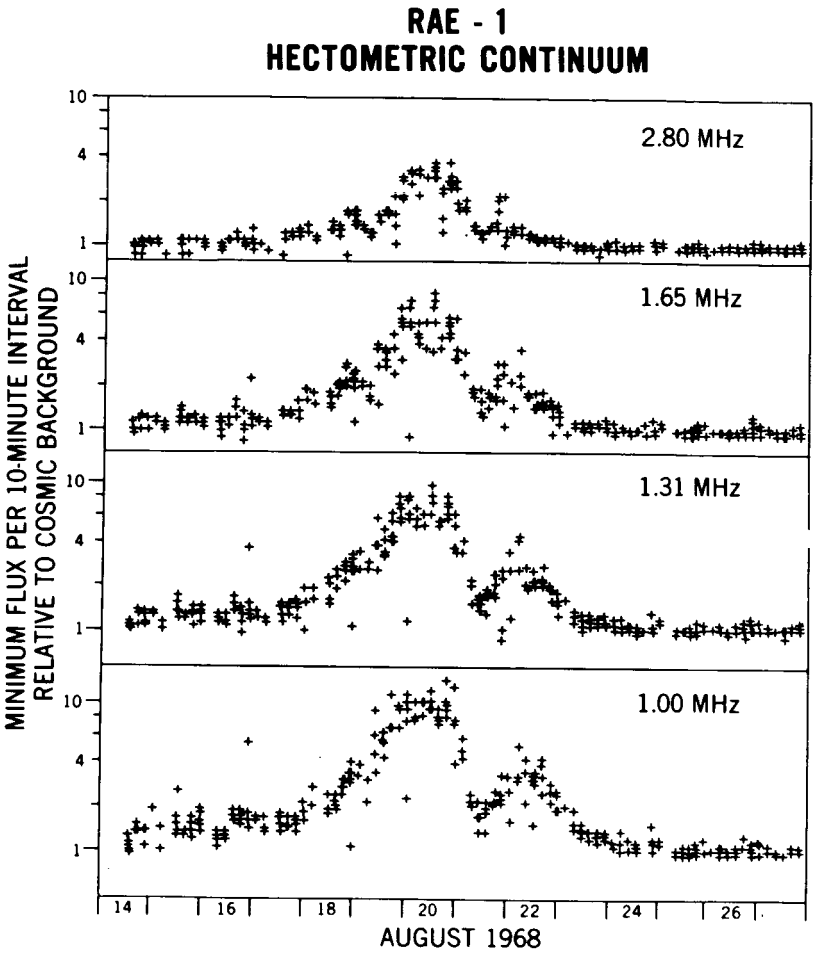
RAE - 1
HECTOMETRIC CONTINUUM
2.80 MHz
1.65 MHz
1.31 MHz
1.00 MHz
MINIMUM FLUX PER 10-MINUTE INTERVAL
RELATIVE TO COSMIC BACKGROUND
10
4
1
14
16
18
20
22
24
26
AUGUST 1968

Figure 1

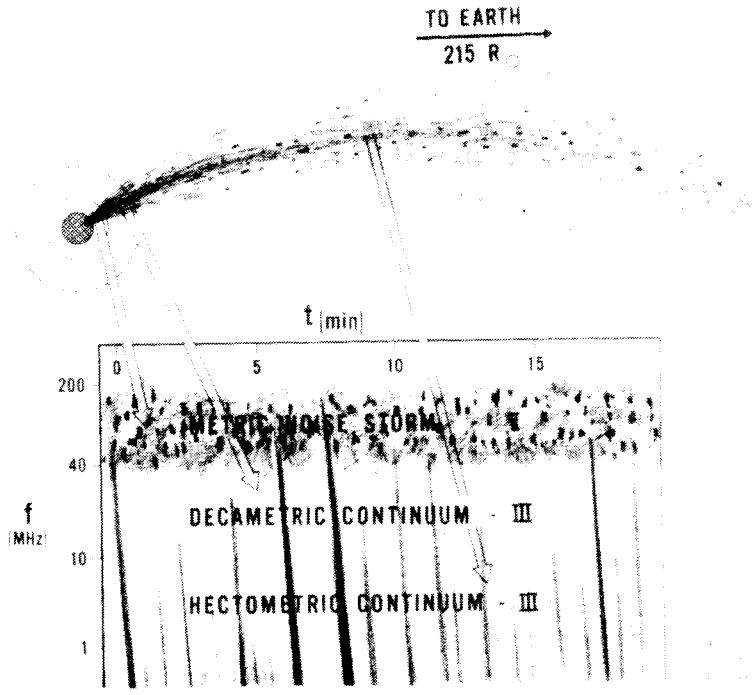
TO EARTH
215 R
t (min)
0
5
10
15
200
40
10
1
f (MHz)
METRIC NOISE STORM
DECAMETRIC CONTINUUM - III
HECTOMETRIC CONTINUUM - III

Figure 2

LONG-DURATION SOLAR ACTIVE REGIONS

Dr. Donald Heath

A monitor of the sun's ultraviolet energy in the 120- to 130-nanometer (1200- to 1300-angstrom) region has been observing the sun since April 1969, when it was launched aboard Nimbus 3. In April 1970, a similar version was launched aboard Nimbus 4. As of this date, both instruments are still operating.

The largest periodic solar-flux variations that have been observed are those with a 27-day period, and they are observed with a sensor that responds to hydrogen Lyman-alpha and the region of the solar continuum from 135 to 160 nanometers (1350 to 1600 angstroms). Figure 1 shows one year of observations with the shortest wavelength sensor.

The sensor current output is proportional to the solar flux. Variations over this period range from 40 to 15 percent, the average being about 25 percent per solar rotation. I might mention that, during this period, there was an experiment by Timothy that monitored Lyman-alpha from OSO 4; he observed that the flux variations from Lyman-alpha were of the order of possibly 1 to 3 percent. It would seem that the large flux variations are not due to Lyman-alpha, even though the sensor does respond to Lyman-alpha, but are probably due to the 135 to 160-nanometer (1350- to 1600A) radiation.

A close look at the figure will show two active regions that have persisted over this period of time and are still present today. In addition to the primary region, there is another secondary region which seems to come and go. Shown for comparison below is the daily sum of Kp, which is a measure of the perturbation of the earth's geomagnetic field by the solarwind particles. Also shown is the 0.8- to 2-nanometer (8- to 20-angstrom) solar X-ray flux taken by the NRL group from the Explorer satellite during the same period, and also the 10.7-cm flux for this time interval. It appears that there is an association or correlation between large perturbations of the geomagnetic field and these UV-active regions. This blank point represents the day of the March 7 solar eclipse last year. And there is also a correlation with the 0.8- to 2-nanometer (8- to 20-angstrom) solar flux. The best correlation is with the 10.7-cm flux.

Now, if we assume that the maxima occur when the UV-active region is on the central meridian, then by plotting the solar longitude as shown in Figure 2 we produce a plot of the solar longitude (or Carrington longitude) as a function of the day number. If we put a point for the solar longitude at the time when the UV maxima occur, then we find two distributions: the lower curve is the primary or strongest active region, and the upper is the secondary or weaker UV-active region that we have been observing. Figure 2 covers twenty rotations of the sun, almost twice the period covered in the previous figure.

The slope of these curves indicates that they are not at the latitude for which the Carrington longitude is defined; the upper curve represents a rotation rate of 13.11 degrees per day, and the lower curve represents a rotation rate of 13.14 degrees per day. Now, in the longer wavelength sensors, taking all the variations together, we see that the total energy involved in a rotation – the change in the total energy output – is of the order of 10^{23} (10^{30} ergs) per rotation of the sun.

It is not clear at this time what is producing these UV-active regions: it could be changes in the overall intensity of the solar continuum near the region of the temperature minimum, or the solar-flux variations that have been seen could be due to a continuous type of absorption like that associated with the ionization limits of elements such as aluminum, silicon, or magnesium.

MEMBER OF THE AUDIENCE:

Do you know of any attempts to correlate these UV maxima with atmospheric parameters?

DR. HEATH:

We plan to do that with Nimbus 4, where we have the BUV instrument determining the high-altitude distribution of ozone. This is one of the correlations that we want to look for.

MEMBER OF THE AUDIENCE:

How about lower than that?

DR. HEATH:

Further down, the energies involved are more apt to be governed by wind transport and so forth – I don't think you will see it lower down.

MEMBER OF THE AUDIENCE:

Are these UV-active regions correlatable to any particular active regions as determined by ground-based solar observations?

DR. HEATH:

Yes. If you look at the sun in H-alpha, and also with the calcium plage areas, you see these regions come in and they disappear. They tend to come in in the regions where we see this continued UV activity. There is a correlation, but the visible-type regions tend to come and go. This seems to be an overall background.

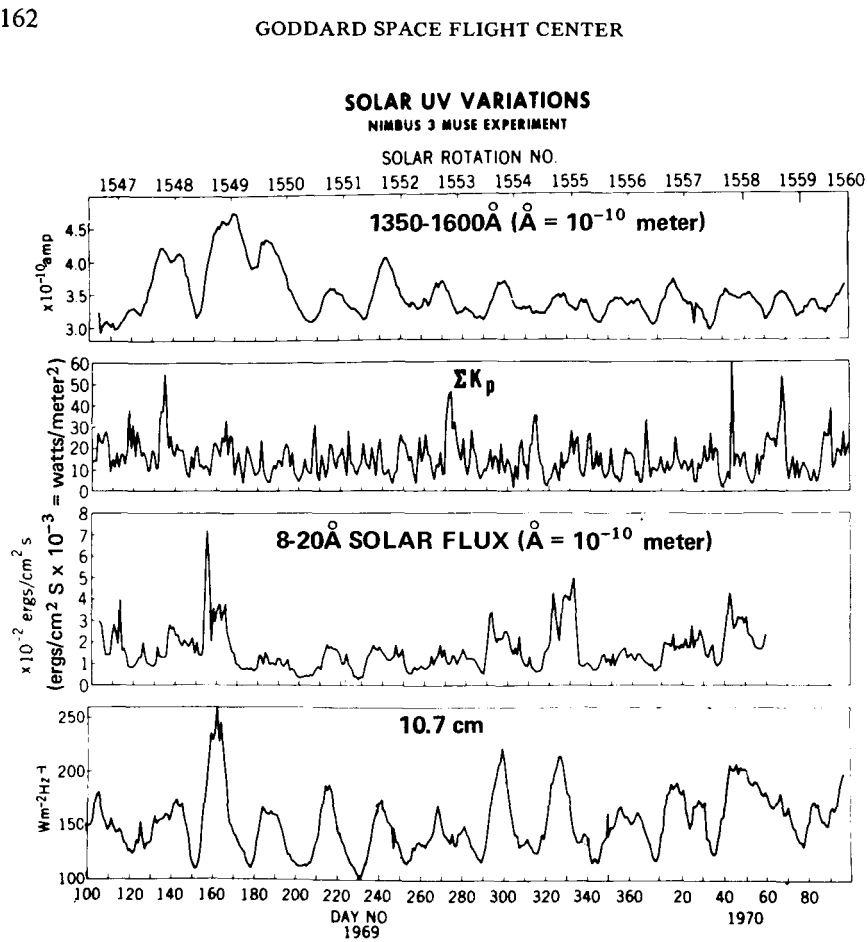
SOLAR UV VARIATIONS
NIMBUS 3 MUSE EXPERIMENT
SOLAR ROTATION NO.
1547 1548 1549 1550 1551 1552 1553 1554 1555 1556 1557 1558 1559 1560
1350-1600Å (Å = 10⁻¹⁰ meter)
x10⁻¹⁰amp
4.5
4.0
3.5
3.0
ΣKp
(ergs/cm² S x 10⁻³ = watts/meter²)
60
50
40
30
20
10
0
8-20Å SOLAR FLUX (Å = 10⁻¹⁰ meter)
x10⁻² ergs/cm² s
8
7
6
5
4
3
2
1
0
10.7 cm
Wm⁻²Hz⁻¹
250
200
150
100
100 120 140 160 180 200 220 240 260 280 300 320 340 360 20 40 60 80
DAY NO
1969
1970

Figure 1

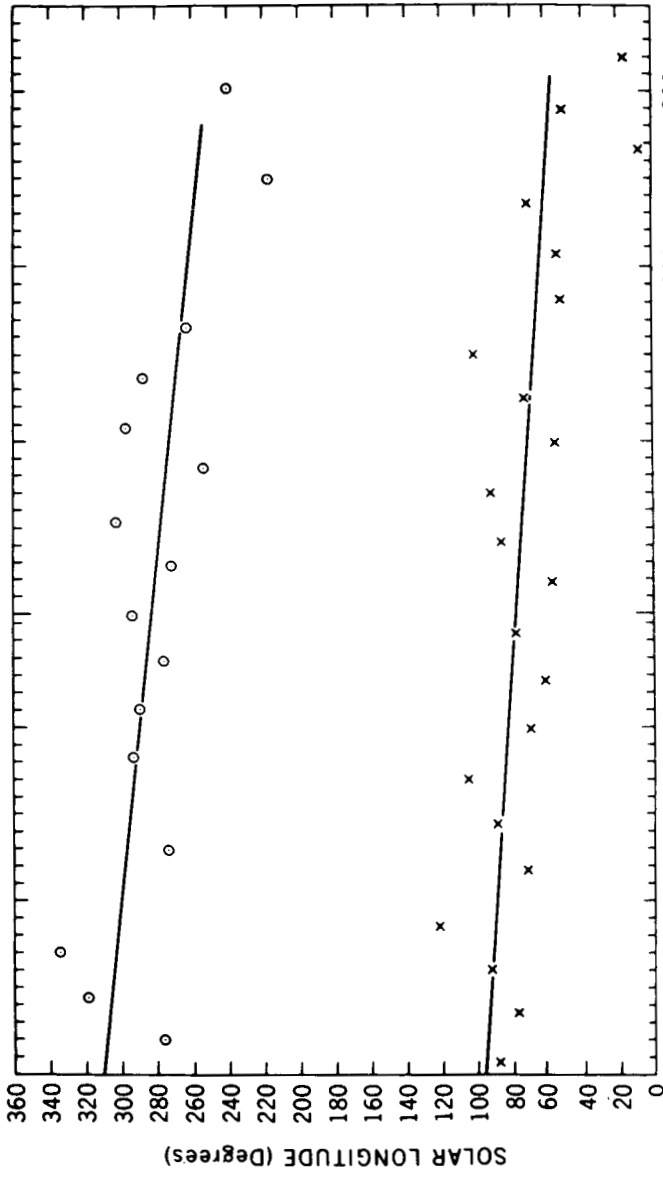
SOLAR LONGITUDE (Degrees)
360
340
320
300
280
260
240
220
200
180
160
140
120
100
80
60
40
20
0
100
200
300
365
100
200
300
1969
1970
DAY NO.

Figure 2

QUASI-SEASONAL VARIATION IN THE SUN

Dr. Sushil Chandra

To relate the sunspot number with the seasons of the earth may appear somewhat unusual, or even absurd, at first sight. We are used to thinking that the sun is the prime mover of our solar system, and we can easily comprehend the seasonal changes of planet earth. But even a suggestion that solar activity has any relation to the seasons of the earth defies our normal rationale.

The study of this problem originated in our effort to understand all those terrestrial phenomena which are to be characterized as seasonal anomalies. Some of these are very well known: for example, the winter anomalies in the D and F regions, and the worldwide increase in thermospheric temperatures in the equinoctial months. Having failed to develop any self-consistent theory to explain these phenomena, we began investigating the characteristics of solar activities to see if the seasonal anomalies in the terrestrial atmosphere can directly be attributed to the sun.

In this presentation, I shall report some of our preliminary findings. The conclusion of this paper is based on a study of the sunspot number for the past 200 years, the decimeter flux over the last two solar cycles, and the recent measurements of X-rays in the 0- to 0.8- and 0.8- to 2-nanometer (0- to 8- and 8- to 20-angstrom) region. These measurements generally reflect the electromagnetic aspect of the solar activity. For studying the corpuscular nature of the solar activity, we have used sigma Kp (the daily sum of the geomagnetic index and the galactic cosmic rays) measured in the interplanetary medium.

Figure 1 shows the running average over 27 days of a number of parameters that reflect both the plasma and the electromagnetic aspect of solar activity for 1966. Plotted from the top is the reciprocal of the counting rates of 8.01 attojoule (50-Mev) protons in the interplanetary medium, the 10.7-cm flux, sigma Kp, and log of X-rays in the wavelength range of 0.8 to 2 nanometers (8 to 20 angstroms). Without discussing the implications of correlation between cosmic rays and solar X-rays – which are quite interesting by themselves –, I wish to draw your attention to the enhancement in the X-ray flux in the months of April, September, and December.

In sigma Kp, we note the enhancement in April and September, and in cosmic rays, the corresponding depression in those months. In the 10.7-cm flux, we can identify the equinoctial peaks, similar to those of the X-rays, although they are not quite as noticeable because of the steep rise in the average curve toward the solar maximum.

On the basis of solar-activity data in 1966, we should conclude that the electromagnetic aspect of solar activity shows enhancement in the equinoctial and winter months and the corpuscular aspect shows enhancement mainly in the equinoctial months. This conclusion can be sustained by studying the solar activity over a much longer period, as the next illustrations will show.

Figure 2 shows the average behavior of the 10.7-cm flux for the period 1958 to 1967. In this plot, we have removed both the 27-day and 11-year periodicities by suitable filtering, and the result is plotted against the month, as shown here. In conformity with the results of the previous figure, we note here the existence of the two peaks in the months of April and September, and a third peak in the month of January. Thus, the seasonal characteristics of X-rays we just noted in the previous figure are essentially present in the average data of 10.7 cm.

Figure 3 shows the behavior of the sunspot number over the past three solar cycles (1938-47, 1948-57, and 1958-67). As in the previous illustration, both the 27-day and 11-year periods have been removed to emphasize the possible periods in the range of 3 to 12 months. The figure clearly shows an enhancement in the winter and the equinoctial months, in all the three cycles; however, the peaks in the three solar cycles do not occur at the same time, and appear to shift around ± one month in the different solar cycles.

A similar analysis of sigma Kp over the past three solar cycles shows only the presence of equinoctial peaks; in sigma Kp, the winter peaks are conspicuously absent. Thus, on the basis of present study, we conclude that both the corpuscular and the electromagnetic aspect of solar activities tend to increase during the equinoctial months. In addition, the electromagnetic aspect of solar activity tends to increase in the winter (northern) months.

The equinoctial enhancements in the corpuscular activity of the sun have been known for a long time; the increase is generally attributed to the favorable angles of arrival of the charged particles in the magnetosphere, as proposed by Bartles and others. We have shown here that, even though the dipole field of the earth may contribute to the equinoctial enhancement of the charged particles in the earth's magnetosphere, the source of this enhancement is the sun itself, which seems to increase its activities in the equinoctial months.

The seasonal changes in the sunspots seem to be caused by the tidal forces and the precessional torques exerted by the various planets on the solar atmosphere. The effect of these sources on the formation of sunspots is currently being investigated; even though the results are promising, it is somewhat premature to present a detailed discussion on it.

I shall therefore conclude this talk with the remark that, even though we do not at present have a full explanation of the season-like changes in solar activities, we are quite clear about the implications and the effect they produce on the terrestrial atmosphere.

MEMBER OF THE AUDIENCE:

The magnetic equator of the sun is not the same as the ecliptic plane, and so these two planes intersect at points which are fixed in the galactic frame and so on. What is the relation between that reference point and your seasonal theory?

DR. CHANDRA:

Well, we are not quite sure what effect, if any, this will have on the season-like behavior of the solar activity. We have been thinking about the possbile effects of the 0.121-rad (7.5-degree) inclination of the solar axis with respect to the plane of the ecliptic. If some of the active centers have very long life, as Dr. Heath's results seem to indicate, it is possible to visualize certain modulations associated with the rotation of the earth around the sun. During the course of a year, the total active area projected toward the earth will depend upon the season. However, since the modulation effect seems to be small, it is not clear how significant the effect of this inclination is in producing the seasonal changes.

MEMBER OF THE AUDIENCE:

I was wondering what the Venus solar physicist would find the results are? or the Jupiter solar physicists? – whether their sunspot numbers would be related to their seasons too?

DR. CHANDRA:

A number of papers have appeared, beginning with Schuster's in 1910, claiming correlation between sunspot and gravitational forces exerted by various planets. Some of these papers have claimed semiannual effects in solar activity when arranged according to the yearly scales of Venus, earth, Jupiter, and Saturn. We are currently investigating the planetary effects on the formation of the active centers; at this stage, however, we cannot take a definite position.

DR. PIEPER:

Well, perhaps next year we will have another report on how the sun knows when it is September. Thank you very much, Dr. Chandra.

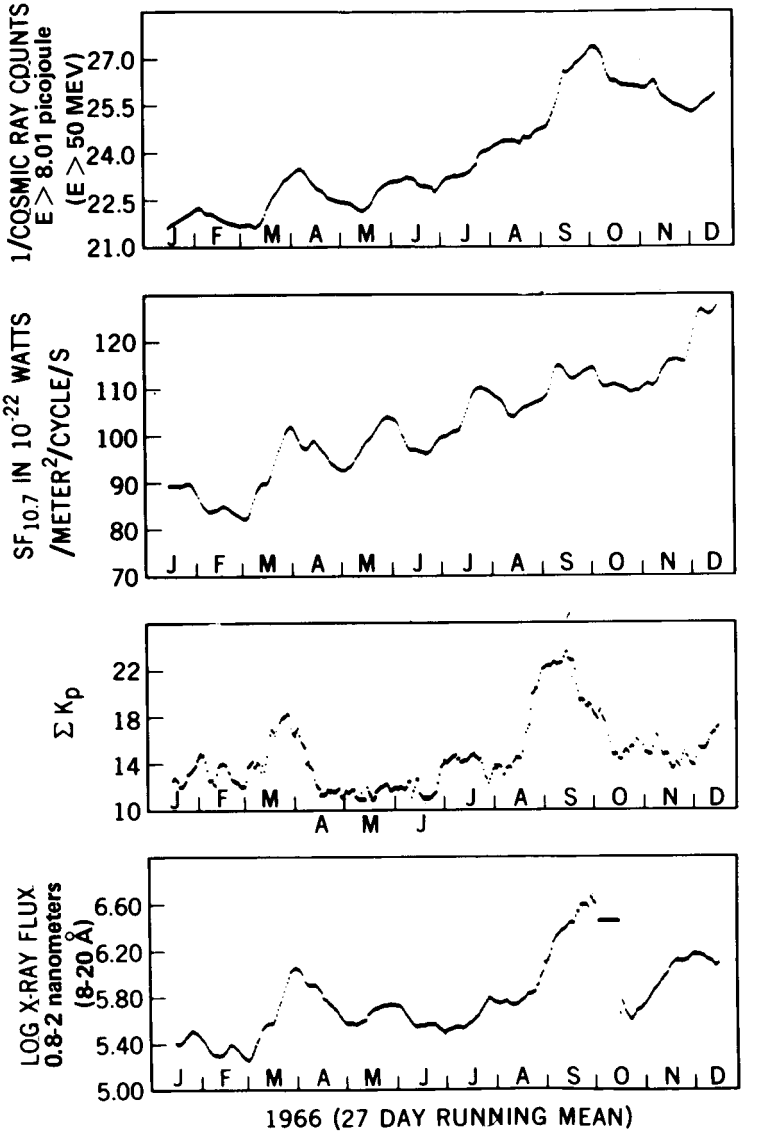
1/COSMIC RAY COUNTS
E > 8.01 picojoule
(E > 50 MEV)
27.0
25.5
24.0
22.5
21.0
J F M A M J J A S O N D
SF10.7 IN 10-22 WATTS
/METER2/CYCLE/S
120
110
100
90
80
70
J F M A M J J A S O N D
Σ Kp
22
18
14
10
J F M A M J J A S O N D
LOG X-RAY FLUX
0.8-2 nanometers
(8-20 Å)
6.60
6.20
5.80
5.40
5.00
J F M A M J J A S O N D
1966 (27 DAY RUNNING MEAN)

Figure 1

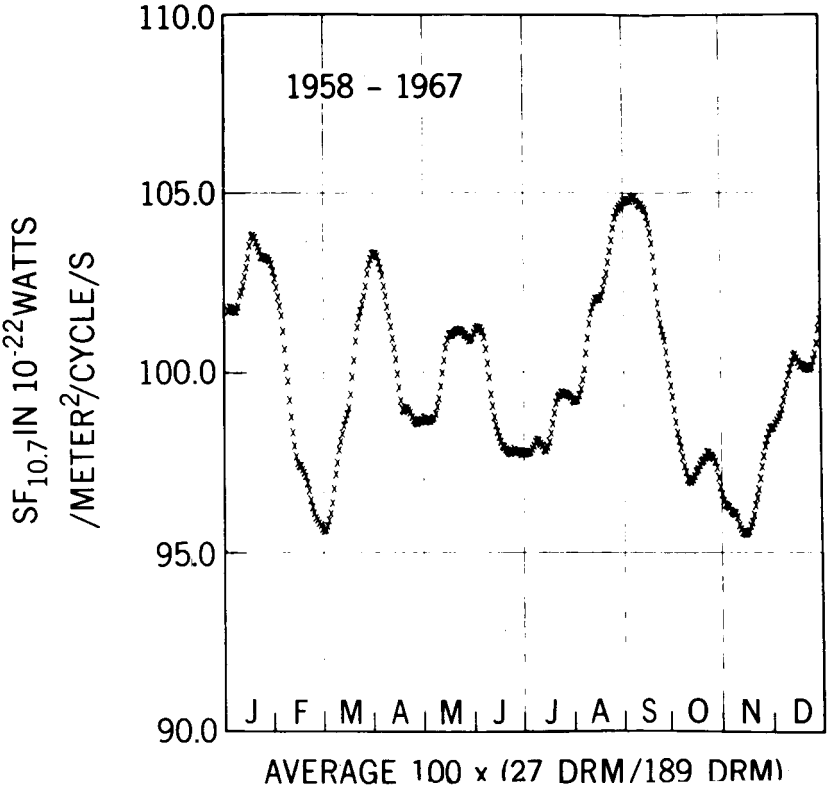
110.0
105.0
100.0
95.0
90.0
1958 - 1967
J F M A M J J A S O N D
AVERAGE 100 x (27 DRM/189 DRM)
SF10.7IN 10-22WATTS
/METER2/CYCLE/S

Figure 2

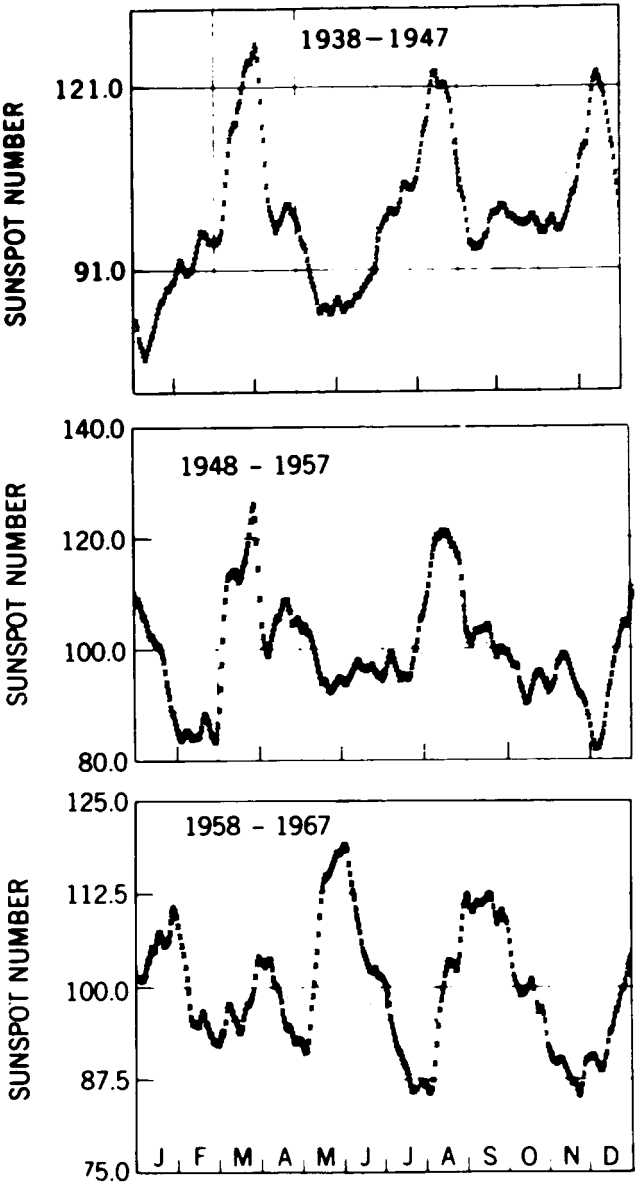
1938–1947
SUNSPOT NUMBER
121.0
91.0
1948 - 1957
SUNSPOT NUMBER
140.0
120.0
100.0
80.0
1958 - 1967
SUNSPOT NUMBER
125.0
112.5
100.0
87.5
75.0
J F M A M J J A S O N D

Figure 3

SOLAR X-RAYS AND PARTICLE ACCELERATION

Kenneth Frost

Ever since the discovery that solar flares inject into interplanetary space charged particles having energies at times up to hundreds of millions of electron volts, the process by which a solar flare accelerates these particles has been actively investigated and discussed.

Among the several mechanisms proposed to explain the acceleration, one claims that acceleration proceeds in two distinct phases. This two-stage acceleration hypothesis is based primarily on radio data – i.e., solar radio bursts associated with flares. In the first stage of acceleration, particles are accelerated to energies up to 16.02 femtojoule (100 keV), perhaps by induced electric field arising from annihilating magnetic fields at the very beginning stages of a flare. Radio observations drawn upon to support this claim are the appearance of type 3 bursts in the solar corona. These bursts are caused by packets of electrons propagating out through the solar atmosphere with velocities up to, but usually less than, 0.8c.

The acceleration in the second phase is conjectured to occur through a Fermi acceleration mechanism operating in a shock front produced by the flare. Evidence for the shock front is drawn from the appearance of type 2 radio bursts in the solar atmosphere. The presence of particles with relativistic energies in this phase is indicated by the appearance of type 4 radio radiation due to synchrotron radiation from relativistic electrons trapped in the solar corona.

An instrument aboard the fifth orbiting solar observatory that measured solar X-rays between 2.40 and 40.05 femtojoule (15 and 250 keV) of energy succeeded in obtaining the first X-ray evidence that the two-stage acceleration hypothesis is a reasonably accurate description of what occurs during a flare. Figure 1 illustrates one of many X-ray bursts that support this hypothesis: the event occurred March 30, 1969, and was associated with a flare behind the west limb of the sun.

(In the following discussion, the X-ray burst is assumed to be generated by bremsstrahlung from the accelerated electrons stopping in the denser regions of the solar atmosphere.) The X-ray burst begins, as shown in

Figure 1, with a very impulsive peak. After the rapid decay of this peak, a second peak having a much slower decay is observed. There are more photons at higher energy in the second peak; this implies that a second acceleration occurs, to produce the higher energy electrons that radiate the more energetic photons observed in the second peak. This second phase of the X-ray burst begins in association with a type 2 burst, suggesting a shock-front mechanism for the second acceleration.

Figure 2 shows the photon spectra observed during the two phases of the X-ray burst. In the first stage, we have a power-law spectrum up to about 16.02 femtojoule (100 keV), where there is an abrupt break in slope with a much steeper spectrum prevailing thereafter. The lower plot in the first-phase sketch is the spectrum obtained during the decay of the impulsive peak; it has about the same shape as found at the maximum. The second-phase drawing shows the power-law fit at the maximum of the second state; 15 minutes later, we find that the photon spectrum still reflects the same power law ($\sim E^{-2}$). The dashed curve represents the spectrum found in the first phase, shown for comparison.

So we have here a rather convincing indication of the two-stage acceleration reflected by the photon spectrum, which is indicative of the accelerated electron spectrum.

MEMBER OF THE AUDIENCE:

Where is all this energy coming from?

FROST:

I would think that the acceleration in the first phase is probably by the annihilation of magnetic field; part of the energy from the annihilation goes into the electric-field acceleration. In the second phase, the accelerated electrons derive their energy from the shock front propagating out from the flare volume.

MEMBER OF THE AUDIENCE:

Shock front develops when the thing moves into low density –

FROST:

I think the shock front is considered to propagate out almost instantaneously at the initial explosion. The electric-field accelerated particles, moving at nearly the velocity of light, instantaneously fill up the magnetic structure of the flare ahead of the shock front. Then, as the shock front comes out, these preaccelerated particles are accelerated further, to higher energies.

MEMBER OF THE AUDIENCE:

Did you see change in the – enter the spectrum of the electrons absorbed in the vicinity of the earth reflecting the change of the two-phase acceleration?

FROST:

Yes. In addition to the radio data that supported the two-phase acceleration argument, there have been some solar-particle observations cited. The 6.41 femtojoule (40-keV) electrons observed by Lynn and Anderson seem to precede the 160.2 femtojoule (Mev) electrons observed by Cline and McDonald. These two electron funds are taken to indicate acceleration in the two different phases, or electrons from the two different phases.

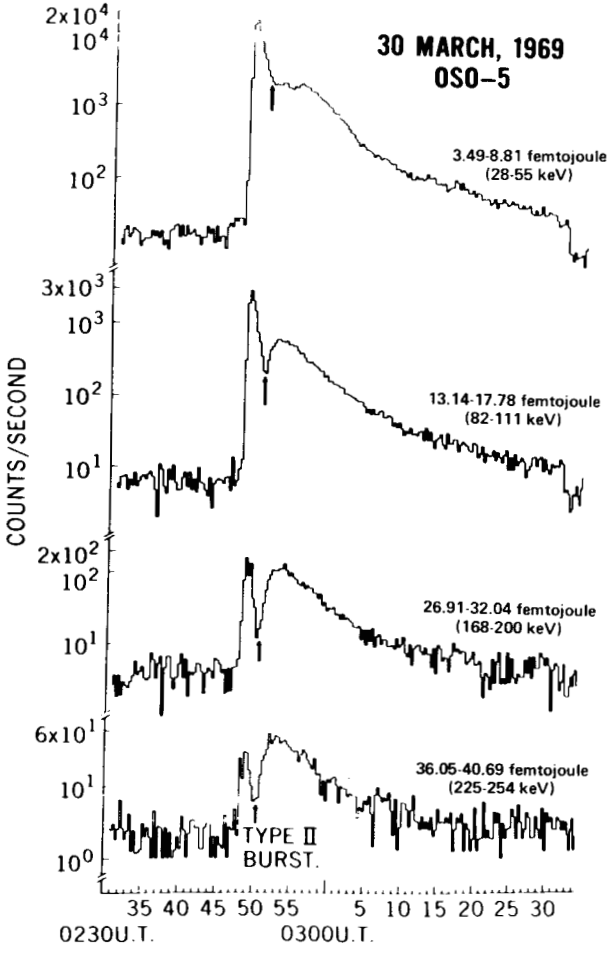

Figure 1. Intensity-time profiles that cover the energy intervals indicated to the right of each profile. Each point in the profiles is computed from ten consecutive and evenly spaced measurements, each of approximately 0.18-second duration, taken over 18 seconds. The vertical arrow indicates the time of appearance of a type 2 burst in the metric band; the abrupt drop in count rate after 0331.5 UT is due to sunset.

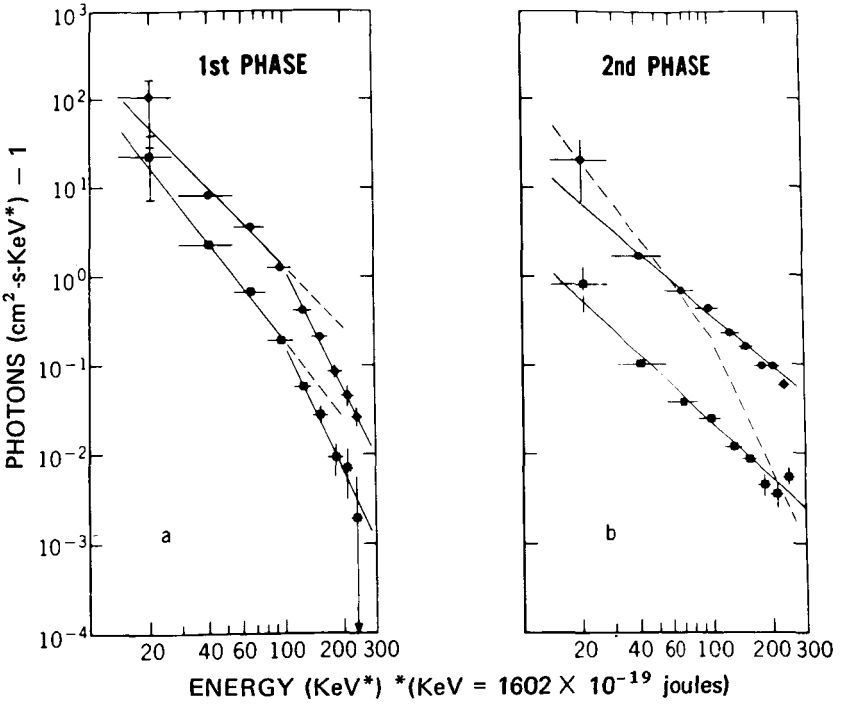

(a) The circles represent the spectrum at the peak of the impulsive burst between 0247.5 and 0.249.8 UT, just before the second increase and the type 2 burst.

(b) The circles represent the spectrum at the peak of the secone phase, between 0251.1 to 0242.5 UT, plotted above the spectrum (squares) observed later between 0306.5 and 0308.5 UT.

Figure 2. The dashed lines on each spectrum emphasize the break in slope that occurs at 16.02 femtojoule (100 keV). The spectrum at the peak is fitted with $\epsilon^{-2.5}$ power law up to 100 keV, and $E^{-4.5}$ power law beyond 16.02 femtojoule (100 keV); the later spectrum, with $E^{-2.8}$ power law to 16.02 femtojoule (100 keV), and $E^{-4.7}$ power law above 16.02 femtojoule (200 keV). The spectrum at the peak may be of the same shape as found later, but distorted by the effects of pulse pileup. Both spectra can be fitted with E^{-2} power between 2.41 and 40.05 femtojoule (15 and 250 keV). In (a), the dashed curve represents the lower spectrum.

HYDROGEN/HELIUM RATIO IN STARS

Dr. David Leckrone

An astrophysical problem that has come of age in recent years is that of establishing, with accuracy, the helium-to-hydrogen abundance ratio that prevails at the present time in stars and in the interstellar medium. This problem is of great current interest, primarily because of its cosmological implications. If we know the present helium-to-hydrogen ratio in stars and nebulas, we may be able to work backward in time and to infer the helium-to-hydrogen ratio that prevailed at the time the galaxy was formed. A knowledge of this primeval helium-to-hydrogen ratio should give us some basis for choosing among alternative cosmological theories.

The approach I have taken in attacking this problem involves the interpretation of the neutral helium-absorption lines observed in the spectra of hot stars. In particular, I have recently completed a study of eleven different neutral helium lines observed in the spectra of seven main-sequence B stars, ranging in effective temperature from about 11,000 to 31,000 kelvins. The object of the game was to match each of the observed neutral helium profiles with a profile calculated theoretically. The free-fitting parameter involved here was the helium-to-hydrogen ratio assumed in the theoretical calculations. Thus, the result of the analysis of each star was an estimate of helium abundance for the star in question.

Most of my spectroscopic materials were obtained with the 120-inch telescope at the Lick Observatory, and the theoretical calculations were carried out here at Goddard.

I would like to illustrate the results of this fitting procedure for one of the seven stars, and then I will merely summarize the results for the other stars.

Each of the curves you see plotted in Figure 1 corresponds to one neutral helium-absorption line observed in the spectrum of the star named HR2154. This is a B5 star whose effective temperature is about 15,000 kelvins. The figure shows flux in the line plotted normal to the local continuum, as a function of displacement from the line's center in angstrom. In each case, the X's represent the observed profile and the

solid curve represents my attempt to fit it theoretically. I have denoted each line by a central wavelength in angstroms.

First of all I would like to point out one line that I couldn't match theoretically, and that is the one at λ587.6 nanometers (λ5876 angstroms). You should note that this line is observed to be very deep and very strong in its core. A number of other workers have recently reported similar problems in attempting to match theoretically the cores of such strong spectral lines; I believe this problem is symptomatic of our failure to understand the physics of line formation in those tenuous outer regions of the stellar atmosphere where such strong line cores are formed.

However, you will note that I was able to obtain a reasonably good match to the weaker neutral helium lines, such as the one at λ402.6 and λ438.8 (λ4026 and λ4388). On this basis, I was able to estimate a helium-to-hydrogen ratio for six of the seven stars that I investigated, and these results are summarized in Figure 2. Here I have listed these six stars by name and by spectral type, and I have given their estimated helium-to-hydrogen ratios by number of atoms in the third column. Note that there is very little scatter from star to star – negligible scatter, in fact. Thus, on the basis of a total of 46 neutral helium lines observed in the spectra of these six stars, I have obtained an overall average helium-to-hydrogen ratio which lies roughly halfway between 10 and 11 percent by number of atoms.

It is interesting to note that all these stars are nearby members of the Orion spiral arm, and that this average (0.006) is in excellent agreement with the results of the most recent optical study of the spectrum of the Orion nebula. It is also in pretty good agreement with the value derived in the most recent study of the mass luminosity relation for eclipsing binary stars observed in spiral arms.

However, we should note that this 10.6 percent value is substantially higher than the value of 6 percent reported recently by a group here at Goddard, on the basis of solar cosmic-ray studies. This latter discordance certainly must be resolved before we can claim that the helium-abundance characteristic of spiral-arm objects is well established.

MEMBER OF THE AUDIENCE:

I wonder if you could remark upon how significant the match to the wings is. You are weighting your results very strongly by that apparent match; I wonder if you have any idea how much you would change your theory of line formation – which we know is somewhat suspect – or the composition of your atmosphere, and still come up with about the same answers. In other words, how do you come by the answers you got?

DR. LECKRONE:

First of all, let's not call this my theory of line formation – it is the LTE theory, which is almost universally utilized in studies of this sort. It is used for two reasons: one, it is simple, and two, in some cases it seems to give reasonably good answers – although you can't be sure in all cases why it gives such good answers. In this particular case, for example, not only was I able to match an individual line profile, but I also obtained remarkably consistent results from line to line for a given star, and from star to star over a rather wide range of physical conditions.

Now, there is no a priori reason why the LTE line-formation theory has to be right: in fact, I am presently undertaking a program to test it by doing some more rigorous non-LTE calculations. These are quite difficult and consume a great deal of computer time. But all I can say at this stage is that, until the non-LTE calculations are completed, I can't give a definite numerical answer to your question. What I can say is that the study I've outlined here represents absolutely the best that one can do within the context of presently accepted methodology. I chose a model atmosphere for each star on the basis of the hydrogen lines I observed in the star and on the basis of the spectral-energy distribution for the star. As an incidental thing, I calculated some magnesium-line profiles in order to estimate the rotational velocity for each star in question; in the magnesium lines, for example, I was also able to obtain a good fit, both in core and in wings of the line profile, even though these lines are rather strong on some of these stars.

MEMBER OF THE AUDIENCE:

I was just wondering if you could tie in this kind of result with the other theory: can you derive the age of those stars –

DR. LECKRONE:

No, one doesn't derive an age for these stars from their helium-to-hydrogen ratios. However, I alluded to the cosmological implications of this work at the beginning, and I can state here that I have some rather straightforward ideas about what this might mean, cosmologically speaking. Experts in stellar evolution have recently pointed out that, if the distribution of mass among stars in the galaxy has always been about the same as we observe it to be now – that is, if we don't postulate really supermassive objects as being a common phenomenon in the galaxy, either now or early in its history –, then it is unlikely that stellar evolution can enrich the interstellar medium in helium-to-hydrogen by more than, say 0.02 or 0.03 over the entire lifetime of the galaxy.

So, if about a 10-percent helium-to-hydrogen ratio holds up as being a good answer for the present value, then I think that one might infer from this in a very simple way that a helium-to-hydrogen ratio of about 7, 8, or 9 percent probably prevailed at the time that the galaxy formed. This is, by the way, just the sort of value that is being predicted by cosmologists like Peebles in studying big-bang cosmologies. So I think this is a very simple picture, but it holds together well from both a theoretical and an observational viewpoint.

MEMBER OF THE AUDIENCE:

You mention a disagreement with some of the cosmic-ray observations which give a value of about 5 percent. These solar values are to be taken with a grain of salt: the solar helium-to-hydrogen ratio cannot be directly measured by spectroscopic means – the 5-percent value results from taking the spectroscopic values for the abundances of medium nuclei and combining these with the cosmic-ray value of alphas to medium nuclei. Now it turns out that the ratio of alphas to medium nuclei in cosmic rays is a function of energy; it has been observed to vary from about 1 in 59 to 1 in 20, and consequently the problems of tying this ratio to the sun are severe. So, unless we can find out precisely why this variation exists and where it comes from – whether it is a propagation effect, or reflects the actual composition of the solar system – any comparison between the spectroscopic value of the stars and the one derived by combining spectroscopic and solar cosmic-ray observations for the sun is not really valid.

DR. PIEPER:

Thank you very much, Tom Krimigis, for a splendid five-minute paper. (Laughter.) That was very good, thanks a lot. Any other comment?

MEMBER OF THE AUDIENCE:

And no slides. (Laughter.)

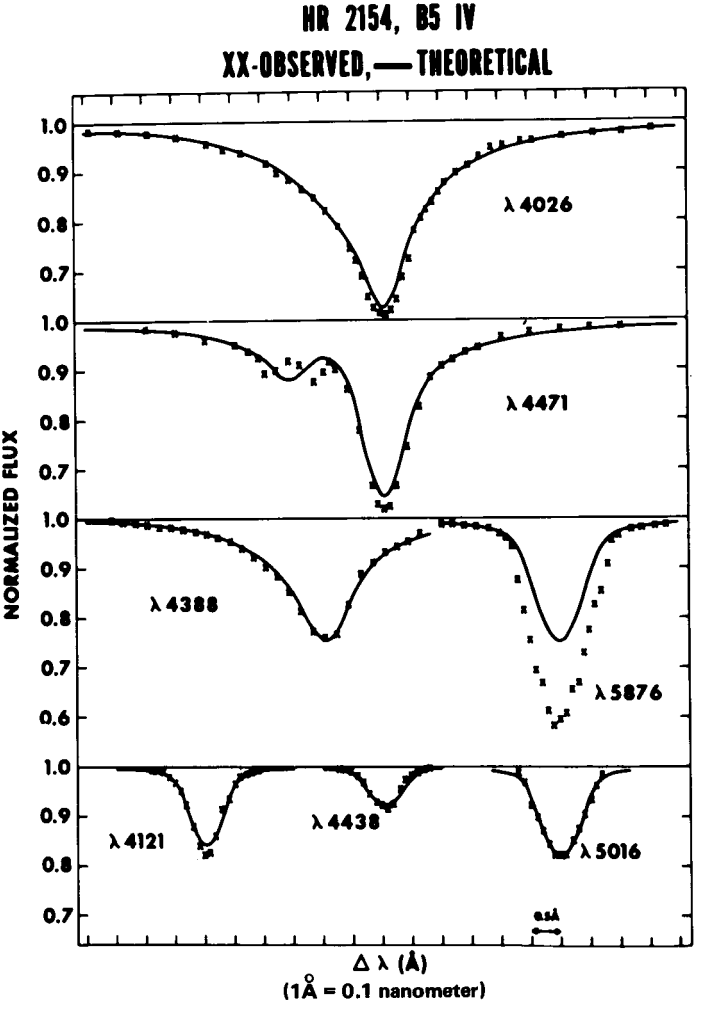

Figure 1

DERIVED He/H RATIOS

STAR	SPECTRAL TYPE	N(He)/N(H)
π CETI	B7 V	.11
HR 2154	B5 IV	.11
ι HERCULIS	B3 V	.11
γ PEGASI	B2 V	.10
HR 1861	B1 V	.11
υ ORIONIS	BO V	.10
		$\langle N(He)/N(H) \rangle = .106$

Figure 2

ABSOLUTE ULTRAVIOLET STELLAR FLUXES

Dennis Evans

In order to understand physics of stars, we need to know the total amount of radiation coming from them. This is also needed to calibrate orbiting astronomical observatories.

So, for both of these reasons, a study was begun to calibrate the ultraviolet spectra of several stars to within an absolute accuracy of ± 10 percent. The ± 10 percent was selected because this will allow clear distinction between different models; also, it is very close to the ultimate limit, which is probably only 3 percent, or something about this, because there are so many calibration transfers that must be made in order to observe a star in the ultraviolet.

The instrument selected to observe these stars, which was already operational as a payload here at Goddard for rocket astronomy, was known as the UVR. It is a 13-inch telescope with a scanning grating that puts the ultraviolet light on to three photomultipliers covering the spectral range from 115 nanometers (1150 angstroms) to the visible at 415 nanometers (4150 angstroms).

The calibration for this payload was carried on over in building 21, in the laboratory for optical astronomy; we illuminated the telescope with a beam of light in a vacuum that was uniform to within ± 10 percent over the aperture of the telescope. We mapped this beam, and we used an average of 75 percent of the energy entering the telescope to determine the levels of light entering the telescope. Our absolute references are traceable to the Bureau of Standards through thermopiles that we used to measure the flux at 253.7 nanometers (2537 angstroms) from a low-pressure mercury lamp.

We used sodium salicylate, and assumed that it is a constant quantum-efficiency detector over the range of note; from the range 250 nanometers (2500 angstroms) to the visible, we have used tungsten iodide lamps that have been calibrated by the Bureau of Standards. Right now the Bureau of Standards is in the process of calibrating some diodes over the region of

115 to 245 nanometers (1150 to 2450 angstroms), so that within the next two or three months we will no longer have to depend on the constant quantum-efficiency assumption of sodium salicylate. However, within 10 percent, this already seems to be a very reasonable assumption.

The rocket program was initiated with four rocket payloads, each rocket to observe four stars, continuing until satisfactory calibration was achieved.

The first rocket (4.251) was launched in March 1969 and observed the first target only; an attitude-control system failure prevented observation of the three other stars. The star observed was Alpha Leonis. I might add that the first payload was not recovered – it came apart at parachute deployment, and the telescope was lost.

The second payload (4.525) was launched in December 1969 and, because of a similar attitude-control system failure, observed no stars. However, it wasn't a total failure, because we recovered the payload and have flown it again.

The interesting thing to note is that the postflight calibration of this otherwise failure was 5 percent less on the average than the preflight calibration, indicating relatively no change in calibration during the flight.

The third flight (13.041) last October observed four stars: Alpha Canis Majoris, Gamma and Kappa Orionis, and a repeat observation of Alpha Leonis.

The fourth flight has been delayed at least 18 months because of the result of the third flight, which we consider very successful.

The agreement between the first observation of Alpha Leonis and the third flight appears to be within 5 percent at all wavelengths, showing the repeatability of our operations. Figure 1 shows the long-wavelength-photometer corrected data from the most recent flight. We can see features in the hydrogen Balmer series, features such as magnesium 2, and many other features which appear real; they are slightly above noise levels which will be identified later.

The ground-based observations by Aller had been normalized to other ground-based observations to show reasonable comparison in the visible for our calibration.

The star was so bright, in fact, that it went offscale at least two positions; by reducing other telemetry records, we will show peaks at approximately the positions indicated by the horizontal lines. Now when you integrate at wide dispersion above 370 nanometers (3700 angstroms), you get a value approximately half the peak. In Figure 2, which shows the same star, you see what looks like a disagreement but is merely integration across these many lines.

Here we have the same star, Alpha Canis Majoris, covering from the range of 120 nanometers (1200 angstroms) to the visible, being compared to the observation of Carruthers, which was a wideband observation in this region, and to the observations of Stecher, using a similar type payload. Our error flags are typical, about ± 10 percent, and show a clear separation from values determined by Stecher at 170 and 300 nanometers (1700 and 3000 angstroms).

There is also a model atmosphere showing that we have to account for items other than hydrogen and helium in the atmosphere in order to fully understand the model. There is no question that the disagreement between the model and the observation is real.

Figure 3 shows an observation of Alpha Leonis taken on the first rocket flight. We have the most recent values, determined by Oke in 1969 at Mt. Palomar. We have a model that I use as 12,000 kelvins which, if based on the spectrum longward of 300 nanometers (3000 angstroms), should be 13,500 K – but, in either case, the observational data are considerably below the model.

Several wideband observations in the ultraviolet indicate a generally good fit to all the UVR data, but the error at 137.5 nanometers (1375 angstroms) is much higher, again, than the 10-percent error by which we assign in this region. Based on the observations of the sun by Don Heath, reported earlier today, I wouldn't be surprised to find that some of this error at least is due to variations in the star and not to differences in calibration.

We have now calibrated OAO-A2 on the basis of the Alpha Leonis data and the Alpha Canis Majoris data, and shown between the two rocket flights we produce a calibration that varies ± 5 percent between the two rocket flights. This is within the goal that we were striving for.

We have much work left to do: we have to continue the calibration work to eliminate the use of sodium salicylate, which is common to most of the observations. We have to search for errors in our procedure, because – although our repeatability is within 10 percent – hidden errors can easily get you out of that range. We have to continue with the detailed spectral analysis of all the features we have observed, and we have to consider the results of all this in preparing for the fourth flight, which will probably be in about 18 months.

MEMBER OF THE AUDIENCE:

Are your ultraviolet reference standards identical to or different from those of the other observers to which you referred?

EVANS:

We have some that are common to all of them; we don't have all common. The choices were not made because these were ideal stars to use as standards; they were made because the trackers available for the sounding rockets demand that you point at the brighter stars.

MEMBER OF THE AUDIENCE:

My question relates to your laboratory standards.

EVANS:

Well, Caruthers was independent, and the ones done in England were independent; some of them use sodium salicylate. Andy Smith's was done at Goddard, but he did it completely separately, although he used the same facilities. Stecher's and mine were calibrated in the same facilities but using different techniques, almost completely different techniques. So there is not complete independence amongst all of the observers. There are considerable differences in technique, and there is some independence, but it is not complete; I think we can probably trace most of it back to the Bureau of Standards, too – but that, instead of making it independent, ties it more together.

MEMBER OF THE AUDIENCE:

When you talk of the Bureau of Standards, you mean the tungsten-quartz-iodine are in there?

EVANS:

Both quartz-iodine lamps, and now diodes, which are being calibrated from about 115 to 245 nanometers (1150 to 2450 angstroms).

MEMBER OF THE AUDIENCE:

My question was more on quartz-iodine: are they NBS lamps or Eppley lamps?

EVANS:

They are NBS lamps.

MEMBER OF THE AUDIENCE:

And what is their case history?

EVANS:

We use quartz-iodine lamps as a relative standard to show shape rather than absolute intensity. We based the absolute references to thermopiles, which were traceable to Eppley and then to the Bureau of Standards.

DR. PIEPER:

I think we will have to go on from here at this point; if you want to discuss the details of lamps, you can have a cup of coffee over it in a little while.

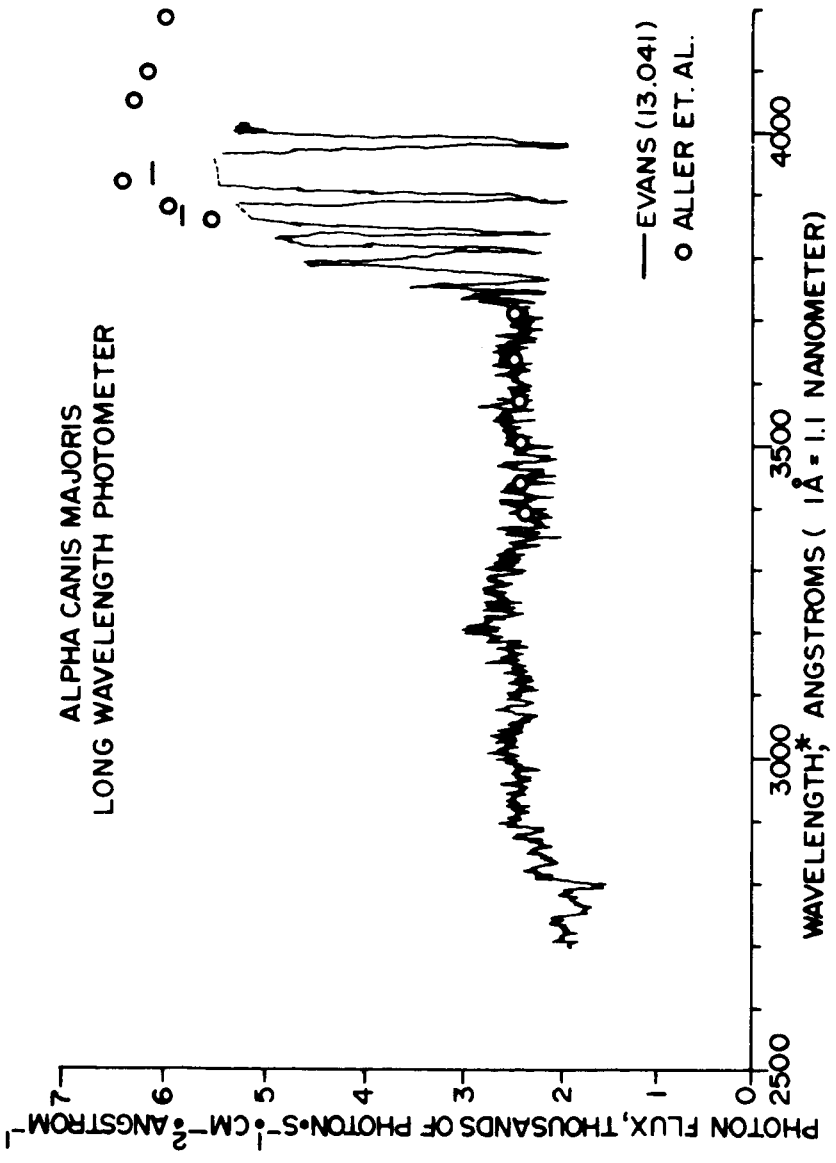
ALPHA CANIS MAJORIS
LONG WAVELENGTH PHOTOMETER
EVANS (13.041)
O ALLER ET. AL.
PHOTON FLUX, THOUSANDS OF PHOTON•S⁻¹•CM⁻²•ANGSTROM⁻¹
WAVELENGTH,* ANGSTROMS (1Å = 1.1 NANOMETER)
0
1
2
3
4
5
6
7
2500
3000
3500
4000

Figure 1

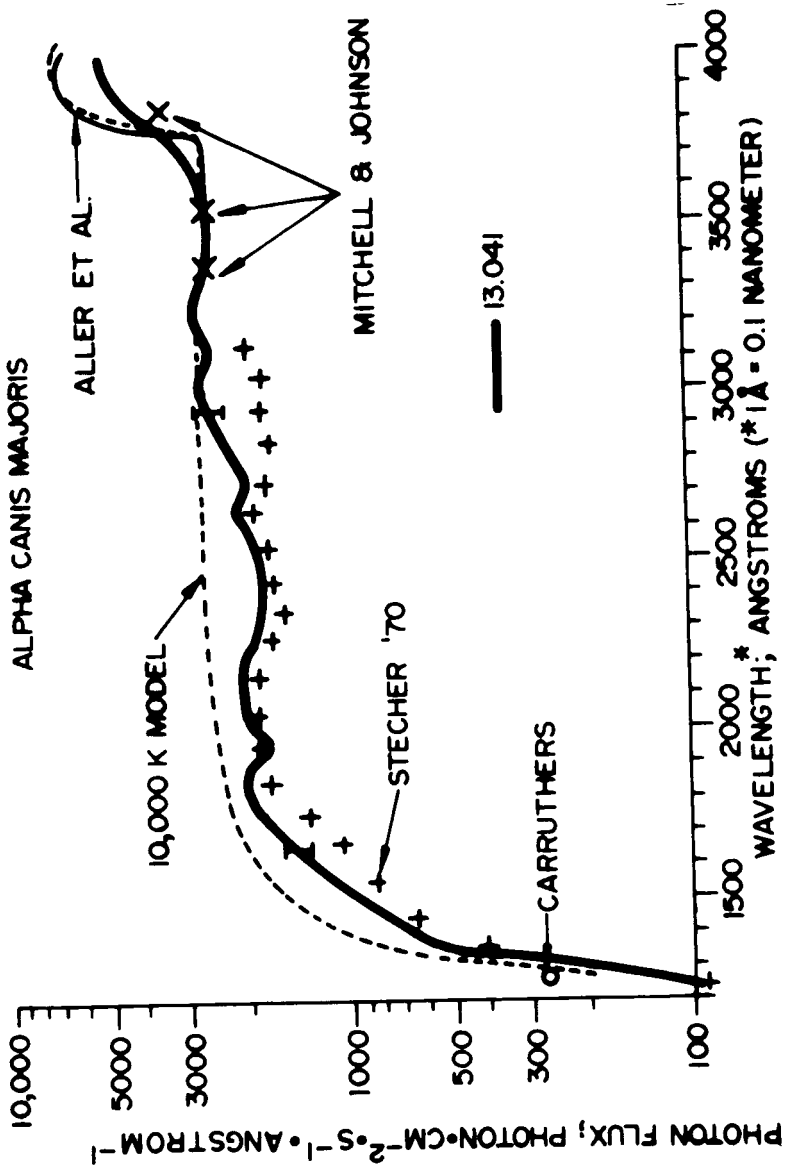
ALPHA CANIS MAJORIS
ALLER ET AL.
MITCHELL & JOHNSON
13.041
10,000 K MODEL
STECHER '70
CARRUTHERS
PHOTON FLUX; PHOTON•CM⁻²•S⁻¹•ANGSTROM⁻¹
10,000
5000
3000
1000
500
300
100
1500
2000
2500
3000
3500
4000
WAVELENGTH; * ANGSTROMS (*1Å = 0.1 NANOMETER)

Figure 2

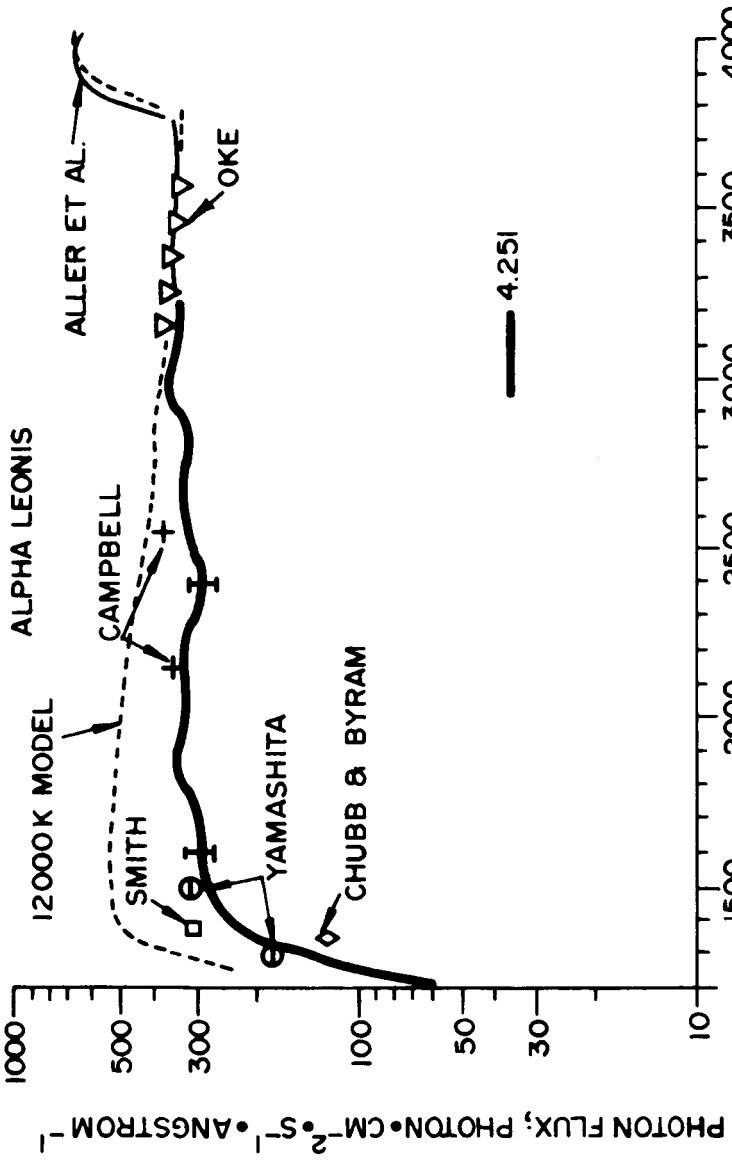
ALPHA LEONIS
12000K MODEL
CAMPBELL
SMITH
YAMASHITA
CHUBB & BYRAM
ALLER ET AL.
OKE
4.25I
PHOTON FLUX; PHOTON•CM⁻²•S⁻¹•ANGSTROM⁻¹
1000
500
300
100
50
30
10
1500
2000
2500
3000
3500
4000
WAVELENGTH; ANGSTROMS (*1Å =0.1 NANOMETER)

Figure 3

THE GUM NEBULA

Dr. John Brandt

In 1952, a certain amount of excitement was generated in the astronomical community by Gum's discovery of a rather large H_{II} (ionized hydrogen) region in the southern hemisphere. Gum continued his work and in 1956 concluded that "Obviously the sun is near to the borders of this H_{II} region, and may even be just inside." Interest was rekindled, but soon died away. Now in 1970 the Gum nebula has again become a topic of considerable interest.

I am only one quarter of the team responsible for this work; other members include Ted Stecher of Goddard, Dave Crawford of the Kitt Peak National Observatory in Tucson, Arizona, and Steve Maran of Goddard. Technical details of this work can be found in Astrophysical Journal Letters, 163, L99 (1971).

Gum's discovery was so exciting because the nebula that he discovered was huge. The projected dimensions in the sky were approximately 1.05 rad by 0.52 rad (60 degrees by 30 degrees). The appearance of the nebula is shown in Figure 1, which is a mosaic composed of individual photographs taken with an H-alpha interference filter. The individual photographs are about 0.14 rad (8 degrees) across.

Gum also noted that there were two very bright stars, Gamma Velorum and Zeta Puppis, in the same area of the sky. He considered that this H_{II} region was ionized by the ultraviolet radiation from these two stars, and maintained in the style of the classical Stromgrem sphere of the kind that Stromgren first discussed from a physical viewpoint in 1939.

In 1952, certain things were known about this nebula: for one thing, we knew how bright the general region was in H-alpha (emission measure). Observations continued to come in. Rocket observations obtained at Goddard of the Lyman-alpha absorption on both Gamma Velorum and Zeta Puppis gave us the column density of hydrogen between us and these stars (hydrogen measure). A very strong nonthermal radio source discovered in the same direction – radio source Vela X – is undoubtedly a

supernova remnant. And, still more recently, a number of pulsars were discovered in the Gum nebula. One is called the Vela pulsar, which we have good reason to believe is in the middle of this nebula, and there are three pulsars on the other side. These data determine the column density of electrons in the nebula (dispersion measure).

So we have a substantial amount of physical information, and we could construct a fairly detailed model of this nebula if we knew one additional item: namely, the distance from the sun to the center of this nebula, which we take as the distance to the star Gamma Velorum.

This determination has been carried out by us. The raw observations were obtained by Dave Crawford at the Cerro Tololo Inter-American Observatory in Chile. Multicolored photometry was done on a companion to Gamma Velorum itself and on a little cluster of stars around it. The distance was determined to be 142×10^{17} meters (460 parsecs), which we consider accurate to about 10 percent.

With this melange of information, we can construct a model of the Gum nebula, which is shown in Figure 2. The distance from the sun to the edge of the nebula is calculated from the local hydrogen density from radio-astronomy studies, and the hydrogen measure. The rest of the model more or less works itself out; it is an ionized region with an average density and an average square density, and these two things together allow us to compute a clumpiness index. In other words, if all the material in the nebula were put into clumps at one density, those clumps would occupy only one sixty-fifth of the total volume.

The general picture that emerges is a huge clumpy ionized region almost 308×10^{17} meters (a kiloparsec (or 3000 light years)) across, with the Vela pulsar – the Vela X supernova remnant – along with the stars Gamma Velorum and Zeta Puppis in the central region. It is at this point that things become interesting. There was a certain temptation to stop the research at this point because we already had a mighty fine H_{II} region indeed, and this was a valid piece of work in itself. But the fun part is yet to come.

We know, for a region this size, what it would take to ionize it and to keep it ionized; this was worked out by Stromgren in 1939 and has been

updated from time to time – for example, in Spitzer's 1968 book. We can check for a region of our rms density with one of the brightest known blue stars, and ask what size of an H_{II} region could be maintained in the area. The answer is 30.8×10^{17} meters (100 parsecs), which doesn't sound too far off from 142×10^{17} meters (460 parsecs), but it is. The size of an H_{II} region goes up as the cube root of the number of equally bright stars. If we were to attempt to ionize and maintain the entire Gum nebula as a Stromgren sphere, we would need approximately $(4.6)^3 = 97$ of the brightest known stars. We can find at most three such stars, so we are low by something like an order of magnitude or more in finding the energy supply to maintain the Gum nebula as a Stromgren sphere.

We do have additional clues, however; the Vela pulsar has been observed to be decelerating, and its age has been estimated at 11,000 years. The other piece of information is that, since we know the size of this region, we know the energy requirements for ionizing it. It comes out to be about 10^{45} joules (10^{52} ergs), which is a lot of energy! Such amounts of energy are found shortward of the Lyman limit only in a supernova outburst.

When you sit back and draw the pieces of this puzzle together, there is strong evidence for something like the following picture: About 11,000 years ago there was one really bright supernova (approximately equal to the quarter moon in brightness) in the southern hemisphere. This supernova produced the remnant which we are now observing as the Vela X radio source. It produced a neutron star, which is now rotating and which we observe as the pulsar. It also produced a tremendous burst of ionizing radiation (perhaps particles, but let's pretend it is radiation) which in turn produced an ionized region roughly 308×10^{17} meters (one kiloparsec, or 3000 light years), across. As far as we know, this is an entirely new class of phenomenon, where an ionized region exists but the source that ionized it is gone. We have suggested the name "fossil Stromgren sphere" for this new class of phenomenon.

The work, as you can appreciate, is rather new. We have not had time to work out all the implication. It may be important in the energy balance of the interstellar gas, and it should be an important feature for determining the gross appearance of spiral galaxies.

MEMBER OF THE AUDIENCE:

Is this the little-bang theory?

DR. BRANDT:

Well, it depends on your reference frame. Locally it is the big one, but it is not cosmologically the big one. But I would say that it is a big enough bang, and there are a lot of things here that one can have a lot of fun with (not being a professional archeologist!) You could wonder what happened 11,000 years ago: if there were any paintings –

MEMBER OF THE AUDIENCE:

If there were just some Chinese astronomers.

DR. BRANDT:

Right! (Laughter.) But in the southern hemisphere. This really gets a little touchy. But something like that may in fact turn up some day: we simply don't know.

DR. PIEPER:

At this point in time, let's take a 10-minute coffee break, and we will re-assemble at 20 after the hour.

Figure 1

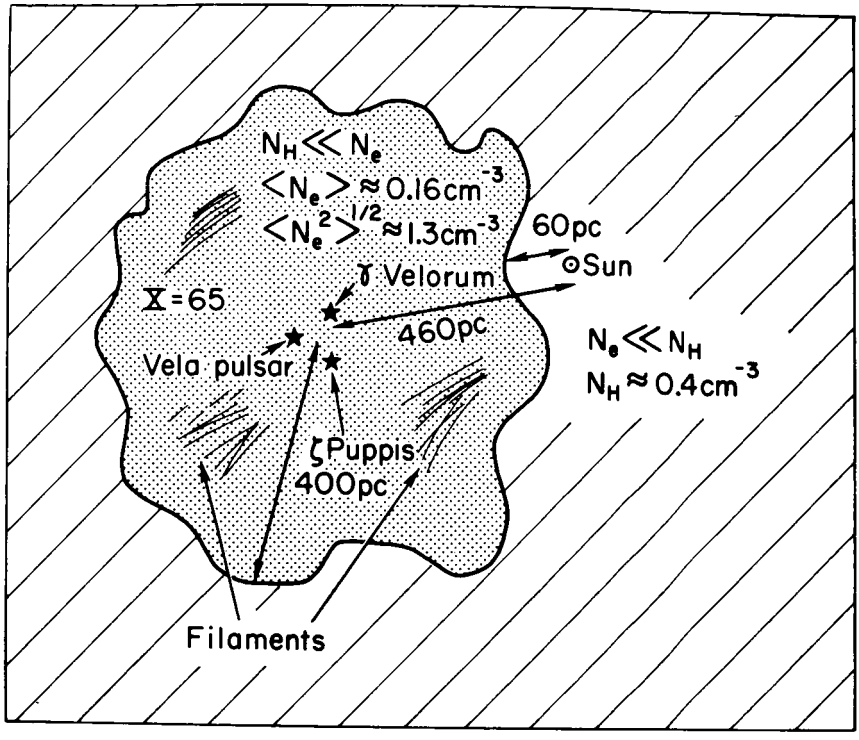
$N_H \ll N_e$
$\langle N_e \rangle \approx 0.16 cm^{-3}$
$\langle N_e^2 \rangle^{1/2} \approx 1.3 cm^{-3}$
60pc
⊙Sun
γ Velorum
X=65
460pc
$N_e \ll N_H$
$N_H \approx 0.4 cm^{-3}$
Vela pulsar
ζPuppis
400pc
Filaments

Figure 2

SPECTRAL CLASSIFICATION OF X-RAY SOURCES

Dr. Peter Serlemitsos

Over the past few years, considerable effort has been directed toward the study of cosmic X-ray sources. X-rays as a means of conveying information from a source are particularly interesting, because they relate to high-energy phenomena. Most of the information, however, is to be found in high-resolution data. Such is not the nature of the available data at this stage of X-ray astronomy. For this reason, aside from statistical estimates, significant astrophysical evidence resulting from the study of X-ray sources has been possible for those few cases in which high-resolution information about a source could be inferred from observations in the optical and radio regions of the spectrum.

The outstanding contribution that X-ray astronomy has made in astrophysics has resulted from such coordinated observations of the Crab nebula and its associated pulsar. It now appears that it will not be possible to identify many of the distant X-ray sources with optical and radio counterparts; in such cases, the X-ray data will have to stand on their own.

There is evidence that certain conclusions about the nature of a source are possible, based on low-resolution information alone: for example, energy spectra of known X-ray sources are primarily continua. Measured shapes generally fall in one of two categories, a power-law or an exponential in photon energy. There is supporting evidence that these two spectral forms are representative of two X-ray-generation processes: synchrotron losses of relativistic electrons in large-scale magnetic fields, and collisional losses in a hot plasma, respectively.

We have sought to extend such a classification to cover other potential spectral features in the region of a few keV and above; such are, for example, emission lines due to the heavy elements in the plasma, absorption effects at the lower energies, and changes in the spectral parameters. To achieve this, we have developed special detectors in an effort to optimize the performance of available instruments, and have designed experiments with the accuracy needed to accomplish this objective. In a recent rocket flight, we measured the energy spectra of X-ray sources in the Cygnus region; our preliminary analysis of the data indicates that substantial

spectral differences among sources exist, that may provide the basis for a detailed spectral classification. Such a classification would of course be phenomenonological until physical models tie it to the nature of the X-ray emission and the intervening medium.

To demonstrate these differences we will present the spectra of two sources. Figure 1 shows the number spectrum measured for Cygnus X-2, as well as the calculated response of our detector to a spectrum of the form

$$\frac{dN}{dE} \sim \frac{(e^{-E/kT})}{E}$$

where E is the photon energy. This spectral shape approximates continuum emission from an isothermal plasma at a temperature T. The good agreement between the calculated and the measured responses confirms previous measurements for this source that have shown a spectrum of this type. This illustration simply establishes a standard by which to compare the spectrum we have obtained for another Cygnus source – Cygnus X-3 – shown in Figure 2. The drawing includes the calculated response of the previous figure, for purposes of comparison. The spectrum of Cygnus X-3 does not fit a simple description; specifically, the large photon deficiency and other features seen at the lower energies are consistent with absorption. A complete understanding of this phenomenon will be possible when more sources have been included in the sample.

If, however, we assume that the absorption takes place in the interstellar medium, our measurement implies some 10^{23} hydrogen atoms per square centimeter in the line-of-sight to the source, provided that the heavier elements primarily responsible for the absorption of our energies have normal abundances. This large amount of matter could be reconciled with the fact that Cygnus X-3 lies almost directly along the densest portion of the Cygnus spiral arm of the galaxy. It has been estimated that sources associated with this arm are at distances around 925×10^{17} meters (3 kiloparsecs); this distance estimate results in a density for the Cygnus arm about one order of magnitude higher than the average density of the galactic disc. Thus we see that the extension of this sort of measurement to many more sources will result in increased knowledge not only of the sources themselves but of the interstellar medium as well.

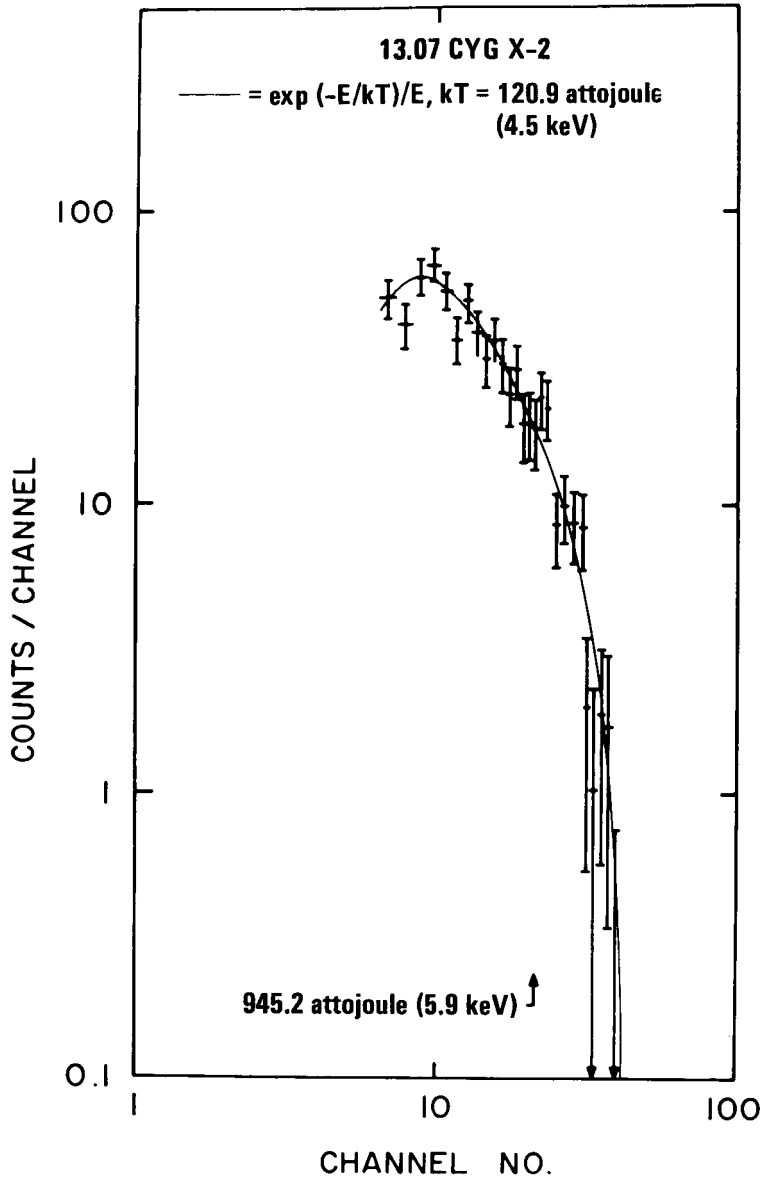
13.07 CYG X-2
—— = exp (-E/kT)/E, kT = 120.9 attojoule
(4.5 keV)
100
10
1
0.1
COUNTS / CHANNEL
945.2 attojoule (5.9 keV)
1
10
100
CHANNEL NO.

Figure 1

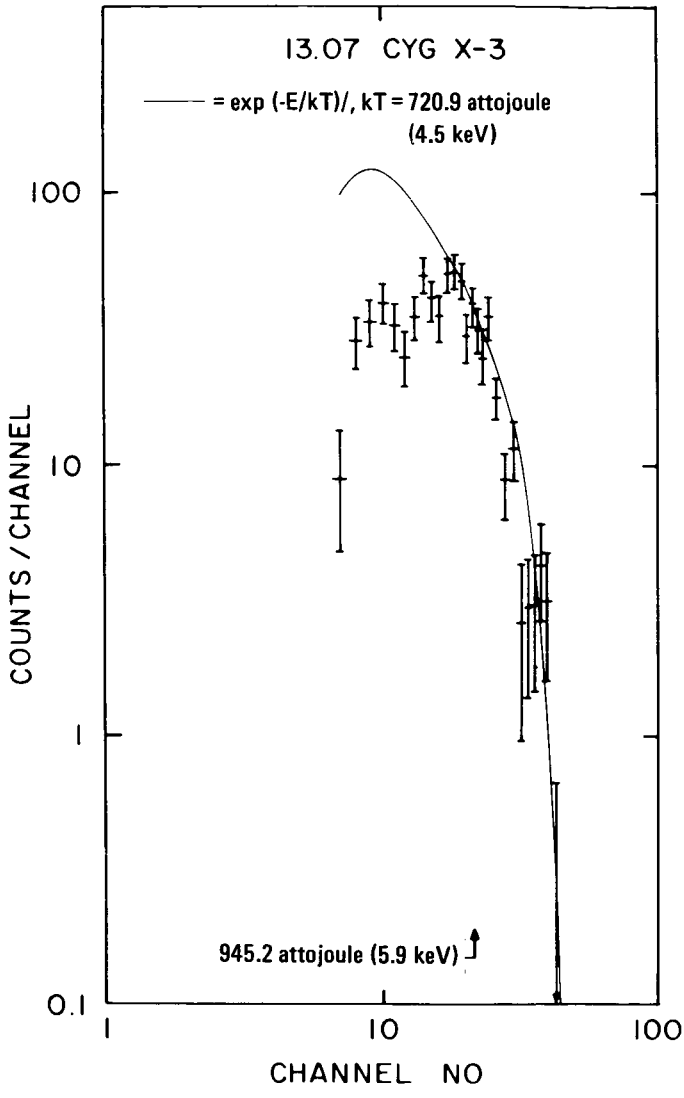
13.07 CYG X-3
——— = exp (-E/kT)/, kT = 720.9 attojoule
(4.5 keV)
100
10
1
0.1
COUNTS / CHANNEL
945.2 attojoule (5.9 keV)
1
10
100
CHANNEL NO

Figure 2

SPECTRAL STRUCTURE OF THE DIFFUSE X-RAY SKY

Dr. Elihu Boldt

DR. PIEPER:

The next paper, which concerns the spectral structure of the diffuse X-ray sky, was prepared by Dr. Elihu Boldt. But Dr. Boldt is unable to be here, so it will be given by Dr. Stephen Holt.

DR. HOLT:

Almost all of the X-ray astronomy performed from rockets is devoted to the study of discrete X-ray stars. But there is an overall diffuse X-ray celestial flux as well. In fact, it is a huge diffuse flux, as I will show you in a moment.

It is hard to study a diffuse component of any kind of radiation, because you must have an unambiguous way of separating what you are looking for from the internal detector background. So, in order to do this kind of experiment, our group has flown detectors with two rather unusual features (in addition to having low internal background, of course): First, we modulated the 0.3- to 3.2-femtojoule (2- to 20-keV) X-ray field-of-view between 0.122 and 0.183 steradians (400 and 600 square degrees), so that we could separate out that portion of the data that varied as the solid angle from the unchanging detector background. Second, we utilized two layers of counters, one above the other and acting as an absorber in front of it, so that we could demand consistency between the spectral shape deduced from pulse-height analysis and that deduced from the range measurement possible with such a two-layer system. We devoted portions of two separate rocket flights to the study of the diffuse flux this way, and the results from both agree.

We found, first, that the count rate which was proportional to the solid angle of the detector aperture was uncorrelated with galactic latitude, to a precision of about 5 percent. In other words, the 0.3 to 3.2 femtojoule (2- to 20-keV) diffuse flux is essentially isotropic, so that it must be extragalactic in origin.

The accompanying illustration should give you a feeling for the kind of energy flux in this sky background. What is plotted here is the response of a completely omnidirectional detector: in other words, one with a solid angle of 4π steradians, in units of energy flux per unit of energy interval, as a function of photon energy. Curve A is the diffuse flux that we measure in this experiment. For purposes of comparison, we have also plotted what this omnidirectional detector would see from the quiet sun – thermal emissions at a temperature of something like a few million kelvins – and the measured spectra from the two strongest X-ray sources in the sky, Scorpio X-1 and the Crab nebula. In fact, both of these spectra were obtained in the same two rocket flights in which we did the diffuse background experiment.

Sco X-1 is a thermal source like the sun, but at a temperature of about 60 megakelvins; of course, all thermal continua exhibit the characteristic fall-off at energies above the temperature of the source. The Crab nebula, on the other hand, has a spectrum that is very well represented by a power law, even out to energies of a few hundred kilovolts. This is characteristic of a different type of emission mechanism: synchrotron radiation. And, in fact, the Crab has the flattest spectrum measured from any discrete source to date.

Now, as you can see from the illustration, the diffuse background intensity we measure is about an order of magnitude larger than that from Sco X-1 in the range 0.3 to 3.2 femtojoule (2 to 20 keV) and is about a factor of 4 larger than all the discrete sources in the galaxy added together. Furthermore, the shape of the spectrum below 3.2 femtojoule (20 keV) is flatter than that of any known source, so that – even if we could energetically account for the sky background by superposing the outputs of normal galaxies (and we can't, by at least an order of magnitude) – the spectral shape is totally unlike anything we might expect from the superposition of such discrete sources. So we are tentatively led to the conclusion that the diffuse flux is not only extragalactic, but probably intergalactic in origin as well. The consensus is that the most likely candidate for the emission process in this case is Compton scattering of 0.052-rad (3-degree) blackbody photons off relativistic electrons leaking out of galaxies.

If we try to tie our data to data at higher energies obtained from balloons, it is obvious that a rather severe spectral break occurs at something like 3.2

femtojoule (20 keV). Now, of course, we have to convince ourselves that this effect is not due to systematics in our experiment, or the balloon experiment, or both experiments. Luckily, we have some data that fill in the gaps – data from the OSO 3 satellite – and, in fact, things are reconciled rather nicely, because our best-fit power law is most heavily weighted by the lowest energy data. If we keep that in mind, there is essentially complete consistency between all the data in the figure.

The surprising thing about this reconciliation is that the net break in the spectral index is about unity, whereas we would expect a break of exactly one-half power theoretically from any single power-law spectrum that loses energy by either the Compton or the synchrotron process. So, if we want to save the model, we must conclude that there must be an intrinsic break in the spectrum of the electrons leaking into the interstellar medium.

To sum up, our rather modest-looking piece of data leads us step by step to a fairly consistent picture of what the diffuse background in this energy range is like. Its isotropy tells us that it must be extragalactic; inconsistency in total energy and in spectral shape with the emission from discrete galactic objects tells us that it is probably intergalactic. And, if we adopt inverse Compton interactions of blackbody photons on intergalactic electrons as the most likely candidate mechanism, the magnitude of the X-ray spectral break-even tells us that the electrons leaking out of galaxies must, on the average, have an intrinsic break in the spectra that they are born with.

MEMBER OF THE AUDIENCE:

How do you account for that intrinsic break in the electron spectra?

DR. HOLT:

I don't know: it would have to be a break in acceleration. In other words, this could not be a break that arose out of energy loss by these electrons in the galaxies before they left them, because that would give you only one-half power. So, in the process which accelerates these galactic electrons before they leak out, there must be something about the acceleration process that produces such an intrinsic break.

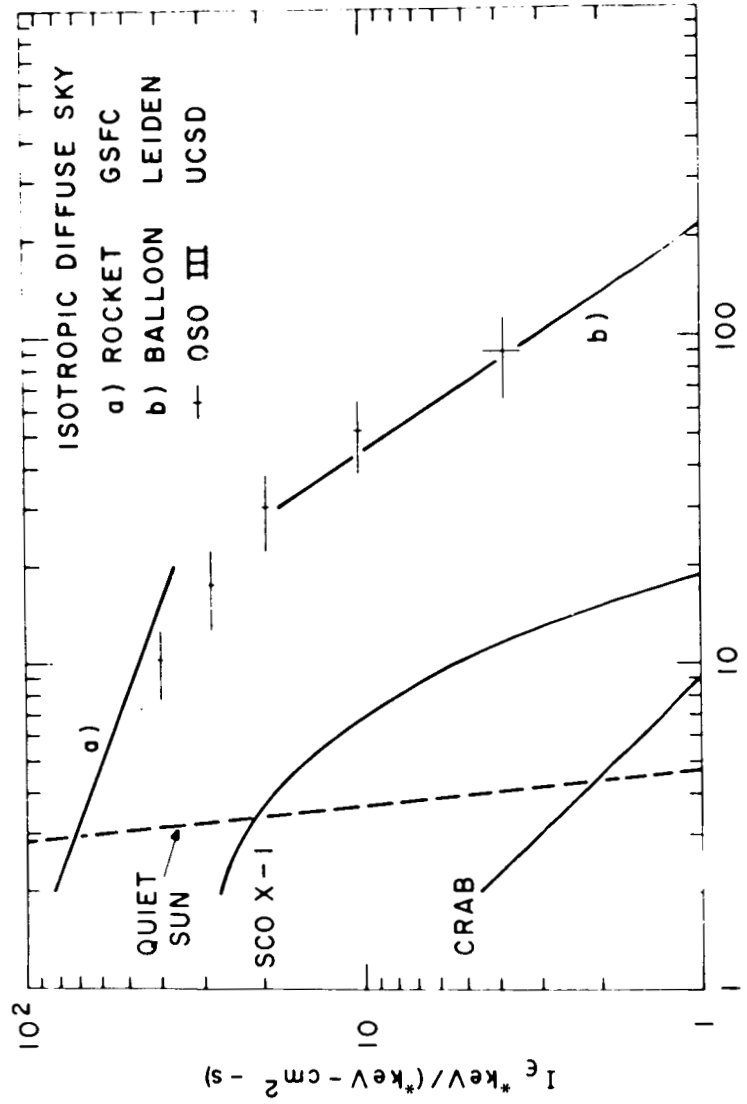
ISOTROPIC DIFFUSE SKY
a) ROCKET GSFC
b) BALLOON LEIDEN
OSO III UCSD
a)
b)
QUIET SUN
SCO X-1
CRAB
10^2
10
1
1
10
100
I_ϵ *keV/(*keV - cm^2 - s)
ϵ (keV*) *(keV = 1602 femtojoule)

Figure 1

GAMMA-RAY FLUXES

Dr. Donald Kniffen

The objective of our experimental gamma-ray program at Goddard has been to design and develop the best detector within the state-of-the-art for the study of greater than 3.2 picojoule (20-MeV) gamma rays. Our investigations of these rays are prompted by the desire to look for the 11.2-picojoule (70 MeV) gammas from the decay of neutral pions, expected to be a most important producer of celestial gammas.

Figure 1 is a schematic representation of a second generation of digitized wire-grid spark-chamber detectors developed at Goddard for balloon-borne gamma astronomy. Major features of this particular detector are a large half-meter by half-meter active area; a large acceptance angle, allowing extended portions of the sky to be examined simultaneously; good angular resolution, within this solid angle, on the arrival direction of the observed gamma rays; satellite adaptability; a positive picture-type identification of the observed gamma rays (they must be observed in a large background of other types of cosmic-ray particles); and a digital readout and memory system that provide the data in a format readily adaptable to computer processing.

Most of the data reported here was obtained from an analysis in which each picture-type gamma-ray event is recognized and processed completely by computer. The data I would like to report were obtained by a balloon flight from Australia, designed to search for gamma-ray emission from the galactic plane in the direction of the galactic center. The impetus for this flight was a remarkably high intensity of greater than 16.02 picojoule (100 MeV) gamma rays detected by the OSO-3 experiment of Clark, Garmire, and Kraushaar in 1968. These gamma rays were observed to be emanating from the galactic disc.

Figure 2 is a plot of the OSO-3 results, with intensity plotted as a function of galactic longitude for data collected over galactic longitudes from minus 15 to plus 15 degrees.

Clearly, the intensity peaks in the direction of the galactic-center region. This high intensity was unexpected, and attempts to explain it theoretically are hampered by a lack of spectral information on angular resolution and by uncertainties in the exact intensities of the galactic gammas.

Our balloon flight was aimed at verifying the existence of the galactic gamma radiation and at providing additional information on its spectral and spatial distribution. The data from our flight indicate an excess (above background) of gamma rays from the galactic disc of 4.3 standard deviations. This is the strongest verification yet obtained of the OSO-3 observations, and the result is particularly important in view of discrepancies in experimental results reported since the original OSO-3 data were released.

Figure 3 shows the results of our analysis of the galactic-line intensity together with revised OSO-3 intensity. Here the observed integral line intensity is plotted in units of 10^{-4} cm^{-2} s^{-1} rad^{-1} as a function of gamma-ray energy in MeV. Our greater-than-16.02-picojoule (100-MeV) intensity, the black point, agrees within the errors with that reported by the OSO-3 experimenters. Also plotted here is the upper limit we obtained for greater than 8.01-picojoule (50-MeV) gammas; it should be emphasized that this upper limit was obtained from a ratio of the gammas in the 8.01- to 16.02-picojoule (50- to 100-MeV) integral to the integral number above 16.02 picojoule (100 MeV), and hence gives an upper limit to the slope of a power-law spectrum in this energy range.

Plotted against the data on this figure are the spectra that would be produced by three proposed gamma-ray production mechanisms, each normalized to our observations above 16.02 picojoule (100 MeV). The dotted line represents the spectrum expected from the decay of neutral pions produced by nucleon-nucleon collisions in interstellar space; this is a spectrum derived by Stecker. The dashed line – the steeper line in the figure – denotes the spectrum expected from the scatter of interstellar photons by energetic cosmic-ray electrons, assuming that the electron-energy spectrum in the galactic-center region is the same as that observed in the vicinity of the earth; this is the so-called inverse Compton-scattering effect. The dash-dot curve in the middle is a combination of the other two, recently proposed by Stecker. Clearly the data appear to rule out the inverse Compton spectrum – the steeper spectrum (dashed line) – but it is not definitive on the other two.

To summarize, then, the data present a solid verification of the galactic-disc gamma radiation first observed by the OSO-3 gamma-ray experiment. It places a limit on the angular width of the observed line intensity of plus or minus 6 degrees in galactic latitude, and it indicates a probable flattening

of the energy spectrum below about 16.02 picojoule (100 MeV). Further data are needed on the spectral and spatial distribution of the gamma radiation to positively identify the source mechanisms, and we hope that our SAS-B gamma-ray experiment scheduled for a fourth-quarter 1971 launch will provide some of this information. The solution of this problem will be helpful in revealing the distribution of cosmic radiation in the galaxy, and the environmental conditions that exist in interstellar space.

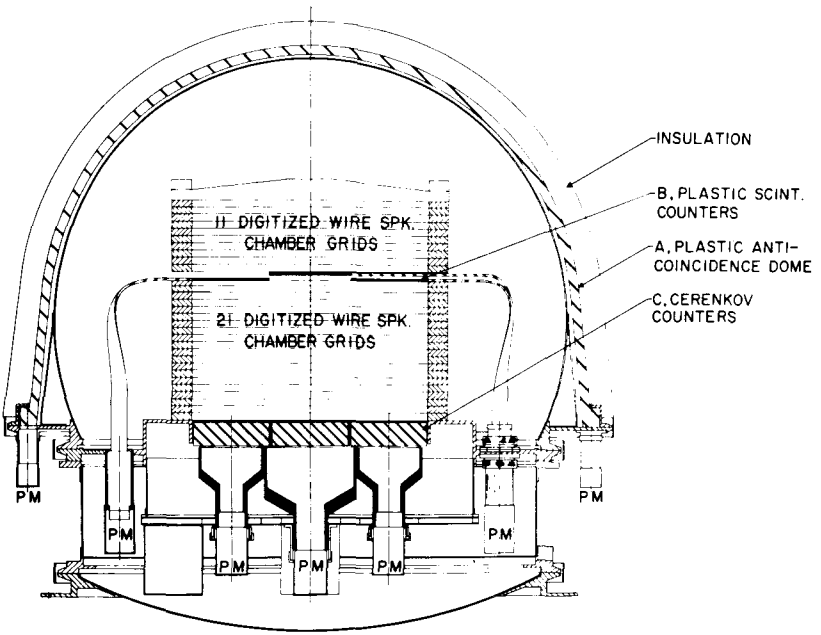

SCHEMATIC OF 1/2 x 1/2 M. DIGITIZED SPARK CHAMBER GAMMA RAY TELESCOPE

Figure 1

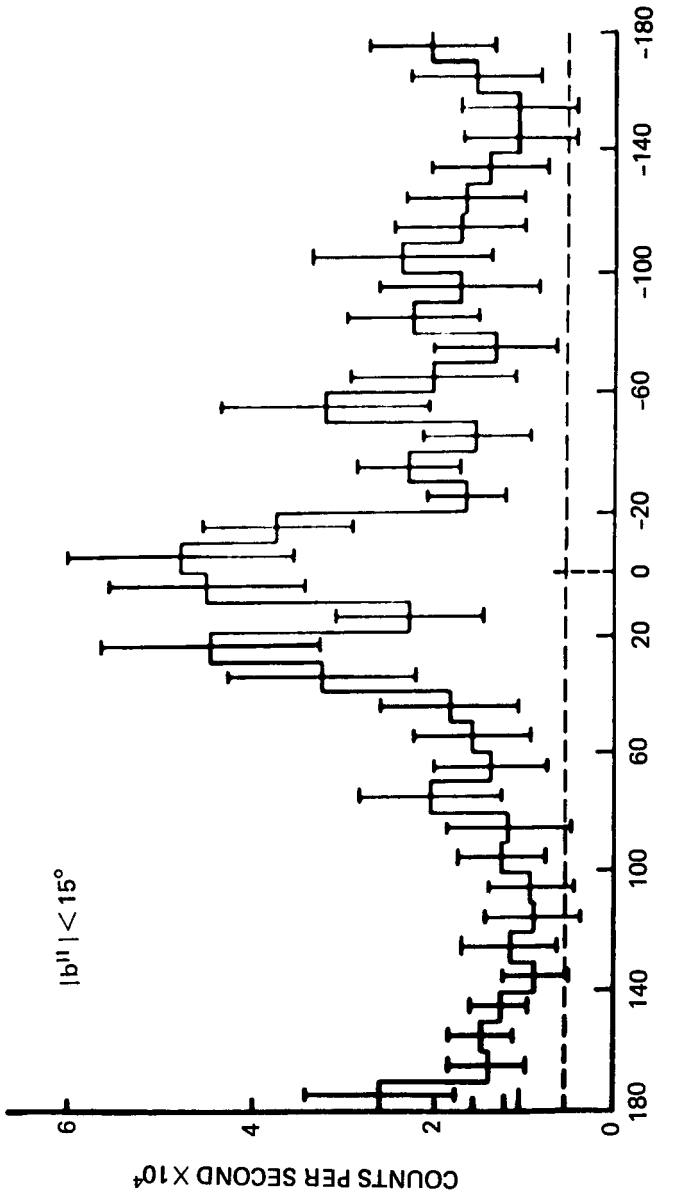
COUNTS PER SECOND X 10⁴
6
4
2
0
180
140
100
60
20
0
-20
-60
-100
-140
-180
GALACTIC LONGITUDE, ℓ¹¹
|b¹¹| < 15°

Figure 2

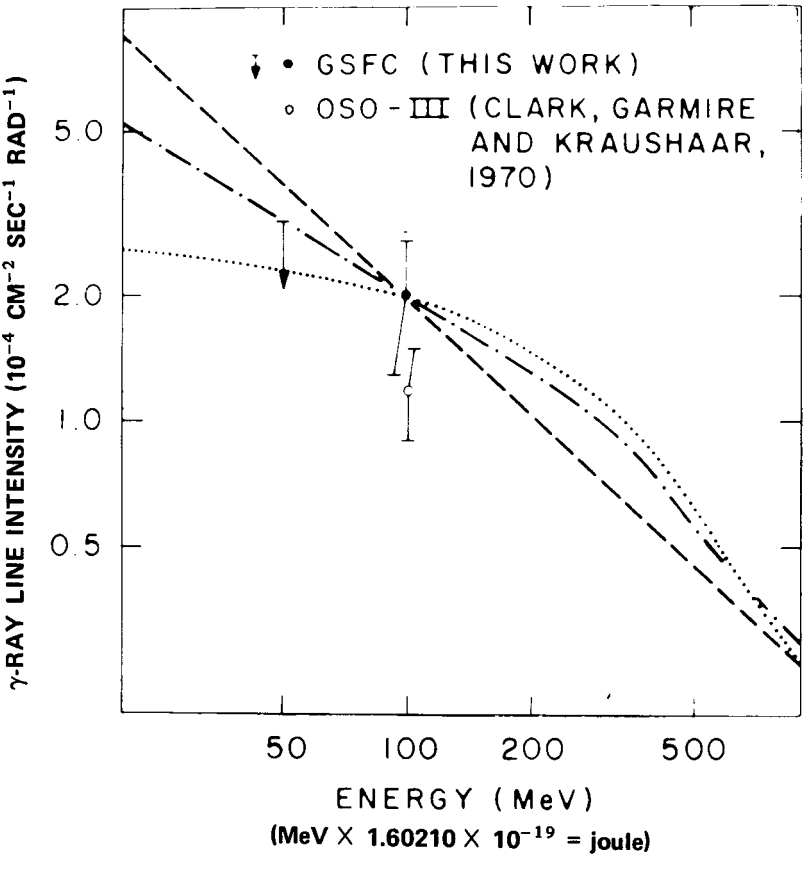
• GSFC (THIS WORK)
o OSO-III (CLARK, GARMIRE AND KRAUSHAAR, 1970)
γ-RAY LINE INTENSITY (10^{-4} CM^{-2} SEC^{-1} RAD^{-1})
5.0
2.0
1.0
0.5
50
100
200
500
ENERGY (MeV)
(MeV × 1.60210 × 10^{-19} = joule)

Figure 3

THEORETICAL IMPLICATIONS OF GAMMA-RAY ASTRONOMY

Dr. Floyd Stecker

There have been three recent successful measurements of cosmic gamma rays: the measurement just discussed by Dr. Kniffen, the famous OSO-3 measurement by Clark et al. of gamma rays above 16.02 picojoule (100 MeV), and the measurement by Vette et al. on the ERS-18 satellite experiment of gamma rays of energies particularly around 0.16 to 0.961 picojoule (1 to 6 MeV). The accompanying illustration summarizes these measurements.

As Dr. Kniffen just discussed, the gamma rays in the 8.01- to 16.02 picojoule (50- to 100-MeV) energy range are known to be primarily of galactic origin, as was found by Clark et al. The point in the figure at 16.02 picojoule (100 MeV) shows the average intensity of gamma rays observed from the galactic disc. The upper limit at 8.01 picojoule (50 MeV) is obtained from the upper limit on the spectral ratio just discussed by Dr. Kniffen, which clearly indicates a hard gamma-ray spectrum from the galactic center. Theoretical indications are that the spectrum from the galactic disc should be even harder, and is probably a pure π^0-spectrum obtained from the decay of neutral pions produced by cosmic-ray interactions in the galaxy.

The last measurement – the measurement of Vette et al. if it represents gamma rays of galactic origin – would have the intensity shown in the figure and would give a spectrum of the form shown, up to 0.96 picojoule (6 MeV). The 0.16- to 0.96-picojoule (1- to 6-MeV) measurement, however, was made with an omnidirectional detector, so the question remains as to whether those gamma rays are coming from the galaxy, as is the case with the 16.02-picojoule (100-MeV) gamma rays, or whether they are primarily extragalactic. And this is the question that I wish to try to resolve here.

If we assume that the 0.16- to 0.96-picojoule (1- to 6-MeV) gamma rays are galactic, the spectrum in the figure as I said would represent the intensity and the shape of the spectrum that would exist up to 0.961 picojoule (6 MeV). We know the upper limit on galactic gamma rays at 8.01 picojoule (50 MeV); this enables us to determine the exponent (Γ) of the flattest

possible power-law spectrum that would connect the 0.96 and 8.01 picojoule (6-MeV and 50-MeV) region. This would require a galactic gamma-ray spectrum with a power index (Γ) of 4.3 or greater in the 0.96 to 8.01 picojoule (6- to 50-MeV) energy range, and a break – a very sharp break – above 0.96 picojoule (6 MeV) of at least 3.3 powers in the energy spectrum. Now, there are only three known mechanisms that produce cosmic gamma rays of the intensities that we are discussing: Compton interactions of cosmic-ray electrons with photons in interstellar or intergalactic space; bremsstrahlung interactions of cosmic-ray electrons interacting with interstellar or intergalactic gas; and the pion-decay mechanism, the pions being produced by interactions of high-energy cosmic-ray nucleons.

None of these production mechanisms will give you a spectrum consistent with the galactic hypothesis. Indeed, the Compton mechanism would give you a spectral break of 0.5, as discussed earlier by Dr. Holt. The bremsstrahlung mechanism would give you a spectral break of 1. The electron spectrum needed here to predict the break shown in the figure would be completely ad hoc and very hard to justify on theoretical grounds.

So, the theoretical implications are that, because of the nature and intensity of the spectrum between 0.16 and 0.96 picojoule (1 and 6 MeV), this part of the spectrum must be of extragalactic origin.

Well, there is indeed an explanation of such an extragalactic flux, which I proposed and discussed here 2 years ago: namely, that these gamma rays are cosmological in origin, and that possibly are the secondary remnants of a tremendous burst of cosmic rays produced during the early stages of galaxy formation, approximately 10 billion years ago. We can see here that not only – as I discussed previously – is the spectral shape consistent with that cosmological origin hypothesis, but also that there is no galactic-origin mechanism which is consistent with the spectral data. Since I have concluded that the 0.16 to 0.96 picojoule (1- to 6-MeV) flux is extragalactic, this therefore indicates that there is a strong background of isotropic gamma rays in this energy region. This would suggest going to higher resolution detectors to help eliminate this background, in order to study any possible galactic or extragalactic point sources of gamma rays in this energy region.

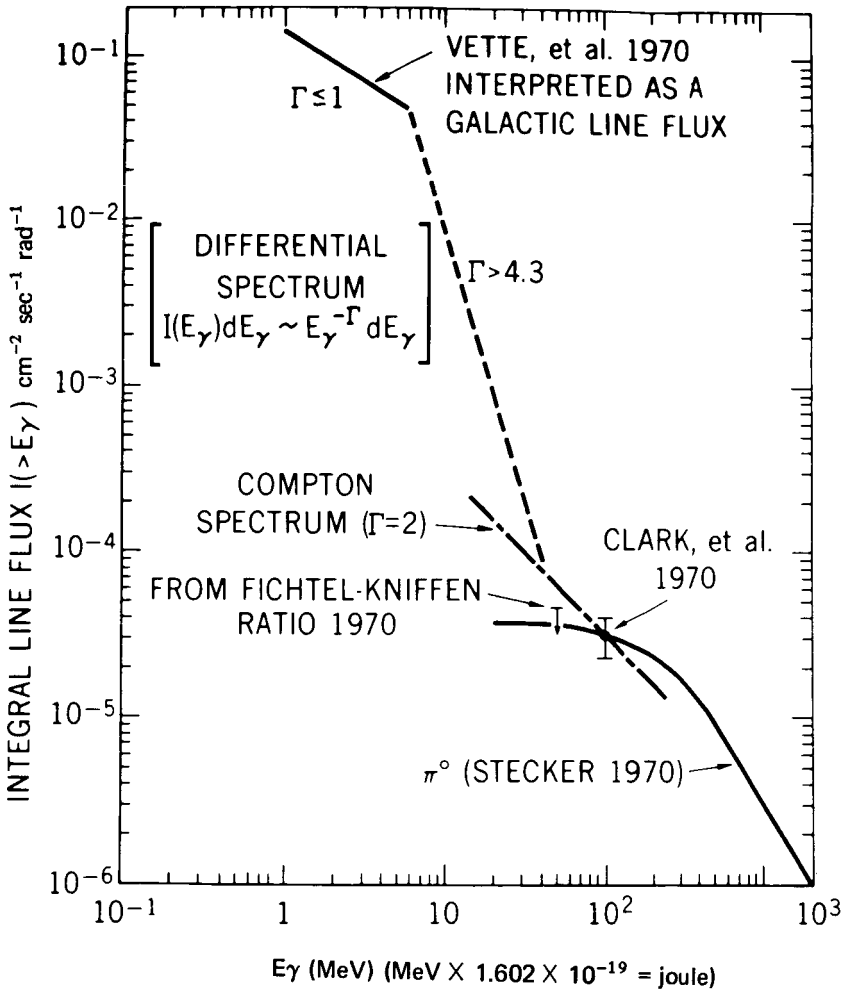
VETTE, et al. 1970
INTERPRETED AS A
GALACTIC LINE FLUX
Γ≤1
DIFFERENTIAL
SPECTRUM
I(Eγ)dEγ ~ Eγ^-Γ dEγ
Γ>4.3
COMPTON
SPECTRUM (Γ=2)
FROM FICHTEL-KNIFFEN
RATIO 1970
CLARK, et al.
1970
π° (STECKER 1970)
INTEGRAL LINE FLUX I(>Eγ) cm^-2 sec^-1 rad^-1
Eγ (MeV) (MeV X 1.602 X 10^-19 = joule)

Figure 1

MUON PRODUCTION

Dr. Kaichi Maeda

DR. PIEPER:

The next paper in our program was prepared by Dr. Kaichi Maeda, and concerns muon production in the atmosphere. It will be given by Dr. Theodore Northrop.

DR. NORTHROP:

Kaichi, would you stand up for a moment, so that if people have questions to ask afterwards they will know who you are? Kaichi has asked me to talk, because perhaps I can make it a little clearer, though the physics won't be as good.

Muons are produced in the atmosphere by the collisions of primary cosmic-ray particles with air nuclei to give pions and kaons, which then decay into muons, or they can be absorbed by the atmospheric particles. Figure 1 shows some experimental observations. The coordinates here are the angle from the zenith and the intensity plotted vertically, normalized by the intensity in the vertical direction. The solid curve and the dashed curve both represent theoretical calculations made by Dr. Maeda, and these calculations are not trivial: they involve straggling, the curvature of the earth, and all the possible energy-loss processes of high-energy particles in the atmosphere.

The experimental data consist of underground data; I think these observations were first made in connection with trying to observe neutrinos. The dashed curve also represents theoretical work done by Kaichi, and it assumes that all the muons are produced from kaons; the upper one assumes they are all produced from pions. Actually, most of the production is from the pions, maybe 20 percent from the kaons.

The data shown as black dots represent data taken by a group at the University of Utah, and I will talk more about that later. The data shown as open circles, that agree quite well with theory, fall between these two curves and represent the Utah data renormalized. The Utah people were not able to measure in the vertical direction, but Kaichi's theoretical expressions make it possible to extrapolate their data to the vertical direction

and get a somewhat different normalization, $L_{\mu}(O)$, than they have. When he uses that, he finds that their data agree quite well with his calculations.

The top point shown here is a very recent one obtained by Flatte of the Lawrence Radiation Lab in Berkeley at the surface of the earth by using a strong magnet instead of the ground depth to select high-energy muons. And you can see that it also agrees fairly well with theory.

The data represented by crosses, marked "Kolar," are Indian data that do not agree, probably because of statistical errors. If you include corrections for straggling effects, then these would agree also.

You may be surprised by the fact that the intensity increases as you go down at the lower angles; however, you know that it is harder to get a sunburn as the sun goes down, and you would expect the absorption to be greater for oblique incidence. The reason for the increase will be clear, if you look at Figure 2.

The reason for this peculiar effect is the production mechanism and the nature of the particle. The curved line here is the surface of the earth; these heavy lines are the primary cosmic-ray protons coming into the atmosphere. We have taken two cases, one for oblique incidence and one for vertical incidence. The short dotted particles represent the pions and the kaons, and the long thin lines represent the muons.

It is true that, at low energy, the muons will be absorbed by the atmosphere, but energies of these muons are of the order of 160 nanojoule (10^{12} electron volts), and after they are produced they come right on down. The reason for the increase with angle goes like this: The protons have to penetrate an average number of grams per square centimeter of atmosphere which is of the order of 0.1 kilogram/cm^2 (100 g/cm^2) before they produce the pions and kaons. In an oblique direction, this penetration occurs at a higher altitude than in the vertical direction. At the higher altitude, the pions and kaons are more likely to escape absorption by the atmosphere than they are at the low altitude, where the density is greater; as you see, they are more likely to result in muon production, rather than being absorbed by the atmosphere when they are produced here at high altitude. And that corresponds to oblique directions. So what happens is that you get an increase in intensity as you go down to larger theta.

Let me just make a comment about the Utah data: Notice, in Figure 1, the dashed curve marked 2 percent X process. There are in the world of physics at times suggestions that you can get a direct production of muons from proton-nucleon collisions. A muon is a weakly interacting particle, so that this path would be very slow, compared to the path by way of pions and kaons, and you couldn't expect much direct production. Without this intermediate step, if the muons resulted directly from the cosmic-ray collisions with the atmosphere, then there would be no change in intensity with theta. If you had all direct production by this slow mechanism – by this small cross section mechanism –, your line should be horizontal. Therefore, if you have experimental data that lie below the theoretical, you would naturally interpret them as containing some of this direct muon production. But what can be said about the Utah data now is, that they do not require any of the X process (direct-production process) in order to agree with calculations, provided you renormalize as Dr. Maeda has.

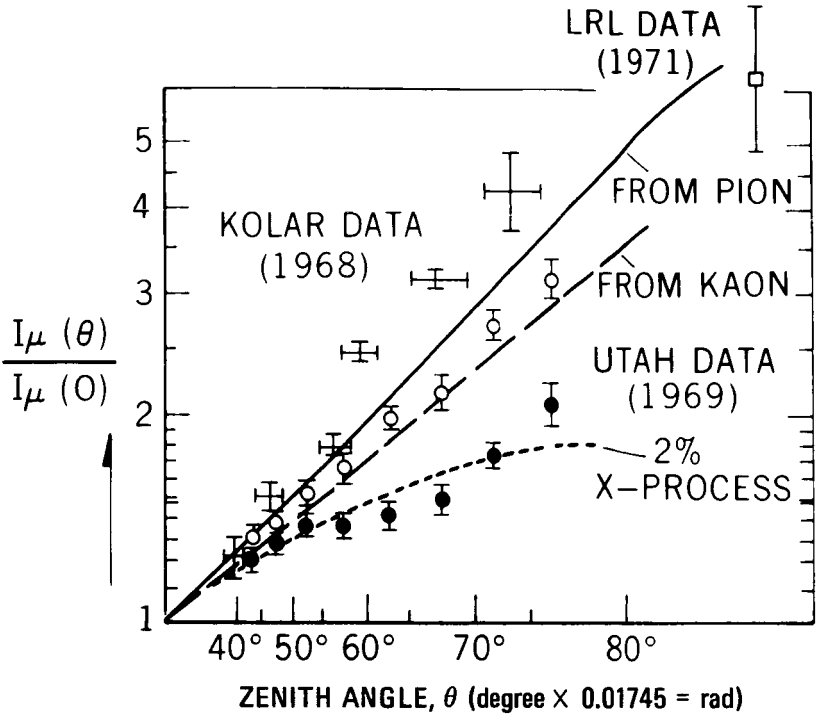
LRL DATA
(1971)
FROM PION
FROM KAON
KOLAR DATA
(1968)
UTAH DATA
(1969)
2%
X–PROCESS
5
4
3
2
1
Iμ (θ)
Iμ (0)
40° 50° 60° 70° 80°
ZENITH ANGLE, θ (degree × 0.01745 = rad)

Figure 1

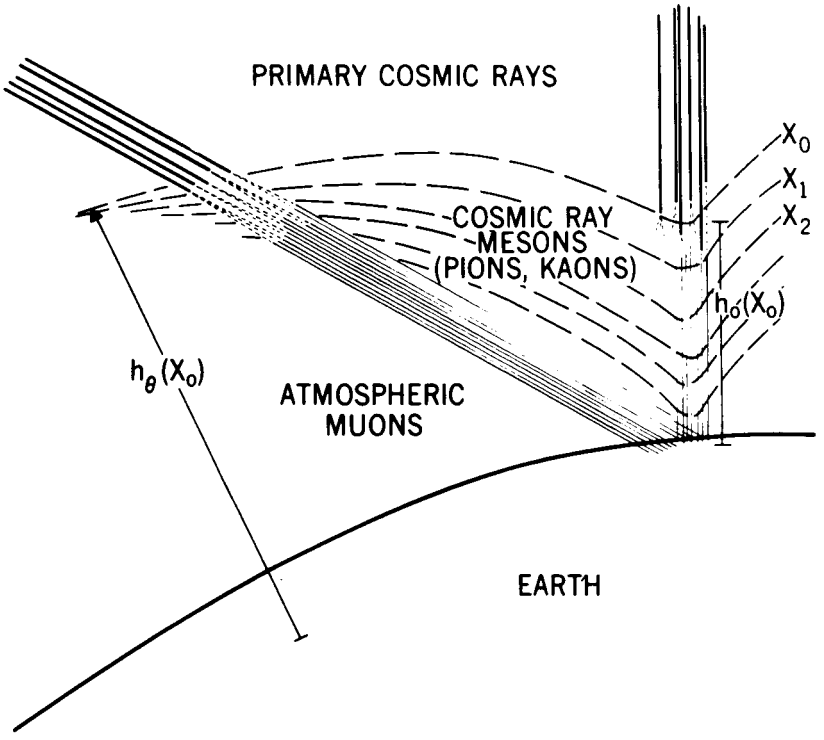
PRIMARY COSMIC RAYS
X_0
X_1
X_2
COSMIC RAY
MESONS
(PIONS, KAONS)
$h_\theta(X_0)$
$h_0(X_0)$
ATMOSPHERIC
MUONS
EARTH

Figure 2

INTERSTELLAR ELECTRON INTENSITY

Dr. Reuven Ramaty

The determination of the interstellar cosmic-ray intensity outside the modulating region of the interplanetary magnetic field is of considerable interest for a variety of problems in astrophysics, such as the heating and ionization of the interstellar medium and the general dynamics of the interstellar medium. However, short of direct measurements aboard satellites at great distances from the inner solar system, the interstellar cosmic-ray intensity can be determined only by indirect methods.

We have studied the electron component of the cosmic rays. By using two independent methods that yielded essentially the same result, we have determined the cosmic-ray electron intensity in interstellar space. In addition, the same study yielded some interesting results on the spatial and temporal constancy of the cosmic-ray electrons in the galaxy.

Cosmic-ray electrons consist of both positrons and negatrons. The first method depends on the study of positrons alone, whereas the second method involves the total electron-intensity positrons as well as the negatrons. Because free positrons are not expected to be present in the cosmic-ray sources, the interstellar cosmic-ray positron intensity is entirely due to positrons produced in nuclear collisions of cosmic rays with interstellar hydrogen. This process involves the production of pions in proton-proton collisions, the decay of the pions into muons, and the subsequent decay of the muons into positrons. Figure 1 shows the results of a detailed calculation of all these processes.

This figure, along with the calculated positron intensity shown by the solid line, also shows the observational data on cosmic-ray positrons. Above a few GeV, the calculated and measured spectra are consistent, supporting the general validity of this theory on the origin of cosmic-ray positrons. Below about 160.2 picojoules (1 GeV), the positron intensity at earth is lower than the interstellar intensity. This is most probably a manifestation of solar modulation: that is, the effects of the solar wind and the interplanetary magnetic field on the cosmic rays. The magnitude of this modulation can be deduced as a function of energy by comparing the calculated interstellar intensity with the observed positron data.

The second method for deducing the magnitude of the solar modulation is based on the fact that cosmic electrons emit synchrotron radiation in the interstellar magnetic field. Figure 2 shows the observed radio spectrum from about 400 kilohertz to about 400 megahertz. The low-frequency measurements were made on board the RAE satellite, whereas the high-frequency data are from various ground-based observations. Above the maximum, the radiation is optically thin; below the maximum, the radiation is absorbed by free electrons in the interstellar medium. The solid curve, which is a good fit to the data, is a computed radio spectrum for a free-electron temperature of 4000 kelvins and an electron density of 0.03 per cubic centimeter, a collection distance of 12.34×10^{19} meters (4 kiloparsecs) toward the anticenter, and the cosmic-ray electron spectrum shown in Figure 3. In other words, the spectrum labeled "interstellar intensity" is that intensity toward the anticenter that is needed to produce the solid line shown in the previous figure, which is a good fit to the observed radio data.

Since radio emission is produced by both positrons and negatrons, we must compare the calculated intensity shown in Figure 2 with measurements of the total electron intensity at the earth, also shown in this figure. As can be seen, above a few GeV the calculated and observed spectra are again consistent, much in the same way as a calculated and an observed positron spectrum are of the same magnitude in this energy range. Below a few GeV, the observed electron spectrum is lower than the calculated one, and the modulation deduced at these energies is approximately the same as that obtained from the positron study.

So we have determined now the interstellar intensity, using two completely independent methods, and our principal conclusion is that the interstellar electron intensity shown in Figure 3 is probably a reasonable representation of the actual interstellar intensity, and can be used in detailed calculations on the modulating mechanism in the interplanetary medium. Furthermore, we can make the following statement regarding the constancy of the cosmic rays: Since the positrons from nuclear collisions represent a time-average intensity over the last few million years in the region of a few hundred parsec around the solar system, whereas electrons from the radio emission correspond to a spatial average over the line-of-sight to anticenter, the general agreement of the calculated intensities with both the positron and the electron observations means that the cosmic-ray intensity at a few GeV has been reasonably constant over the last few million years in a sizeable portion of the galaxy.

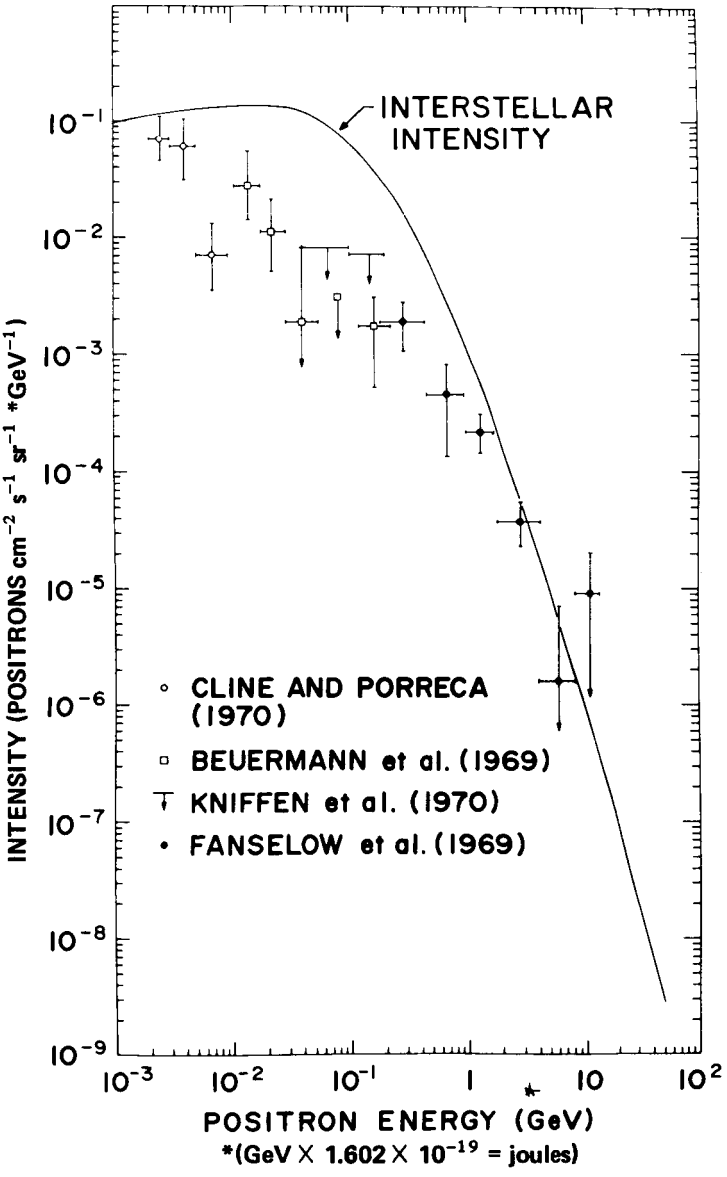
INTERSTELLAR INTENSITY
INTENSITY (POSITRONS cm^{-2} s^{-1} sr^{-1} *GeV^{-1})
10^{-1}
10^{-2}
10^{-3}
10^{-4}
10^{-5}
10^{-6}
10^{-7}
10^{-8}
10^{-9}
° CLINE AND PORRECA (1970)
□ BEUERMANN et al. (1969)
KNIFFEN et al. (1970)
• FANSELOW et al. (1969)
10^{-3}
10^{-2}
10^{-1}
1
10
10^{2}
POSITRON ENERGY (GeV)
*(GeV X 1.602 X 10^{-19} = joules)

Figure 1

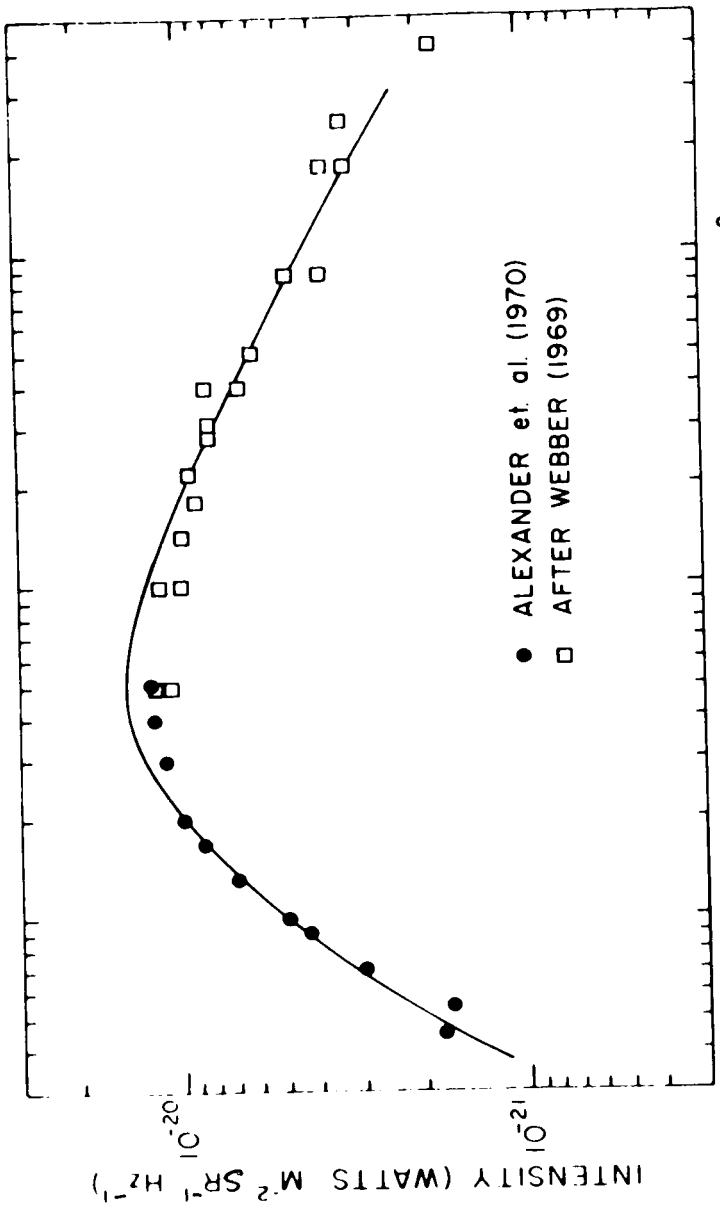
INTENSITY (WATTS M⁻² SR⁻¹ Hz⁻¹)
10⁻²⁰
10⁻²¹
1
10
10²
FREQUENCY (MHz)
● ALEXANDER et. al. (1970)
□ AFTER WEBBER (1969)

Figure 2

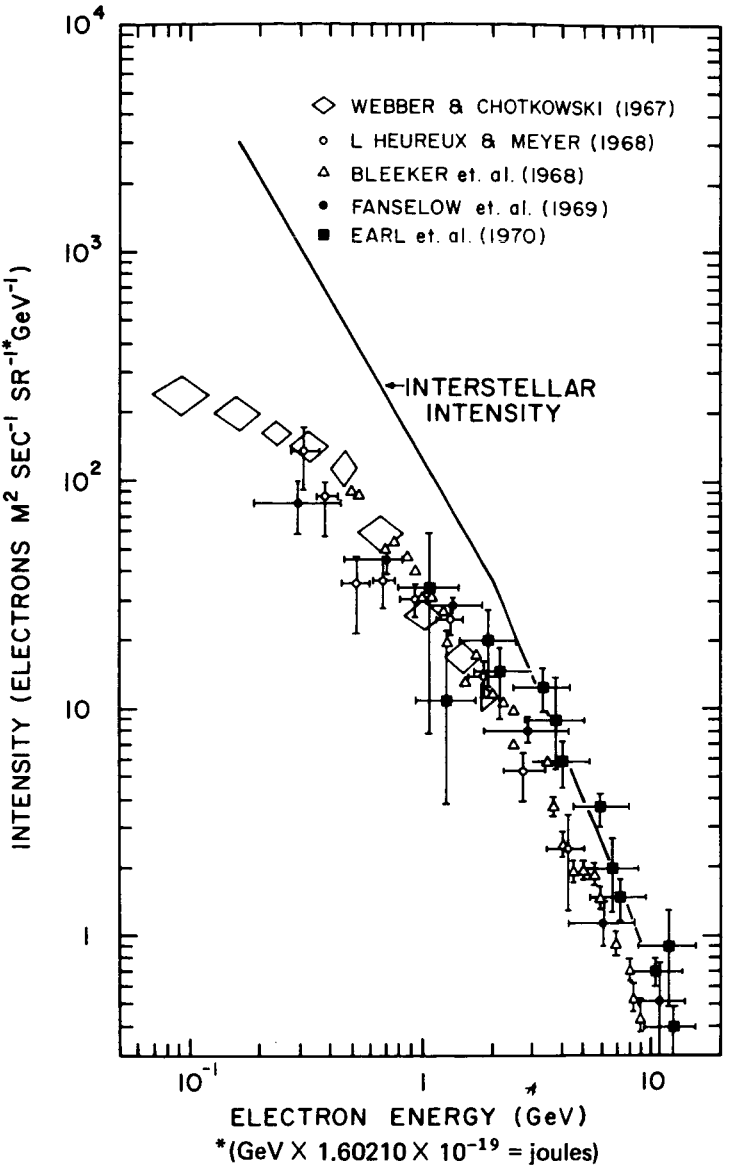
WEBBER & CHOTKOWSKI (1967)
L HEUREUX & MEYER (1968)
BLEEKER et. al. (1968)
FANSELOW et. al. (1969)
EARL et. al. (1970)
INTERSTELLAR INTENSITY
INTENSITY (ELECTRONS M² SEC⁻¹ SR⁻¹*GeV⁻¹)
ELECTRON ENERGY (GeV)
*(GeV X 1.60210 X 10⁻¹⁹ = joules)

Figure 3

ENERGY LOSS OF COSMIC RAYS IN THE INTERPLANETARY

Dr. Lennard Fisk*

All species of particles, electrons, positrons, and nuclei, will be influenced by the interplanetary magnetic fields as they attempt to pass from the interstellar medium to the vicinity of earth. At energies below a few tens of GeV per nucleon, the intensity of these particles will be reduced and their spectrum modified by their passage through the interplanetary medium. We therefore observe at earth only a modulated interstellar intensity. Clearly, to understand the behavior of cosmic rays in the galaxy, we must perform some sort of demodulating process.

Now, this can be done in a fairly simple way. As Reuven Ramaty described to you in the previous talk, we have been able to calculate likely forms for the truly interstellar spectra of electrons and positrons. We know, therefore, how much modulation the electrons and positrons suffer. Once we know how the electrons and positrons behave in the interplanetary medium, we can predict how protons and higher Z particles will behave there.

Over the last few months, we have enjoyed some good success in using the apparent modulation of electrons and positrons to demodulate the proton and higher Z-particle spectra. However, we have also encountered an interesting complication in doing this – a complication that prohibits us from being able to determine the low-energy portion of interstellar proton and higher Z spectra based solely on observations made near earth. It is about this complication that I would like to talk today.

Figure 1 shows what we believe to be reasonable approximations of the actual interstellar spectra of protons and alpha particles over a wide range of energy. These data points represent proton and alpha-particle intensities observed during solar-minimum conditions in 1965; here we have plotted intensity versus energy per nucleon. The upper curves represent our best guesses for the interstellar proton and alpha-particle spectra, based on the apparent modulation of electrons and positrons.

---

*National Academy of Sciences resident research associate

Clearly, in order to determine interstellar spectra throughout this energy range solely on the basis of observations made near the earth, we must ensure that the particles reaching us at earth are indeed coming from throughout this energy range. Unfortunately, this is not the case.

We have established that low-energy particles lose so much energy in the interplanetary medium, because of the process of adiabatic deceleration, that the vast majority of particles which we see at earth originated at interstellar energies in excess of about 16.02 picojoules (100 MeV) per nucleon. We are free to predict that interstellar spectra above 16.02 picojoules (100 MeV) have these shapes, but below this energy we can only guess.

We can illustrate the extent and influence of this energy loss by considering how individual particles entering the interplanetary medium at various interstellar energies are likely to behave. Figure 2 shows the results of these calculations, assuming that the particles are protons. The upper curve is again our best guess for the interstellar proton spectrum.

Now, suppose we single out particles that enter the interplanetary medium within each of these various energy ranges, and watch how these particles behave. The numbered curves represent the probability, plotted as a function of energy, that a particle will reach the orbit of earth, having entered the interplanetary medium with the intensity and within the energy range of the corresponding number. As you can see, at high energies the effects of the modulation are rather small: only a slight reduction in the number of particles that we would expect to see at earth, and a slight shift in the most probable energy due to the energy loss. At intermediate energies, this reduction and shift are more pronounced. Note also the considerable spread in the energy range by the time the particles reach earth. The energy loss is a statistical process; not all the particles lose the same amount of energy.

By the time we get to low energies, this reduction and shift combination is extreme. Note in particular that, at energies below about 16.02 picojoules (100 MeV), the probability of observing at earth a particle that originated in the interstellar medium at energies above 16.02 picojoules (100 MeV) is many times the probability of observing a particle that originated below 16.02 picojoule (100 MeV). Consequently, our observations on earth are virtually insensitive to particles

that originate at interstellar energies below 16.02 picojoules (100 MeV), and cannot be used to infer anything about the shape of low-energy interstellar spectra.

This is, of course, truly regrettable. The low-energy portion of the interstellar spectrum is perhaps its most interesting part. Low-energy galactic cosmic rays may well have a profound influence on the dynamics of the galaxy. In all probability, however, we will have to wait until we can make space-probe observations closer to the boundary of the modulating region before we have any hope of determining this portion of the spectrum.

Fortunately, our calculations indicate that we may not have to go too far – perhaps only 2 to 5 astronomical units – before we will be effectively out of the modulating region. Thus, we hope that on Pioneer F or G, or perhaps on the Grand Tour missions, we will be able to determine low-energy interstellar spectra and begin to understand their important astrophysical consequences.

MEMBER OF THE AUDIENCE:

On what do you base your estimate of going to only 300 or 750 gigameters (2 or 5 AU's) before you can get out of modulation?

DR. FISK:

We base it on the modulation of electrons. As Reuven described, we predicted what the interstellar electron spectrum looks like.

DR. PIEPER:

Well, it is a nice consistent story at this point in time. All it needs is a good measurement at about 750 gigameters (5 AU) to prove that you are right.

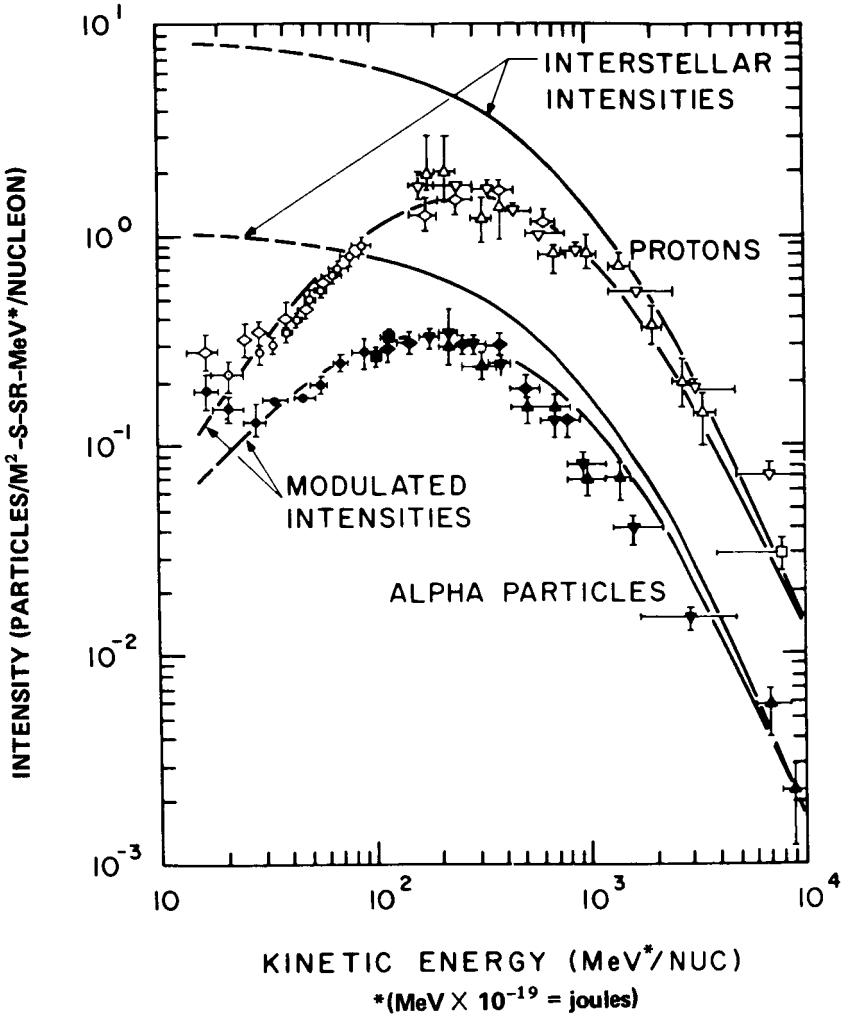
INTERSTELLAR
INTENSITIES
PROTONS
MODULATED
INTENSITIES
ALPHA PARTICLES
INTENSITY (PARTICLES/M²-S-SR-MeV*/NUCLEON)
KINETIC ENERGY (MeV*/NUC)
*(MeV × 10⁻¹⁹ = joules)

Figure 1

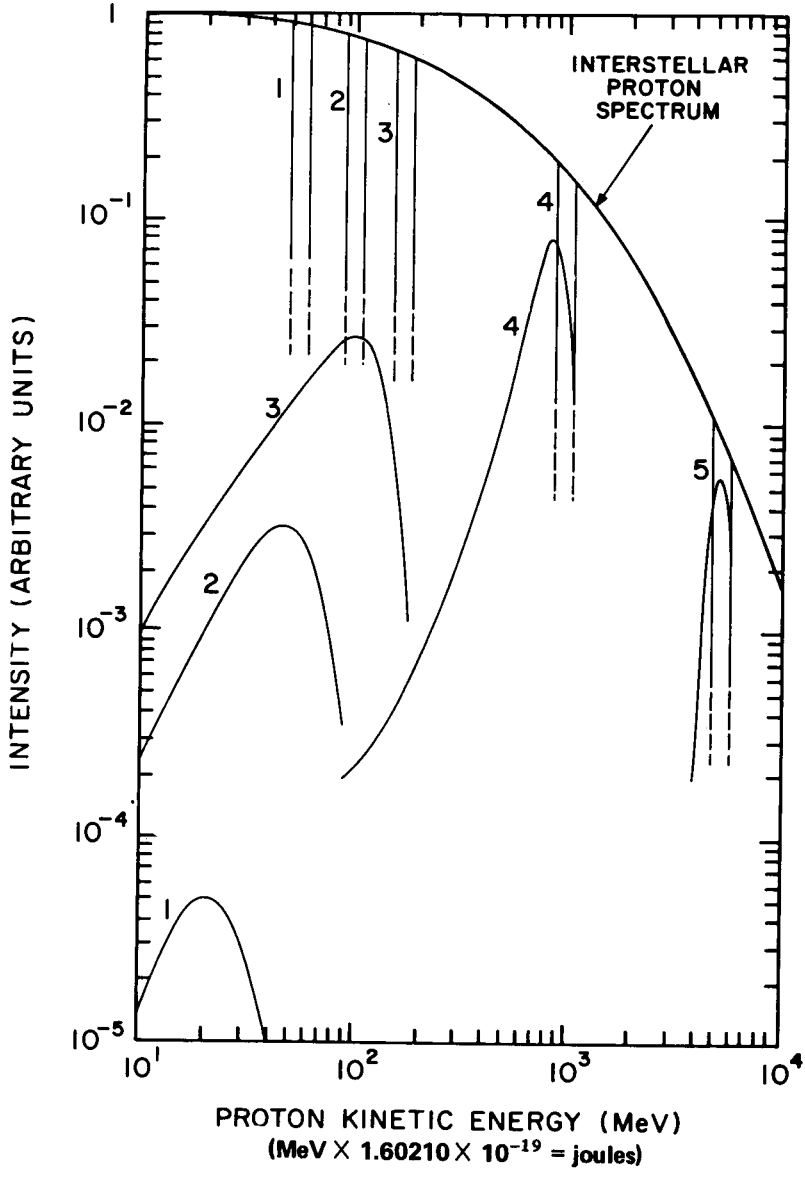
INTERSTELLAR
PROTON
SPECTRUM
INTENSITY (ARBITRARY UNITS)
1
10^{-1}
10^{-2}
10^{-3}
10^{-4}
10^{-5}
10^{1}
10^{2}
10^{3}
10^{4}
PROTON KINETIC ENERGY (MeV)
(MeV X 1.60210 X 10^{-19} = joules)

Figure 2

EXTRAGALACTIC RADIO SPECTRUM

Larry Brown

The Radio Astronomy Explorer spacecraft has provided measurements of the average cosmic-noise background spectra between the frequencies of 400 kilohertz and 7 megahertz. Since the data were obtained from a dipole antenna, the spectrum obtained is representative of the average features of broad regions approximately 1.74 rad (100 degrees) in angular extent. The problem then is to build a model for the observed continuous emission.

Preliminary work indicated that the medium from which the radiation is coming must be composed of a number of small regions of emitters and absorbers uniformly mixed over the large region. Further, we have shown that the most probable mechanisms involved are synchrotron emission by low-energy cosmic-ray electrons and free-free absorption by thermal electrons associated with ionized hydrogen.

Figure 1 shows the amount of radiation observed in measurements by the RAE spacecraft at low frequencies, and ground-based observations at higher frequencies. We show here the spectra for the anticenter – the region in the galactic plane directly opposite the galactic center – and the north halo minimum region perpendicular to this plane.

For the lowest RAE frequencies, the absorption by ionized hydrogen has become so large that only nearby radiation is not heavily absorbed. Such a condition leads to a constant spectral slope from which the power spectrum of the low-energy cosmic-ray electrons is deduced. Our value of 1.8 shows a flatter spectrum than that observed for higher energy cosmic rays. Having derived a power law for the emitters, we now determine the amount of absorption from the difference between the deduced and the observed emission spectrum, yielding in essence a complete low-frequency model of the observed radiation. With this model, we can extrapolate to the high frequencies, as shown by the dashed line in the figure. We can see that an excess of radiation is observed at the higher frequencies: this additional component is extragalactic in nature, coming from other radiating galaxies.

The separation shown in the figure for the anticenter and the north halo minimum region illustrates this. The extragalactic component is the same in the mutually perpendicular directions and, when added to the extrapolated low-frequency models, yields exactly the same shape as the observed total radiation. We can see this clearly in the north halo minimum region near 2 MHz.

In Figure 2, the solid line represents the derived extragalactic spectrum with all the absorption effects of our galaxy removed. There is excellent agreement with previous measurements at high frequencies.

In the low-frequency region of the RAE measurements, we see that some mechanism is altering the spectra: the first indications are that this is again free-free absorption by ionized hydrogen, but it is occurring now in the extragalactic sources themselves and in the intergalactic medium in which they are immersed. Thus, we are finally led to new problems to probe, through the continued use of the RAE spacecraft.

DR. PIEPER:

Another good one for RAE. Thank you very much.

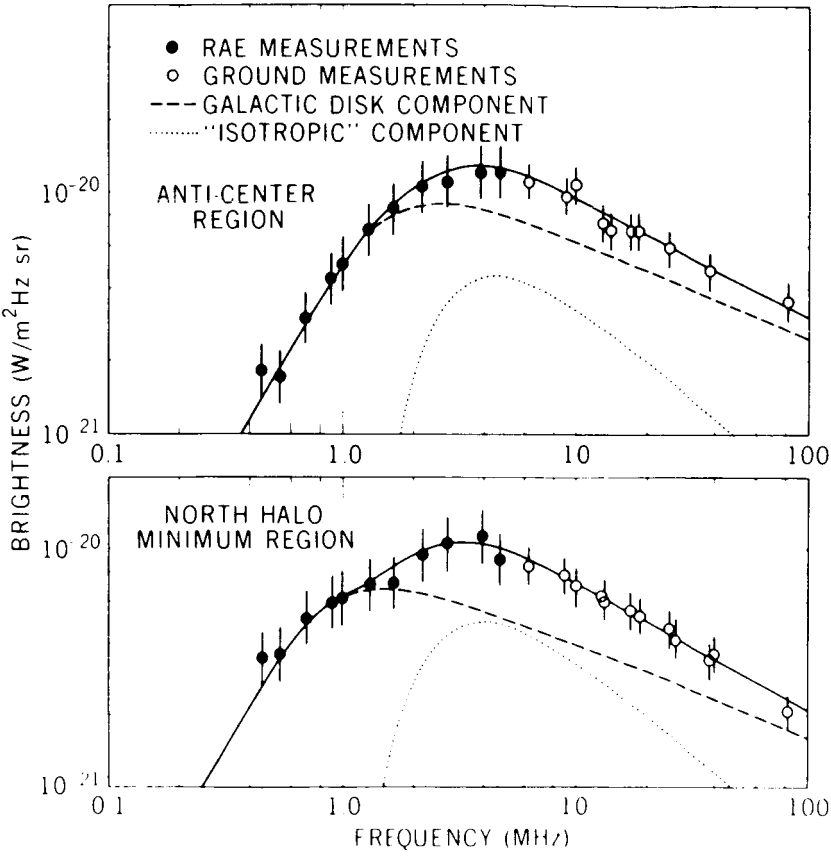
RAE MEASUREMENTS
GROUND MEASUREMENTS
GALACTIC DISK COMPONENT
"ISOTROPIC" COMPONENT
ANTI-CENTER REGION
NORTH HALO MINIMUM REGION
BRIGHTNESS (W/m²Hz sr)
FREQUENCY (MHz)
0.1
1.0
10
100

Figure 1

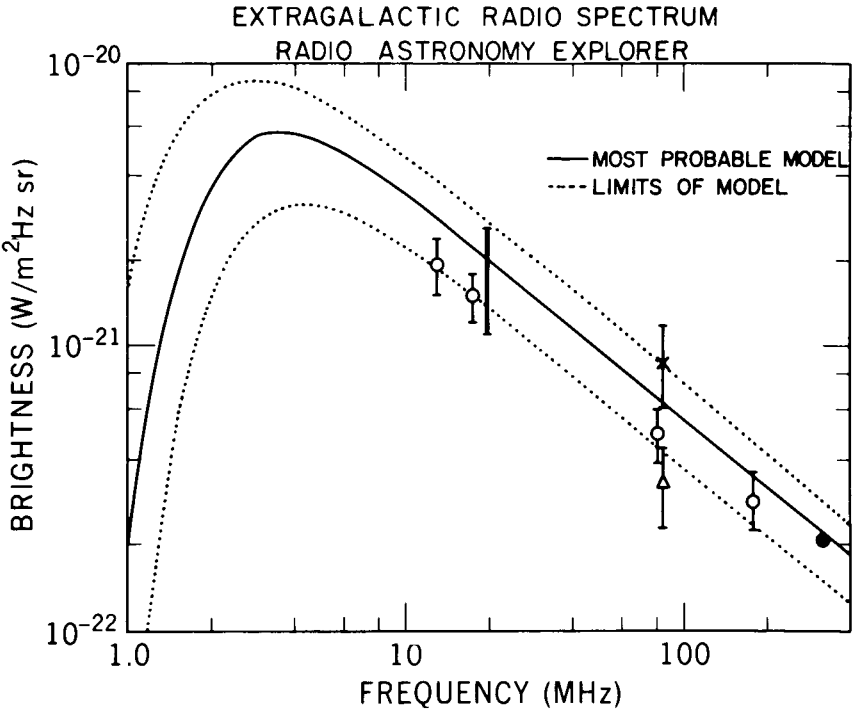
EXTRAGALACTIC RADIO SPECTRUM
RADIO ASTRONOMY EXPLORER
MOST PROBABLE MODEL
LIMITS OF MODEL
BRIGHTNESS (W/m²Hz sr)
10⁻²⁰
10⁻²¹
10⁻²²
1.0
10
100
FREQUENCY (MHz)

Figure 2

100-MICROMETER (100-MICRON) MAP OF THE GALACTIC CENTER

Dr. William Hoffmann

This is a report on the latest results of a program of far-infrared surveys at the Goddard Institute for Space Studies. An early result in 1968 was the discovery, with a 1-inch balloon-borne telescope, of the very intense far-infrared emission from the galactic center. Since that time, we have built a 12-inch telescope with a fully stabilized gondola and telemetry control.

In July, that new instrument was used to survey the galactic-center region with a greater sensitivity and resolution than was previously possible. The instrument was operated at a wavelength of 100 micrometers (100 microns) with a passband between 75 and 125 micrometers (75 and 125 microns). The beamwidth at half-power was 3.5 millirad (12 arc/minutes). The telescope was commanded to cover a region of the sky along the galactic plane approximately 87 millirad (5 degrees) wide, with a succession of overlapping scans perpendicular to the plane.

Figure 1 shows a portion of the scans covering 17 millirad (1 degree) along the galactic plane. The coordinate at the bottom indicates the scale along the scan. Features that show up immediately are:

- The far-infrared emission in the galactic-center region is a continuous band along the galactic plane.
- Its extent perpendicular to the plane is on the order of 35 millirad (2 degrees).
- In this portion of the scans, peaks of emission show up clearly at the positions of the radio sources Sagittarius A and Sagittarius B-2.

Figure 2 is a contour map made from these and other scans covering a region 70 millirad (4 degrees) along the galactic plane and 35 millirad (2 degrees) across it. The positions of the five peaks – Sagittarius A, B-2, and three others – agree extremely well with the radio sources in the region.

The 100-micrometer (100μ) luminosity of the entire region, 3.4×10^8 $L_\odot$, agrees very well with 1-inch telescope results. The general picture here supports the hypothesis that this emission comes from interstellar dust grains heated to 20 to 50 kelvins by the absorption of starlight.

Figure 3 is a summary of the positions of the peaks. The first four agree with the radio sources indicated by name; the fifth one does not have an associated radio source, but it is at the position of a distinct structure at the shortest radio wavelength mapped. The physical extent of the Sagittarius A source is approximately 308×10^{16} meters (100 parsecs), and the luminosity of Sagittarius A is 7.4×10^7 $L_\odot$.

For comparison I have shown the results of the only other observations of the galactic center at the long wavelengths, those of Low and Aumann. Those reported results are in distinct agreement with our own; in particular, the sizes of the sources reported and the luminosities by Low and Aumann are considerably lower than what we observe. Also, Low reports these sources to be discrete, without the continuous bridge of radiation which we find, and he is unable to detect the extended emission shown in the previous illustration.

The astronomical significance of these results is considerable: I would point out three items in particular.

- We have confirmed the very high infrared luminosity, most probably due to a large conversion of energy to the long wavelengths by dust absorption and remission. This large component of interstellar radiation at the long wavelengths could contribute to the gamma-ray flux from the galactic center through the inverse Compton effect.

- For the first time, it has been possible to map in detail the distribution of dust in the galactic-center region. This dust is too cold to be observable by radiation at shorted wavelengths from the ground and too opaque to be observed by its attenuating effect on starlight passing through it.

- The very good coincidence between the peaks of this radiation and the radio maps that map out the H_{II} ionized regions which are sources of interesting interstellar chemistry provides a new

source of information about these regions and about the dust which plays an important role in the production and protection of interstellar molecules from dissociating radiation.

We plan to extend this survey to a large portion of the celestial sphere and to add three more channels so that we can do four-channel photometry simultaneously.

MEMBER OF THE AUDIENCE:

How do you know the dust temperature?

DR. HOFFMANN:

The brightness temperatures observed are 20 to 22 kelvins; the physical temperatures are most likely between 20 to 50 kelvins. A reasonable estimate of the total optical thickness through this material is about 1 percent, at which the physical temperature would be 50K. If the temperatures were a good deal higher than that and the opacity a good deal lower, then the energy emitted at shorter wavelengths would be extremely high. The four-band photometry should give us very good temperatures and a better handle on the separation between the dust temperature and its distribution.

MEMBER OF THE AUDIENCE:

Can you derive the concentrations of dust in the galactic-center region by this technique?

DR. HOFFMANN:

No, not without more knowledge of what the dust is. The uncertainties are the amount of dust along the line-of-sight, and the infrared opacity of the individual dust grains. There simply is not enough information at present to disentangle these two effects.

MEMBER OF THE AUDIENCE:

How do you know that the dust is not optically thick?

DR. HOFFMANN:

If the dust were optically thick, it would be 22 kelvins. But I think – from our other knowledge of the amount of material we expect, and the normal ratio of dust to total mass in the galaxy – that optically thick dust at 100 micrometer (100 μ) would be very unlikely.

MEMBER OF THE AUDIENCE:

Do you know what range of wavelengths the absorbed radiation has? Could it include soft X-rays?

DR. HOFFMANN:

No, I don't know; I assume that most of the energy comes not from X-rays but from normal stellar emission. But, even then, what normal stellar emission in that area is, is a huge question. By obtaining more detail through the four-band photometry on the temperature and the total amount of radiation, we can perhaps infer the total source energy more accurately, and from that an expected mass-luminosity ratio. Then we can infer how hot the stars are.

MEMBER OF THE AUDIENCE:

Is it not necessary to have nonstellar unusual source of energy to provide the observed luminosity?

DR. HOFFMANN:

The total luminosity you would expect from this region with a reasonable mass-to-luminosity ratio would be adequate if essentially all the stellar radiation were absorbed by the dust. And that is not unreasonable, because of the thickness of the dust. Along the line-of-sight to the earth, it absorbs visual wavelengths by a factor of 10^{10}. And even out of the disc, it is going to take most of it.

MEMBER OF THE AUDIENCE:

But that dust and stuff is pretty close to the centers. This is within 308 $\times 10^{17}$ meters (a thousand parsecs) or so, isn't it?

DR. HOFFMANN:

Yes, up to about 308×10^{17} meters (1000 parsecs). It is a very exciting region.

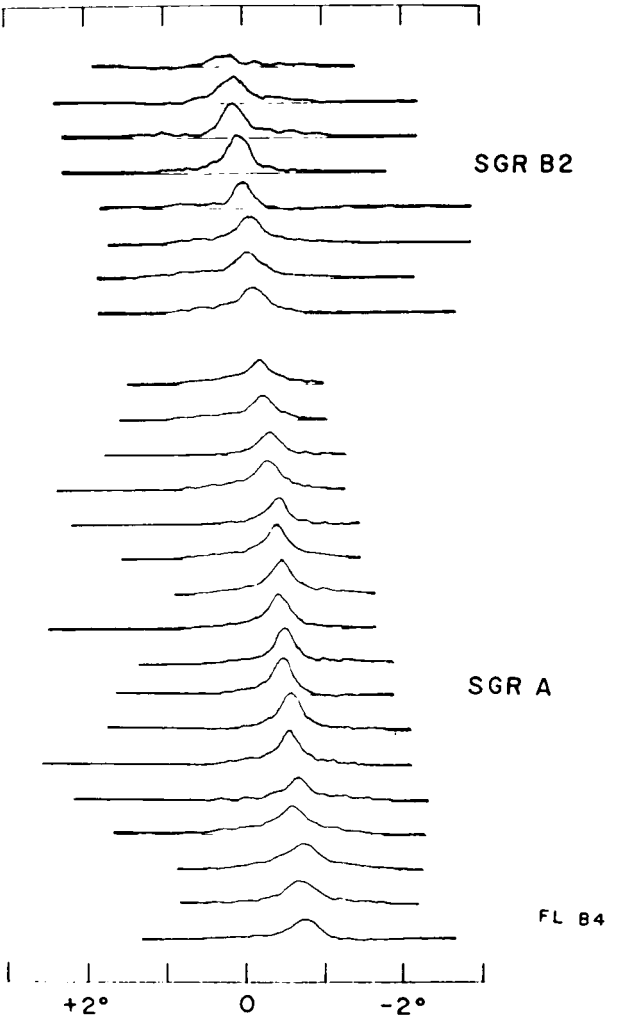

Figure 1

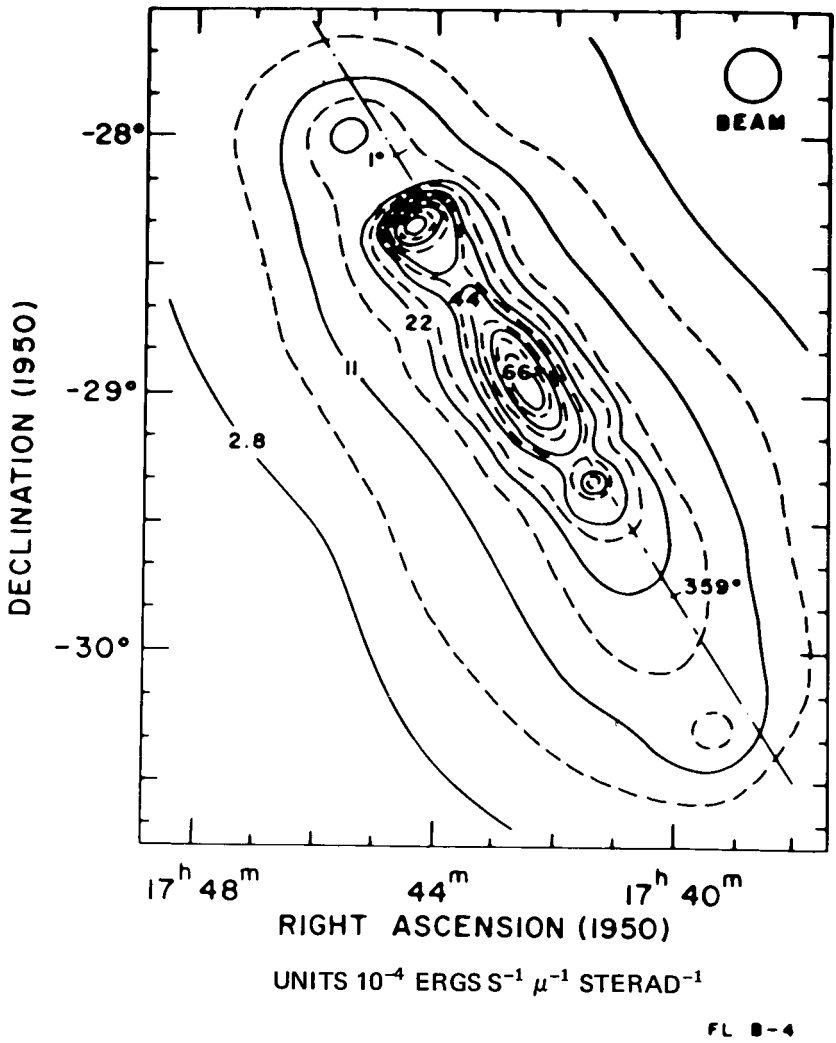
BEAM
-28°
-29°
-30°
DECLINATION (1950)
1°
22
66
11
2.8
359°
17h 48m
44m
17h 40m
RIGHT ASCENSION (1950)
UNITS 10-4 ERGS S-1 μ-1 STERAD-1
FL 8-4

Figure 2

GALACTIC CENTER OBSERVATIONS

	PRESENT WORK			LOW AND AUMANN	
	Position (1950)	Size	Luminosity 75-125μ $L_\odot$ ($1\mu = 1\mu m$)	Size	Luminosity 10 - 300μ $L_\odot$ ($1\mu = 1\mu m$)
A Sgr A	$17^h\ 42^m\ 29^s$ $-28°\ 59'$	38' x 15'	7.4×10^7	8'	3.5×10^7
B Sgr B2	$17^h\ 44^m\ 21^s$ $28°\ 22'$	15' x 15'	3.1×10^7	8'	1.7×10^7
C G-0.6-0.1	$17^h\ 41^m\ 21^s$ $-29°\ 22'$	10' x 10'	2.0×10^7	7'	1.2×10^7
D KE 56	$17^h\ 45^m\ 31^s$ $-28°\ 01'$	7' x 7'	1.1×10^7		
E	$17^h\ 39^m\ 26^s$ $-29°\ 47'$	—	—		

Figure 3

VERY LONG-BASELINE INTERFEROMETRY

Dr. Thomas Clark

This is a report on some more work by the Radio Astronomy Explorer group. However, being radio astronomers, we also make use of conventional radio-astronomy instruments, such as large dish antennas. And it is some of this ground-based work that I am going to report on today.

When we speak of a radio interferometer, we normally think of two large antennas connected together with receivers at each of these antennas. The noise that emerges from these receivers is then cross correlated and, as the earth turns under the sky, a sinusoidal fringe pattern is observed in this output correlation coefficient.

The angular scale of this correlation coefficient in terms of sky dimensions is such that, if we have N wavelengths between the two elements of the interferometer, then there are N fringes per radian of angle in the sky.

In the past, radio astronomers have been limited to a few miles of baseline where the two elements are connected together by a "string" – such as wire, coaxial cable, or radio links. When we desired to get higher angular resolution, we obviously had to do something to break this string, and this brings us to the very long-baseline interferometry.

Figure 1 shows the baselines that we have connected together as interferometers in the past 2 years. You will note a large number of sites around the world, connected together. As these are isolated sites, an individual group can't perform such experiments by itself; it requires a collaborative effort. So, in general, the results I report today are the results of collaborations of a large number of groups.

How do we make this connection, to break the "string"?

Well, the basic technique we use is to simultaneously record on magnetic tape the noise signals received from radio sources, then play the tape back in synchronism at a later time. Thus the "string" that would be required in the normal interferometer is replaced with magnetic tape, and the cross correlation is done at a later time. In our experiments, the cross correlation is done in a digital computer.

To achieve this synchronization, each station requires a high-stability timing signal that is recorded along with the noise signals. We require stabilities

of the order of a microsecond per day or so in this timing. We also do our correlation in the frequency domain, and in order to establish the correlation there we require frequency stabilities of the order of parts in 10^{14}. Here at Goddard, the VLBI has been pioneering in the use of very high-stability frequency standards for such work. We have been using hydrogen masers developed here at Goddard by Dr. Coates and his group.

Computer processing to extract cross correlations is done here at Goddard, using the high-speed digital computers like the IBM 360-91. When we use computer processing to match up these two noise signals in both the time and the frequency domain, we must also account for the fact that the stations are not coincident. This gives rise to time delays because of the relative geometry of the baseline and the source location in the sky. We also must account for constant or slowly changing clock errors to accuracies of $\sim 1\mu$ sec.

Conversely, once we have made the connection and find that we have made some small errors, we can invert that error and correct our a priori assumptions about the baseline and the locations of the radio sources, and synchronize the clocks.

So, a portion of our work is devoted to applications of this technique such as geodesy, general relativity tests, astrometry, and clock synchronization. The results I am going to tell you about now pertain to the baseline from Haystack, Massachusetts, where there is a 120-foot dish operated by MIT, to Goldstone, California, where we use the 210-foot JPL Mars dish. These are the result of a collaborative effort involving our group and the VLBI and planetary radar group at the Massachusetts Institute of Technology, and the Jet Propulsion Laboratory. The observations reported here were made at 3.8 centimeters over the 3900-kilometer baseline, or about 10^8 wavelengths. That gives us 10^{-8} radians of angle separating the fringes.

If the source is larger than 10^{-8} radians, it is going to wipe out the sinusoidal fringe pattern. Hence these observations are of sources which are smaller than 10^{-8} radians. (10^{-8} radians works out to about 2 milliseconds of arc, which is about the size of a dime over Houston, as seen from here.) So we are talking about very small sources when we are discussing this work.

The sources we observe are usually quasi-stellar objects or the nuclei of external galaxies: in some cases, objects within our own galaxy, like the

maser OH spectral line sources and pulsars. We have also observed satellites and have succeeded in using VLBI to track them. However, being an astronomer, I am going to report today on some astronomical results on quasi-stellar sources.

Just to refresh your memory on quasi-stellar sources, I would like to show here one of the typical (if such a thing exists) quasi-stellar sources, source 3C273, which shows up in the best-quality optical photographs we can obtain with the 200-inch Mt. Palomar telescope (Figure 2) as a very small compact starlike image, which happens to have a jet sticking out that you see going off about 785 millirad (45 degrees) to the left of straight up.

When we combine all the knowledge in the radio domain with some degree of artistic license, we find that the source in radio wavelengths looks something like the righthand side of Figure 2, with an overall source that has the same kind of 97.7-microrad (20-second-of-arc) angular extent (from the tip of the jet to the other end of the image) that the optical object has. We find a source out at the tip of the jet, which I have colored in blue. We find in the center of that starlike image a compact radio source with a diameter of a second-of-arc or so, which I have shown in green. We find within that 4.9 microrad (1-second-of-arc) source a source that has a size of the order of 49 nanorad (a hundredth of a second of arc), which is shown in red.

We have also found a source within that source which as a size smaller than 4.9 nanorad (a thousandth of a second-of-arc), which is symbolically represented by the black dot in the center of the source.

Figure 3 shows the result when you expand that black dot in the center of the red in the center of the green, which has an angular size of the order of 4.9 nanorad (a millisecond-of-arc).

We have succeeded in resolving the nucleus of a quasi-stellar source. These figures are for a different one, 3C279, but it has many of the same properties as the last one; had I shown you a picture of 3C279, it would have just looked like a dot – it doesn't have a jet. Now the units, the 0.9, 1.2, et cetera, are given in units of milliseconds of arc. Again, remember that is the dime over Houston.

We have succeeded in resolving the nucleus into two components, each one of which has an angular size smaller than 4.9 nanorad (a thousandth of a second-of-arc); we don't know how much smaller, because we haven't made a long enough interferometer yet, so the permitted size for these sources is about a fourth of the separation between them. We have been able to measure this separation with the precision of the order of 242 picorad (50 microseconds-of-arc), which is shown in the error box in the upper left-hand corner. That is the relative position of the upper left one compared to the one in the lower righthand corner.

When we put this object at the distance that we believe it is – something like 5.24×10^{25} meters (1.7 gigaparsecs, or 5 giga light years) –, that separation, the 7.51 nanorad (1.55 milliseconds-of-arc), turns out to be something of the order of 189 terameters (20 light years), and our error box there is much smaller than 9.46 terameters (one light year) in size.

Now, from what we know about quasi-stellar sources, they are objects in which many violent events are occurring. We see variations in their radio brightness, in some cases in their optical luminosity, over timescales of a year or two. One possible model that has been proposed is that there are explosions, and mass is thrown off in a couple of directions. We know that older and larger radio sources frequently show double structure, so one can envision a model where an object is blown apart, and in this case we see two objects which may be moving apart.

Well, the velocity with which they are moving apart is probably some appreciable fraction of the velocity of light; hence, in the period of the order of a year or so, we should be able to see if they are moving. This is going to answer a lot of questions of what are quasi-stellar sources. It may also answer questions about how far away they are. Although I quoted 5.24×10^{25} meters (1.7 gigaparsecs), there is some question whether they might be closer than that.

We have an experiment coming up in the next months, in which case we will repeat this observation. I should just mention that this observation was made during another program, where we were doing a precise general-relativity test; the results of that experiment have not yet been definitive. However, we fully anticipate that we will be able to resolve the difference between Brans-Dicke relativity and Einstein relativity with that test. We

envision that we should end up with a test which gives a significance of the order of 1 to 2 percent, whereas the difference of those two theories, or very fundamental physical significance, is of the order of 7 percent.

MEMBER OF THE AUDIENCE:

Why should your accuracy be so poor as a few percent in the relativistic experiment, because you have such extraordinary resolutions?

DR. CLARK:

Well, one of the big problems is identifying which of these fringes you are on. In this particular case, we knew that we weren't over one fringe apart on these objects in the center. In the case of the relativity experiment we performed, this same quasi-stellar source, 3C279, is occulted by the sun every October as an annual event. We are doing the general relativity bending with respect to something. The nearest object is about 175 millirad (10 degrees) away; that is 3C273, the first illustration you saw. Ten degrees amounts to several million fringes of separation, and we have to be very careful in keeping track of the change in the number of fringes between the sources. In keeping track of which fringe we are on, many of our uncertainties arise, and it is that part of the analysis that we are in right now in that experiment.

MEMBER OF THE AUDIENCE:

Just a quickie: How do you distinguish between relativistic bending and bending around the sun due to the plasma?

DR. CLARK:

Well, we know that the refraction effects due to the corona are frequency-dependent, whereas the relativistic effects are independent of frequency. A test we did a year ago, which is also still being processed, used two frequencies to separate the effects. However, in this October 1970 experiment, we used a sufficiently high frequency that a simple model will correct for the coronal effects to a rather high degree of accuracy. Typically, we are talking about the refraction effect's being only about 1 percent of the relativistic bending in the range where we made observations.

MEMBER OF THE AUDIENCE:

You said that you can correct the baseline by going back and forth. With about what precision could you measure that 4000-km baseline?

DR. CLARK:

Well, we have measured some other baselines where we have different kinds of data – a little different kind of observing program – and there we demonstrated that we can repeat from now, 6 months from now, to an accuracy of the order of a meter or so. We are hoping to be able to get down to better accuracy than that. That meter is also perspective ground-survey data.

MEMBER OF THE AUDIENCE:

Are those absolutes, or are those some arbitrary constants in such determinations?

DR. CLARK:

No, that one is an absolute number in the particular case I just mentioned. The precision and the accuracy are somewhat in question. We can repeat the measurement to some level; however, we aren't sure yet that we have all the instrumental parameters calibrated out so that we have an accuracy at the same level. However, it looks promising right now at the meter level, and we think we see how to get to the 10-cm level.

MEMBER OF THE AUDIENCE:

This is a comment: The concept of VLBI is being used now, or thought of – there is a lot of thinking going on, on the use of it – in orbit determination, and one of the things that some of the people at Langley are looking at is the use of the two Viking landers in '75 and '76 as the baselines. And if they can use the VLBI concept, they may be able to get a better fix on the polar location for Mars. Just a comment.

DR. CLARK:

We talk about a similar experiment in terms of the ALSEP beacons on the lunar surface, which we are planning to do as soon as there are a pair of

them up, which will occur at the end of this month. Our group did perform the first satellite VLBI, where we observed a satellite in X-band in synchronous orbit to an error box of something like 10 meters on a side. These data are still being analyzed, and we may refine the errors even more.

DR. PIEPER:

With that, I think we have come to the end of our 2-day science and technology symposium. The only event remaining is the reception in the library. For those of you who have been with us from start to finish for two days, I think you deserve a drink. I would like to thank the several speakers, and those who assisted in putting the program together. I ask Dr. Clark – any concluding remarks, sir? If there are no concluding remarks from the boss, we will consider the meeting adjourned. (Applause.)

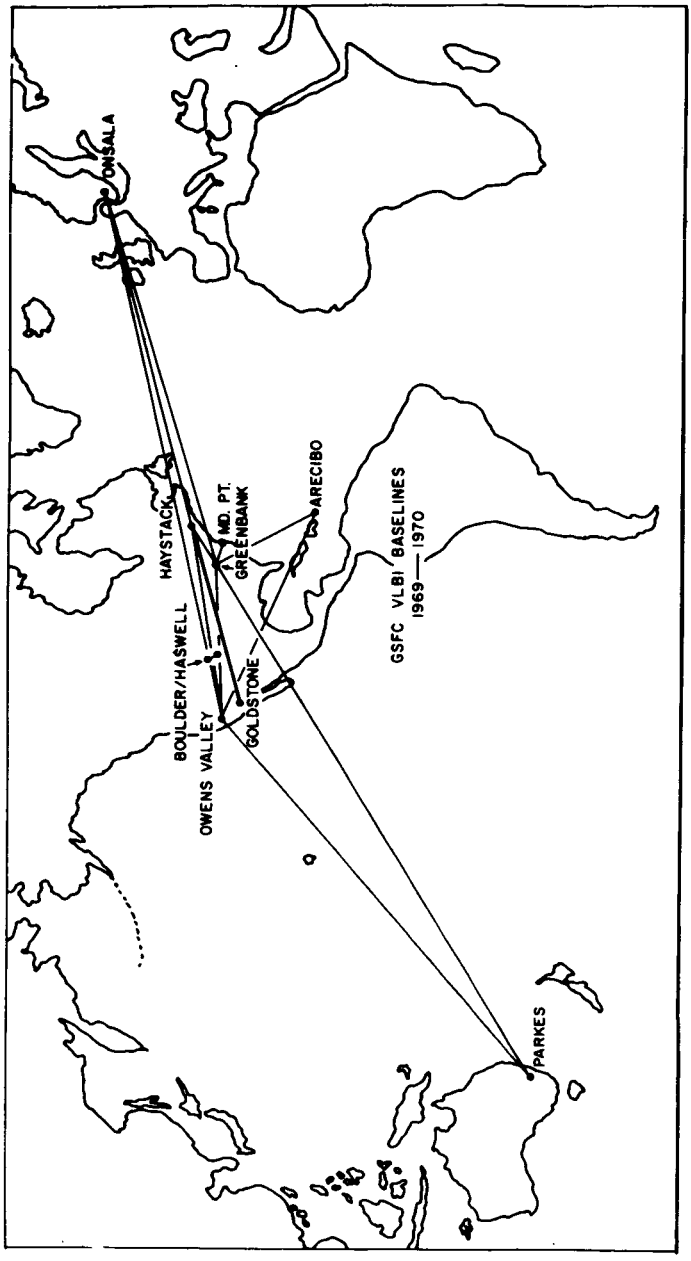
ONSALA
HAYSTACK
MD. PT.
GREENBANK
ARECIBO
GSFC VLBI BASELINES
1969 — 1970
BOULDER/HASWELL
OWENS VALLEY
GOLDSTONE
PARKES

Figure 1

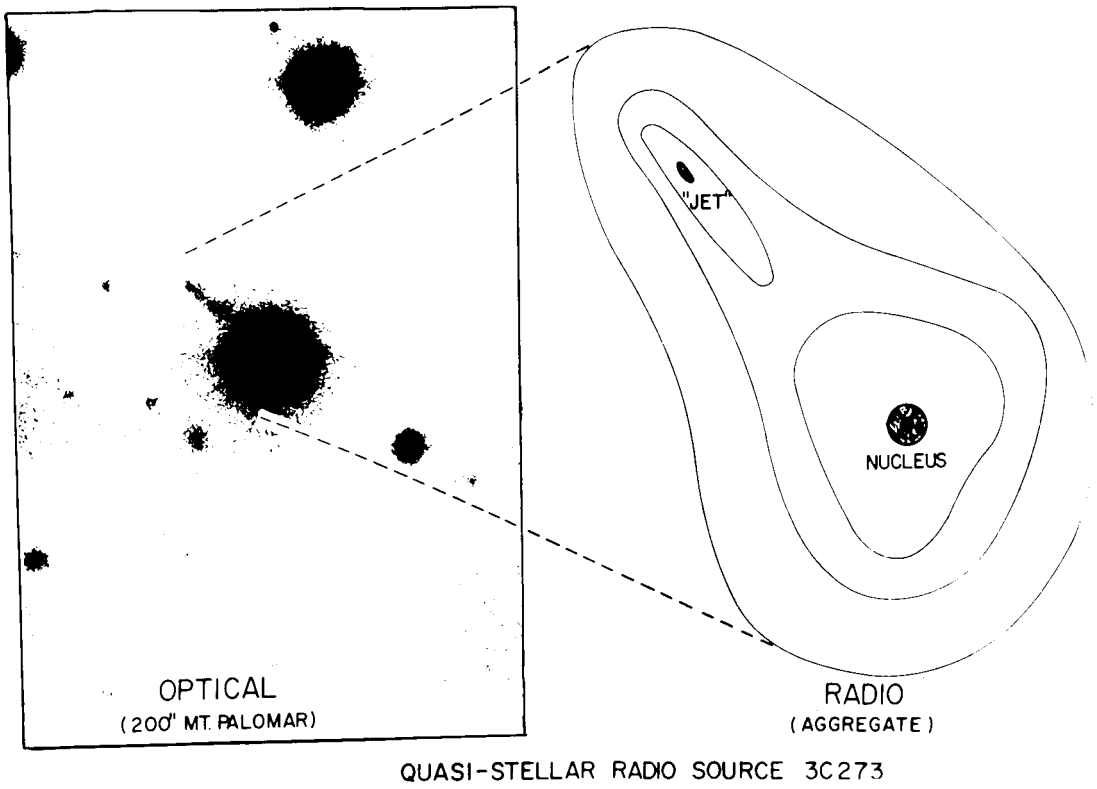
"JET"
NUCLEUS
OPTICAL
(200" MT. PALOMAR)
RADIO
(AGGREGATE)
QUASI-STELLAR RADIO SOURCE 3C273

Figure 2

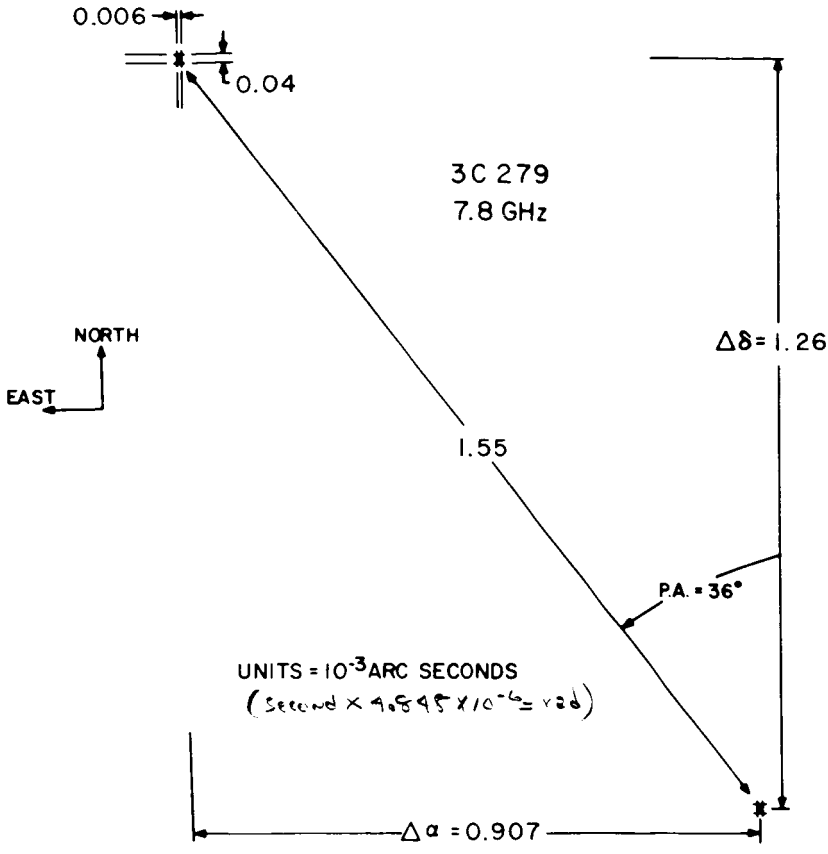

STRUCTURE IN THE NUCLEUS OF THE
QUASI-STELLAR RADIO SOURCE 3C279

(DATA FROM GSFC/MIT HAYSTACK-GOLDSTONE VLBI, OCTOBER, 1970)

Figure 3